Shock and Vibration

Dynamic Analysis and Vibration Control of Mechanical Structures Coupled with Rotational Systems

Lead Guest Editor: Jiaqiang E.
Guest Editors: Kexiang Wei and Kwong Ming Tse

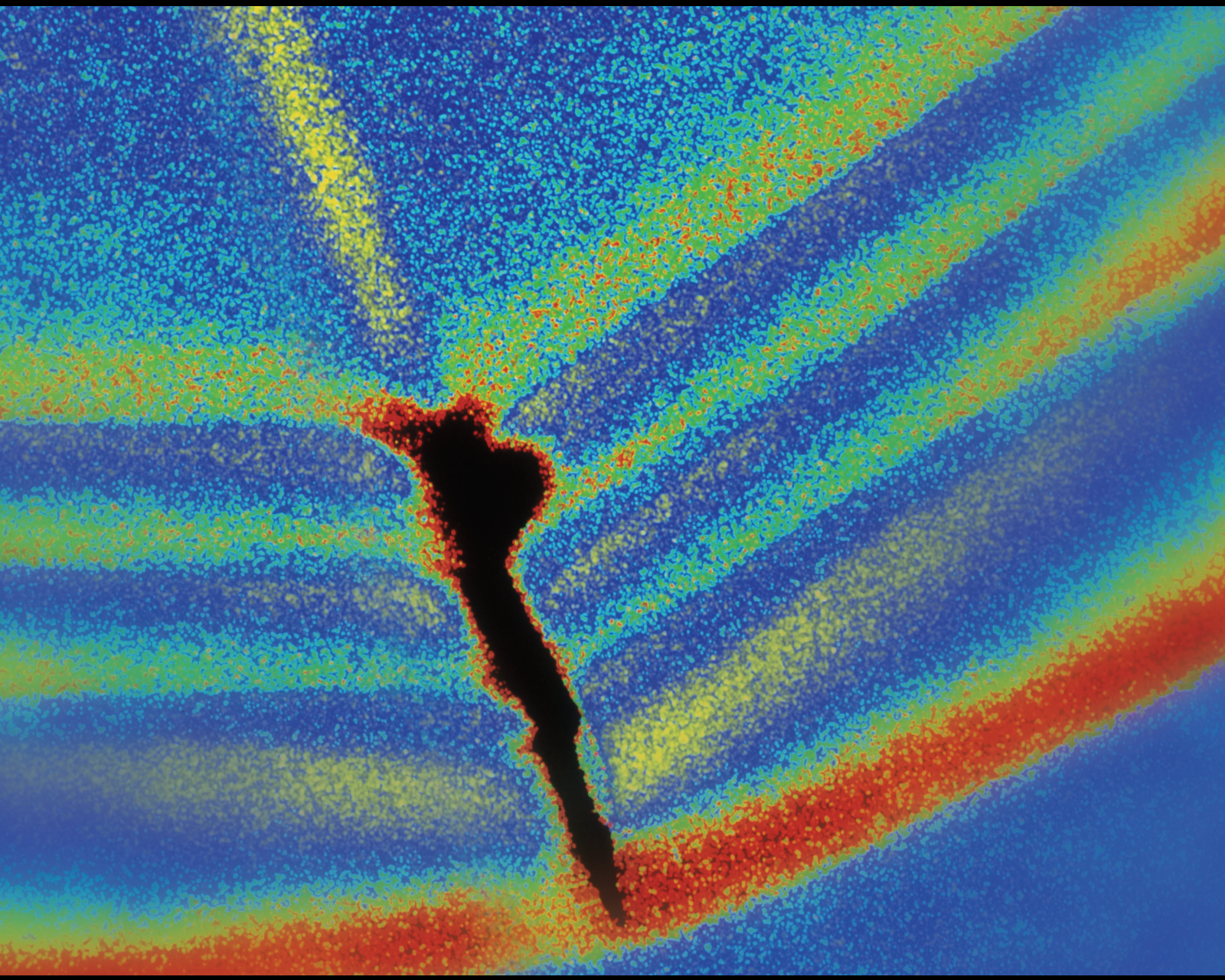

Dynamic Analysis and Vibration Control of Mechanical Structures Coupled with Rotational Systems

Shock and Vibration

Dynamic Analysis and Vibration Control of Mechanical Structures Coupled with Rotational Systems

Lead Guest Editor: Jiaqiang E.
Guest Editors: Kexiang Wei and Kwong Ming Tse

Chief Editor

Associate Editors

Academic Editors

Contents

Generation and Evolution Conditions of Polygonal Wear of High-Speed Wheel

Yahong Dong and Shuqian Cao

Research Article (10 pages), Article ID 6793351, Volume 2021 (2021)

Hindawi
Shock and Vibration
Volume 2022, Article ID 2924836, 19 pages
https://doi.org/10.1155/2022/2924836

Research Article

Seismic Performance Assessment of Ordinary Moment Resisting Frame Equipped with Viscous Dampers under Pulse-Like Earthquakes

Amir Yousefpour, Hamid Mazidababdi Farahani, and Mohsen Ali Shayanfar

Department of Civil Engineering, Iran University of Science and Technology, Tehran, Iran

Correspondence should be addressed to Amir Yousefpour; amir_yousefpour@cmps2.iust.ac.ir

Received 17 October 2021; Accepted 27 January 2022; Published 31 March 2022

Academic Editor: Jiaqiang E

In conventional structures, the earthquake-resistant design is based on flexibility after yielding of structural members to provide a loss of earthquake input energy, while, using dampers, the input energy loss can be concentrated in predetermined points to prevent the nonlinear behavior of the main members that are also in the gravity bearing path. However, near-fault earthquakes might cause unexpected failure and severe structural damage, especially those with the pulse-like effect. A pulsed movement in the near field records in this system will, however, result in unusual behavior. Technology advances and the creation of vibration control systems have helped control this type of behavior since the earthquake forces are applied indirectly to the structure. For further investigation of this issue, in this study, some traditional two-dimensional frames were modeled for 3, 8, and 12 floors. Seven near-fault pulsed and seven far-fault nonpulsed accelerometers are applied. The structural behavior in four modes is examined: (1) without damper and soil-structure interaction effect, (2) without damper and considering soil-structure interaction effect, (3) with damper and considering soil-structure interaction, and (4) with damper without considering soil-structure interaction. Each model is analyzed in OpenSees software under incremental dynamic analysis. Then, the fragility curve is plotted based on the results. The results indicate that frame (4) reaches the failure level at a higher spectral acceleration, which means that the performance of the viscous damper in reducing drift between floors is one of the main criteria for predicting damages. It also shows the effect of soil-structure interaction on increasing the drift between floors and reaching failure at lower spectral acceleration in all models. Also, by comparing the fragility curves of the models under near-field and far-field records, it is found that the probability of failure under far-field documents (without pulse) is less than that under near-field documents (with a pulse).

1. Introduction

During ground motions, much energy is applied to the structure. If this energy exceeds the capacity, it will cause damage to the member and eventually the entire network. On the other hand, long-period pulses in near-field earthquakes weaken the performance of systems. Many researchers like MacRae et al. [1], Tothong and Cornell [2], Alavi and Krawinkler [3], Hall et al. [4], Champion and Liel [5], and Özuygur and Noroozinejad [6] have examined the dynamic response of the structures in the near-fault region. The key conclusion regarding the effect of near-fault ground motions on structural response is that near-fault pulse-like records tend to increase the displacement response in structures relative to nonpulse-like movements. These displacement demands could increase structural and nonstructural damage. The pulse-like earthquake generally imposes a high seismic need on the structure, so the damper must resist the earthquake motion. Experiments have demonstrated that dampers can dissipate more than 90% of the total earthquake input energy [7].

For this purpose, an energy dissipation system transfers some of the energy applied to the structure to this device, thus minimizing the damage to the structure. In recent decades, energy dissipation systems in structures have been widely used to reduce the forces caused by earthquakes and

reduce the lateral displacement of buildings within the limits of the code. One type of these consumables, as passive control systems, is viscous dampers, which have attracted the attention of many researchers like Zahrai and Mohammadi [8] and Silwal et al. [9]. A viscous damper consists of a piston with some orifices inside the cylinder containing highly viscous fluid. Energy dissipation of this damper is through pushing viscous fluid out of the orifices. Luo et al. [10] examined the effects of stochastic traffic loads, corrosion, and fatigue on aging polymer composite bridges. In this study, numerical data were used to estimate the fatigue life of a PC bridge and to maintain it as it ages. According to Zhang et al. [11], the time-harmonic point-, ring-, and disc-loadings of the soil at the inner surface and the rigid foundation caused the soil layer to exhibit three-dimensional intensity Green's functions. Liu et al. [12] examined 3-dimensional ground-penetrating radar imaging to detect road cavities in urban areas. Morai-dastjerdi et al. [13] investigated the mesh-free dynamic analysis of FGM sandwich plates resting on an elastic base. Accordingly, Ghaffarzadeh et al. [14] analyzed the seismic response of building frames supplemented with variable orifice dampers under near-fault earthquakes. They found out that the influence of the pulse effect on seismic performance of damper systems has not been well understood because of the individual differences in each near-fault earthquake record. Prasad and Mazumder [15] investigated the seismic response of a set of steel buildings with and without viscous dampers installed in the inner bay for energy dissipation. Viscous dampers were reported to reduce the displacements, which decreased the amount of steel needed for the overall stability. Wang et al. [16] used a gas physisorption test (CO_2 and N_2) to analyze pore heterogeneity and its underlying causes in overmature Wufeng-Longmaxi shales and their isolated organic matter (OM). Jiang et al. [17] studied tectonothermal histories of the Dongpu Depression from thirteen wells to reconstruct Cenozoic tectonothermal histories. Zhang et al. [18] investigated the progress of friction-based seismic isolation and energy dissipation technologies.

The study conducted by Balkanlou et al. [19] demonstrated that the structure with dampers could be designed optimally to justify the cost spent using dampers. Silvestri et al. [20] proposed a five-step procedure for creating viscous dampers to achieve target performance levels. Using viscous dampers to mitigate the pounding of the adjacent buildings was the subject of Milanchian and Hosseini's research [21]. Nonlinear and linear viscous dampers interconnected the buildings to provide vertical seismic isolation. The final results did not indicate a preferable performance of nonlinear viscous dampers over linear viscous dampers. However, the authors revealed that employing appropriate link parameters proportional to mass and stiffness ratios could lead to satisfactory levels of seismic response reduction in cases of both types of dampers. De Demonico et al. [22] gave energy-based perspectives to interpret the seismic performance in terms of the dissipated energy by the viscous dampers out of the total earthquake-induced energy. Xu et al. [23] constructed a model for the coupling of water, heat, and solute transport in saline loess, taking sodium sulfate crystallization into account. Li et al. [24] investigated the feasibility and drawbacks of applying the PFDD technique to combat FDI assaults on power grid state estimates. Wang et al. [25] suggested a novel technique for bioinspired defect diagnostics based on rough sets (RSBFDM). The suggested solution outperforms existing options in experiments conducted on genuine 110 kV and 750 kV substations.

Moreover, in conventional structural analysis and design, the effect of soil beneath the foundation is mainly ignored. However, Ghalami [26] indicates that soil flexibility may have a significant impact on the structural response. Amiri et al. [27] evaluated several three-dimensional steel moment-resisting frames to investigate the effect of soil-structure interaction (SSI) in structural retrofitting. The studied models were considered three-dimensional models of 3-, 7-, and 13-story steel moment-resisting frames. The analysis results showed that considering the soil-structure interaction increases the natural period of the structure. The results also show that the number of buildings' natural period increases in soil-structure interaction. However, this effect can be ignored in low-rise structures. Šago et al. [28] have identified many of the several obstacles that occurred concurrently with the COVID-19 epidemic and the severe earthquake in Zagreb. The findings indicate that quick developments broadened our area of practice without delay during these exceedingly trying times. Xu et al. [29] used the reactive Euler equations coupled with a comprehensive chemical model to study the interactions between two ODWs created by symmetrical finite wedges in hydrogen-air mixtures. Arbabi and Tahghghi [30] simulated multistory building-foundation systems through a Winkler-based approach using OpenSees finite element framework. Four typical 4-, 8-, 12-, and 16-story steel moment-resisting frame (MRF) buildings on three hypothetically soft, medium, and hard soil sites with shear wave velocities less than 600 m/s subjected to actual ground motion records of varied hazard levels are modeled with and without SSI. It is observed that the performance level of models supported by the flexible foundation, particularly in an intense earthquake event, may alter significantly in comparison to fixed-base structures. Moreover, for MRFs on soft soil, the nonlinear foundation is found to have a significant effect on the force and displacement demands. The authors indicate the necessity of considering the SSI effect to accomplish an economical yet safe structural design.

In this study, an ordinary two-dimensional moment-resisting steel frame of 3, 8, and 12 floors was designed under seven near-fault pulsed records and seven far-fault non-pulsed records. Despite the fact that ordinary moment resisting frames are widely used, they do not comply with special detailing requirements for ductile behavior. It is, therefore, essential to evaluate the behavior of these frames in the presence of dampers and SSI effects. The structural behavior was examined in four modes: (1) without damper and soil-structure interaction (SSI) effect; (2) without damper and considering SSI effect; (3) with damper and considering SSI; and (4) with damper without considering SSI. OpenSees software analyzed each model under incremental dynamic analysis (IDA). Then, based on the results of a comprehensive active study, the fragility curve was drawn. Vulnerability levels introduced in HAZUS MH-MR4 [31]

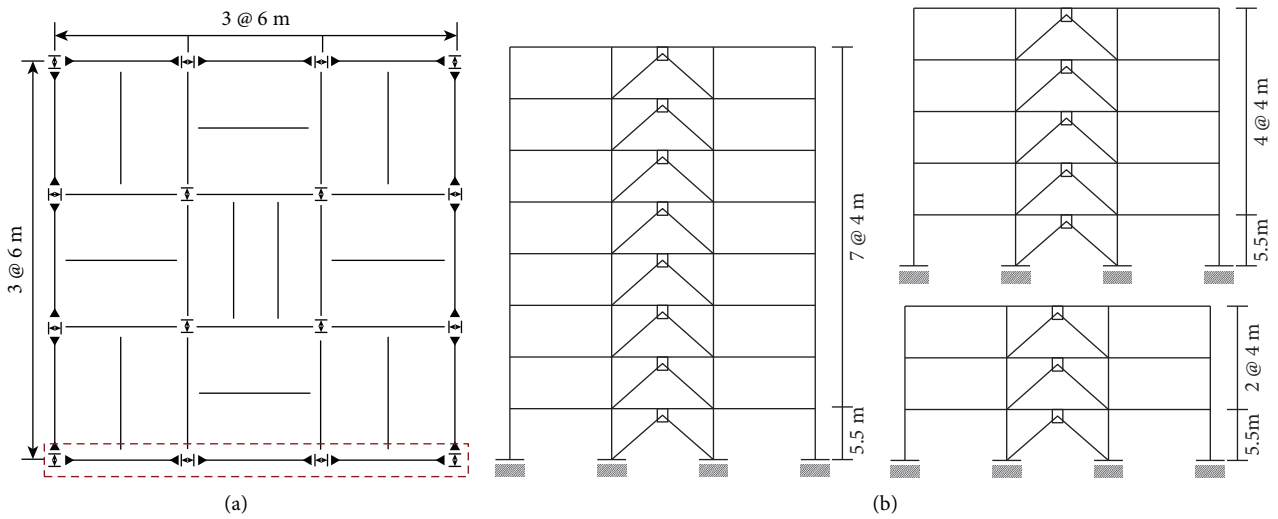

Figure 1: An analysis of model structures: (a) structural plans; (b) elevations of structures that include dampers [34].

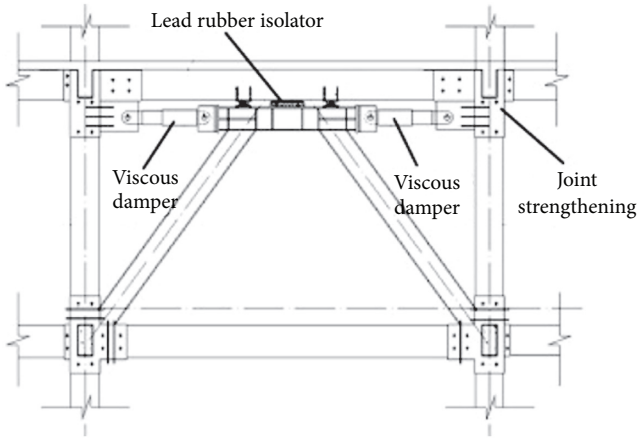

Figure 2: Configuration of viscous dampers [35].

Table 1: Basic information of studied buildings.

No. Stories	Fundamental period	Added damping ratio	Reflection coefficient	Seismic coefficient
3-Story	0.5454	0.1	2.75	0.165
8-Story	1.1381	0.1	1.848	0.1109
12-Story	1.5425	0.1	1.471	0.0883

were used to investigate different failure modes in the models. Finally, the performance of the building-damper system under near-fault pulsed-like earthquakes and the SSI effect are systematically investigated.

2. Details of Steel Frames, Modeling, and Analysis

In this research, three ordinary moments resisting steel frames of 3, 8, and 12 stories are modeled by the LRFD method [32]. Each frame has three openings with 5 meters and a floor height of 3.2 meters. The dead load in the structure's design was 500 kg/m, and the live load was 200 kg/m [33]. HEB profile was used for column design, and IPE profile was used for beam. Double channel is used for bracing elements (see Figure 1).

Also, for Incremental Dynamic Analysis (IDA), by assigning values of 0.1 g to 3 g for each acceleration, the analyses were performed for four modes of the frame, frame with damper, frame with soil-structure interaction, and frame with damper and soil-structure interaction.

Dampers were considered as diagonal members, as part of a chevron brace, horizontally at the top. The horizontal chevron configuration is applied here, as shown in Figure 2.

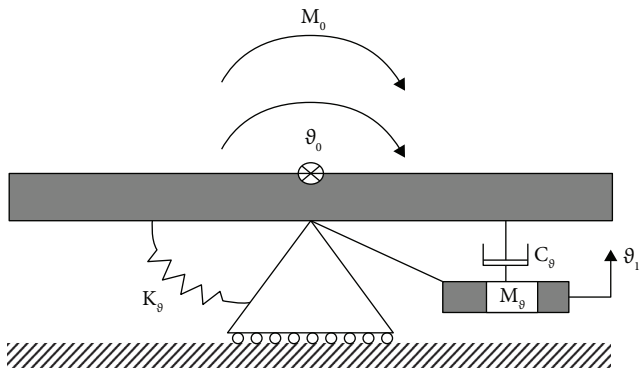

Figure 3: Spring-dashpot-mass model with an additional internal degree of freedom for the rotational degree of freedom [37].

Table 2: Detailed parameters for the springs used to consider the SSI effect.

	Spring stiffness	γ_0	μ_0
Vertical	$4G.r_0/1-u$	0.58	0.095
Horizontal	$8G.r_0/1-u$	0.85	0.27
Rocking	$8G.r_0^3/3\,(1-u)$	$1+\frac{0.3/3\,(1-\nu)m}{8r_o 5p}$	0.24

This system was proposed by Lu and Zhou and tested on a shaking table in 2002 [35]. Two viscous dampers are installed in a parallel way and supported by a steel chevron brace. Lead rubber bearings are installed at the top of the brace to keep the brace's stability and dissipate the energy under minor earthquakes.

The added damping ratio, reflection coefficient, seismic coefficient, and entire period of the studied buildings are summarized in Table 1. It is necessary to explain that the additional damping ratio is an important indicator for evaluating the damping effect of structures with energy-dissipation devices [36].

For modeling in OpenSees software, viscous material was used to design the damper. The Winkler model (BNWF) was modeled on the soil and foundation system linearly and nonlinearly. The infinite underlying soil medium is modeled using the concept of Cone Models with vertical, horizontal, and rocking degrees of freedom, as shown in Figure 3 and Table 2. A spring and a damper are introduced for each degree of freedom, which shows the effect of soil on that degree of freedom.

Selecting the appropriate seismic and failure intensity parameters to use IDA analysis is important and influential. Also, the selection of a proper seismic intensity parameter, in addition to causing less scattering and thus greater generality of the response created in the structure under the effect of earthquake records, must include the dynamic characteristics of a document such as frequency content and energy (Vamvatsikos and Cornell, 2002) [38]. To enter the main rotation time of the structure into the field of scaling records and consider the parameters of vibration and damping time, the spectral acceleration of the first model of the structure Sa (T_1) has been used as a measure of seismic intensity.

In this study, failure modes defined in the HAZUS MH-MR4 guidelines were used (National Institute of Building Sciences, 2004). Failure modes were introduced in the HAZUS instruction for steel buildings with a moment frame system with low and medium. In high stories, four failure modes are considered based on the Interstory DRIFT ratio: slight mode and moderate, extensive failure mode, and complete failure mode. Numerical values for each failure mode are presented in the Table 3 (see Table 3).

The DRIFT value obtained for each model under each of the earthquake records is compared with the values presented in the table above to check the arrival or passage of each model in each PGA value to each of these failure states.

(i) Fragility curve: to draw the fragility curve, a fragility function is required. The fragility function is a conditional probability, which expresses the possibility of failure of a structure at a certain level of failure or beyond for a given earthquake intensity. When the seismic requirements and structural capacity follow the normal log probability distribution, the fragility equation according to the HAZUS instruction is given as follows:

Table 3: Interstory Drift ratio in 4 failure modes according to HAZUS.

Type	Slight	Moderate	Extensive	Complete
S1L	0.006	0.012	0.03	0.08
S1M	0.004	0.008	0.02	0.0533
S1H	0.003	0.006	0.015	0.04

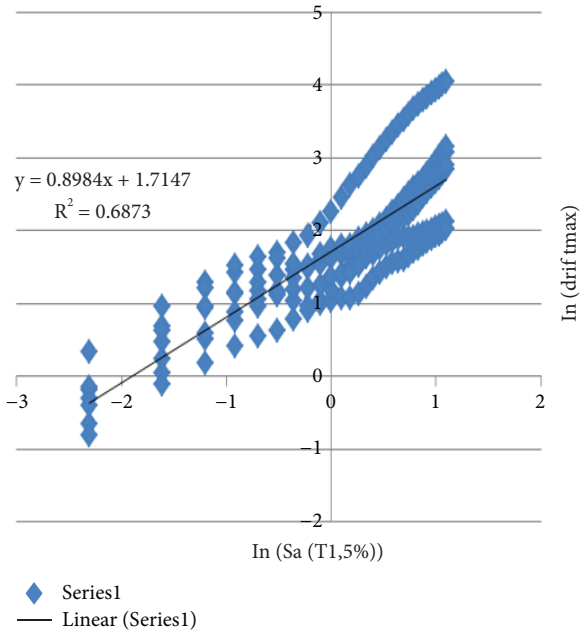

Figure 4: Maximum probabilistic seismic requirement for the relative displacement of floors.

Table 4: Different types of Steel moment frames in HAZUS MH-MR4 instruction.

Models name	Type of structural system		Number of stories
S1L	Steel moment frame	Low-rise	1–3
S1M		Mid-rise	4–7
S1H		High-rise	+8

$$P[C - D \leq 0.0|IM] = \varphi\left[\frac{\ln\left(S_d/S_c\right)}{\sqrt{\beta_{DI\ M}^2 + \beta_C^2}}\right]. \quad (1)$$

Respectively, the standard logarithm deviations are in capacity and need. The mean value of the limit state or seismic capacity and the mean value of the seismic requirement are the Intensity Measure (IM) function and the normal cumulative distribution function. The discount is combined according to the HAZUS instructions and converted to a parameter. Finally, the fragility relationship is written as follows:

Table 5: Values provided for S_c and β_{sd} for Steel moment frames in HAZUS MH-MR4 instruction.

Type	S_c	$_{sd}\beta$	S_c	$_{sd}\beta$	S_c	$_{sd}\beta$	S_c	$_{sd}\beta$
S1L	1.3	0.80	2.59	0.76	6.48	0.69	17.28	0.72
S1M	2.16	0.65	4.32	0.66	10.80	0.67	28.80	0.74
S1H	3.37	0.64	6.74	0.64	16.85	0.65	44.93	0.67

Table 6: Near-field earthquakes characteristics.

Record no.	Earthquake name	Station	Occurrence time	Magnitude	Epicentral distance (km)
1	Chi-chi, Taiwan	TCU120	1999	7.62	9.96
2	Darfield, New Zealand	Lincoln School	2010	7	5.28
3	Imperial Valley-06	El Centro Array #4	1979	6.53	4.9
4	Kobe, Japan	CEOR Station	1995	6.9	3.31
5	Morgan Hill	Gilroy Array #6	1984	6.19	3.45
6	Northridge-01	Pacoima Dam	1994	6.69	3.16
7	Parkfield-02, CA	CSMIP station 36419	2004	6	4.81

Table 7: Far-field earthquakes characteristics.

Record no.	Earthquake name	Station	Occurrence time	Magnitude	Epicentral distance (km)
8	Cape Mendocino	CSMIP station 89156	1992	7.01	16.54
9	Friuli, Italy-01	Bolzano	1976	6.5	33.32
10	Imperial Valley-06	Niland Fire Station	1979	6.53	35.2
11	Landers	Yermo Fire Station	1992	7.28	26.96
12	Northridge-01	LA - Saturn st	1994	6.69	27.0
13	San Fernando	OWNER station 0220	1971	6.61	22.77
14	Tabas, Iran	Dayhook	1978	7.35	24.07

$$Pf = \varphi\left[\frac{\ln\left(S_d/S_c\right)}{\beta_{s\,d}}\right]. \quad (2)$$

The parameter S_d is the average value of the seismic requirement obtained from the following equation:

$$\ln\left(S_d\right) = a.\ \ln\left(IM\right) + b. \quad (3)$$

In this equation, IM is the measure of seismic intensity, considered $\mathrm{Sa}(T_1)$ in this paper. a and b are regression coefficients obtained through linear regression analysis with the number of damage situations against different Sa. The X-Axis is the spectral acceleration parameter corresponding to the structure's first mode for each step. Its Y-axis is the logarithm of the criterion of maximum damage intensity and the relative displacement of the floors in each step. Figure 4 shows an example of the relationship between Sa (T_1) and the Engineering Demand Parameter (EDP), which is the maximum relative displacement of the floors in a logarithmic environment.

The values in the HAZUS MH-MR4 instruction are given for different types of constructions and other failure modes, which are shown in the following table (Tables 4–7).

3. Earthquake Excitations

The earthquake record selection should be made so that the analysis results include all the behavioral states of the structure in the range of elastic, plastic, and complete failure [39] although the soil type should be the same for the selected records so that the documents have a good resemblance to each other. The higher the number of forms used, the more valid the analysis results. On the other hand, adding the number of records will increase the analysis time and output volume. Therefore, seven near-field accelerometers and seven far-field accelerometers with the following characteristics have been used in this research [40].

The selected earthquakes have the following specifications:

(i) Occur in soil type 3.

(ii) Magnitude between 6 and 9 Richter.

(iii) Epicentral distance for near-field earthquakes is below 10 km, and for far-field earthquakes, it is above 15 km.

(iv) To maintain the seismic parameter of near-fault ground motions, they are not scaled [41].

4. Results

In the following, the analysis results of two-dimensional 3-, 8-, and 12-story steel moment frames in the form of IDA curves in 16%, 50%, and 84% percentiles and fragility curves are presented.

4.1. Three-Story Frame. The summary of the IDA curve with 16%, 50%, and 84% percentiles and fragility curves in a 3-

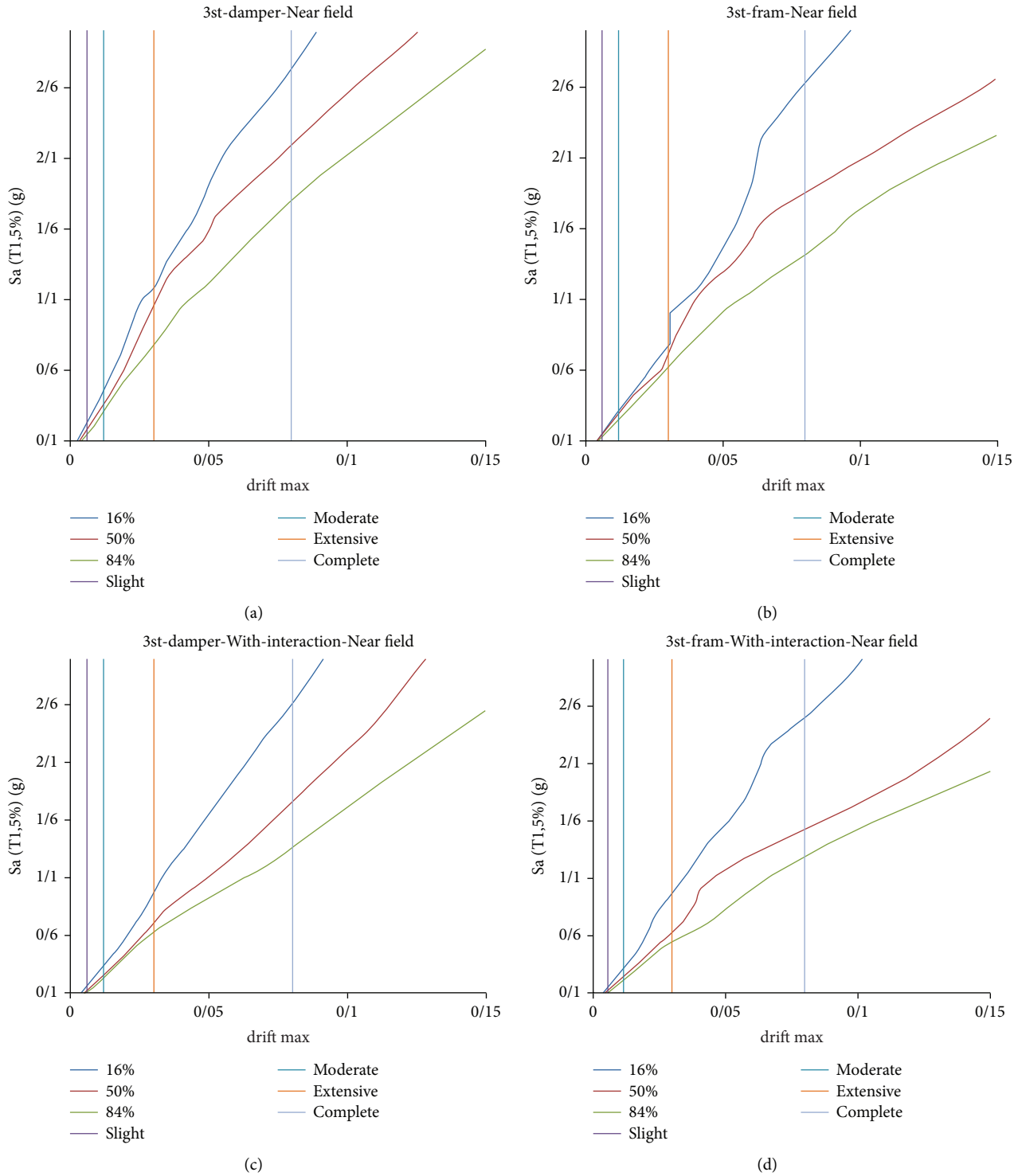

Figure 5: Summary of IDA curves for 16%, 50%, and 84% percentiles in 3-story Ordinary moment resisting frame affected by near-field earthquakes. Examined cases: (a) with damper without considering SSI; (b) without Damper and SSI effect; (c) with damper and considering SSI; (d) without damper but considering SSI effect.

story frame under seven pairs of near-field and far-field earthquakes is presented.

As can be seen, the slope of the linear region in the (a) case, with damper and without considering SSI, is less than that in other cases, which shows a softer behavior. In the case of the damper, it enters the collapse region at a higher acceleration, which indicates better performance than other cases. Considering that the criterion of damage is interstory drift, the results of the above diagram show that the frame with damper reaches the level of failure at a higher spectral

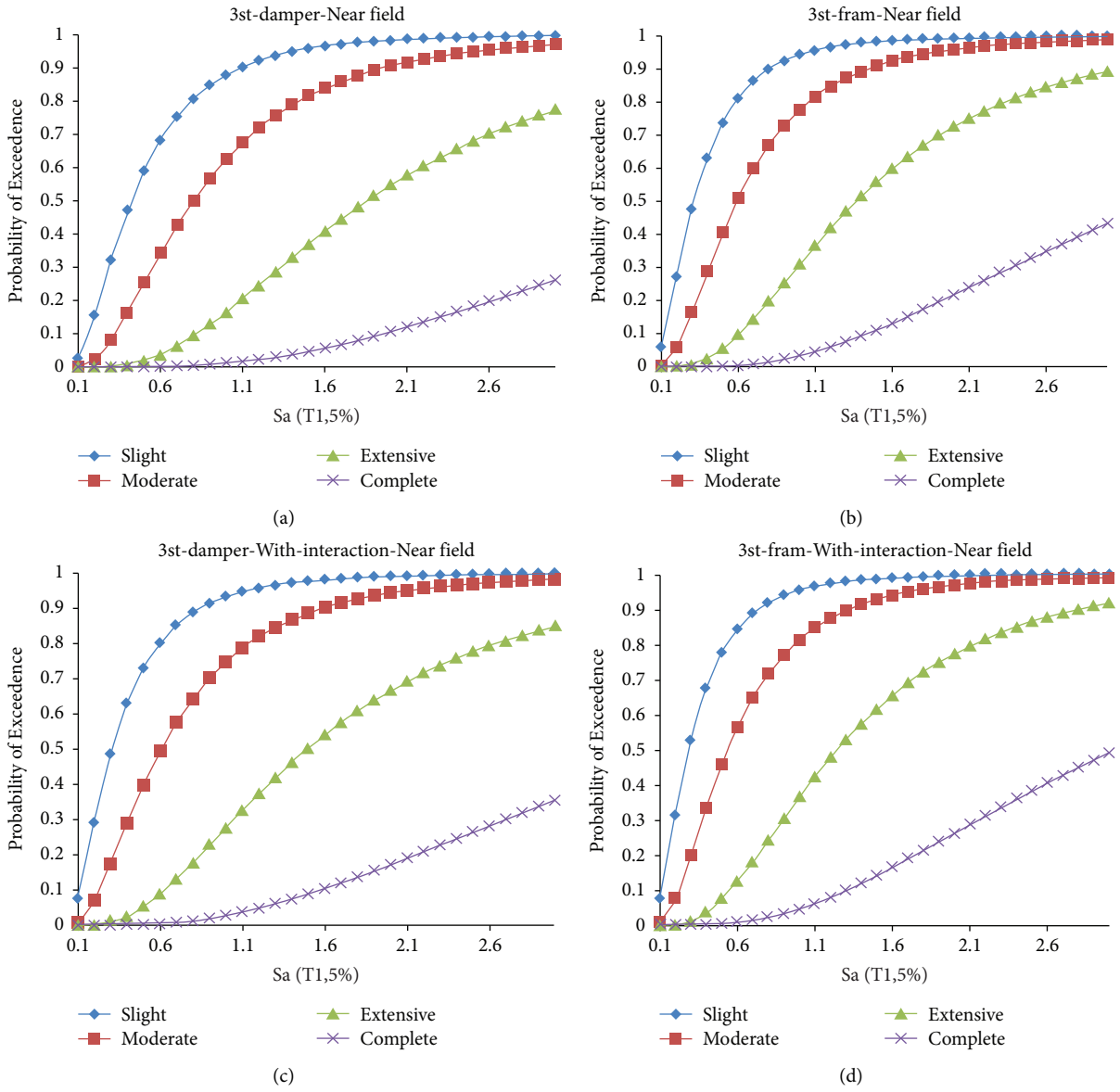

Figure 6: Fragility curves in 3-story ordinary moment resisting frame affected by near-field earthquakes. Examined cases: (a) with damper without considering SSI; (b) without Damper and SSI effect; (c) with damper and considering SSI; (d) without damper but considering SSI effect.

acceleration, respectively, compared to the frame without soil-structure interaction, the frame with soil-structure interaction, and the damper and the frame with interaction. This indicates the damper's performance in reducing interstory drift as one of the criteria for predicting damage and shows the effect of soil-structure interaction on increasing displacement between floors and reaching the level of failure at lower spectral acceleration. The fragility curves of 3-story frames under seven pairs of near-field acceleration are shown in Figures 5 and 6.

The fragility curve shows that the probability of structural failure in low failure mode occurs in less Sa values, and moderate, extensive, and complete failure modes occur in higher Sa values. In all curves, for low and moderate failure situations, the slope of the curve is first increased and then decreased. For extensive failure mode, the angles change with an almost uniform slope. For complete failure mode, the slope changes are extremely small. According to the coefficient of acceleration scale of near field earthquakes for 3-story structures, fragility occurs at a spectral acceleration of 1.284 g for type three soil. The results also show that soil-structure interaction has a significant effect on increasing the probability of structural failure. Also, dampers in both cases with and without soil-structure interaction reduce the likelihood of failure. In the following, a summary of the IDA curve of a 3-story frame under seven pairs of far-field earthquakes is shown in Figure 7.

The slope of the linear region in case (a), with damper and without SSI, is less than that in other states, which shows a softer behavior. In the cases with the damper, it enters the

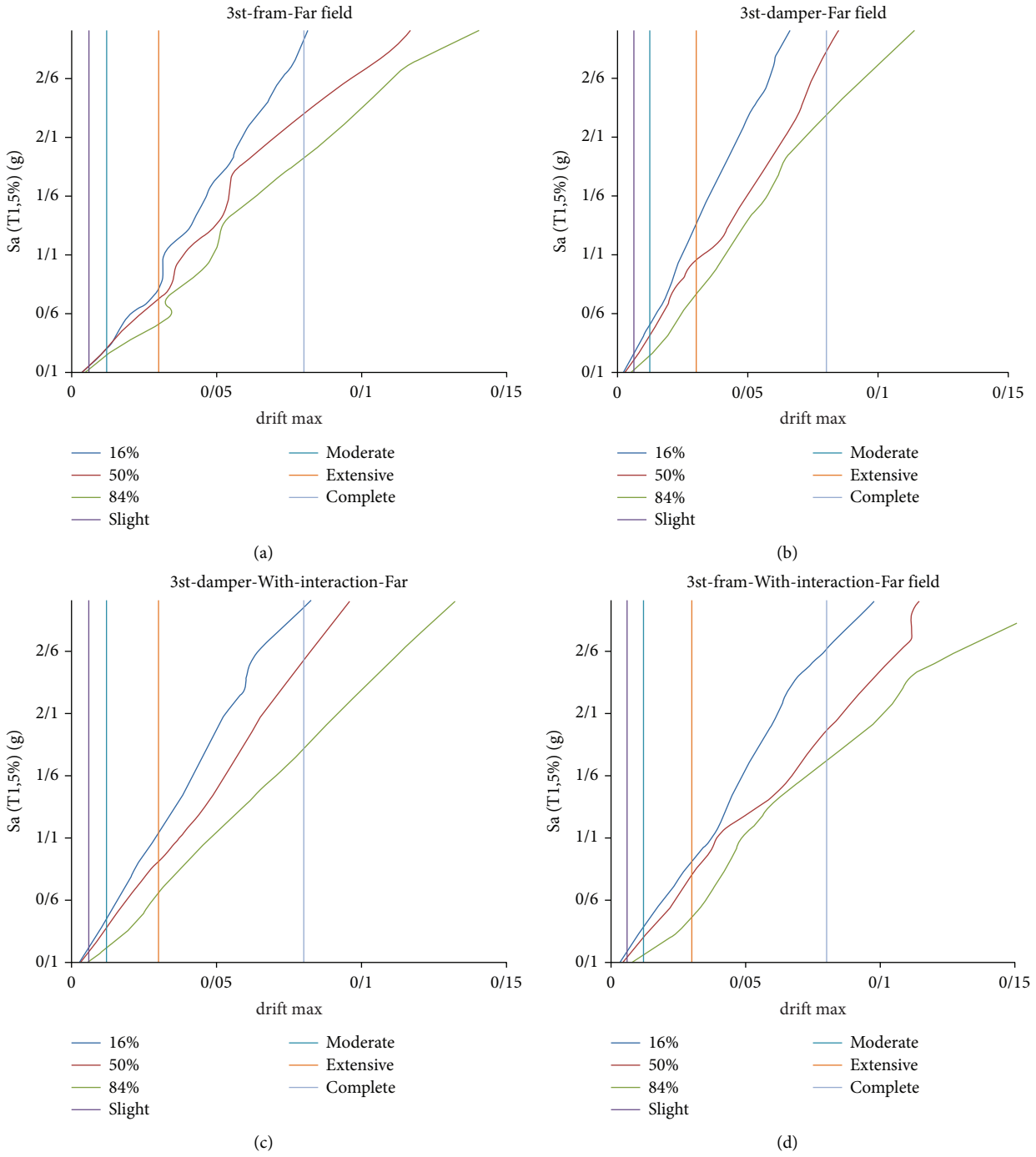

Figure 7: Summary of IDA curves for 16%, 50%, and 84% percentiles in 3-story ordinary moment resisting frame affected by far-field earthquakes. Examined cases: (a) with damper without considering SSI; (b) without Damper and SSI effect; (c) with damper and considering SSI; (d) without damper but considering SSI effect.

collapse region at a higher acceleration, which indicates better performance than other cases. Considering that the criterion of damage is interstory drift, the results show that the frame with damper reaches the level of failure at a higher spectral acceleration, respectively, compared to other frames. This indicates the damper's performance in reducing displacement between floors as one of the criteria for predicting damage and shows the effect of soil-structure interaction on increasing drift between floors and reaching the level of failure at lower spectral acceleration. The fragility curves of 3-story frames under seven pairs of far-field earthquakes are shown in Figure 8.

The fragility curve shows that the probability of structural failure in low failure mode occurs in less Sa values, and moderate, extensive, and complete failure modes occur in higher Sa values. In all curves, for low and moderate failure situations, the slope of the curve is first increased and then decreased. For extensive failure mode, the curves change

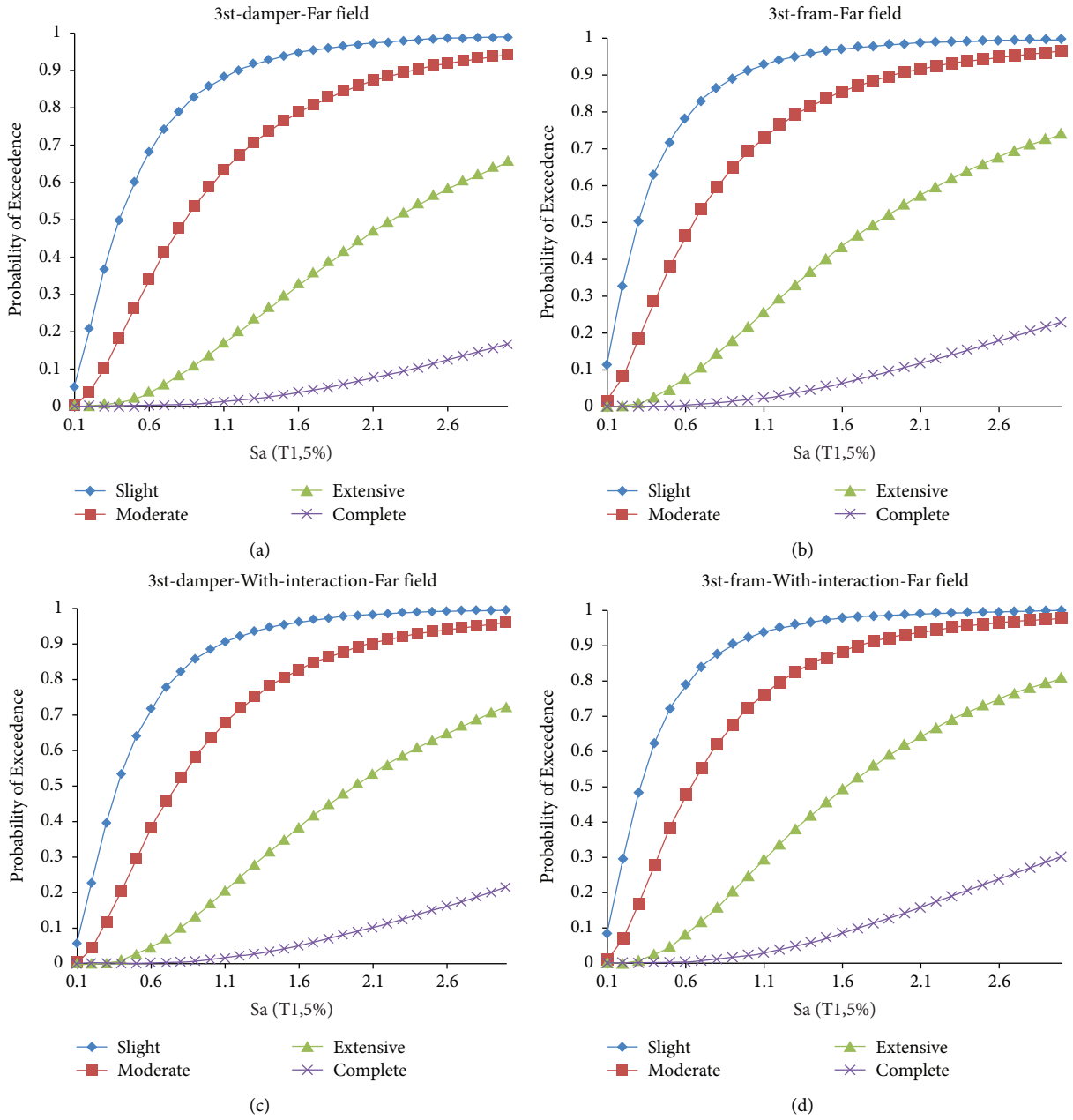

Figure 8: Fragility curves in 3-story ordinary moment resisting frame affected by far-field earthquakes. Examined cases: (a) with damper without considering SSI; (b) without Damper and SSI effect; (c) with damper and considering SSI; (d) without damper but considering SSI effect.

with an almost uniform slope. For complete failure mode, the slope changes are extremely small. According to the coefficient of acceleration scale of far-field earthquakes for 3-story structures, fragility occurs at a spectral acceleration of 1.63 g for type three soil. The results also show that soil-structure interaction has a significant effect on increasing the probability of structural failure. Also, dampers in both cases with and without soil-structure interaction reduce failure likelihood.

4.2. Eight Story Frame. The summary of the IDA curve with 16%, 50%, and 84% percentiles and fragility curves in an 8-story frame under seven pairs of near-field and far-field earthquakes is presented in Figure 9.

In an 8-story OMRF structure, like the previous models, the slope of the linear region in case (a), with damper and without SSI, is less than that in other states, which shows a softer behavior. In the cases with the damper, it enters the collapse region at a higher acceleration, which indicates better performance than other cases. Considering that the criterion of damage is interstory drift, the results show that the frame with a damper reaches the level of failure at a higher spectral acceleration than other frames. This indicates the damper's performance in reducing displacement

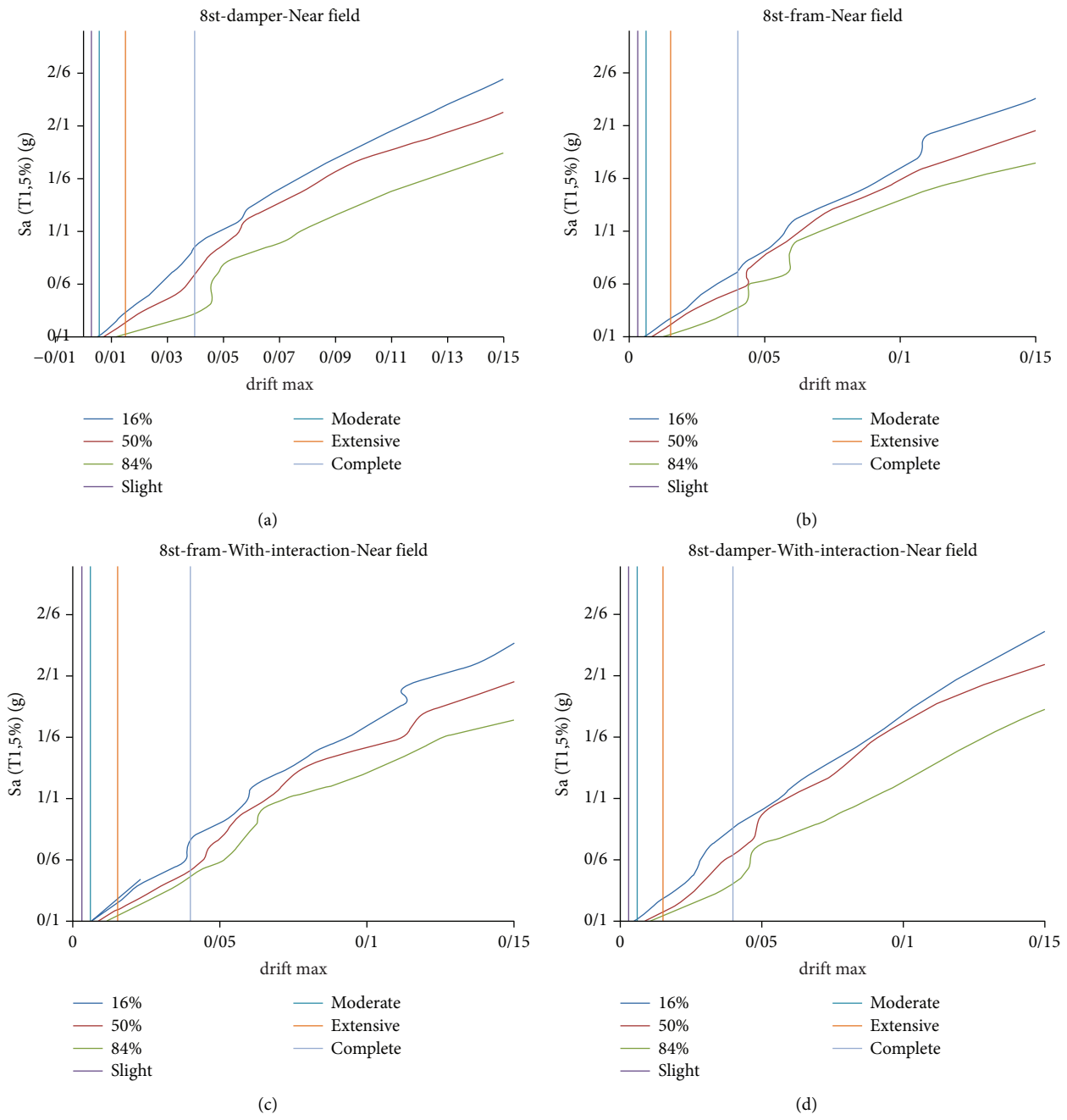

Figure 9: Summary of IDA curves for 16%, 50%, and 84% percentiles in 8-story ordinary moment resisting frame affected by near-field earthquakes. Examined cases: (a) with damper without considering SSI; (b) without damper and SSI effect; (c) with damper and considering SSI; (d) without damper but considering SSI effect.

between floors as one of the criteria for predicting damage and shows the effect of soil-structure interaction on increasing drift between floors and reaching the level of failure at lower spectral acceleration. The fragility curves of 8-story frames under seven pairs of near-field earthquakes are shown in Figure 10.

The fragility curve shows that the probability of structural failure in low failure mode occurs in less Sa values, and moderate, extensive, and complete failure modes occur in higher Sa values. In all curves, for low and moderate failure situations, the slope of the curve is first increased and then decreased. For extensive failure mode, the curves change with an almost uniform slope. For complete failure mode, the slope changes are extremely small. According to the coefficient of acceleration scale of far-field earthquakes for 3-story structures, fragility occurs at a spectral acceleration of 1.276 g for type three soil. The results also show that soil-structure interaction has a significant effect on increasing the

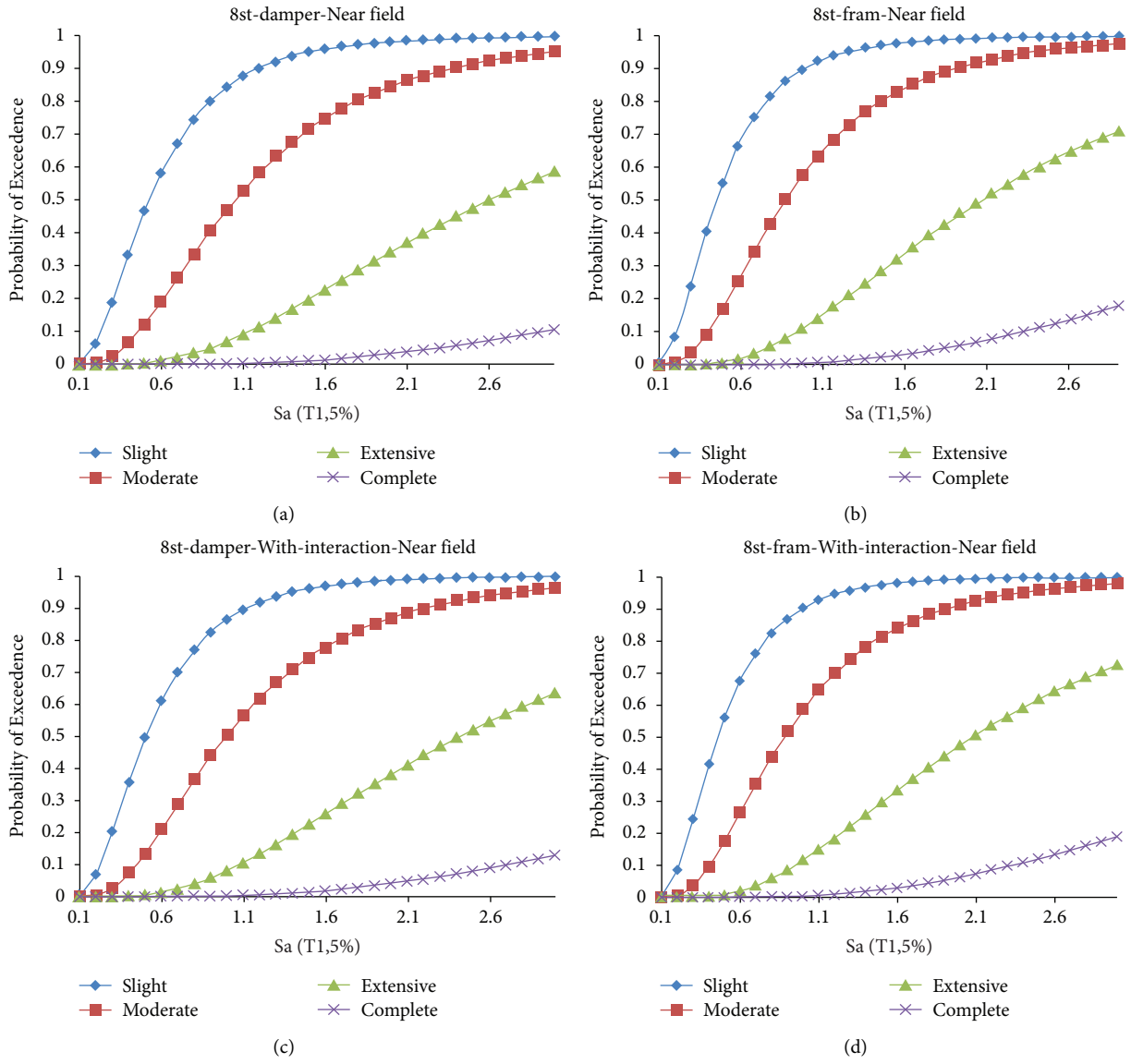

Figure 10: Fragility curves in 8-story ordinary moment resisting frame affected by near-field earthquakes. Examined cases: (a) with damper without considering SSI; (b) without damper and SSI effect; (c) with damper and considering SSI; (d) without damper but considering SSI effect.

probability of structural failure. Also, dampers in both cases with and without soil-structure interaction reduce failure probability. A summary of the IDA curve of a 3-story frame under seven pairs of far-field earthquakes is shown in Figure 11.

In the 8-story OMRF structure affected by far-field earthquakes, like the previous models, the slope of the linear region in the case (a), with damper and without SSI, is less than that in other states, which shows a softer behavior. In the cases with the damper, it enters the collapse region at a higher acceleration, which indicates better performance than other cases. Considering that the criterion of damage is interstory drift, the results show that the frame with damper reaches the level of failure at a higher spectral acceleration, respectively, compared to other frames. This indicates the damper's performance in reducing displacement between floors as one of the criteria for predicting damage and shows the effect of soil-structure interaction on increasing drift between floors and reaching the level of failure at lower spectral acceleration. The fragility curves of 8-story frames under seven pairs of far-field earthquakes are shown in Figure 12.

The figures mentioned above indicate that the probability of structural failure in low failure mode occurs in less Sa values, and moderate, extensive, and complete failure modes occur in higher Sa values. In all curves, for low and moderate failure situations, the slope of the curve is first increased and then decreased. For extensive failure mode, the curves change with an almost uniform slope. For complete failure mode, the slope changes are extremely small. According to the coefficient of acceleration scale of far-field earthquakes for 3-story structures, fragility occurs at a spectral acceleration of 2.12 g for type three soil. The results also show that soil-structure

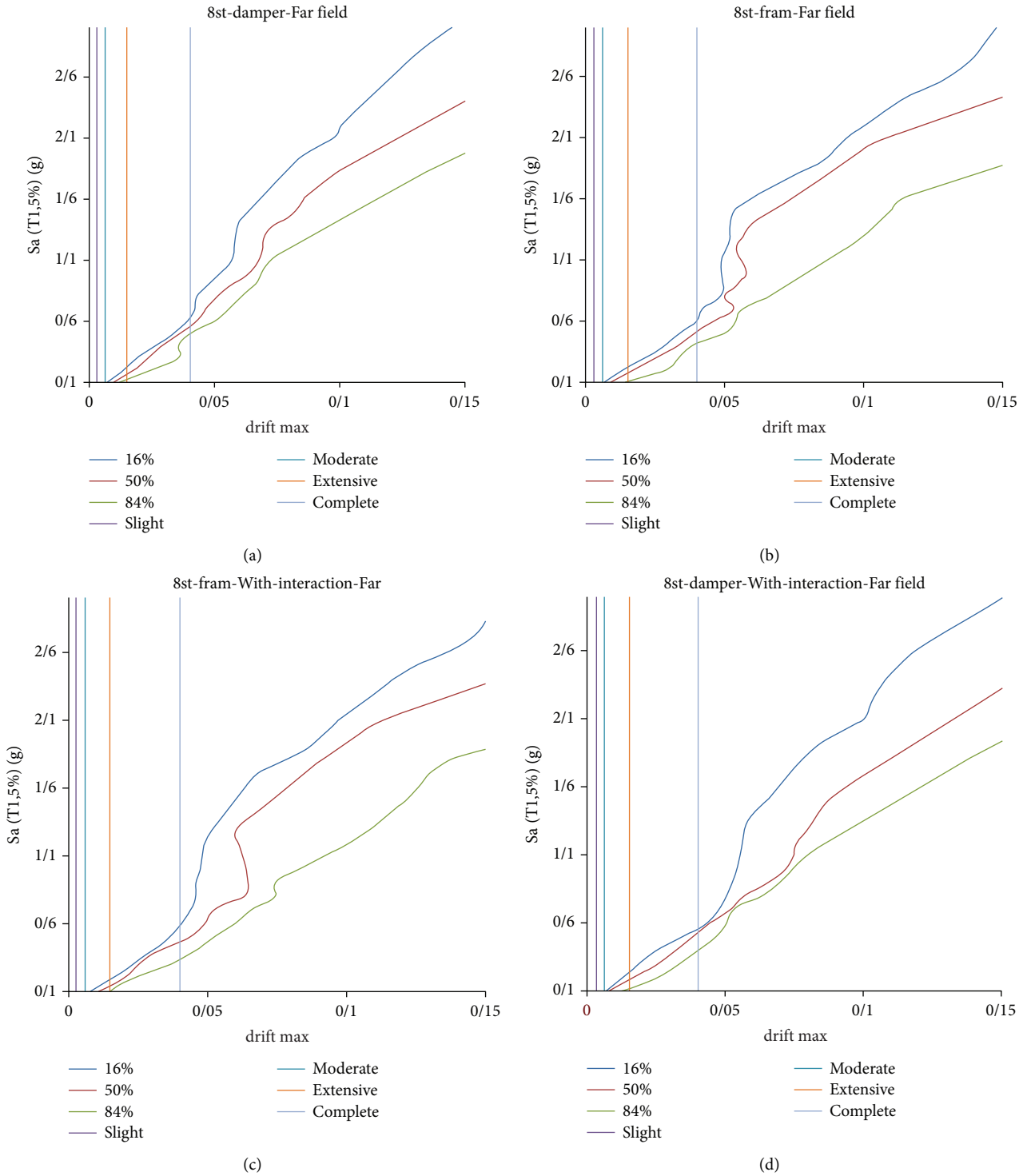

Figure 11: Summary of IDA curves for 16%, 50%, and 84% percentiles in 8-story ordinary moment resisting frame affected by far-field earthquakes. Examined cases: (a) with damper without considering SSI; (b) without damper and SSI effect; (c) with damper and considering SSI; (d) without damper but considering SSI effect.

interaction has a significant effect on increasing the probability of structural failure. Also, dampers in both cases with and without soil-structure interaction reduce the likelihood of failure.

4.3. 12-Story Frame. The summary of the IDA curve with 16%, 50%, and 84% fractiles and fragility curves in a 12-story frame under seven pairs of near-field and far-field earthquakes is presented in Figure 13.

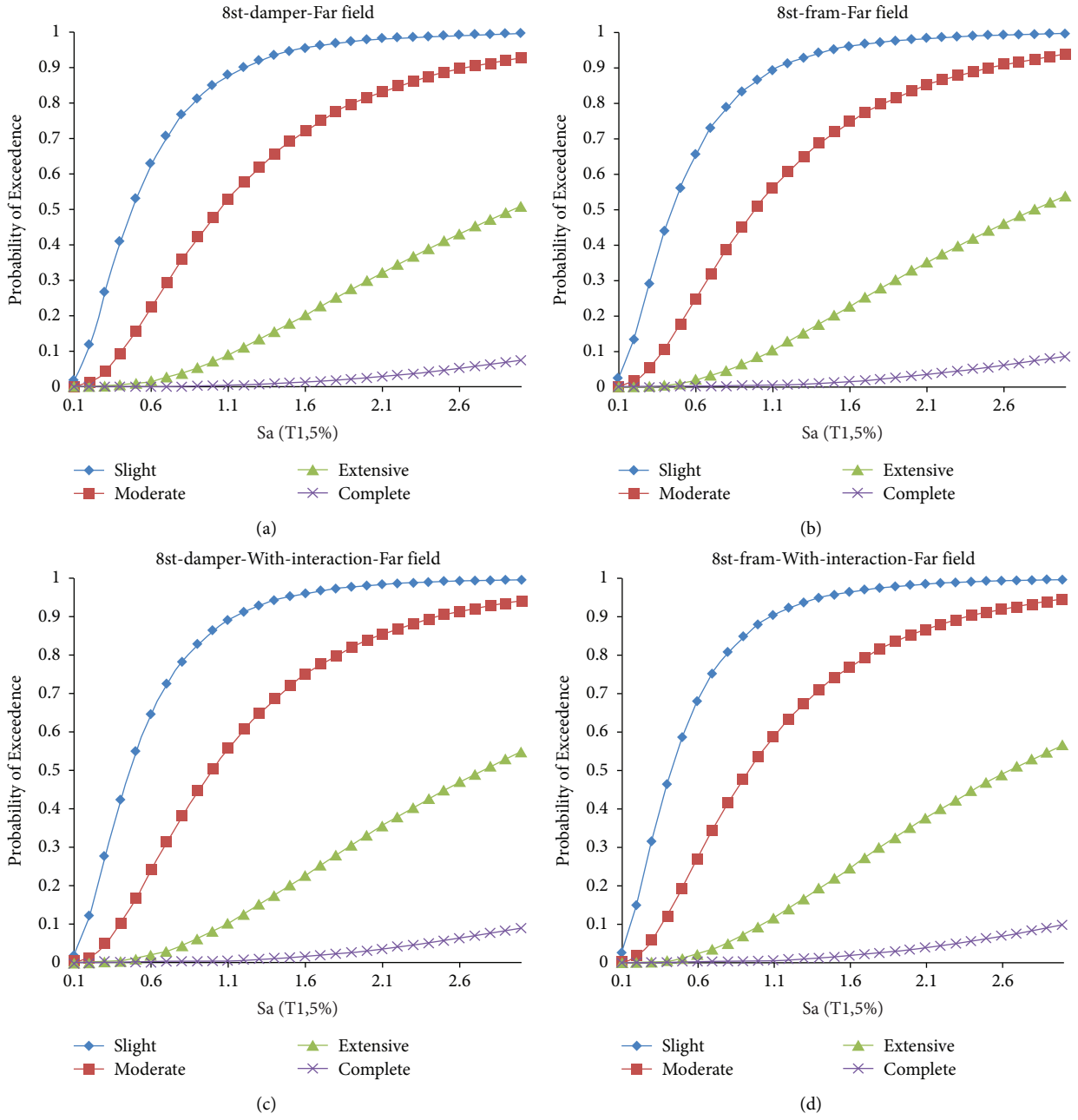

Figure 12: Fragility curves in 8-story ordinary moment resisting frame affected by far-field earthquakes. Examined cases: (a) with damper without considering SSI; (b) without damper and SSI effect; (c) with damper and considering SSI; (d) without damper but considering SSI effect.

In the 12-story OMRF structure affected by near-field earthquakes, like the other models, the slope of the linear region in the case (a), with damper and without SSI, is less than that in other states, which shows a softer behavior. In the cases with the damper, it enters the collapse region at a higher acceleration, which indicates better performance than other cases. Considering that the criterion of damage is interstory drift, the results show that the frame with a

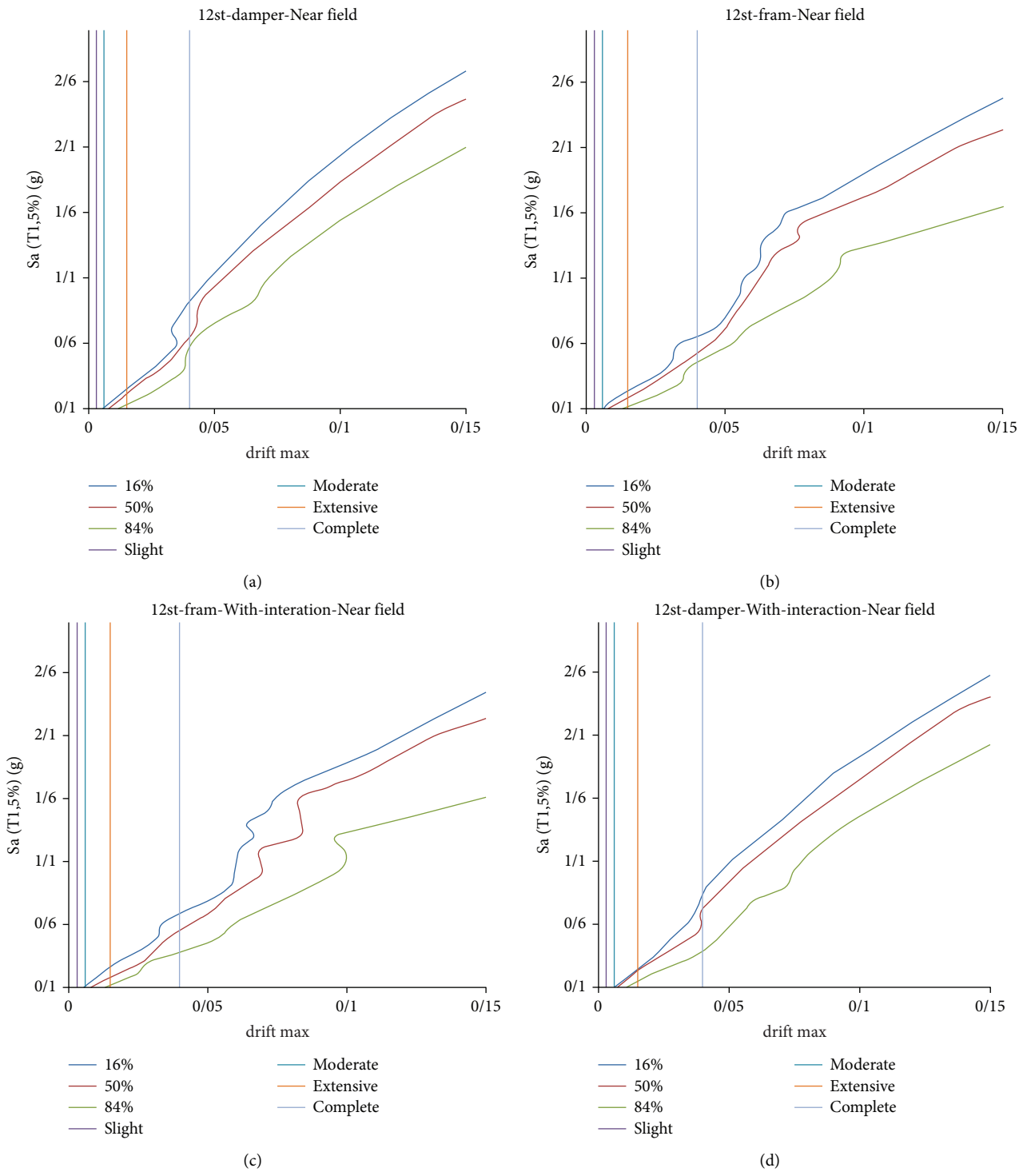

FIGURE 13: Summary of IDA curves for 16%, 50%, and 84% percentiles in 12-story ordinary moment resisting frame affected by near-field earthquakes. Examined cases: (a) with damper without considering SSI; (b) without damper and SSI effect; (c) with damper and considering SSI; (d) without damper but considering SSI effect.

damper reaches the level of failure at a higher spectral acceleration than other frames. This indicates the damper's performance in reducing displacement between floors as one of the criteria for predicting damage and shows the effect of soil-structure interaction on increasing drift between floors and reaching the level of failure at lower spectral acceler-

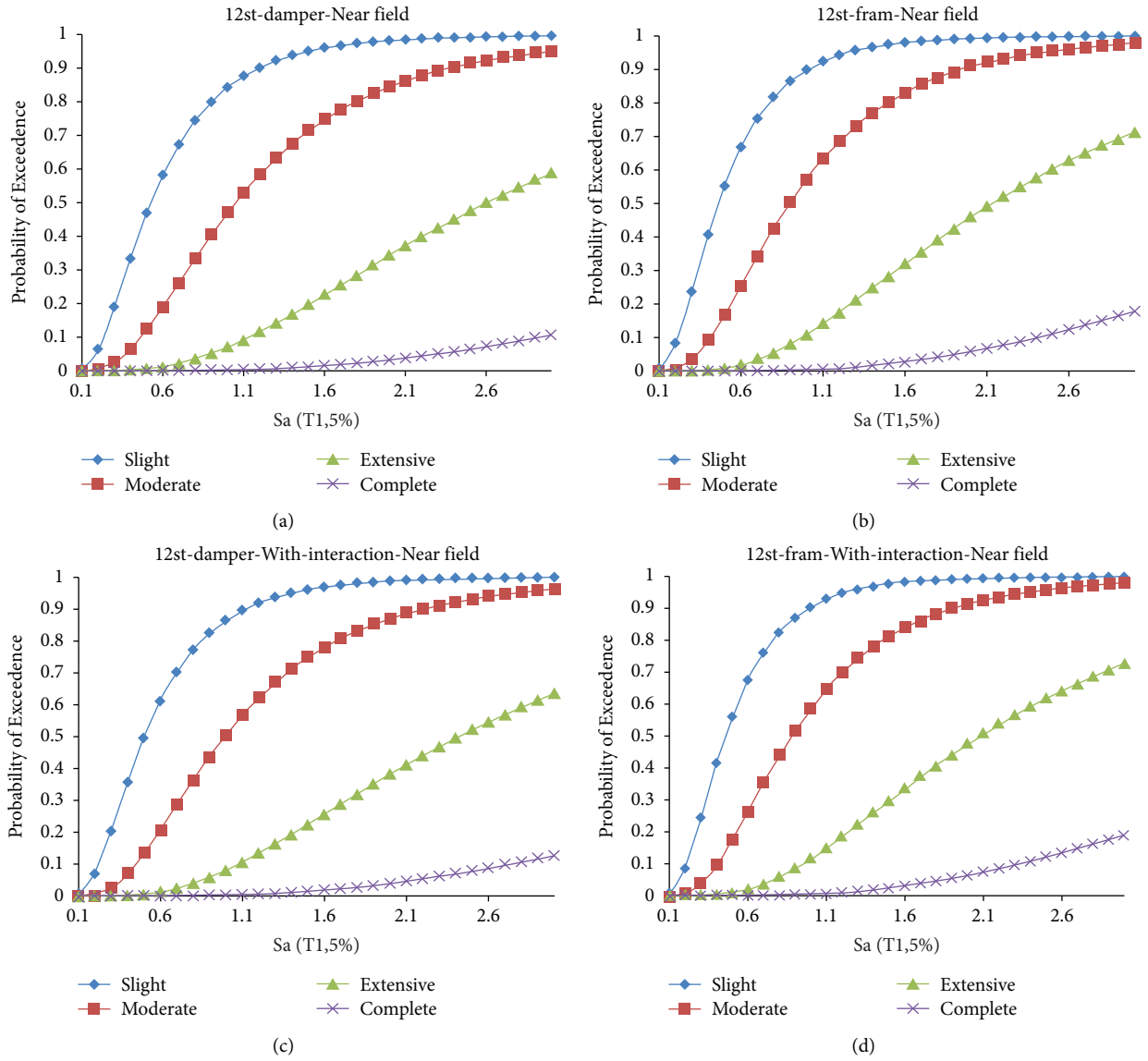

Figure 14: Fragility curves in 12-story ordinary moment resisting frame affected by near-field earthquakes. Examined cases: (a) with damper without considering SSI; (b) without damper and SSI effect; (c) with damper and considering SSI; (d) without damper but considering SSI effect.

ation. The fragility curves of 12-story frames under seven pairs of near-field acceleration are shown in Figure 14.

The fragility curve shows that the probability of structural failure in low failure mode occurs in less Sa values, and moderate, extensive, and complete failure modes occur in higher Sa values. In all curves, for low and moderate failure situations, the slope of the curve is first high and then decreased. For extensive failure mode, the curves change with an almost uniform slope. For complete failure mode, the slope changes are extremely small. According to the coefficient of acceleration scale of far-field earthquakes for 3-story structures, fragility occurs at a spectral acceleration of 1.344 g for type three soil. The results also show that soil-structure interaction has a significant effect on increasing the

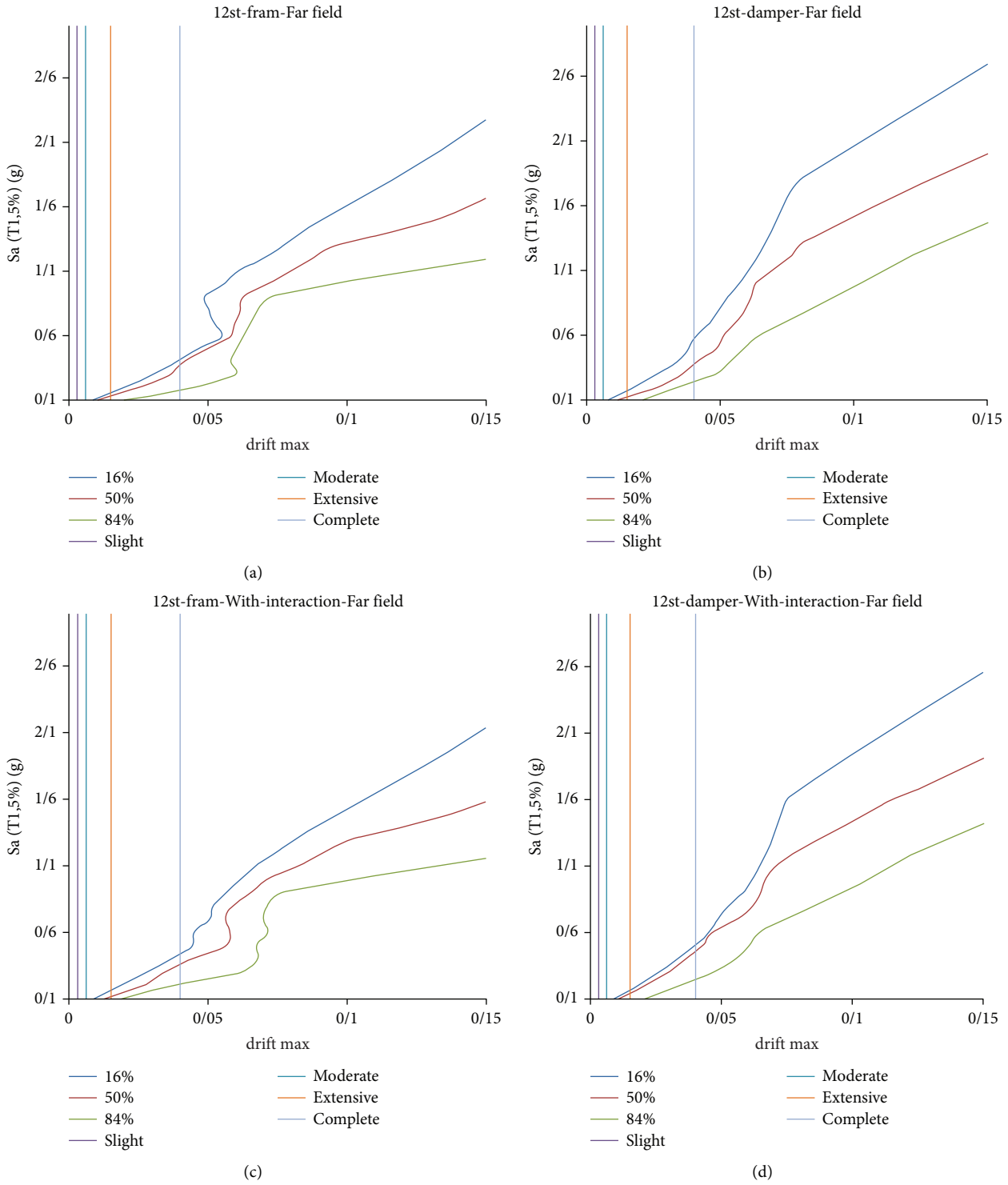

Figure 15: Summary of IDA curves for 16%, 50%, and 84% percentiles in 12-story ordinary moment resisting frame affected by far-field earthquakes. Examined cases: (a) with damper without considering SSI; (b) without damper and SSI effect; (c) with damper and considering SSI; (d) without damper but considering SSI effect.

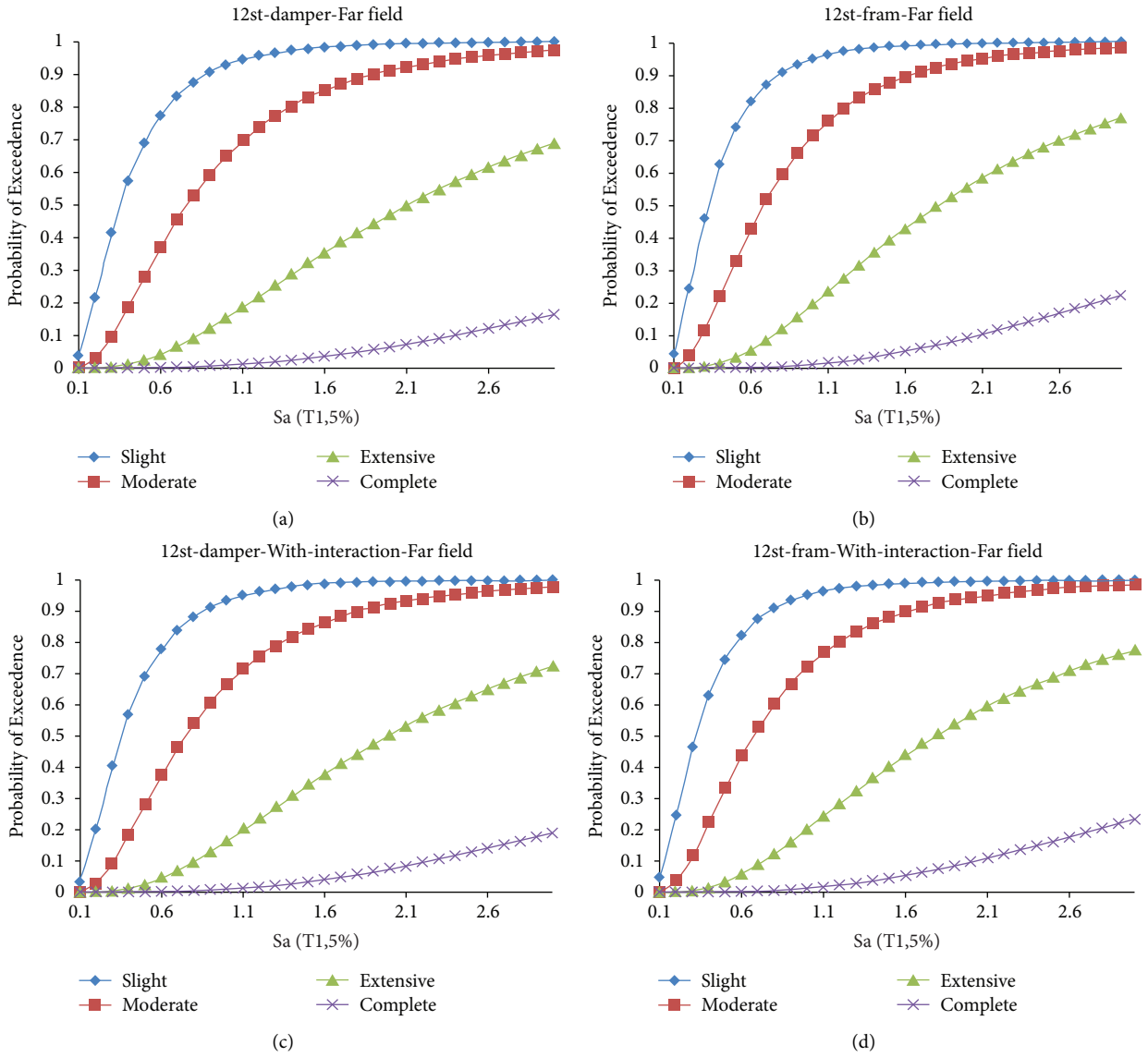

Figure 16: Fragility curves in 12-story ordinary moment resisting frame affected by far-field earthquakes. Examined cases: (a) with damper without considering SSI; (b) without damper and SSI effect; (c) with damper and considering SSI; (d) without damper but considering SSI effect.

probability of structural failure. Also, dampers in both cases with and without soil-structure interaction reduce failure likelihood. In the following, a summary of the IDA curve of a 3-story frame under seven pairs of far-field earthquakes is shown in Figure 15.

In the 8-story OMRF structure affected by far-field earthquakes, like the previous models, the slope of the linear region in the case (a), with damper and without SSI, is less than that in other states, which shows a softer behavior. In the cases with the damper, it enters the collapse region at a higher acceleration, which indicates better performance than other cases. Considering that the criterion of damage is interstory drift, the results show that the frame with a damper reaches the level of failure at a higher spectral acceleration than other frames. This indicates the damper's performance in reducing displacement between floors as one of the criteria for predicting damage and shows the effect of soil-structure interaction on increasing drift between floors and reaching the level of failure at lower spectral acceleration. The fragility curves of 12-story frames under seven pairs of far-field earthquakes are shown in Figure 16.

The fragility curve shows that the probability of structural failure in low failure mode occurs in less Sa values, and moderate, extensive, and complete failure modes occur in higher Sa values. In all curves, for low and moderate failure situations, the slope of the curve is first high and then decreased. For extensive failure mode, the curves change with an almost uniform slope. For complete failure mode, the slope changes are extremely small. According to the coefficient of acceleration scale of far-field earthquakes for 3-story structures, fragility occurs at a spectral acceleration of 2.12 g for type three soil. The results also show that soil-

structure interaction has a significant effect on increasing the probability of structural failure. Also, dampers in both cases with and without soil-structure interaction reduce the probability of failure.

5. Conclusion

In this study, three two-dimensional models of 3-, 8-, and 12-story ordinary steel moment frames were studied to evaluate the fragility of steel frames equipped with viscous dampers and consider SSI under near and far-field earthquakes. Each model was analyzed in OpenSees software. To draw the IDE curve, Sa (T1, 5%) was considered a parameter of seismic intensity, and interstory drift as a measure of damage intensity was selected. Then, the HAZUS instruction was used to draw the fragility curve based on the interstory drift ratio in 4 modes of slight, moderate, extensive, and complete failure. Therefore, the seismic response of the abovementioned structures is summarized as follows:

(1) The frame equipped with dampers, compared to other models, reaches the level of failure at a higher spectral acceleration, which indicates the damping function in reducing interstory drift.

(2) The effect of soil-structure interaction on increasing the displacement of stories and reaching the level of failure at spectral acceleration was less evident in all models.

(3) As the number of floors increases, the level of failure occurs at lower spectral acceleration.

(4) The level of failure occurs in the lower spectral acceleration in far-field earthquakes than in near-field earthquakes.

(5) In all models, low failure probability occurs in less Sa values (T1, 5%), and moderate, extensive, and complete failure modes occur in higher Sa values (T1, 5%), respectively.

The results support that as the number of floors of the studied structures increases, the probability of failure also increases. By comparing the fragility curves of the studied models under near-field and far-field accelerometers, it is clear that the probability of failure under far-field accelerometers is less than near-field [42].

Data Availability

Data are available and can be provided over the emails querying directly to the author at the corresponding author (amir_yousefpour@cmps2.iust.ac.ir).

Conflicts of Interest

The authors declare that they have no conflicts of interest.

References

[1] G. A. MacRae, D. V. Morrow, and C. W. Roeder, "near-fault ground motion effects on simple structures," *Journal of Structural Engineering*, vol. 127, no. 9, pp. 996–1004, 2001.

[2] P. Tothong and C. A. Cornell, "Structural performance assessment under near-source pulse-like ground motions using advanced ground motion intensity measures," *Earthquake Engineering & Structural Dynamics*, vol. 37, no. 7, pp. 1013–1037, 2008.

[3] B. Alavi and H. Krawinkler, "Behavior of moment-resisting frame structures subjected to near-fault ground motions," *Earthquake Engineering & Structural Dynamics*, vol. 33, no. 6, pp. 687–706, 2004.

[4] J. F. Hall, T. H. Heaton, M. W. Halling, and D. J. Wald, "Near-Source ground motion and its effects on flexible buildings," *Earthquake Spectra Journal*, vol. 11, no. 4, pp. 569–605, 1995.

[5] C. Champion and A. Liel, "The effect of near-fault directivity on building seismic collapse risk," *Earthquake Engineering and Structural Dynamics Journal*, 2012.

[6] A. R. Özuygur and E. Noroozinejad, "Influence of pulse-like near-fault ground motions on the base-isolated buildings with LRB devices," *Practice Periodical on Structural Design and Construction Journal*, vol. 26, no. 4, 2021.

[7] T. T. Song and G. F. Dargush, "Passive energy dissipation and active control," in *Structural Engineering Handbook*CRC Press LLC, Boca Raton, FL, USA, 1999.

[8] S. M. Zahrai and O. Mohammadi, "Seismic Behavior Upgrade of Steel Moment Frames Using Viscous Dampers and Determination of Their Proper Damping Forces," *Journal of Structural and Earthquake Analysis*, vol. 13, pp. 1–14, 2016.

[9] B. Silwal, O. E. Ozbulut, and R. J. Michael, "Seismic collapse evaluation of steel moment resisting frames with superelastic viscous damper," *Journal of Constructional Steel Research*, vol. 126, pp. 26–36, 2016.

[10] Y. Luo, H. Zheng, H. Zhang, and Y. Liu, "Fatigue reliability evaluation of aging prestressed concrete bridge accounting for stochastic traffic loading and resistance degradation," *Advances in Structural Engineering*, vol. 24, no. 13, pp. 3021–3029, 2021.

[11] S. Zhang, R. Y. Pak, and J. Zhang, "Three-dimensional frequency-domain green's functions of a finite fluid-saturated soil layer underlain by rigid bedrock to interior loadings," *International Journal of Geomechanics*, vol. 22, no. 1, Article ID 04021267, 2022.

[12] H. Liu, Z. Shi, J. Li et al., "Detection of road cavities in urban cities by 3D ground-penetrating radar," *Geophysics*, vol. 86, no. 3, pp. WA25–WA33, 2021.

[13] R. Moradi-dastjerdi, H. Momeni-Khabisi, and R. Baghbani, "Mesh-free dynamic analyses of FGM sandwich plates resting on a pasternak elastic foundation," *Mechanics of Advanced Composite Structures*, vol. 4, no. 2, pp. 153–168, 2017.

[14] H. Ghaffarzadeh, E. A. Dehrod, and N. Talebian, "Semi-active fuzzy control for seismic response reduction of building frames using variable orifice dampers subjected to near-fault earthquakes," *Journal of Vibration and Control*, vol. 19, no. 13, pp. 1980–1998, 2016.

[15] M. L. A. Prasad and E. A. Mazumder, "Use of viscous damper as an energy dissipative device in steel structures," *Int. J. Mech. Prod. Eng.*vol. 4, pp. 59–66, 2016.

[16] Y. Wang, H. Cheng, Q. Hu et al., "Pore structure heterogeneity of Wufeng-Longmaxi shale, Sichuan Basin, China: evidence from gas physisorption and multifractal geometries," *Journal of Petroleum Science and Engineering*, vol. 208, Article ID 109313, 2022.

[17] S. Jiang, Y. Zuo, M. Yang, and R. Feng, "Reconstruction of the Cenozoic tectono-thermal history of the dongpu depression, bohai bay basin, China: constraints from apatite fission track and vitrinite reflectance data," *Journal of Petroleum Science and Engineering*, vol. 205, Article ID 108809, 2021.

[18] C. Zhang and A. Ali, "The advancement of seismic isolation and energy dissipation mechanisms based on friction," *Soil Dynamics and Earthquake Engineering*, vol. 146, Article ID 106746, 2021.

[19] V. S. Balkanlou, M. R. B. Karimi, B. B. Azar, and A. Behravesh, "Evaluating effects of viscous dampers on optimizing seismic behavior of structures," *Int. J. Curr. Eng. Technol., Vl.*vol. 3, pp. 1150–1157, 2013.

[20] S. Silvestri, G. Gasparini, and T. Trombetti, "A five-step procedure for the dimensioning of viscous dampers to be inserted in building structures," *Journal of Earthquake Engineering*, vol. 14, no. 3, pp. 417–447, 2010.

[21] R. Milanchian and M. Hosseini, "Study of vertical seismic isolation technique with nonlinear viscous dampers for lateral response reduction," *Journal of Building Engineering*, vol. 23, pp. 144–154, 2019.

[22] D. De Domenico, G. Ricciardi, and I. Takewaki, "Design strategies of viscous dampers for seismic protection of building structures: a review," *Soil Dynamics and Earthquake Engineering*, vol. 118, pp. 144–165, 2019.

[23] J. Xu, W. Lan, C. Ren, X. Zhou, S. Wang, and J. Yuan, "Modeling of coupled transfer of water, heat and solute in saline loess considering sodium sulfate crystallization," *Cold Regions Science and Technology*, vol. 189, Article ID 103335, 2021.

[24] B. Li, G. Xiao, R. Lu, R. Deng, and H. Bao, "On feasibility and limitations of detecting false data injection attacks on power grid state estimation using D-FACTS devices," *IEEE Transactions on Industrial Informatics*, vol. 16, no. 2, pp. 854–864, 2019.

[25] T. Wang, W. Liu, J. Zhao, X. Guo, and V. Terzija, "A rough set-based bio-inspired fault diagnosis method for electrical substations," *International Journal of Electrical Power & Energy Systems*, vol. 119, Article ID 105961, 2020.

[26] M. Ghalami, M. Sc. Thesis, *The Effect of Soil-Structure Interaction in Tall Building Equipped with Passive Dampers under Seismic Loads"*, Department of Civil Engineering (Structure), University of Mohaghegh Ardabili, 2020.

[27] A. Amiri, S. Mohaseb, and J. khazaie, "The Effect of Soil-Structure Interaction on Seismic Retrofitting of Steel Structures," in *Proceedings of the 5th national and 1st international conference of steel and structures*, Tehran, Iran, July 2015.

[28] D. Šago, V. Martić, D. Šmida, N. Mayer, V. Lovretić, and I. Filipčić, "Telepsychiatry in the time of the COVID-19 and earthquake in zagreb as odysseus between scylla and Charybdis," *Psychiatria Danubina*, vol. 32, no. 3-4, pp. 478–481, 2020.

[29] G. Xiang, Y. Zhang, X. Gao, H. Li, and X. Huang, "Oblique detonation waves induced by two symmetrical wedges in hydrogen-air mixtures," *Fuel*, vol. 295, Article ID 120615, 2021.

[30] M. Arbabi and H. Tahghighi, "Influence of nonlinear SSI on the seismic response of low-to-mid-rise steel moment resisting frame buildings," *Journal of Structural and Construction Engineering*, vol. 7, no. 3, pp. 35–52, 2019.

[31] M. H. Hazus, *Hazus-MH MR4 Technical Manual: Multi-hazard Loss Estimation Methodology"*, FEMA, Washington, D.C, 2003.

[32] American National Standards Institute/American Institute of Steel Construction, *Seismic provisions for structural steel buildings*, ANSI/AISC, Chicago, IL, 2010.

[33] American Society of Civil Engineering (Asce), *Structural engineering Institute (SEI). "Minimum design loads for buildings and other structures*, ASCE Standard, Chicago, IL, 2010.

[34] M. NourEldin, A. Naeem, and J. Kim, "Life-cycle cost evaluation of steel structures retrofitted with steel slit damper and shape memory alloy-based hybrid damper," *Advances in Structural Engineering*, vol. 22, no. 1, pp. 3–16, 2019.

[35] X. Lu and Q. Zhou, "Dynamic analysis method of a combined energy dissipation system and its experimental verification," *Earthquake Engineering & Structural Dynamics*, vol. 31, no. 6, pp. 1251–1265, 2002.

[36] C. Fang, Y. Ping, Y. Chen, M. Yam, J. Chen, and W. Wang, "Seismic performance of self-centering steel frames with SMA-viscoelastic hybrid braces," *Journal of Earthquake Engineering*, pp. 1–28, 2020.

[37] M. Khakpour and M. Hajialilue Bonab, "Soil-structure-interaction using Cone model in time domain for horizontal and vertical motions in layered half space," *Journal of Earthquake Engineering*, vol. 24, no. 4, pp. 529–554, 2018.

[38] D. Vamvatsikos and C. A. Cornell, "Incremental dynamic analysis," *Earthquake Engineering & Structural Dynamics*, vol. 31, no. 3, pp. 491–514, 2002.

[39] P. Christovasilis, G. P. Cimellaro, S. Barani, and S. Foti, "On the selection and scaling of ground motions for fragility analysis of structures," in *Proceedings of the 2nd European Conference of Earthquake Engineering and Seismology*, 2014.

[40] PEER Ground Motion Database, https://peer.berkeley.edu/peer-strong-ground-motion-databases, 2011.

[41] C. Fang, Q. Zhong, W. Wang, S. Hu, and C. Qiu, "Peak and residual responses of steel moment-resisting and braced frames under pulse-like near-fault earthquakes," *Engineering Structures*, vol. 177, pp. 579–597, 2018.

[42] OpenSees, *Open System for Earthquake Engineering Simulation", Pacific Earthquake Engineering Research Center*, University of California, Berkeley, California, 2007, http://opensees.berkeley.edu/.

Hindawi
Shock and Vibration
Volume 2022, Article ID 4132673, 16 pages
https://doi.org/10.1155/2022/4132673

Research Article

Self-Excited Vibration Analysis of Gear-Bearing System with Multipoint Mesh and Variable Bearing Dynamic Coefficients

Hao Zhang,[1] **Shiheng Cao**,[1] **Pengyu Li**,[1] **and Qingkai Han**[2]

[1]*College of Mechanical Engineering and Automation, Liaoning University of Technology, Jinzhou, China*
[2]*Key Laboratory of Vibration and Control of Aero-Propulsion System Ministry of Education, Northeastern University, Shenyang, China*

Correspondence should be addressed to Hao Zhang; neu20031924@163.com

Received 7 January 2022; Revised 23 February 2022; Accepted 2 March 2022; Published 25 March 2022

Academic Editor: Jiaqiang E

The gear-bearing system is the most important part of integrally centrifugal compressors. According to statistics, the majority of integrally geared compressor accidents are caused by excessive vibration of the geared rotor. However, its complicated dynamic characteristics and inevitable vibration faults in actual operation present significant challenges throughout the analysis and design stages. In this paper, the coupled self-excited vibration of the gear system characterized by multipoint meshing and oil film bearing supporting is investigated. Firstly, the structure of the gear system in an integrally geared compressor is used as a research object. The modeling approach of meshing excitation, including time-varying mesh stiffness, gear meshing error, and tooth backlash are introduced. However, the variable stiffness and damping coefficient equations of journal bearing and oil film thrust bearing are modeled and utilized to approximate the variable bearing force and simplify the vibration computation under the assumption of Newtonian fluid. Then, a dimensionless modeling method of the gear system considering gyroscopic moment of gear disk, variable meshing force, as well as variable stiffness and damping coefficient is proposed. Based on the dynamic model, the influence of the bearing dynamic coefficients and load on the vibration of the entire gear system is studied. Among which, the vibration displacement and meshing force are examined using frequency-domain and time-domain analysis methods. The results suggest that the flexible support can restrain the system's nonlinear motion, whilst increasing load on the gear system can improve gear operation stability and reduce load fluctuation.

1. Introduction

Integrally geared compressor is one of the most representative assembling units among big rotating machines, which are widely utilized in the domains of natural gas, petroleum, and coal chemical processing and meets the requirements, such as higher flux and longer running time. It is characterized by higher parameter, better performance and stability under various condition, extreme condition and multi-interference. The dynamic stability of compressor geared rotor system has always attracted much attention. For example, it happened that self-excitation leads to the large vibration of compressor, as reported by Wachel (1975), Fulton (1984), Kirk(1985), Kuzdzal (1994), and Memmott (2000) [1].

The gear-bearing system is the key component in integrally centrifugal compressor which is often characterized by one helical gear meshing with many other gears at the same time and coupled in different directions, and also the nonlinear oil film support of rotors, which cause the vibration characteristics of the rotor systems in integrally geared compressors are different from those of the general gear system. According to the statistics, most accidents of integrally geared compressors are caused by excessive vibration of geared rotor [2], which is resulted by rotor unbalance, shafting coupling resonance, bearing instability, and so on. The rotor system in integrally centrifugal compressor always runs at high speed and high load. Due to the alternative engagement of teeth and the nonlinear film force, the meshing state changes during the meshing process, while

the impact among the gear teeth caused by the mesh clearance and transmission error during the meshing process would excite the vibration of the whole rotor system. The excessive vibration will not only lead to the wear between rotors and stators, but also serious damage of the whole system. Although researchers have formed a relatively perfect theory and technology of nonlinear dynamic analysis and dynamic design for the main problems of the rotor system of a single shaft centrifugal compressor, and have a good means of prediction and control of its vibration problems, it is still impossible to make a reasonable explanation for the new vibration phenomenon of the geared rotor system in integrally centrifugal compressor and put forward an effective solution. In many times, the safe operation of the integrally centrifugal compressor can only be ensured by sacrificing the production capacity. Thus, the meshing characteristics and performance of the gear system have important influences on the whole system even the whole devices as well as the system security.

Researchers have proposed many modeling methods on gear meshing force and oil film force. The main modeling methods of gear meshing force include linear meshing model and nonlinear meshing model. In linear meshing model, the meshing stiffness is regarded as a constant or harmonic value, which is usually used to solve the resonance frequency of the rotor or the vibration response of the rotor with less influence of meshing excitation. For example, Doan [3] presents a method for determining the resonance regions of the gear system under different design parameters according to the linear meshing assumption. Kang [4] considers the dynamics of a gear system with viscoelastic supports, in which, the gear pairs are simplified as two rigid discs connected by springs along meshing lines. In addition, in order to express the meshing excitation of gears, Shi [5] proposed a dynamics model for hypoid gears, considered the interaction between mesh stiffness and dynamic response, and the simulations show evident impact of dynamic mesh stiffness on hypoid gear dynamic response. Han [6] introduced time-dependent mesh stiffness to realize steady response analysis of rotor system, where meshing stiffness fluctuates in simple harmonic form, while the influence of various nonlinear factors on vibration is ignored, such as tooth backlash and meshing error. In many cases, the linear meshing model cannot describe the meshing force well, especially when the mesh clearance and gear transmission error to be taken into account. Feng [7] studied the increased vibration of geared rotor system caused by gear wear, and propose a gear wear model to describe wear process. With the continually updated model coefficient according to the real-time test data, the wear process of the gear mesh can be well monitored. Then, Feng [8] demonstrated the ability and effectiveness of the proposed vibration-based methodology in monitoring and predicting gear wear, Inalpolat [9] analyzed the influence of different gear meshing error on dynamic meshing force of gear pair by experiment. Theodossiadas [10] applied the non-linear meshing model to identify the periodic steady response of gear system involving backlash and time-dependent mesh stiffness under torsional moments. Eritenel [11] proposed nonlinear dynamic model to investigate the gear loads and bearing forces of the gear system with backlash and time-varying stiffness. Cho [12] studied the dynamics of a two-stage differential wind generator gearbox, where the non-linear meshing model was adopted. Guerine [13] investigated the influence of random uncertainty of mass, damping coefficient, bending stiffness, and torsion stiffness on the dynamic response of single-stage gear system, as well as the synthetically impact of these random parameters. Luo [14] proposed an improved analytical model to calculate the time-varying mesh stiffness of a planetary gear set, where the effect of sliding friction and spalling defects are considered. Zheng [15] considered centrifugal effect and developed an analytical-FEM framework to integrate the centrifugal field into the mesh stiffness and nonlinear dynamics, where the reasonable accuracy is demonstrated between the simulation and experiment results. Wang [16] studied the bending-torsion coupling response of spur gear system, taking into account mesh stiffness variations, backlash, transmission errors, and loads. The results show that, due to the coupling effects of bending and torsional vibrations, the system exhibits a diverse range of periodic, subharmonic, and chaotic motion. Sánchez [17] investigated the contact conditions of modified teeth influenced by the profile modification on the load sharing and transmission error under load. Wang [18] suggested two approaches for determining time-varying meshing stiffness in internal gear pairs with tiny tooth differences, both of which were validated using the finite element method. Ma [19] established a fractal contact model suited for gear pair contact, where the influence of roughness on the normal contact stiffness of gears is considered. On the basis of modified fractal contact model, the asperity contact stiffness and the fractal contact compliance are calculated.

Also included are two methods that are commonly used in the numerical calculation of bearing force. The first one is to directly calculate the oil film force using a numerical or analytic method, while the other is an approximation of the dynamic coefficients of the oil film, such as stiffness and damping coefficients. It always takes a long time to solve the dynamic oil film force by finite element method or variation method in the first method. Thus, the Reynolds equation is often simplified to analyzing and solving practical problems, where the oil film force model of long bearing proposed by Sommerfeld and the short bearing proposed by Capone is the most representative. For example, Chang-Jian [20] and Amamou [21] use the long bearing hypothesis to investigate the non-linear dynamic features of a disk rotor system supported by a circular tile bearing and the dynamic stability of a circular tile bearing. However, Lin [22] and Soni [23] used the short bearing hypothesis to investigate the lubrication features of bearings in non-Newton ferromagnetic fluid and the nonlinear dynamic characteristics of circular tile bearings in thin film lubrication. Due to the complexity of the first technique's calculation process, the second method is extensively utilized in engineering applications to solve the rotor response problem due to its simple calculation procedure. Srikanth [24] ignores the degree of freedom of the tile thrust bearing block and solves the stiffness and damping parameters of tile thrust bearings of various

sizes. Furthermore, several researchers investigated the nonlinear vibration of a rotor system with oil film support from the perspectives of external stimulation and rotor fault. Zhang [25] investigates the change in bearing force of rotor system due to the change of submarine position. Liang [26] analyzes the influence of the film force in the squeeze film damper on the nonlinear vibration suppression of the rotor system produced by the misalignment. Cable [27] studies the static angular misalignment of the thrust collars and the main bull gear in integrally geared compressor induced by manufacturing inaccuracies and poor assembly process, which has major impact on the dynamics of the rotor system.

Despite the fact that many studies have been done on the dynamic of gear system, they have always focused on gear systems with classical configurations. There are few works concentrate on the time-varying features and non-linear coupled vibration of gear systems with multipoint mesh. Meanwhile, in some vibration analyses of complicated gear systems, bearings are always treated as invariable stiffness and damper coefficients, which would make the analysis results lose some important information. Many compressor manufacturing companies still lack a dynamic analysis process of the gear system during the design phase, resulting in many vibration problems of the gear system that cannot be effectively solved, and the safe operation of the equipment can only be ensured by sacrificing production capacity, such as reducing the working speed and load.

The modeling approach of the gear system with multipoint mesh according to the structure of the gear system in integrally geared compressor is proposed in this study, where the variable meshing force and variable bearing dynamic coefficients are taken into account. In addition, the non-linear coupled vibrations of the gear system and meshing properties at various speeds and loads are investigated. The findings of this work could provide theoretical support for the dynamic design and fault diagnostics of multipoint mesh gear systems aiming for high reliability and minimal vibration.

2. Gear Bearing System with Multipoint Mesh and Its Modelling Method

2.1. Structure of Gear System in Integral Centrifugal Compressor. Figure 1 depicts an entire centrifugal compressor rotor system comprised of five shafts engaged by helical gear, including one input shaft, one middle gear driving shaft, and three high speed output shafts, all supported by journal bearings and oil film trust bearings. The maximum speed of the input shaft of the rotor system is 4000r/min, and the maximum output speed of the output shaft is 12800r/min.

The gears are treated as rigid body and the dynamic model of gear system is shown in Figure 2. Gears 1–5 refer to the gears on the input shaft, center shaft, and three output shafts. $k_{ij}(t)$, $2b_{ij}$, and $e_{ij}(t)$ are the time-variant stiffness parameter, gear clearance parameter, and transfer error parameter between Gears i and Gear j, respectively.

As shown in Figure 2, each gear is located in the center of the two supporting, and Gear i rotates around the rotation center O_i at rotation speed ω_i. $k_{ij}(t)$, c_{ij} , $e_{ij}(t)$, and b_{ij} are the meshing stiffness, meshing damping, transfer error, and unilateral backlash between Gears i and j, respectively. k_{ix} is axial stiffness of the thrust bearing on Gear i, k_{iyL}, k_{izL} and k_{iyR}, k_{izR} are the vertical and horizontal stiffness of left and right journal bearings on Gear i, respectively.

2.2. Modelling Approach of Meshing Excitation

2.2.1. Time-Variant Meshing Stiffness. Due to the alternation of meshing teeth, the meshing stiffness changes periodically, which result in the dynamic stiffness excitation during the meshing process, the Ishikawa Formula shown as the following equation is used to describe the deformation of the tooth under mesh force F:

$$\delta = \delta_{Br} + \delta_{Bt} + \delta_s + \delta_G, \tag{1}$$

where δ_{Br} and δ_{Bt} are the bending deformations of the rectangular and trapezoid section, respectively, and δ_s and δ_G are the shear and elasticity deformations, respectively. Then the stiffness of the tooth can be described as

$$k = \frac{F}{\delta}. \tag{2}$$

The meshing stiffness appears obvious periodicity during the meshing process and can be expressed as a Fourier series:

$$k(t) = k_0 + \sum_{j=1}^{\infty}\left[a_j \cos\left(j\omega_\Lambda t\right) + b_j \sin\left(j\omega_\Lambda t\right)\right] = k_0 + \sum_{j=1}^{\infty} k_j \cos\left(j\omega_\Lambda t + \varphi_j\right), \tag{3}$$

where k_0 is the average meshing stiffness; a_i, b_i, and k_i are the Fourier coefficients; φ_j is the phase angle; and ω_Λ is the meshing frequency.

If only the first order of Fourier series is preserved, Eq. (3) can be written as

$$k(t) = k_0\left[1 + \varepsilon \sin\left(\omega_\Lambda t + \varphi\right)\right], \tag{4}$$

where ε is the fluctuation coefficient of stiffness.

2.2.2. Gear Transfer Error. The transfer error of the gear pair is mainly caused by manufacture error and gear wear. Transfer errors make the meshing tooth profile deviate from the ideal meshing position, which destroy the correct meshing method of gear pairs, and resulting in tooth-to-tooth collisions and impacts during the meshing process.

Because the transfer error is of periodicity during the transfer process, the transfer error could also be expressed in the form of Fourier series:

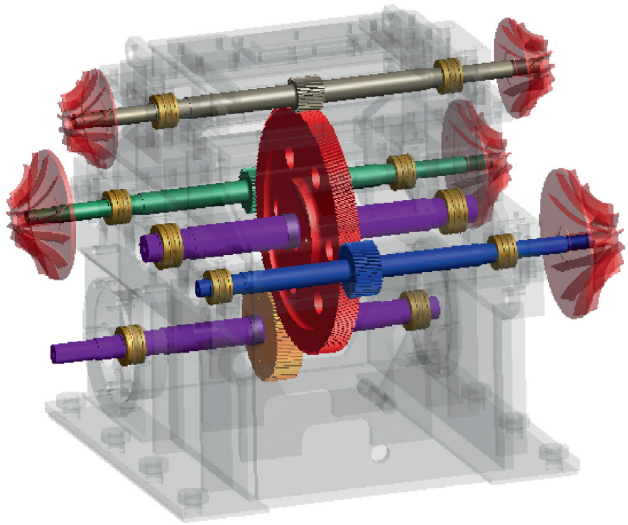

Figure 1: Rotor system of integral centrifugal compressor.

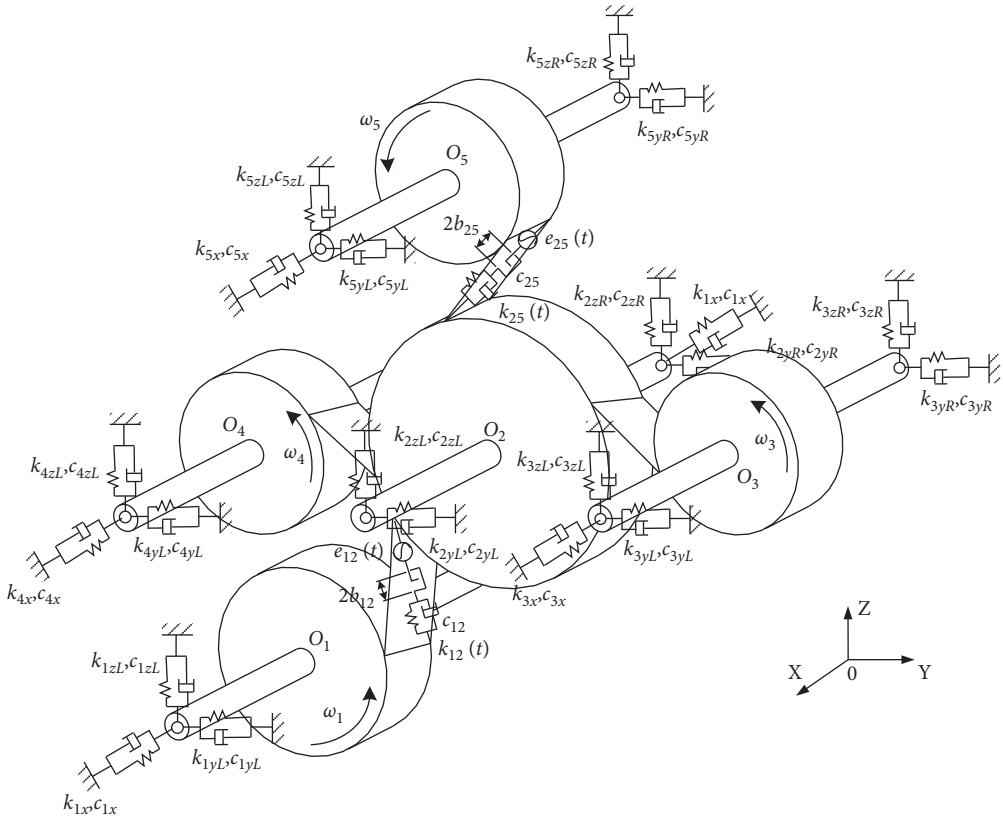

Figure 2: Dynamic model of the gear system.

$$e(t) = e_0 + \sum_{j=1}^{\infty}\left[c_j \cos(j\omega t) + d_j \sin(j\omega t)\right] = e_0 + \sum_{j=1}^{\infty} e_j \cos\left(j\omega_\Lambda t + \varphi_j\right), \tag{5}$$

where e_0 is the average transfer error and c_i and d_i are the Fourier coefficients.

Similarly, if only the first order of this Fourier series is preserved, and average transfer error is equaled to zero, Equation (3) can be written as

$$e(t) = e_s \sin(\omega_\Lambda t + \varphi), \tag{6}$$

where e_s is the fluctuant amplitude of transfer error.

2.2.3. Backlash. Backlash between gear pair changes the contact state and causes continuous impact between the gear pairs, which has a significant impact on the dynamic characteristics of the gear system. Assuming the teeth backlash of a gear pair is $2b_n$, and the relative deformation between the meshing teeth is Δ. Therefore, the deformation functions of the tooth along the meshing line can be expressed as

$$g(\Delta) = \begin{cases} \Delta - b_n, & \Delta > b_n, \\ 0, & -b_n \le \Delta \le b_n, \\ \Delta + b_n, & \Delta < -b_n, \end{cases} \tag{7}$$

Equation (7) is a step function, and when the meshing point is within the scope of teeth backlash, there is no deformation. Otherwise, the teeth begin to deform.

2.3. Modelling Approach of Bearing Dynamic Coefficients. The journal bearings on shafts can be modeled as Figure 3. Here, the journal rotates at the speed of Ω with stable load F. O and O_b are the center of journal and bearing, respectively. r and R_b are the radius of journal and bearing bore. φ is the displacement angle. E is the eccentric distance.

After coordinate translation, the Reynolds equation for oil film force analysis in journal bearing and its oil film boundary can be shown as

$$\frac{1}{R_b^2}\frac{\partial}{\partial\theta}\left(\frac{h^3}{12\eta}\frac{\partial p}{\partial\theta}\right) + \frac{\partial}{\partial x}\left(\frac{h^3}{12\eta}\frac{\partial p}{\partial x}\right) = \frac{1}{2}\Omega\frac{\partial h}{\partial\theta} + \frac{\partial h}{\partial t}, \tag{8}$$

$$\begin{cases} p(\theta_1, x) = p(\theta_2, x) = 0, \\ p\left(\theta, -\dfrac{L}{2}\right) = p\left(\theta, \dfrac{L}{2}\right) = 0, \end{cases} \tag{9}$$

where η is the dynamic viscosity of the oil; p is the oil film pressure; x is the position along the width direction; θ_1 and θ_2 are the starting angle boundary and end angle boundary; and L is the width of the bearing.

Nondimensional parameters are defined as $\overline{p} = p/[6\eta\Omega(R_b/C)^2]$, $\overline{x} = x/(L/2)$, $\lambda = 2R_b/L$, $\overline{e} = e/C$, $\dot{\overline{e}} = \dot{e}/(C\Omega)$, $\overline{h} = h/C = 1 + \overline{e}\cos(\theta - \varphi)$, and $\tau = \Omega t$. Equation (8)-(9) can be transferred to

$$\frac{\partial}{\partial\theta}\left(\overline{h}^3\frac{\partial\overline{p}}{\partial\theta}\right) + \lambda^2\frac{\partial}{\partial\overline{x}}\left(\overline{h}^3\frac{\partial\overline{p}}{\partial\overline{x}}\right) = -\overline{e}\sin(\theta - \varphi) + 2\dot{\overline{e}}\cos(\theta - \varphi_{\mathrm{de}}) = f(\theta), \begin{cases} p(\theta_1, \overline{x}) = p(\theta_2, \overline{x}) = 0, \\ p(\theta, -1) = p(\theta, 1) = 0. \end{cases} \tag{10}$$

To simplify the vibration calculations, stiffness and damping coefficients can be used to approximate the bearing force of the lubricant film, which can be calculated by linearization of the unsteady load capacity in the vicinity of the static position of equilibrium and developed to the first derivative in a Taylor series as Equation (11), where the force caused by dip angle of the journal is neglected:

$$\begin{Bmatrix} F_y \\ F_z \end{Bmatrix} = \begin{Bmatrix} F_{y0} \\ F_{z0} \end{Bmatrix} + \begin{bmatrix} k_{yy} & k_{yz} \\ k_{zy} & k_{zz} \end{bmatrix}\begin{Bmatrix} y \\ z \end{Bmatrix} + \begin{bmatrix} c_{yy} & c_{yz} \\ c_{zy} & c_{zz} \end{bmatrix}\begin{Bmatrix} \dot{y} \\ \dot{z} \end{Bmatrix}, \tag{11}$$

where

$$\begin{bmatrix} k_{yy} & k_{yz} \\ k_{zy} & k_{zz} \end{bmatrix} = \int_{-L/2}^{L/2}\int_{\theta_1}^{\theta_2}\begin{bmatrix} \dfrac{\partial p}{\partial y}\cos\theta & -\dfrac{\partial p}{\partial y}\sin\theta \\ \dfrac{\partial p}{\partial z}\cos\theta & -\dfrac{\partial p}{\partial z}\sin\theta \end{bmatrix} R_b d\theta\, dx,$$

$$\begin{bmatrix} c_{yy} & c_{yz} \\ c_{zy} & c_{zz} \end{bmatrix} = \int_{-L/2}^{L/2}\int_{\theta_1}^{\theta_2}\begin{bmatrix} \dfrac{\partial p}{\partial \dot{y}}\cos\theta & -\dfrac{\partial p}{\partial \dot{y}}\sin\theta \\ \dfrac{\partial p}{\partial \dot{z}}\cos\theta & -\dfrac{\partial p}{\partial \dot{z}}\sin\theta \end{bmatrix} R_b d\theta\, dx. \tag{12}$$

The oil film thrust bearing on shafts can be modeled as Figure 4, which consists of many bearing bushes. θ_0, θ_1, and θ_2 are the angle of bush, side oil seal lip, and thrust face, respectively; b is the width of the outer oil seal lip; r_i and r_o are the inner and outer radius of thrust face; φ is the angle of thrust face; θ and r are the coordinates in radial and circumferential directions; $h(\theta)$ is the film thickness with radial coordinate θ; C is the bearing clearance; and e is the relative displacement between trust bearing and thrust runner collar.

The Reynolds equation for each bush in oil film thrust bearing and its oil film boundary can be shown as

$$\frac{1}{r^2}\frac{\partial}{\partial\theta}\left(\frac{h^3}{12\eta}\frac{\partial p}{\partial\theta}\right) + \frac{\partial}{\partial r}\left(\frac{h^3}{12\eta}\frac{\partial p}{\partial r}\right) = \frac{1}{2}\Omega\frac{\partial h}{\partial\theta} + \frac{\partial h}{\partial t}, \tag{13}$$

$$\begin{cases} p(r_i, \theta) = p(r_o, \theta) = 0, \\ p(r, \theta_1) = p(r, \theta_2) = 0, \end{cases} \tag{14}$$

where η is the dynamic viscosity of the oil; p is the oil film pressure; and θ_1 and θ_2 are the starting angle boundary and end angle boundary.

Nondimensional parameters are defined as $\overline{p} = p/[6\eta\Omega(r_i/C)]^2$, $\overline{r} = r/r_i$, $\overline{b} = b/r_i$, $\overline{h} = h/C$, $\overline{e} = e/C$, $\dot{\overline{e}} = \dot{e}/(C\Omega)$, $\tau = \Omega t$, and $\kappa = 1/\overline{r}$. Equations (14)-(15) can be transferred to

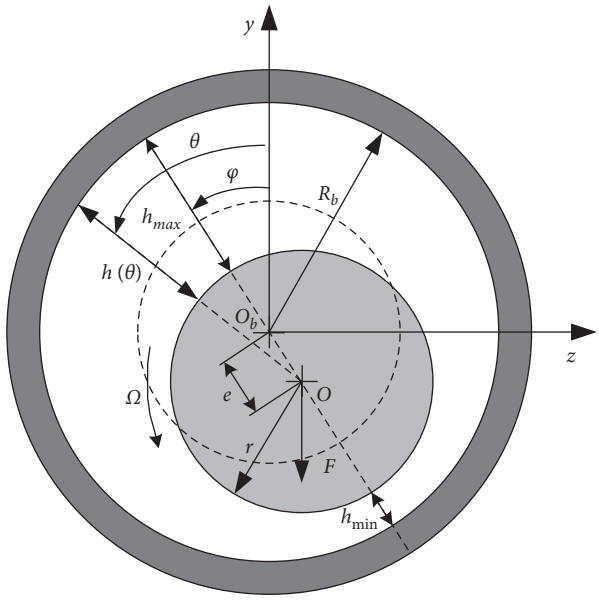

Figure 3: Dynamic model of the journal bearing.

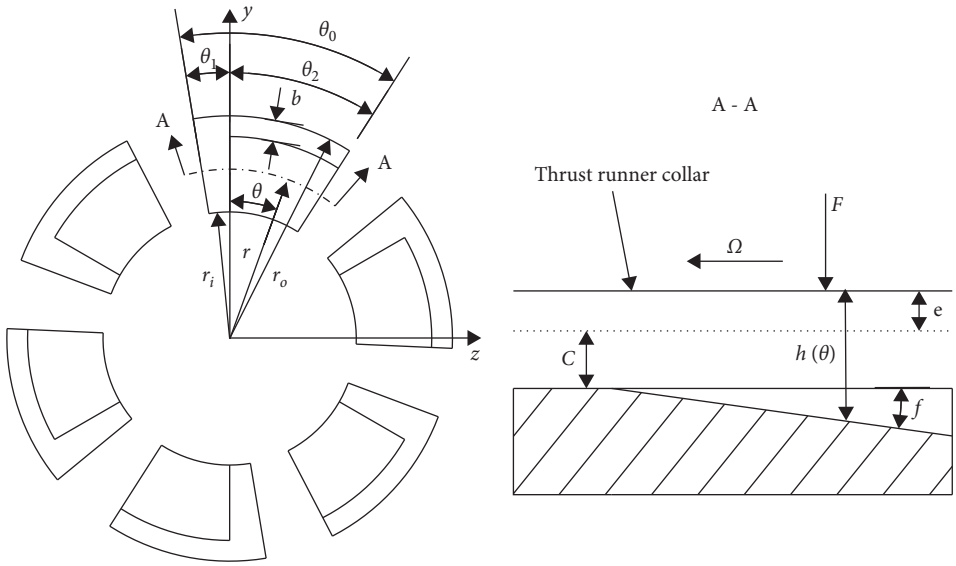

Figure 4: Dynamic model of the oil film thrust bearing.

$$\kappa^2 \frac{\partial}{\partial \theta}\left(\overline{h}^3 \frac{\partial \overline{p}}{\partial \theta}\right) + \frac{\partial}{\partial \overline{r}}\left(\overline{h}^3 \frac{\partial \overline{p}}{\partial \overline{r}}\right) = \frac{\partial \overline{h}}{\partial \theta} + 2\frac{\partial \overline{h}}{\partial \tau},$$
$$\begin{cases} p(1,\theta) = p(\overline{r}_o,\theta) = 0, \\ p(\overline{r},\theta_1) = p(\overline{r},\theta_2) = 0. \end{cases} \tag{15}$$

Similarly, the linearization result of nonlinear bearing force can be shown as Equation (18), where the force caused by dip angle of the thrust runner collar is neglected:

$$F_x \approx F_{x0} + k_{xx}\Delta x + c_{xx}\Delta \dot{x}, \tag{16}$$

where

$$k_{xx} = -\int_{r_i}^{r_o}\int_{\theta_1}^{\theta_2}\frac{\partial p}{\partial x}rd\theta\mathrm{d}r,$$
$$c_{xx} = -\int_{r_i}^{r_o}\int_{\theta_1}^{\theta_2}\frac{\partial p}{\partial \dot{x}}rd\theta\mathrm{d}r. \tag{17}$$

2.4. Dynamic Model of the Gear-Bearing System. For the shaft of Gear i, if total length is l_i, average diameter is d_i, and Young's modulus is E, the supporting stiffness of the shaft to Gear i is expressed as

$$k_s = \frac{3\pi d_i^4 E}{4l_i^3}. \tag{18}$$

The turnover stiffness of geared shaft to gear is expressed as

$$k_o = \frac{\pi d_i^4 E}{2l_i}. \tag{19}$$

Define k_{iyL} and k_{izL} as the left supporting bearing stiffness of Gear i along axis-x, y, and define k_{iyR} and k_{izR} as the right supporting bearing stiffness of Gear i along axis-x, y. The lateral supporting stiffness of Gear is expressed as

$$k_{\mathrm{iy}} = \frac{\left(k_{\mathrm{iyL}} + k_{\mathrm{iyR}}\right)k_s}{k_{\mathrm{iyL}} + k_{\mathrm{iyR}} + k_s},$$
$$k_{\mathrm{iz}} = \frac{\left(k_{\mathrm{izL}} + k_{\mathrm{izR}}\right)k_s}{k_{\mathrm{izL}} + k_{\mathrm{izR}} + k_s}. \tag{20}$$

The tilting stiffness of Gear i is expressed as

$$k_{i\theta y} = \frac{l_i\left(k_{\mathrm{izL}} + k_{\mathrm{izR}}\right)k_o}{l_i\left(k_{\mathrm{izL}} + k_{\mathrm{izR}}\right) + 2k_o},$$
$$k_{i\theta z} = \frac{l_i\left(k_{\mathrm{iyL}} + k_{\mathrm{iyR}}\right)k_o}{l_i\left(k_{\mathrm{iyL}} + k_{\mathrm{iyR}}\right) + 2k_o}. \tag{21}$$

Define c_{ix}, c_{iy}, c_{iz}, $c_{\mathrm{i}\theta\mathrm{y}}$, and $c_{\mathrm{i}\theta\mathrm{z}}$ as the shaft damping coefficient of Gear i along axis-x, y, z and around axis-y, z, respectively. The dynamic functions of gear system shown in Figure 2 are shown in Equations (22)–(26).

The dynamic functions of Gear 1 are shown as follows:

$$\begin{aligned}
&m_1\ddot{x}_1 + c_{1x}\dot{x}_1 + k_{1x}x_1 - \left[c_{12}\dot{p}_{12} + k_{12}g_{12}(t)\right]\sin\beta = 0,\\
&m_1 y_1 + c_{1y}\dot{y}_1 + k_{1y}y_1 + \left[c_{12}\dot{p}_{12} + k_{12}g_{12}(t)\right]\cos\beta\sin\left(\alpha - \phi_{12}\right) = 0,\\
&m_1 z_1 + c_{1z}\dot{z}_1 + k_{1z}z_1 + \left[c_{12}\dot{p}_{12} + k_{12}g_{12}(t)\right]\cos\beta\cos\left(\alpha - \phi_{12}\right) = 0,\\
&I_{p1}\ddot{\theta}_{x1} + c_{1\theta x}\dot{\theta}_{x1} + r_1\left[c_{12}\dot{p}_{12} + k_{12}g_{12}(t)\right]\cos\beta = T_1,\\
&I_{d1}\ddot{\theta}_{y1} + c_{1\theta y}\dot{\theta}_{y1} + \omega_1 I_{p1}\dot{\theta}_{z1} + k_{1\theta y}\theta_{y1}\\
&\quad + r_1\left[c_{12}\dot{p}_{12} + k_{12}g_{12}(t)\right]\sin\beta\sin\left(\alpha - \phi_{12}\right) = 0,\\
&I_{d1}\ddot{\theta}_{z1} + c_{1\theta z}\dot{\theta}_{z1} - \omega_1 I_{p1}\dot{\theta}_{y1} + k_{1\theta z}\theta_{z1}\\
&\quad + r_1\left[c_{12}\dot{p}_{12} + k_{12}g_{12}(t)\right]\sin\beta\cos\left(\alpha - \phi_{12}\right) = 0.
\end{aligned} \tag{22}$$

The dynamic functions of Gear 2 are shown as follows:

$$
\begin{aligned}
&m_2\ddot{x}_2 + c_{2x}\dot{x}_2 + k_{2x}x_2 + [c_{12}\dot{p}_{12} + k_{12}g_{12}(t)]\sin\beta - \sum_{i=3}^{5}[c_{2i}\dot{p}_{2i} + k_{2i}g_{2i}(t)]\sin\beta = 0,\\
&m_2\ddot{y}_2 + c_{2y}\dot{y}_2 + k_{2y}y_2 - [c_{12}\dot{p}_{12} + k_{12}g_{12}(t)]\cos\beta\sin(\alpha - \phi_{12}),\\
&\quad + \sum_{i=3}^{5}[c_{2i}\dot{p}_{2i} + k_{2i}g_{2i}(t)]\cos\beta\sin(\alpha - \phi_{12}) = 0,\\
&m_2\ddot{z}_2 + c_{2z}\dot{z}_2 + k_{2z}z_2 - [c_{12}\dot{p}_{12} + k_{12}g_{12}(t)]\cos\beta\cos(\alpha - \phi_{12}),\\
&\quad + \sum_{i=3}^{5}[c_{2i}\dot{p}_{2i} + k_{2i}g_{2i}(t)]\cos\beta\cos(\alpha - \phi_{12}) = 0,\\
&I_{p2}\ddot{\theta}_2 + c_{2\theta x}\dot{\theta}_{x2} - r_2[c_{12}\dot{p}_{12} + k_{12}g_{12}(t)]\cos\beta + r_2\sum_{i=3}^{5}[c_{2i}\dot{p}_{2i} + k_{2i}g_{2i}(t)]\cos\beta = 0,\\
&I_{d2}\ddot{\theta}_{y2} + c_{2\theta y}\dot{\theta}_{y2} + \omega_2 I_{p2}\dot{\theta}_{z2} + k_{2\theta y}\theta_{y2} + r_2[c_{12}\dot{p}_{12} + k_{12}g_{12}(t)]\sin\beta\sin(\alpha - \phi_{12}),\\
&\quad + r_2\sum_{i=3}^{5}[c_{2i}\dot{p}_{2i} + k_{2i}g_{2i}(t)]\sin\beta\sin(\alpha - \phi_{12}) = 0,\\
&I_{d2}\ddot{\theta}_{z2} + c_{2\theta z}\dot{\theta}_{z2} - \omega_2 I_{p2}\dot{\theta}_{y2} + k_{2\theta z}\theta_{z2} + r_2[c_{12}\dot{p}_{12} + k_{12}g_{12}(t)]\sin\beta\cos(\alpha - \phi_{12}),\\
&\quad + r_2\sum_{i=3}^{5}[c_{2i}\dot{p}_{2i} + k_{2i}g_{2i}(t)]\sin\beta\cos(\alpha - \phi_{12}) = 0.
\end{aligned}
\tag{23}
$$

The dynamic functions of Gear 3 are shown as follows:

$$
\begin{aligned}
&m_3\ddot{x}_3 + c_{3x}\dot{x}_3 + k_{3x}x_3 + [c_{23}\dot{p}_{23} + k_{23}g_{23}(t)]\sin\beta = 0,\\
&m_3\ddot{y}_3 + c_{3y}\dot{y}_3 + k_{3y}y_3 - [c_{23}\dot{p}_{23} + k_{23}g_{23}(t)]\cos\beta\sin(\alpha - \phi_{23}) = 0,\\
&m_3\ddot{z}_3 + c_{3z}\dot{z}_3 + k_{3z}z_3 - [c_{23}\dot{p}_{23} + k_{23}g_{23}(t)]\cos\beta\cos(\alpha - \phi_{23}) = 0,\\
&I_{p3}\ddot{\theta}_{x3} + c_{3\theta x}\dot{\theta}_{x3} - r_3[c_{23}\dot{p}_{23} + k_{23}g_{23}(t)]\cos\beta = T_3,\\
&I_{d3}\ddot{\theta}_{y3} + c_{3\theta y}\dot{\theta}_{y3} + \omega_3 I_{p3}\dot{\theta}_{z3} + k_{3\theta y}\theta_{y3} + r_3[c_{23}\dot{p}_{23} + k_{23}g_{23}(t)]\sin\beta\sin(\alpha - \phi_{23}) = 0,\\
&I_{d3}\ddot{\theta}_{z3} + c_{3\theta z}\dot{\theta}_{z3} - \omega_3 I_{p3}\dot{\theta}_{y3} + k_{3\theta z}\theta_{z3} + r_3[c_{23}\dot{p}_{23} + k_{23}g_{23}(t)]\sin\beta\cos(\alpha - \phi_{23}) = 0.
\end{aligned}
\tag{24}
$$

The dynamic functions of Gear 4 are shown as follows:

$$
\begin{aligned}
&m_4\ddot{x}_4 + c_{4x}\dot{x}_4 + k_{4x}x_4 + [c_{24}\dot{p}_{24} + k_{24}g_{24}(t)]\sin\beta = 0,\\
&m_4\ddot{y}_4 + c_{4y}\dot{y}_4 + k_{4y}y_4 - [c_{24}\dot{p}_{24} + k_{24}g_{24}(t)]\cos\beta\sin(\alpha - \phi_{24}) = 0,\\
&m_4\ddot{z}_4 + c_{4z}\dot{z}_4 + k_{4z}z_4 - [c_{24}\dot{p}_{24} + k_{24}g_{24}(t)]\cos\beta\cos(\alpha - \phi_{24}) = 0,\\
&I_{p4}\ddot{\theta}_{x4} + c_{4\theta x}\dot{\theta}_{x4} - r_4[c_{24}\dot{p}_{24} + k_{24}g_{24}(t)]\cos\beta = T_4,\\
&I_{d4}\ddot{\theta}_{y4} + c_{4\theta y}\dot{\theta}_{y4} + \omega_4 I_{p4}\dot{\theta}_{z4} + k_{4\theta y}\theta_{y4} + r_4[c_{24}\dot{p}_{24} + k_{24}g_{24}(t)]\sin\beta\sin(\alpha - \phi_{24}) = 0,\\
&I_{d4}\ddot{\theta}_{z4} + c_{4\theta z}\dot{\theta}_{z4} - \omega_4 I_{p4}\dot{\theta}_{y4} + k_{4\theta z}\theta_{z4} + r_4[c_{24}\dot{p}_{24} + k_{24}g_{24}(t)]\sin\beta\cos(\alpha - \phi_{24}) = 0.
\end{aligned}
\tag{25}
$$

The dynamic functions of Gear 5 are shown as follows:

$$
\begin{aligned}
&m_5\ddot{x}_5 + c_{5x}\dot{x}_5 + k_{5x}x_5 + [c_{25}\dot{p}_{25} + k_{25}g_{25}(t)]\sin\beta = 0,\\
&m_5\ddot{y}_5 + c_{5y}\dot{y}_5 + k_{5y}y_5 - [c_{25}\dot{p}_{25} + k_{25}g_{25}(t)]\cos\beta\sin(\alpha - \phi_{25}) = 0,\\
&m_5\ddot{z}_5 + c_{5z}\dot{z}_5 + k_{5z}z_5 - [c_{25}\dot{p}_{25} + k_{25}g_{25}(t)]\cos\beta\cos(\alpha - \phi_{25}) = 0,\\
&I_{p5}\ddot{\theta}_{x5} + c_{5\theta x}\dot{\theta}_{x5} - r_5[c_{25}\dot{p}_{25} + k_{25}g_{25}(t)]\cos\beta = T_{,5}\\
&I_{d5}\ddot{\theta}_{y5} + c_{5\theta y}\dot{\theta}_{y5} + \omega_5 I_{p5}\dot{\theta}_{z5} + k_{5\theta y}\theta_{y5} + r_5[c_{25}\dot{p}_{25} + k_{25}g_{25}(t)]\sin\beta\sin(\alpha - \phi_{25}) = 0,\\
&I_{d5}\ddot{\theta}_{z5} + c_{5\theta z}\dot{\theta}_{z5} - \omega_5 I_{p5}\dot{\theta}_{y5} + k_{5\theta z}\theta_{z5} + r_5[c_{25}\dot{p}_{25} + k_{25}g_{25}(t)]\sin\beta\cos(\alpha - \phi_{25}) = 0,
\end{aligned}
\tag{26}
$$

where T_i is the load on the Gear i; m_i, I_{pi}, and I_{di} are the mass, polar moment of inertia, and diameter moment of inertia of Gear i, respectively; p_{ij} is the length of meshing line between Gear i and Gear j; ϕ_{ij} is the position angle of Gear j respect to Gear i; α is the pressure angle of gear; and $g_{ij}(t)$ is the clearance function expressed as

$$
g_{ij}(t) = \begin{cases} p_{ij} - b_{ij}, & p_{ij} > b_{ij},\\ 0, & |p_{ij}| \le b_{ij},\\ p_{ij} + b_{ij}, & p_{ij} < -b_{ij}, \end{cases}
\tag{27}
$$

where $2b_{ij}$ is the clearance length between Gear i and j.

The space vector of the system totally has 30 DOFs and can be expressed as

$$
\mathbf{X} = \left[x_1, y_1, z_1, \theta_{x1}, \theta_{y1}, \theta_{z1}, \cdots, x_5, y_5, z_5, \theta_{x5}, \theta_{y5}, \theta_{z5}\right]^{\mathrm{T}}.
\tag{28}
$$

Equations (22)-(26) can be written as

$$
\mathrm{M}\ddot{X} + (\mathrm{C}_s + \mathrm{C}_m + \mathbf{H})\dot{X} + \mathrm{K}_s\mathbf{X} + \mathrm{K}_m\mathbf{G}(p) = \mathrm{F},
\tag{29}
$$

where M, C_s, K_s, C_m, and K_m are the mass matrix, supporting damping matrix, supporting stiffness matrix, meshing damping matrix, and meshing stiffness matrix of gear system, respectively; $\mathbf{H}$ is the gyro matrix of the gear system; $\mathbf{G}(p)$ is a tooth gap function related to p; and F is load vector.

Through defining that $x_{\theta i} = r_i\theta_{xi}$, $y_{\theta i} = r_i\theta_{yi}$, and $z_{\theta i} = r_i\theta_{zi}$, the angle variable of space vector can be transformed into the arc length turning around the basic circle. Assume the characteristic frequency and length are ω_c and b_c, and define that

$$
\begin{aligned}
&\tau = \omega_c t, \overline{X}_{ij} = \frac{\mathbf{X}_{ij}}{b_c}, \overline{e}_{ij} = \frac{e_{ij}}{b_c}, \overline{b}_{ij} = \frac{b_{ij}}{b_c},\\
&\overline{X} = [\overline{x}_1, \overline{y}_1, \overline{z}_1, \overline{x}_{\theta 1}, \overline{y}_{\theta 1}, \overline{z}_{\theta 1}, \cdots, \overline{x}_5, \overline{y}_5, \overline{z}_5, \overline{x}_{\theta 5}, \overline{y}_{\theta 5}, \overline{z}_{\theta 5}]^{\mathrm{T}},\\
&\frac{d\overline{X}}{d\tau} = \dot{\overline{X}}, \frac{d^2\overline{X}}{d\tau^2} = \ddot{\overline{X}},\\
&\mathbf{S} = \mathrm{diag}(1, 1, 1, r_1, r_1, r_1, \cdots, 1, 1, 1, r_5, r_5, r_5).
\end{aligned}
\tag{30}
$$

(25) can be converted into proper dimensionless indexes and expressed as

$$
\ddot{\overline{X}} + (\overline{\mathrm{C}}_s + \overline{\mathrm{C}}_m + \overline{\mathbf{H}})\dot{\overline{X}} + \overline{\mathrm{K}}_s\overline{X} + \overline{\mathrm{K}}_m\overline{G}(\overline{p}) = \overline{\mathrm{F}},
\tag{31}
$$

where $\overline{\mathrm{C}}_s = \mathbf{S}\mathrm{M}^{-1}\mathrm{C}_s\mathbf{S}^{-1}/\omega_c$, $\overline{\mathrm{C}}_m = \mathbf{S}\mathrm{M}^{-1}\mathrm{C}_m\mathbf{S}^{-1}/\omega_c$, $\overline{\mathrm{K}}_s = \mathbf{S}\mathrm{M}^{-1}\mathrm{K}_s\mathbf{S}^{-1}/\omega_c$, $\overline{\mathrm{K}}_m = \mathbf{S}\mathrm{M}^{-1}\mathrm{K}_m\mathbf{S}^{-1}/\omega_c^2$, $\overline{\mathrm{H}}_s = \mathbf{S}\mathrm{M}^{-1}\mathrm{H}\mathbf{S}^{-1}/\omega_c$, and $\overline{\mathrm{F}} = \mathbf{S}\mathrm{M}^{-1}/b_c\omega_c^2\mathrm{F}$。

The backlash function of each gear pair can be defined as

$$
\overline{G}_{ij}(\overline{p}_{ij}) = \begin{cases} \overline{X}_{ij} - \dfrac{1}{4}\mathbf{S}_{ij}\mathbf{B}_{ij}\overline{b}_{ij}, & \overline{p}_{ij} > \overline{b}_{ij},\\ 0, & |\overline{p}_{ij}| \le \overline{b}_{ij},\\ \overline{X}_{ij} + \dfrac{1}{4}\mathbf{S}_{ij}\mathbf{B}_{ij}\overline{b}_{ij}, & \overline{p}_{ij} < -\overline{b}_{ij}. \end{cases}
\tag{32}
$$

3. Self-Excited Vibration Analysis of Gear-Bearing System

3.1. Vibration Behaviors of the Gear System by Self-Excited Vibration. The main parameters of gear pairs in Figure 2 are shown in Table 1. The backlash and meshing error of the gear pairs are 100 μm and 20 μm, respectively.

Rated loads on the three output shafts are $T_3 = 24$ Nm, $T_4 = 20$ Nm, and $T_5 = 18$ Nm. The following three simulated conditions are depicted.

Condition 1. Rated load with constant bearing damping and stiffness at 4000 r/min.

Condition 2. Rated load and variable bearing damping and stiffness calculated by Equations (13) and (17).

Condition 3. 1.5 times the rated load with variable bearing damping and stiffness calculated by Equations (13) and (17).

The Newmark-β method is used to analyze the dynamics of the above three working conditions according to (31), in which the Newmark constants are 0.25 and 0.5. In order to describe the vibration and meshing behavior of the gear system in the whole process of increasing speed, the vibration bifurcation diagrams of Gear 4 along y-axis at different input speeds ranging from 500r/min to 4000r/min are obtained and presented in Figure 5 based on the dynamic analysis of the vibration of gear system under the three conditions.

The nonlinear vibration characteristics of the gear system under the impact of speed are shown in Figure 5(a). Before the input speed reaches 1600r/min, the gear vibration

Table 1: Parameters of gears.

	Gear 1	Gear 2	Gear 3	Gear 4	Gear 5
Modulus (mm)			2.5		
Face width (mm)			45		
Pressure angle (deg)			20		
Tooth number	80	193	41	33	25
Radius of basic circle (mm)	191.6	462.3	98.2	79.1	59.9
Mass (kg)	13	50	3.8	2.5	1.7
Polar inertia moment (kgm^2)	0.07	1.6	0.007	0.004	0.003
Inertia moment (kgm^2)	0.04	0.8	0.005	0.003	0.002

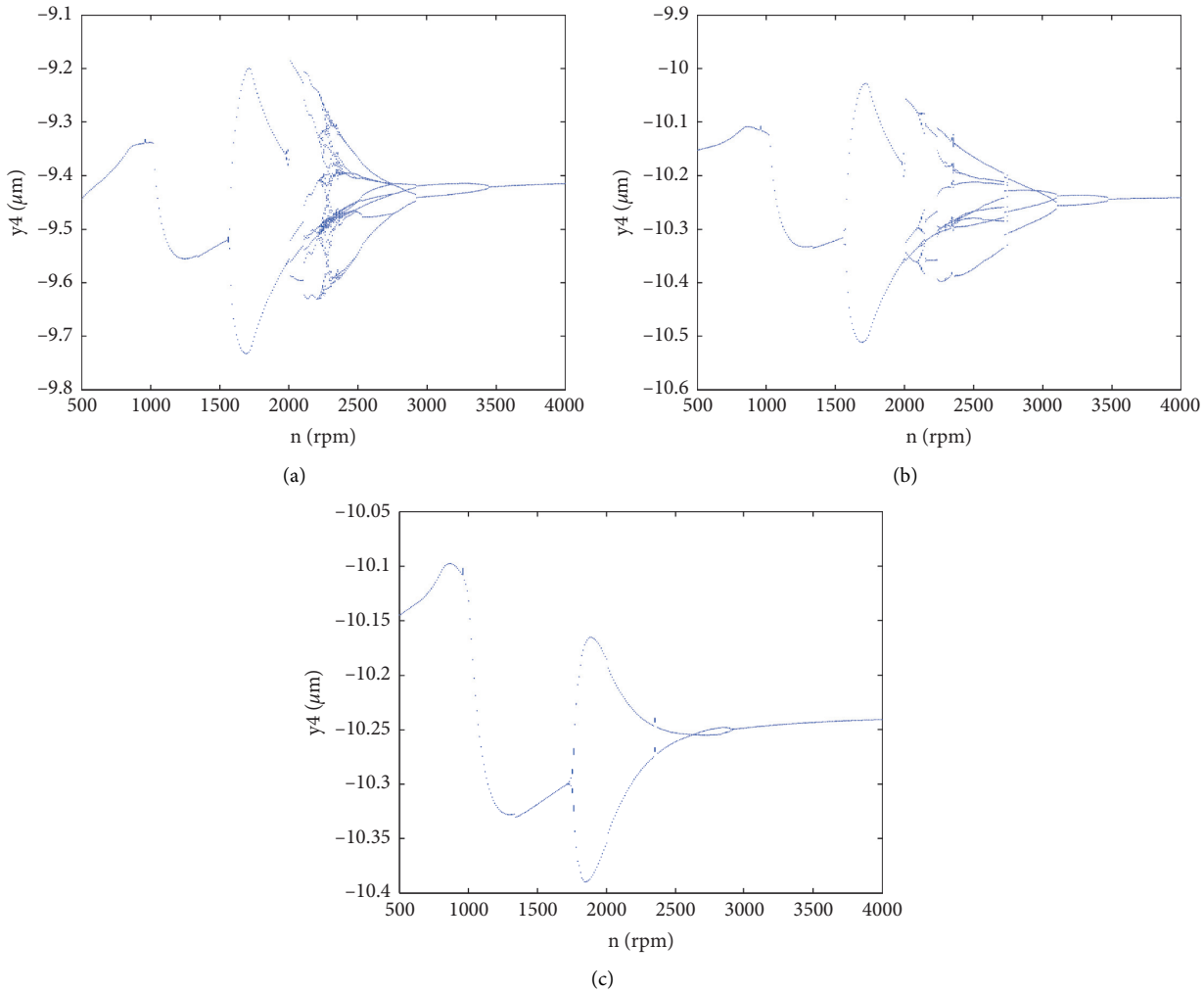

Figure 5: Bifurcation diagram of y4. (a) Condition 1. (b) Condition 2. (c) Condition 3.

is harmonic. Then the vibration signals begin to period doubling bifurcate, and gradually evolve into chaos near 2280 r/min. With the increasing of the input speed, the vibration signal of the gear begins to return to the multi period motion, and eventually returning to harmonic motion at 3500r/min.

When bearing variable stiffness is taken into account, nonlinear vibration of gears is reduced. Although there is no further evolution after the vibration signal evolved to eight periods' motion, the non-linear speed region, which is also from 1600r/min to 3500r/min, is not greatly reduced in Figure 5(b). The stiffness and the damping of the bearing are positively correlated with the speed of the bearing, according to Equations (13) and (17). The dynamic stiffness of each oil film bearing before 4000 r/min is relatively low in comparison to Condition 1, so the stiffness of the entire gear system with Condition 2 is lower than Condition 1. These show that the flexible support has inhibition to the nonlinear

motion of the system, whereas the support with greater stiffness could aggravate the nonlinear vibration of the system.

The calculated result of the gear system under 1.5 times rated load differs significantly from that shown in Figure 5(c) under rated load. With a heavy load, the non-linear speed interval decreases noticeably. The vibration of the system begins to bifurcate after 1800r/min, and there is no further evolution after two periods' motion and back to harmonic motion after 3000r/min. The gear vibration signal alternates between two periods' motion and on period motion throughout the entire input speed range. The comparison results show that the load on the gear system has a significant impact on the gear system's nonlinear vibration.

Figure 6 depicts the frequency-domain characteristics of the vibration displacement of Gear 4 along y-direction under the three conditions. There is no discernible difference between Condition 1 and Condition 2 in terms of frequency-domain features. Except for the meshing frequency f_m and its double frequency of $2f_m$, the subfrequency $f_m/2$ begins to appear from 1500r/min to 3500r/min. $F_m/4$ and $f_m/8$ can also be found from 2000 r/min to 3000 r/min, and the peaks of the subfrequencies are even higher than the peak of meshing frequency at some speeds. The peak value of meshing frequency gradually decreases as the speed increases. It also shows that if nonlinear vibration in the nonlinear speed region is ignored, the higher the speed is, the relatively less the effect of self-excited vibration on the system vibration is. The frequency-domain features of Condition 3 are quite different from those of the first two conditions. Except for the meshing frequency f_m and its double frequency of $2f_m$, only the subfrequency $f_m/2$ can be found between 1700r/min to 3000r/min, and no other subfrequencies are presented. The peak value of subfrequency $f_m/2$ with heavy load is much lower than in Conditions 1 and 2, due to the load effect, but there is no discernible difference in the peak value of f_m compared to Conditions 1 and 2.

The influence of variable bearing coefficients on the analysis results is compared using a correlation analysis between Condition 1 and Condition 2. Figure 7 depicts the results of the vibration signals in the time domain and frequency domain at various speeds. When the input speed is below 1000 r/min or above 3200 r/min, the correlation coefficients between time-domain and frequency-domain data are close to 1. The correlation coefficient of frequency-domain data decreases slightly in the nonlinear region, but it remains above 0.95. However, time-domain data has lower correlation coefficients than frequency-domain data, though there is still some correlation (above 0.6). It shows that variable stiffness and damper of bearing have a minor impact on the simulation results at frequency-domain features analysis, but have a significant impact at time-domain features analysis. Variable bearing coefficients should be considered in vibration analysis and non-linear characteristic analysis.

The vibration signals of y4 under Condition 1 at different rotational speeds are shown in Figure 8 to compare and analyze the change of gear vibration with input speed. The variation of the vibration period with rotational speed can be clearly seen from the diagram. In order to compare the vibration information under the three conditions more clearly. Time-domain analysis methods are adopted in Figure 9, where the peak to peak value and standard deviation of vibration data in these three conditions are analyzed.

It can be seen that the peak to peak and standard deviation values of the vibration data in the non-linear speed region are much larger than the other speeds. The vibration will act directly on the supporting bearing, producing disturbed vibration force. The peak to peak value and standard deviation of the central displacement of Gear 4 are nearly identical under Conditions 1 and 2, but the result calculated using the variable dynamic parameter of bearing is slightly lower and smoother than constant one. Due to the influence of heavy load, the peak to peak value and standard deviation values are clearly reduced, while the fluctuated force of the bearing in the non-linear speed region is also relatively small.

3.2. Meshing Force of the Gear System by Self-Excited Vibration. Figure 10 depicts the frequency-domain features of meshing force between Gear 2 and Gear 4 at various speeds.

There is also no discernible difference between the frequency-domain features of meshing force under Conditions 1 and 2. In comparison to the results in Figure 6, the peaks of meshing frequency are unaffected by changing speed, and they are significantly greater than the peaks of subfrequency $f_m/2$ even in the non-linear speed region. $f_m/4$ and $f_m/8$ can also be found from 1500 r/min to 3500 r/min, but their peaks of these subfrequencies are far smaller than $f_m/2$. The frequency-domain features of meshing force differ significantly from those shown in Figure 6(c). Except for the meshing frequency f_m and its double frequencies, the subfrequencies are quite small. Condition 3 has significantly higher peaks of meshing frequency than the other conditions due to the heavy load.

Figure 11 compares and analyzes the mean, peak to peak, and RMS of the meshing force in these three conditions. The mean value of the three groups of meshing forces varies little as the rotational speed increases. The values under Condition 3 are roughly 1.5 times those of Conditions 1 and 2, which are proportional to the load. The peak to peak values and RMS values in the nonlinear speed region are obviously higher than the other speeds at rated load. The result calculated using a variable dynamic parameter of bearing changes slightly smoother than constant one. When the load have increased to 1.5 times rated load, the peak to peak values and RMS values in the nonlinear speed region do not increase, and are far lower than the results under rated loads. Meanwhile, the RMS values under high load are clearly higher than that under low load.

The main cause of non-linear vibration in compressor gear systems is the impact between gears. With the increasing of the speed, the meshing state between the tooth surfaces would change from continuous meshing to collision, and different non-linear meshing states could be evolved. In the nonlinear speed region, the vibration and

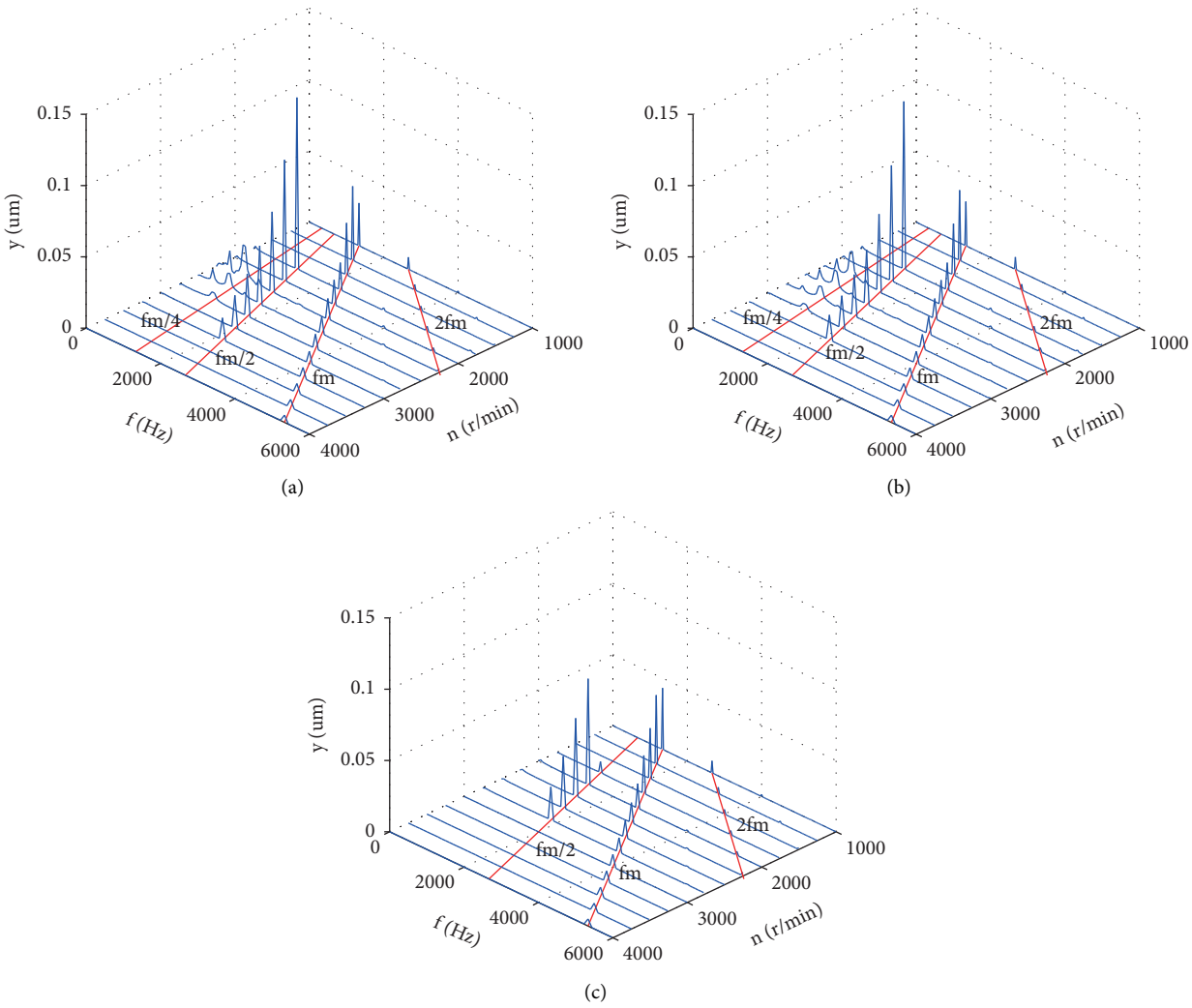

Figure 6: Frequency-domain analysis of y4. (a) Condition 1. (b) Condition 2. (c) Condition 3.

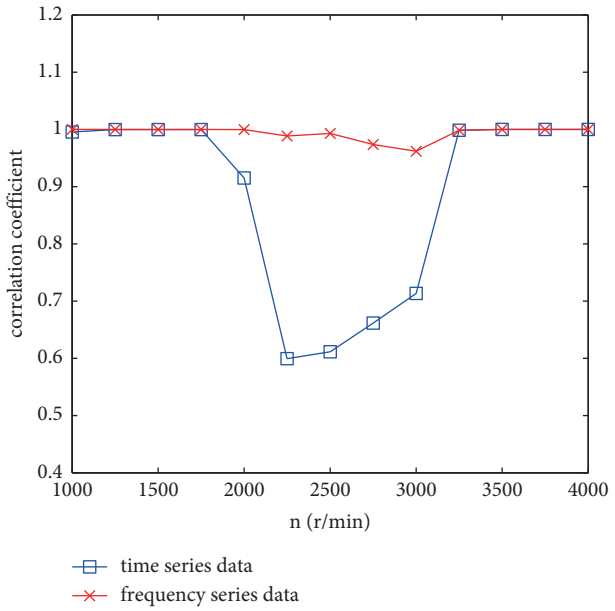

Figure 7: Correlation coefficient of vibration results between Conditions 1 and 2.

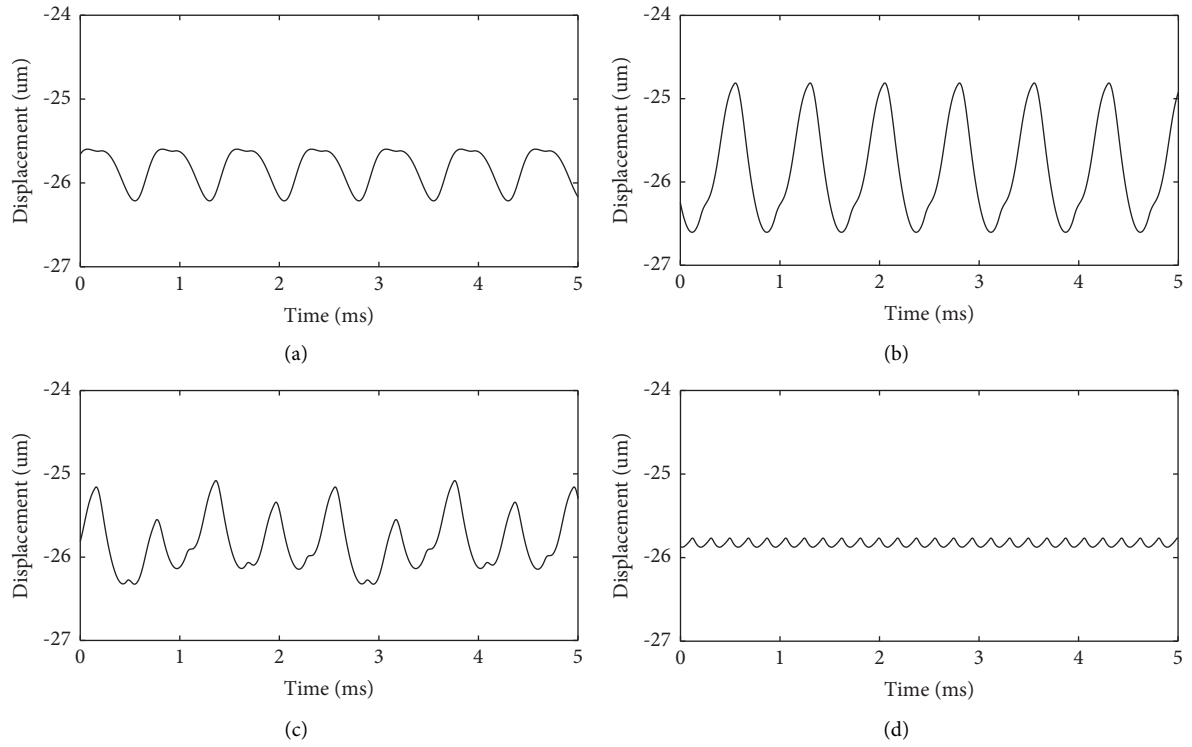

Figure 8: Time-domain signals of y4 under Condition 1. (a) 1000r/min. (b) 2000r/min. (c) 2500r/min. (d) 4000r/min.

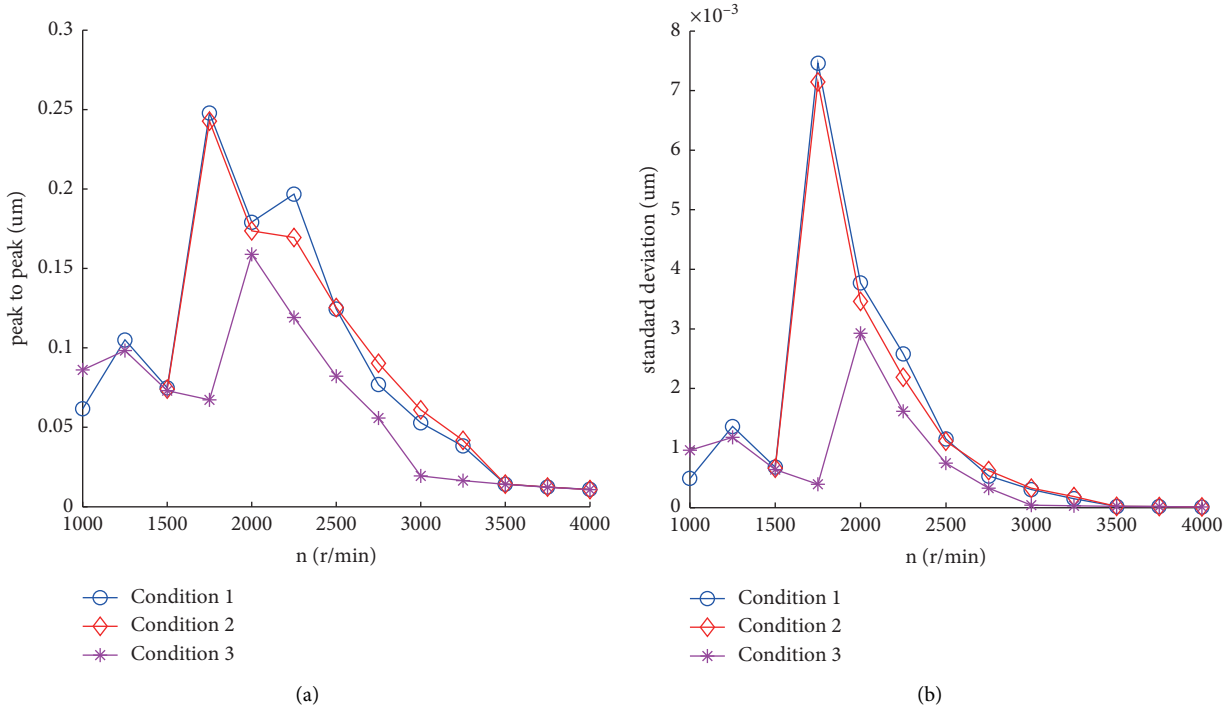

Figure 9: Time-domain analysis of meshing force between Gear 2 and Gear 4. (a) Peak to peak value. (b) Standard deviation.

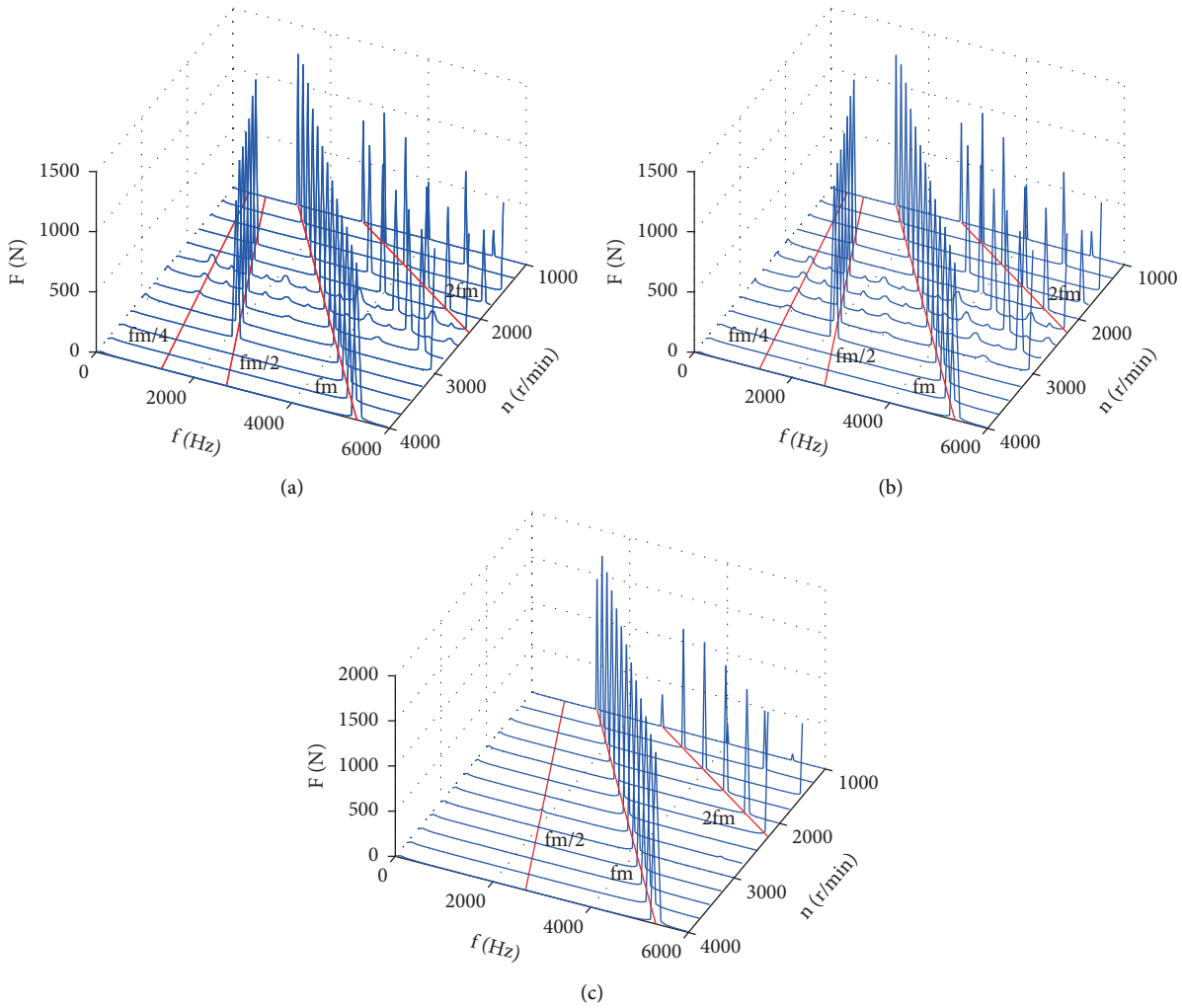

Figure 10: Frequency-domain analysis of meshing force between Gear 2 and Gear 4. (a) Condition 1. (b) Condition 2. (c) Condition 3.

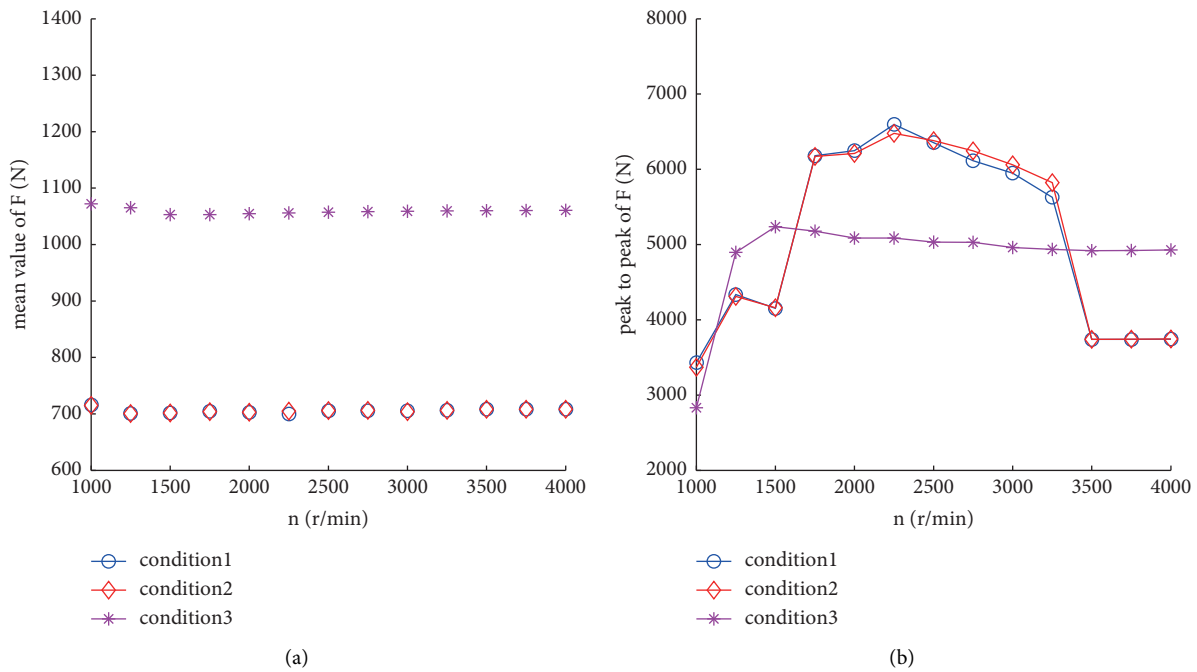

Figure 11: Continued.

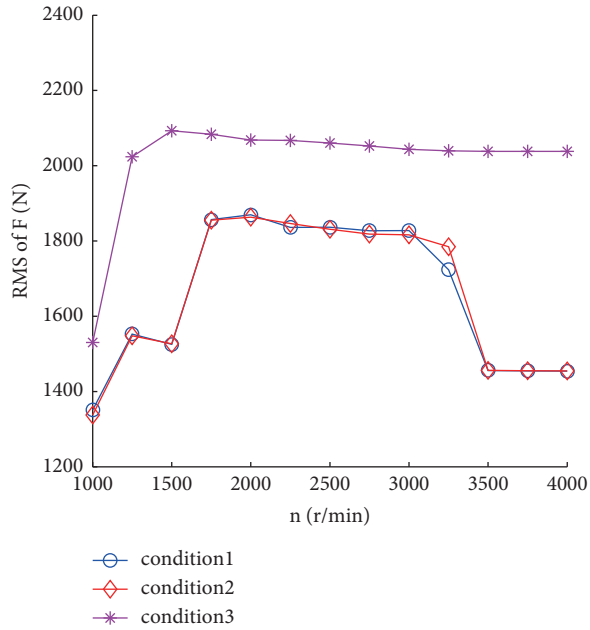

(c)

Figure 11: Time-domain analysis of meshing force between Gear 2 and 4. (a) Mean value. (b) Peak to peak value. (c) RMS.

meshing force will change. In general, increasing the load and decreasing the stiffness of the bearing appropriately can improve the stability of meshing.

4. Conclusion

The modeling approach of the geared-rotor system in integrally centrifugal compressors considering changing multipoint meshing force and variable bearing stiffness and damper is proposed in this research, and the non-linear coupled vibrations of the gear system and meshing properties are explored at different speeds and loads.

The nonlinear vibration might appear as the meshing frequency increases due to the effect of nonlinear parameters such as meshing clearance and transmission error. The flexible support inhibits the system's nonlinear motion, whereas the bearing with increased stiffness may aggravate the system's nonlinear vibration. Considering the influence of the rotating shaft's dynamic stiffening effect, increasing the driven speed will not change the peak of meshing frequency of meshing force, but decrease the peak of meshing frequency of vibration in the gear system.

The peak to peak and standard deviation values of the vibration data are substantially bigger in the nonlinear speed area than in the other speeds. This means that the disturbance force acting on the supporting bearing would be raised as well. The disrupted force in the nonlinear speed area would plainly diminish as the load increased. The peak to peak and RMS values of the meshing force are greater in the nonlinear speed area than in the other speeds at rated load. However, when the load is increased to a certain level, this phenomenon disappears, and the changes in peak to peak and RMS values in the nonlinear speed area are not significant. The large load of the gear-bearing system can effectively reduce nonlinear vibration and increase meshing stability.

Data Availability

The data used to support the findings of this study are included within the article.

Conflicts of Interest

The authors declare that there are no conflicts of interest regarding the publication of this paper.

Acknowledgments

The study was supported by the Natural Science Foundation of Liaoning Province (granted No.2019-KF-01-08) and Key Laboratory of Vibration and Control of Aero-Propulsion System Ministry of Education, Northeastern University (granted No. VCAME201903).

References

[1] J. J. Moore, S. T. Walker, and M. J. Kuzdzal, "Rotordynamic stability measurement during full-load, full-pressure testing of a 6000 psi re-injection centrifugal compressor," in *Proceedings of the Thirty-First Turbomachinery Symposium*, September 2002.

[2] H. Arihara, Y. Baba, S. Morinaka, and Y. Kameyama, "The experimental rotordynamic stability evaluation method using magnetic excitation system for an integrally geared compressor," *Proceedings of the ASME Turbo Expo*, vol. 10B, p. 11, 2020, Structures and Dynamics Paper No: GT2020-14883.

[3] O. Doan, F. Karpat, O. Kopmaz, and S. Ekwaro-Osire, "Influences of gear design parameters on dynamic tooth loads

and time-varying mesh stiffness of involute spur gears," *Sadhana*, vol. 45, no. 258, pp. 1–15, 2020.

[4] C. H. Kang, W. C. Hsu, E. K. Lee, and T. N. Shiau, "Dynamic analysis of gear-rotor system with viscoelastic supports under residual shaft bow effect," *Mechanism and Machine Theory*, vol. 46, no. 3, pp. 264–275, 2011.

[5] Z. Shi and S. Li, "Nonlinear dynamics of hypoid gear with coupled dynamic mesh stiffness," *Mechanism and Machine Theory*, vol. 168, Article ID 104589, 2022.

[6] Q. Han and F. Chu, "Dynamic behaviors of a geared rotor system under time-periodic base angular motions," *Mechanism and Machine Theory*, vol. 78, no. 4, pp. 1–14, 2014.

[7] K. Feng, P. Borghesani, W. A. Smith et al., "Vibration- based updating of wear prediction for spur gears," *Wear*, vol. 426-427, pp. 1410–1415, 2019.

[8] K. Feng, W. A. Smith, R. B. Randall, H. Wu, and Z. Peng, "Vibration-based monitoring and prediction of surface profile change and pitting density in a spur gear wear process," *Mechanical Systems and Signal Processing*, vol. 165, pp. 1–25, Article ID 108319, 2022.

[9] M. Inalpolat, M. Handschuh, and A. Kahraman, "Influence of indexing errors on dynamic response of spur gear pairs," *Mechanical Systems and Signal Processing*, vol. 60-61, pp. 391–405, 2015.

[10] S. Theodossiades and S. Natsiavas, "Non-linear dynamics of gear-pair systems with periodic stiffness and backlash," *Journal of Sound and Vibration*, vol. 229, no. 2, pp. 287–310, 2000.

[11] T. Eritenel and R. G. Parker, "Three-dimensional nonlinear vibration of gear pairs," *Journal of Sound and Vibration*, vol. 331, no. 15, pp. 3628–3648, 2012.

[12] J. R. Cho, K. Y. Jeong, M. H. Park, D. S. Shin, O. K. Lim, and N. G. Park, "Finite element structural analysis of wind turbine gearbox considering tooth contact of internal gear system," *Journal of Mechanical Science and Technology*, vol. 27, no. 7, pp. 2053–2059, 2013.

[13] A. Guerine, A. El Hami, L. Walha, T. Fakhfakh, and M. Haddar, "A perturbation approach for the dynamic analysis of one stage gear system with uncertain nnparameters," *Mechanism and Machine Theory*, vol. 92, pp. 113–126, 2015.

[14] W. Luo, B. Qiao, Z. Shen, Z. Yang, and X. Chen, "Time-varying mesh stiffness calculation of a planetary gear set with the spalling defect under sliding friction," *Meccanica*, vol. 55, pp. 245–260, 2020.

[15] X. Zheng, W. Luo, Y. Hu, Z. He, and S. Wang, "Study on the mesh stiffness and nonlinear dynamics accounting for centrifugal effect of high-speed spur gears," *Mechanism and Machine Theory*, vol. 170, Article ID 104686, 2022.

[16] J. Wang, J. Zhang, Z. Yao, X. Yang, R. Sun, and Y. Zhao, "Nonlinear characteristics of a multi-degree-of- freedom spur gear system with bending-torsional coupling vibration," *Mechanical Systems and Signal Processing*, vol. 121, pp. 810–827, 2019.

[17] M. B. Sánchez, M. Pleguezuelos, and J. I. Pedrero, "Influence of profile modifications on meshing stiffness, load sharing, and trasnsmission error of involute spur gears," *Mechanism and Machine Theory*, vol. 139, pp. 506–525, 2019.

[18] G. Wang, Q. Luo, and S. Zou, "Time-varying meshing stiffness calculation of an internal gear pair with small tooth number difference by considering the multi-tooth contact problem," *Journal of Mechanical Science and Technology*, vol. 35, no. 9, pp. 4073–4083, 2021.

[19] Z. Zhao, H. Han, P. Wang, H. Ma, and Y. Yang, "An improved model for meshing characteristics analysis of spur gears considering fractal surface contact and friction," *Mechanism and Machine Theory*, vol. 158, pp. 1–18, Article ID 104219, 2021.

[20] C. W. Chang-Jian and C. K. Chen, "Bifurcation and chaos analysis of a flexible rotor supported by turbulent long journal bearings," *Chaos, Solitons & Fractals*, vol. 34, no. 4, pp. 1160–1179, 2007.

[21] A. Amamou and M. Chouchane, "Nonlinear stability analysis of long hydrodynamic journal bearings using numerical continuation," *Mechanism and Machine Theory*, vol. 72, pp. 17–24, 2014.

[22] J. R. Lin, P. J. Li, and T. C. Hung, "Lubrication performances of short journal bearings operating with non-Newtonian ferrofluids," *Zeitschrift für Naturforschung- Section A Journal of Physical Sciences*, vol. 68, pp. 249–254, 2013.

[23] S. Soni and D. P. Vakharia, "Performance analysis of short journal bearing under thin film lubrication," *ISRN Mechanical Engineering*, vol. 2014, Article ID 281021, 8 pages, 2014.

[24] D. V. Srikanth, "Oil film angular stiffness determination in a hydroelectric tilting pad thrust bearing," in *Proceedings of the STLE/ASME 2010 International Joint Tribology Conference*, pp. 131–133, American Society of Mechanical Engineers (ASME), San Francisco, CA, USA, October 2010.

[25] G. Zhang, S. Liu, R. Ma, and Z. Liu, "Nonlinear dynamic characteristics of journal bearing–rotor system considering the pitching and rolling motion for marine turbo machinery," *Proceedings of the Institution of Mechanical Engineers - Part M: Journal of Engineering for the Maritime Environment*, vol. 229, no. 1, pp. 95–107, 2015.

[26] M. A. Liang, J. H. Zhang, J. W. Lin, J. Wang, and X. Lu, "Dynamic characteristics analysis of a misaligned rotor-bearing system with squeeze film dampers," *Journal of Zhejiang University - Science*, vol. 17, no. 8, pp. 614–631, 2016.

[27] T. A. Cable, L. S. Andres, and K. D. Wygant, "On the predicted effect of angular misalignment on the performance of oil lubricated thrust collars in integrally geared compressors," *Journal of Engineering for Gas Turbines and Power-transactions of The Asme*, vol. 139, no. 4, p. 11, 2016.

Hindawi
Shock and Vibration
Volume 2022, Article ID 8303722, 11 pages
https://doi.org/10.1155/2022/8303722

Research Article

A Novel Denoise Method of Acoustic Signal from Train Bearings Based on Resampling Technique and Improved Crazy Climber Algorithm

Yali Sun,[1] **Hua Li**,[2] **Xing Zhao**,[2] **Jiyou Fei**,[2] **Xiaodong Liu**,[2] **and Yijie Niu**[3]

[1]*College of Mechanical Engineering, Dalian Jiaotong University, Dalian 116028, China*
[2]*College of Locomotive and Rolling, Dalian Jiaotong University, Dalian 116028, China*
[3]*College of Software, Dalian Jiaotong University, Dalian 116028, China*

Correspondence should be addressed to Jiyou Fei; fjy@djtu.edu.cn

Received 29 November 2021; Accepted 2 March 2022; Published 24 March 2022

Academic Editor: Kexiang Wei

The wayside acoustic defective bearing detector system (TADS) is located on both sides of the railway, so that the acoustic signals recorded by the microphone not only include the sound from the train bearings but also include it from the other disturbance sources. The heavy noise and multisource acoustic signals would badly reduce the reliability and accuracy of the detection result of the TADS. In order to extract the useful information from the recorded signal exactly and efficiently, a novel denoising method based on the Short-time Fourier transform (STFT) and improved Crazy Climber algorithm was improved in this paper. Firstly, the STFT was performed on the recorded acoustic signals in order to obtain the time-frequency distribution matrix. Based on the original algorithm, the novel movement rule and the fitting process of the ridge lines were presented which could extract the time-frequency ridge lines of the acoustic signal accurately and rapidly. In this way, the important information from the train bearings could be divided from the heavy noise and other signals. Finally, the simulation and experimental verifications were carried out, and the denoising method based on the STFT and improved Crazy Climber algorithm has proved to be effective in extracting ridge lines of the time-frequency distribution matrix and dividing the useful information form the recorded acoustic signals.

1. Introduction

The failure of the rolling bearings has already become one for the main reasons of the train breakdown in the past decade, which could lead to irretrievable loss of life and property in serious cases. Therefore, it is essential to develop the techniques of fault diagnosis and condition monitoring for the train bearings in the transportation industry [1–4]. The wayside acoustic defective bearing detector system (TADS) [5] was developed in the 1980s to detect bearing flaws, which could collect the acoustic signal from the bearings of trains by monitoring microphones on the rail-mounted wayside [6–8]. And, the service status monitoring of the train bearings can be realized by processing and analyzing the acoustic signals. Just one set of such systems could be used to monitor all the trains passing through the section, which improves the efficiency of bearing monitoring and reduces the monitoring cost greatly [9–11]. Meanwhile, the TADS has some unique characteristics as no-contact and no-disintegration versus traditional contact measurement (vibration-based methods). Therefore, the wayside acoustics-based techniques have aroused considerable interest over the past years in the field of train monitoring. However, some key issues still need to be solved, such as there is serious noise in received acoustic signals. Besides the important information from the train bearing, the audio signals usually contain lots of useless content like the ambient noise, the rolling noise, the air-noise and traction noise. What is important is that the intensity of the noise signal in the received signal is much greater than that of the bearing signal, and the signals from various sources are mixed together, which makes it difficult to obtain useful signals effectively, so that it is still a great

challenge for train bearing detecting with acoustic methods at present.

There are some scholars being committed to the problem mentioned above. Yu-xing and Long [12] proposed a novel noise reduction method for underwater acoustic signals. Such method was based on the complete ensemble empirical mode decomposition with adaptive noise, minimum mean square variance criterion and least mean square adaptive filter. This method has a better performance on suppression of mode mixing and also has a better noise reduction performance. Moreover, it is beneficial to the further processing of underwater acoustic signals. Ni et al. [13] proposed a fault information-guided variational mode decomposition method for extracting the weak bearing information. In this method, the sensitivity to the bearing fault signature, which was achieved through the integration of the bearing fault cyclic period, enables early bearing fault diagnosis competently. The method mentioned above provided a good reference for noise reduction and bearing fault diagnosis. However, due to the special position of TADS, the signals received by the microphone are not repeatable, so it is still difficult to effectively detect train bearings. And other scholar found that the ridge energy intensity of the bearing's time domain signal was much higher than that of the noise and other useless signals. In addition, the instantaneous frequency (IF) of the bearing signal can be obtained by the ridges of the time-domain signal, and the objects of denoise and bearings diagnosis could be achieved. Zhang et al. [14]. proposed a time-frequency ridge extract method based on instantaneous frequency estimation. By this method, the ridge lines of the signal could be extracted completely in the case of low noise. To some extent, this method realized the noise cancellation and useful signals extraction. Xu et al. [15] aiming at the problem of the ridge lines could not extract completely, they propose to extract the instantaneous the ridge lines of sound signal effectively by compressing and rearranging the time spectrum in the time-frequency plane under the low noise environment. The method mentioned above provides good references and experience for extracting time-frequency ridge lines. However, these denoising methods based solely on frequency domain processing have poor performance in high ambient noise and can only extract useful information in low noise environment. However, there is a lot of noise in the sound signal received by the microphone, which limits the application of the above method in practical application.

Further, some researchers are looking for ways to remove noise and extract useful information in higher-noise environments. The Crazy Climber algorithm was proposed by Carmona et al. [16], which could extract multiple instantaneous frequencies at the same time under a certain degree of strong noise interference. Such algorithm has been demonstrated valid in extracting the ridges of the signal with multi-ridges in higher-noise environments, which makes it convenient to obtain the IFs based on the time-frequency domain. So the Crazy Climber algorithm has already attracted the attention of research institutions and detector system equipment manufacturers at present.

Some scholars extracted the ridge lines of the time-frequency domain with this algorithm directly in their own research. Such as Kailiang Xu et al. [17] and Li et al. [18], in their research, the wavelet transform method is used to obtain the time-frequency matrix, and the ridge lines of the time-frequency matrix is obtained through the Crazy Climber algorithm, and finally the acoustic detection of train bearings is realized. Chen and Xu [19] proposed a method similar to Li et al. [18]. Unlike the research mentioned above, they obtained the frequent-domain signal by the Fourier transform. In addition to this, some similar strides have been done by some other researchers [8, 20–23]. Their research has achieved noise reduction in high noise environment to a certain extent and extracted useful train bearing signals, but there are still some problems such as incomplete extraction of ridge lines and inconsistency between the instantaneous frequency obtained and the actual frequency. And some scholars consider such issues were caused by the low accuracy of the frequent-domain signal. Therefore, they further improve the extraction method of time-frequency matrix. Zheng et al. [24] proposed a method to improve the accuracy of time-frequency matrix though the continuous wavelet transform. After this, the Crazy Climber algorithm was used to extract the ridge lines from the high-precision frequent-domain signal. Hu et al. [25] and Wang et al. [26] came up with a similar approach that was used to extract the ridge lines. What's different is that they improved the accuracy of the frequent-domain signal with the method of the short-time Fourier transform (STFT). Although the accuracy of time-frequency matrix is quite improved effectively, it is still difficult to identify the whole ridge lines when extracting it with Crazy Climber algorithm. As a result, there is still a deviation between the extracted ridge line and the actual ridge line. Meanwhile, the effect of noise removal is not obvious, and it is difficult to accurately extract useful information. Therefore, some scholars recognize that may the Crazy Climber algorithm exist defects which lead to it being deficient in ridge lines recognition among higher noise. So they try to improve the ridge extract ability of the algorithm itself. For example, Lin and Zhang [27] and Peng et al. [28] attempted to make changes to the metric matrix of the Crazy Climber algorithm. They changed the counting function of the metric matrix and the move frequency of the climbers, which improved the speed of the algorithm greatly, but had little effect on the accuracy.

In summary, the Crazy Climber algorithm still has some disadvantage at present. The particles have disordered phenomena in the process of moving and unable to effectively avoid the low energy points, which will be resulting in particles cannot be accurately reach high frequency energy region. In addition, because the starting point is randomly selected during the extraction of ridge line, it takes a long time to extract ridge line, and it also causes the extracted ridge line to be not smooth, and even some high energy points are omitted. These problems lead to the low recognition accuracy of ridge line extraction in high noise environment. And simultaneous extraction of multiple signals requires a variety of complex processing, resulting in incomplete and inefficient extraction of ridges.

Aiming at the difficulties and present situation of noise reduction in acoustic diagnosis of train bearing defects with multi-source separation, a denoising method based on short-time Fourier transform (STFT) and an improved Crazy Climber algorithm is proposed. Firstly, the short-time Fourier transform is used to extract the time-frequency matrix from the received acoustic signal. Then, the crazy climber algorithm is improved. By changing the motion law of the particles (climbers) in the metric matrix, it can actively avoid the low energy point it has passed under any circumstances, and then can reach the high energy point more accurately and faster. The extraction rule of local optimal peak value was changed. The center time of time-frequency matrix is taken as the starting point of ridge line extraction and the location of local optimal peak value is determined by multiple points. This can make the extracted ridge line more smooth and accurate. Finally, the performance of the method is verified by simulation and experiment. The results show that this method can extract ridge effectively and accurately in high noise environment.

2. The Crazy Climber Algorithm and Improve Method

2.1. The Crazy Climber Algorithm. The Crazy Climber algorithm is a ridge lines extraction method based on Markov chain. The main idea of this algorithm is as follows: Firstly, a large number of points are scattered in the time-frequency randomly, and each of them could be regarded as the density distribution. Then each particle moves in the region according to the transition mechanism of the Markov chain. And they are gradually attracted to the position of ridges which distribution on the plane of the time-frequency. The rule of the motion on the horizontal axis is the standard symmetric random walk, and it on the vertical axis is like climbing a mountain, so that, these randomly distributed points also could be called climbers. The processing of climbers reaching the ridges is also like the simulated annealing algorithm, and according to this algorithm, all the ridges of the time-frequency curve could be finally found. The system needs to set an initial temperature *Ttemp*, and as the temperature drops, the particles that can move stabilize and eventually converge into the high energy area where the ridge is located.

The processing of this algorithm as shown in Figure 1, and it could be divided into two parts, the one is the movement process of the Climbers and the other one is looking for the appropriate ridge lines. There are four steps in the first part and three steps in the second part. Assume the discussed time-frequency domain is $\mathbf{T}(j, k)$ which size is $B \times A$, and it represents the value at position (j, k) in time-frequency distribution. In the horizontal axis $j = 1, 2, \ldots, B$, and in the vertical axis $k = 1, 2, \ldots, A$.

The operational process of the Crazy climber algorithm is described as follows, and each climber is independent of each other. Create and initialize the metric matrix **D**, the Times of move n, and the number of the climbers N, And the N is determined by the size of the domain **T**. The climbers

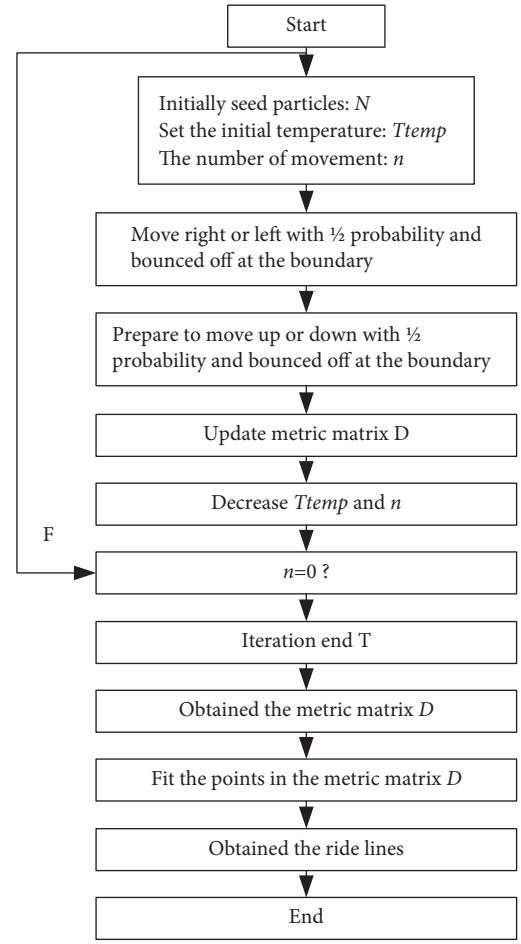

Figure 1: Flowchart of the Crazy Climber algorithm.

are evenly distributed on grid **S**, which could described as follow: $\mathbf{S} = \{1, 2, \ldots, B\} \times \{1, 2, \ldots, A\}$

The maximum number of Climbers N will not be more than $B \times A$. The initial position of the particle is $X_a(0)$, and $a = 1, 2, 3, \ldots, N$.

(1) After setting the necessary parameters, assuming that the initial temperature of the system is Ttemp, and a particle stays at the position $X_a(t) = (j, k)$ at some time t, then its next position (j', k') will be determined by two conditions. Firstly, the particle moves horizontally. If j is between 2 and $B - 1$, then $j' = j - 1$ or $j' = j + 1$ both of which have the same probability of 50%. If the particle is exactly on the boundary, then it will move one space in the opposite direction, that is, if $j = 1$, then $j' = j + 1$, and if $j = B$, then $j' = j - 1$. After horizontal movement, the particle moves vertically. The movement rule in the vertical direction is similar to that in the horizontal direction, with a 50% probability of moving up or down (the same rule at the boundary as in the horizontal direction), but it is also possible to make no movement, but if the particle must move, i.e. $X_a(t + 1) = (j', k')$. The probability of particle movement is p_k. p_k can be expressed by the following formula.

$$p_k = \exp\left\{\frac{[T(j',k') - T(j',k)]}{T_k}\right\}, \quad (1)$$

where $T_k = [\max(T) - \min(T)]/\log_2^k$.

In this case, the probability of not moving is $1 - p_k$. And after the move, the temperature of the system is update to $T_{\text{temp}+1}$. When the temperature of the system falls below a certain threshold, the iterative moving process ends.

(2) After the iteration has been completed, each point on the metric matrix D needs to be measured. At time t, a particle moves to a certain position $X_a(t)$, and the point corresponding to this position in the metric matrix **D** needs to be added by 1. Assuming that each Climber corresponds to a mass of $1/N$, it can be considered that the metric of the metric matrix and the metric of the final metric matrix at time t are

$$D(t) = \frac{1}{N} \cdot \sum_{a=1}^{N} \delta(X_a(t) - S). \quad (2)$$

In order to further improve the accuracy of extracted ridge line and make the change of ridge line parameters more close to the change of parameters on the original time-frequency plane, it is necessary to weight the measurement values, so the weighted measurement value is

$$D_e(t) = \sum_{a=1}^{N} E \cdot \delta(X_a(t) - S). \quad (3)$$

Meanwhile, since the movement of each moving point is a random process, the measurement value is also a random quantity. Therefore, in order to make the final measurement to each grid point, the mean value of the measurement value is needed to represent the measurement value. And, the mean value of the measurement value is expressed as

$$D^I = \frac{1}{T_{\text{time}}} \sum_{t=1}^{T_{\text{time}}} D(t),$$
$$D_e^I = \frac{1}{T_{\text{time}}} \sum_{t=1}^{T_{\text{time}}} D_e(t), \quad (4)$$

where T_{time} is the total length of time.

After all the ridge lines are obtained, the length of each ridge line is calculated and the length threshold value is determined. The ridge lines which are shorter than threshold value will be eliminated and the remaining ones will be extracted.

What should be noticed is that take into account the effect of noise a threshold value e should be decided before step 5 in order to pull the ridge lines out from low measurement value in Dn. And the threshold should be set as the integral multiple of the mean value or the decimal multiple of the maximum value of the metric matrix. This process could be written as the following equation:

$$D_n(i,j) = \begin{cases} D_n(i,j) & D_n(i,j) \geq e \\ 0 & D_n(i,j) < e \end{cases}. \quad (5)$$

After the process mentioned above, the ridge points are clearly visible. Since the instantaneous frequency is a curve slowly changing along the time axis. So, the algorithm will start at the left end of the grid and extract the ridge point along the time axis that is close to the frequency coordinate of the ridge point at the previous point as the ridge point frequency value at the next point. And connect the two points to form a ridge line and repeat the process until all ridge lines are found.

2.2. Evolutionary Rules. As described about the Crazy Climber algorithm in Section 2.1, it could be found that although such an algorithm could extract multiple ridge lines at the same time, what should be noticed is that, the processing speed of the algorithm depends on the number of the climbers. When the magnitude of climbers is very huge, it will take up so much time to compute. But on the contrary, the accuracy of the algorithm will be declining. Therefore, it is very important to improve the accuracy under the condition of finite particles. It is necessary to improve the rules of particle movement and ridge extraction. In the traditional Crazy Climbing algorithm, the movement of particles is random, and it takes several iterations to make the particles reach the high energy position, or even repeatedly reach the position that the particles have already passed through, which leads to the low efficiency of obtaining the metric matrix. At the same time, the process of fitting the ridge after obtaining the ridge point is also accompanied by randomness. The ridge starts fitting from the zero point of the time axis. In this process, it is difficult to find the maximum value and effective value of the metric matrix quickly and accurately, so the extracted ridge is not necessarily the real matrix of the system.

Aim such problems, an improved crazy climber algorithm was put forward in this part. The rules of particles movement and the fitting process of ridge lines are improved based on the original algorithm. The basic implementation process is as follows:

(1) In order to improve the accuracy and efficiency of the metric matrix, a novel movement rule of the climbers in time-frequency domain is proposed which makes it could move towards the ridge lines faster. Assume that the position corresponding to particle at tk is $X_a(t_k) = (j,k)$, then the position corresponding to the particle at $tk+1$ is $X_a(t_{k+1}) = (j',k)$, and at $tk+2$ is $X_a(t_{k+2}) = (j',k')$.

As shown in Figure 2, each block represents where the particle is likely to move in. It is assumed that the particle is at A5 (j,k) at $t = tk$, According to the movement rule of the algorithm, the particle will move left and right at $t = tk+1$ (A2 and A8, (j',k)). And the probability of movement at this time will be affected by the corresponding frequency amplitude of the particle at $t = tk$ and $t = tk+1$. Zu is assumed to be the increment between the amplitude of two

	A1	A4	A7				B1	B4	B7
	A2	A5	A8				B2	B5	B8
	A3	A6	A9				B3	B6	B9

Figure 2: Schematic diagram of Climber movement.

positions, and the larger the increment is, the greater the probability of moving to the position of this point is. The movement probability is calculated by the following formula:

$$P_z = \frac{Z_u}{\sum_1^2 \left(Z_u + \left|\min\left(S\left(X_a\left(t_k\right)\right)\right) - S\left(\left(X_a\left(t_{k+1}\right)\right)\right)\right|\right)}, \quad (6)$$

$$Z_u = \left(S\left(X_a\left(t_k\right)\right)\right) - S\left(\left(X_a\left(t_{k+1}\right)\right)\right).$$

Assuming the particle move to A8 at $t = tk + 1$. In the following movement, the traditional algorithm is used to determine whether the particle moves or does not move. If it moves, then at $t = tk + 2$, the particle moves toward A7 or A9 according to the above probability. If it does not move, at $t = tk + 3$, the particle is still at A8, and at $t = tk + 4$, the particle starts to move left and right. Since A5 is the point that the particle has passed, the probability of moving to A5 is 0, and the probability of moving to the right is 100%.

The rules for particle movement at the boundary are slightly different. It can be explained as follows: assume the particle at the location B5 at $t = tk$ as shown in Figure 1, it could only in block B2 or B8 in the next movement. It will follow the rules of movement above if the particle in the block B2. Assume that the particle in the block B8 at $t = tk + 1$. If it moves, then the particle may appear at B7 or B9, and at the next moment, the iteration starts again. If it does not move, If the particle does not move, the frequency increment of B4~B9 relative to B8 should be calculated and the probability of movement also should be recalculated. According to the new movement rules, particles can effectively avoid passing through a point repeatedly, and can quickly reach the high energy region. In this way, the efficiency and accuracy of extracting the ridge lines could be improved sharply.

(2) On the condition of actual working, there is not only noise or multi-source signal in the acoustic signal received by microphone but also be influenced by the Doppler effect, which results in distorting. It is worth noting that, after eliminating the distortion through STFT, it can be found the situation of distortion at the center time of signal (the straight-line distance between the train and the microphone is the shortest) is the minimum. That is, the difference between the received signal and the actual signal generated by the bearing is the minimum at that time. Therefore, it can be judged that the ridge lines through the center time in the time-frequency matrix must belong to the useful signals. So that, taking the center time as the starting position can be more accurate and rapid than taking random point as the starting position for fitting the ridge lines. In addition, the process of fitting ridge lines will also be improved.

The selection fitting point at a certain time will be affected by the points at the previous two times. For example, the fitting point is C1 at tk, and C2 at $tk + 1$, then the direction of the selected fitting point at time t is the connecting line direction of C1 and C2. If the connecting line direction is pointing the C3 at time $tk + 2$, and the C4 and C5 are the nearest points to C3 in the vertical direction. Then the fitting point at time t should be the peak value among C3, C4 and C5, as shown in Figure 3. It can be found that the smoothness and accuracy of the ridge lines can be improved by the improved fitting method mentioned above.

3. Simulation Signal Analysis

3.1. Simulation Signal Construction. Effects of the improved denoise method on extracting ridge lines were verified by simulation and experimental. An acoustic signal with Gaussian white noise is built as follows:

$$\begin{cases} \mathrm{sig}_1(t) = 0.5\ \sin\left(40\ \sin\left(4\pi t\right) + 1600\pi t\right), \\ \mathrm{sig}_2(t) = 0.5\ \cos\left(700\pi t\right), \\ \mathrm{sig} = \mathrm{sig}_1(t) + \mathrm{sig}_2(t) + \eta(t), \end{cases} \quad (7)$$

where $\eta(t)$ is a Gaussian white noise signal, sig is the simulation signal with noise.

There are two parts in instantaneous frequency of (7), which could be described by mathematization as (8):

$$\begin{cases} f_1(t) = 800 + 80\ \cos\left(4\pi t\right), \\ f_2(t) = 350, \end{cases} \quad (8)$$

where t is the program running time, which values is [0, 1/fs, 1]. And fs is the sampling frequency in this simulation, and $fs = 1024$ Hz.

Before analysis the time-frequency of the simulation acoustic signal, the Gaussian white noise with signal-to-noise ratio of 10 dB was added which make the signal image more confusing, and closer to real situation, Doppler simulation is also carried out according to the method of reference [26]. The time-domain waveform with and without Gaussian white noise is shown in Figures 4 and 5, respectively.

3.2. Ridge Lines Extracting. The established simulation signal eliminated the Doppler distortion through the STFT, used by the method same as reference [14]. Figure 6 shows the time-frequency matrix after transform. As shown in Figure 6, the situation of time-frequency distribution reflects the change low between the instantaneous frequencies of the signal with time. According to (8), the instantaneous

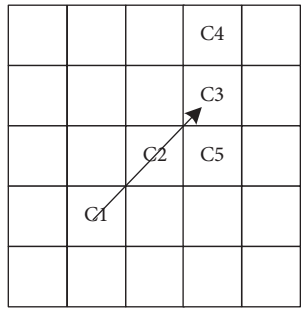

Figure 3: Schematic diagram of local optimal peak extraction.

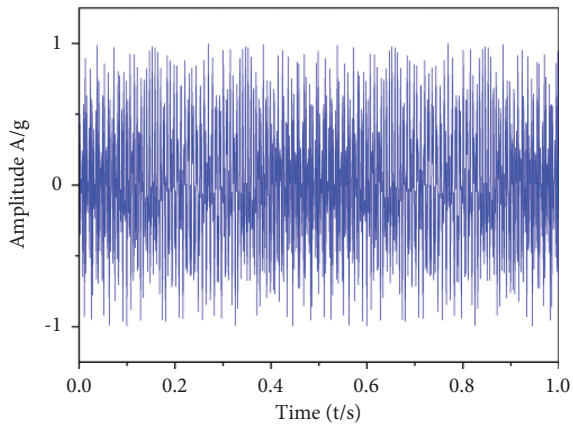

Figure 4: The time-domain waveform without noise of the analog signal.

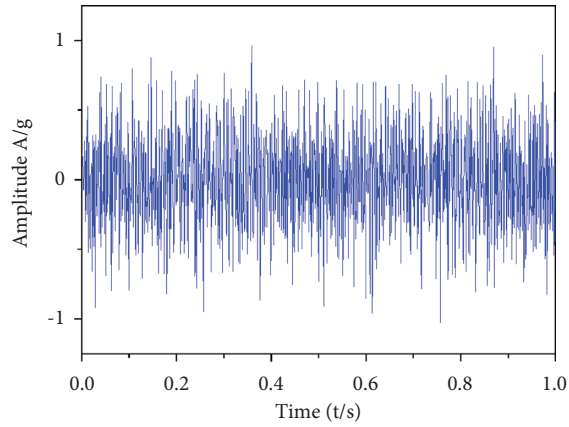

Figure 5: The time-domain waveform with 10 dB noise of the analog signal.

frequency of the analog signal should be a straight line and a sinusoid, and it could be found that the highlighted in Figure 6. And this proves the correctness of the simulation signal and the validity of the short-time Fourier transform.

The original algorithm and the improved algorithm are used to extract the time-frequency ridge of the established simulation signal, respectively. The number of movement(n) in both algorithms is 134. Figure 7 is the actual frequency

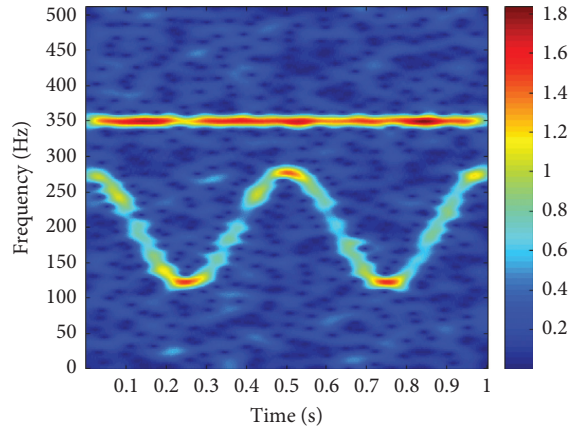

Figure 6: Short-time Fourier Transform of analog signal.

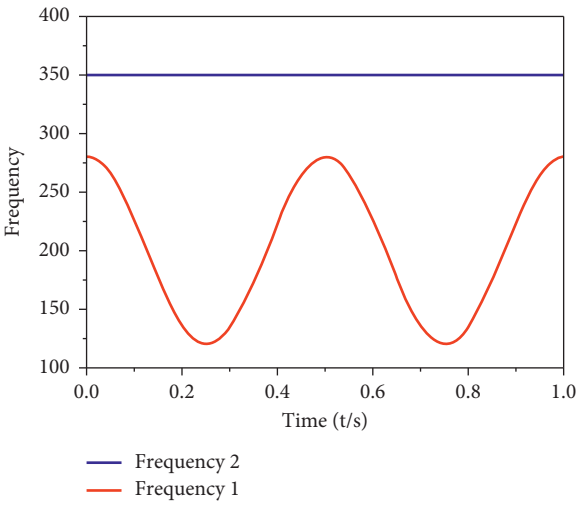

Figure 7: Actual frequency ridge lines.

ridge lines of the signal, and the Figure 8(a) and Figure 8(b) are the metric matrix and the ridge lines obtained by the improved Crazy Climber algorithm respectively. Figure 9(a) and Figure 9(b) are the metric matrix and the ridge lines obtained by the traditional algorithm. It can be found that the two ridge lines are significantly highlighted compared to other positions in Figure 8(a), but this situation is not obvious in Figure 9(a). Though the ridge line of frequency $f2$ has a higher metric value, the one of frequency $f1$ is not quite clear. And this may lead to an inability to extract the ridge line effectively. What's more, compare the measurement value in Figure 8(a) with the one in Figure 9(a), it can be found that the maximum measurement value on the ridge lines obtained by the improved Crazy Climber algorithm almost reached 700, but there is only 300 in Figure 9(a) which is obtained by the ordinary one. Meanwhile, by comparing Figures 8(b) and 9(b), it can be found that the traditional algorithm cannot extract the ridge line of $sig1(t)$, while the improved algorithm can clearly display the ridge lines of both signals. So that, the improved algorithm had better performance in extracting ridge lines compare with the ordinary one in the same number of movement.

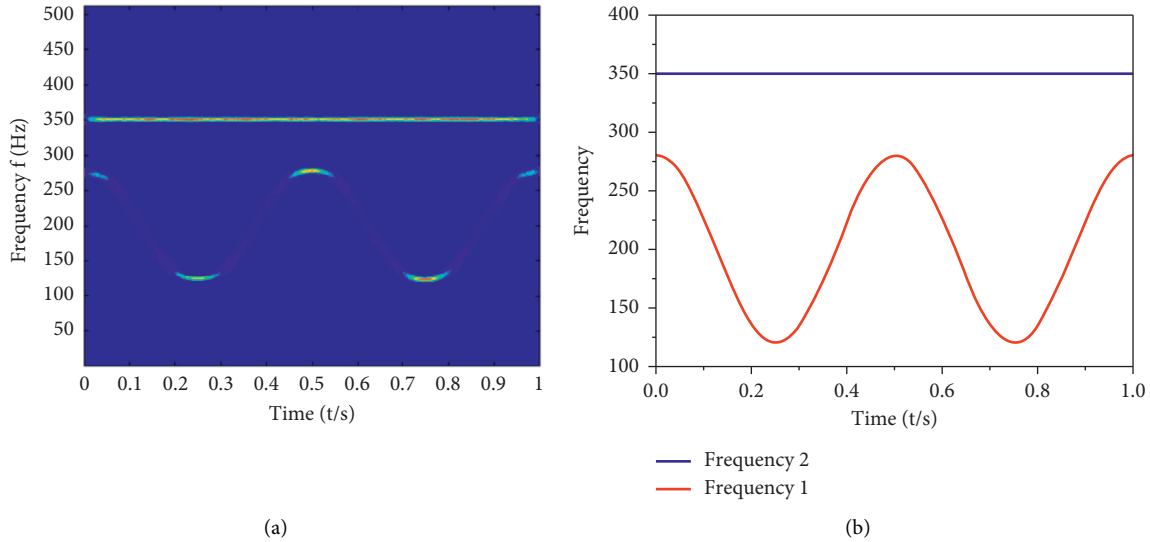

Figure 8: Metric matrix and the ridge lines obtained by the improved algorithm.

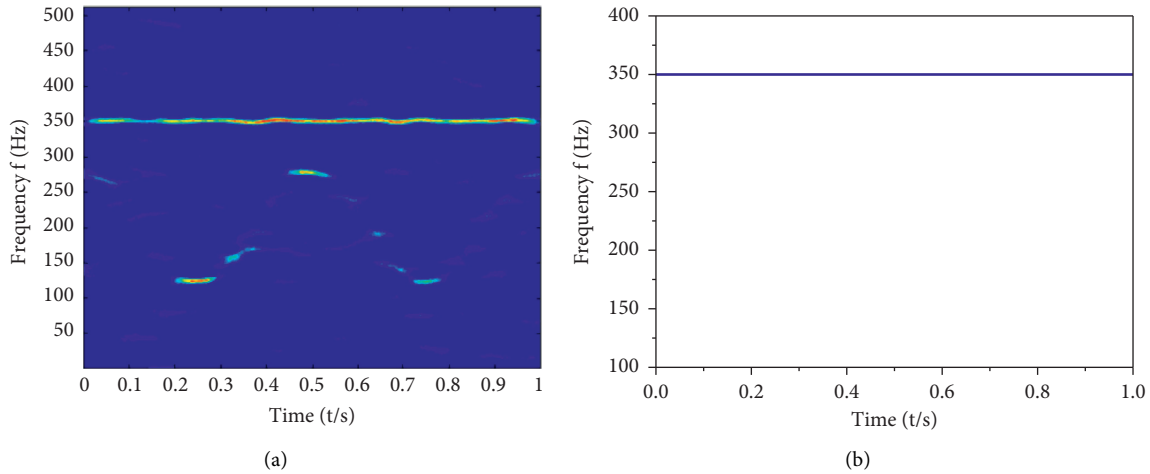

Figure 9: Metric matrix and the ridge lines obtained by the traditional algorithm.

The number of moves is continuously increased until the extraction accuracy of the traditional algorithm is close to that of the improved algorithm, and the number of moves of the traditional algorithm is close to 300. Compare the operating speed of two algorithms with the situation of same extraction accuracy. In order to minimize the influence of other factors as much as possible, ten tests were carried out for each algorithm, and the average results of ten tests were taken as the final result. The average operation time as shown in Table 1. It can be found that in Table 1, the average operation time of improved algorithm is about 0.87 s, while the traditional one will take more than 1.1 s Therefore, the amelioration of the algorithm can improve the operation speed to a certain degree.

In order to further verify the accuracy of the improved crazy climbing algorithm, the average deviation between the actual ridge line and the extracted ridge line was taken as the evaluation standard to evaluate the two algorithms. The calculation formula of this index is as follows:

$$\overline{\lambda} = \frac{\sum_{r=1}^{a} |Y_r - y_r|}{a}, \tag{9}$$

where a is the length of the extracted ridge line, Yr is the frequency value of the extracted ridge line at point r, and yr is the frequency value of the actual ridge line at point r.

The average deviation of two algorithms as shown in Table 2, and from the algorithm's accuracy, the average deviation is as small as possible. It can be found that the average deviation of the modified algorithm is close to zero and much smaller than it of the traditional algorithm, especially in the signal of the $sig2(t)$. So that it can prove the accuracy, operation speed and integrity of the improved Crazy Climber algorithm are better than that of the original algorithm.

Table 1: The average operation time of both algorithms.

Algorithm	$t1$ (s)	$t2$ (s)	$t3$ (s)	$t4$ (s)	$t5$ (s)	$t6$ (s)	$t7$ (s)	$t8$ (s)	$t9$ (s)	$t10$ (s)	t (s)
Improved	0.87	0.86	0.88	0.88	0.86	0.85	0.86	0.90	0.88	0.85	0.87
Ordinary	1.14	1.12	1.10	1.11	1.11	1.13	1.14	1.15	1.12	1.11	1.12

Table 2: The average deviation of two algorithm.

Algorithm	Average deviation for $sig1(t)$	Average deviation for $sig2(t)$
Improved	2.45 Hz	0
Ordinary	—	1.32

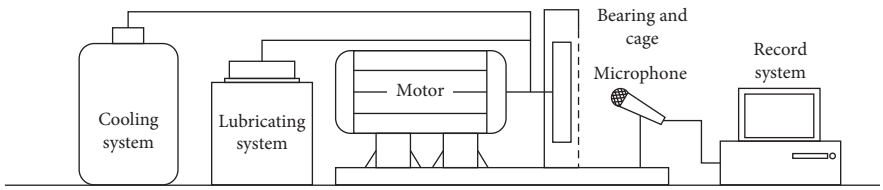

Figure 10: The schematic Figure of the experimental equipment.

4. Experimental Verification

The accuracy and efficiency of the algorithm are verified by simulation analysis, and the superiority of the proposed method is further verified by experiments. An experimental platform was designed to obtain the acoustic signals of train bearings in static states. In this experiment, the bearings of the railway locomotive were taken as the experiment subject. The outside diameter of the wheel is 840 mm and the diameter of the wheel bearing is 165 mm. There are 16 rollers in the bearing and the diameter is 25 mm. There is only one microphone in the experiment system which takes as signal acquisition equipment, the train speed in simulation is 25 m/s, therefore the spindle speed experiment is 1400 r/min.

The motor used in this experiment is Realland VFG, which the maximum revolving speed is 8000 rpm. The connection between the train bearing and the motor is rigid. The rotational movement of the bearing is driven by the motor, which could simulate the working state of the bearing when the train is running. In order to ensure the safety of the experiment, there is a protective device installed outside the bearing. And there is a cooling device and a lubricating device in the experiment system. Moreover, an operating data acquisition system is added to detect the running status of the experimental equipment. After the experiment started, the microphone began to collect the signal data when the bearing and motor ran smoothly. The schematic of the experimental equipment as shown in Figure 10.

Figure 11 represents the time domain waveform of the train bearing outer-ring in experiment, and the time-frequency matrix as shown in Figure 12. 4000 sample points were selected from the signal data which was collected by the microphone, and the STFT was used for time-frequency transformation to obtain the time-frequency matrix of the acoustic signal. The time-frequency spectrum of fault signal as shown in Figure 13. The improved and the ordinary Crazy Climber algorithm were used for extracting the ridge lines of the time-frequency matrix, respectively. Some key parameters were set as follows in the calculation process, the number of Climber movement is 200, the threshold value of the metric matrix is 0.1 times of the maximum measurement value, the length threshold value of the ridge lines is 0.5 times the width of the time-frequency matrix. The ridge lines obtained by improved and ordinary algorithms were shown in Figures 13(a) and 13(b), respectively.

As shown in the image, both algorithms could extract the ridge lines of the time-frequency matrix, but the ridge lines obtained by the ordinary Crazy Climber algorithm are not quite clear and exact relative to the improved one. On the other hand, the ridge lines extracted by the improved algorithm are more smooth and complete, and much closer to the ridge lines in reality. Therefore, the improved Crazy Climber algorithm is better than the original one overall.

According to (9), the average deviation between actual ridge line and extracted ridge line of the two algorithms under experimental conditions was calculated, as shown in Table 3. It can be seen from Table 3 that the average deviation of the improved algorithm is close to 0 Hz, while that of the traditional algorithm is around 1.5 Hz, which indicates that the ridge line obtained by the improved algorithm is closer to the real situation, and this also shows the accuracy of the improved algorithm to a certain extent. In order to further verify the deviation between the two algorithms, the number of movement of the traditional algorithm is constantly improved. When the accuracy of the traditional algorithm reaches that of the improved algorithm, the number of movement is 378. In the case of the same accuracy, the time consumption of the traditional algorithm is 1.12 s, and the time consumption of the improved algorithm is 0.83 s. Therefore, it can be judged that the improved algorithm is better than the traditional algorithm in accuracy and efficiency.

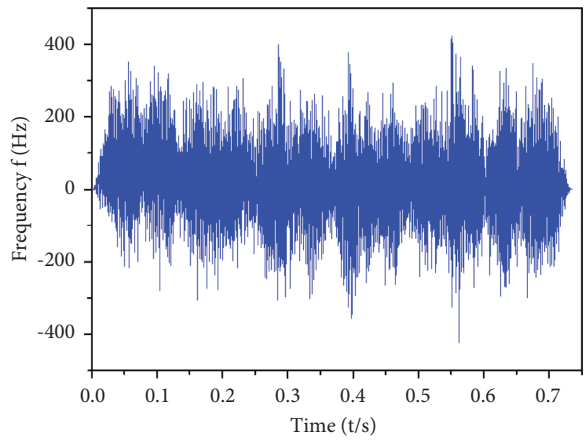

Figure 11: The time domain waveform of the train bearing.

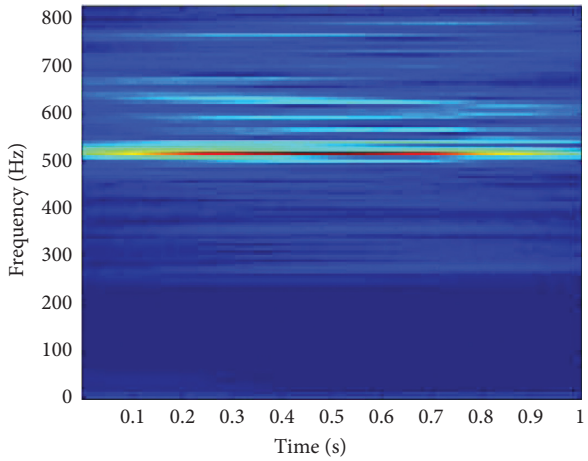

Figure 12: Time-frequency matrix of the train bearing.

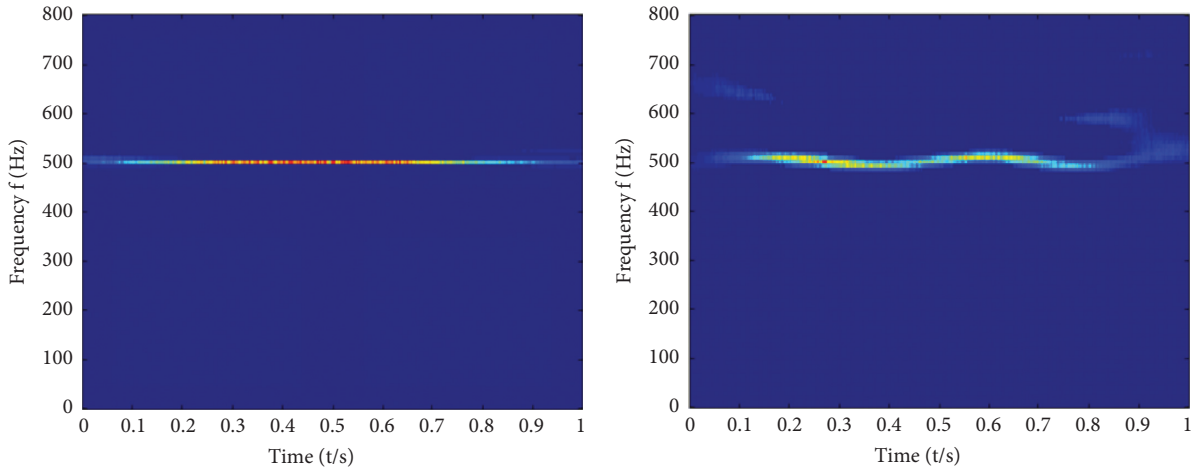

Figure 13: Time-frequency spectrum of fault signal adopted by two algorithms.

Table 3: The average deviation of two algorithm in experiment.

Algorithm	Average deviation for acoustic signal (Hz)
Improved	0.3
Ordinary	1.51

Furthermore, in order to verify whether the established algorithm can realize bearing fault diagnosis, the order of the ridge line proposed in Figure 12 is extracted. And the order of bearing outer ring fault is calculated according to (10).

$$O_o = 0.5z\left(1 - \frac{\mathrm{d}}{D}\cos\ \alpha\right), \tag{10}$$

where z is the number of the rollers. d is the diameter of the rolling body, D is the nodal diameter of the bearing, and the α is the contact angle.

According to the (10), the fault order of the outer ring can be obtained, which is 6.83. And the order of the ridge line also could be obtained by further calculation. However, there is no obvious fundamental ridge lines in the time-frequency diagram, so that, the extracted ridge line is not the corresponding fundamental frequency ridge line. What should be noticed is that, the fundamental frequency of the train bearing in this condition is 74.11 *Hz*. By calculating, it can be found that the average value of order is 6.787, which is close to the calculated order of the outer ring fault. And it can be judged that the outer ring is faulty, and the diagnosis result is consistent with the reality. The results show that the improved Crazy Climber algorithm proposed in this paper can realize the diagnosis of bearing faults in practical applications.

5. Conclusion

This paper proposes a novel denoise method based on the STFT and improved Crazy Climber algorithm. The time-frequency of the received acoustic signal was obtained by STFT. And for the Crazy Climber algorithm, the movement rule of Climber in the metric matrix and the fitting method of the ridge lines are improved. Then, the ridge lines in time-frequency domain are extracted accurately and efficiently. The effectiveness of the proposed method is verified by simulation and experiment on actual train bearing signals. The results show that the method proposed in this paper can effectively detect the train bearing, and the detection results are reliable and feasible. The features of this method are apparent as follows: (1) the movement law of the particle (climber) is improved, so that the particle can move to the high-energy area actively during the movement process, and can actively avoid the point already passed or low energy point, so that the particle can reach the high energy point more accurately and faster. (2) The ridge line fitting method in metric matrix is improved and the local optimal peak extraction method is proposed. In order to improve the speed, precision and smoothness of ridge line extraction, the center time of time-frequency curve is taken as the starting point and the point with higher height value is selected as the line point during the fitting process. (3) Through simulation and experiment, compared with the improved algorithm and the common algorithm, the proposed crazy climber algorithm has obvious advantages in calculation accuracy and efficiency, and can realize acoustic detection of train bearings.

It should be noted that the method proposed in this paper is mainly applied to noise reduction and detection of single bearing, and the effectiveness of the method is verified by theory and experiment. This provides some theoretical and technical support for The Wayside Acoustic Defective Bearing Detector System. However, according to the running process and detection results of the algorithm, it can be found that the algorithm can be applied to noise reduction and detection of multiple bearings. Therefore, in further work, the potential application of the proposed method in noise reduction and detection of two or more bearings will be involved and discussed.

Data Availability

The data of the acoustic signal used to support the findings of this study are included within the article.

Conflicts of Interest

The authors declare that there are no conflict of interest regarding the publication of this paper.

Acknowledgments

This work was supported by the National Science Foundation for Young Scientists of China (Grant no. 62001079).

References

[1] X. Chiementin, F. Bolaers, and J.-P. Dron, "Early detection of fatigue damage on rolling element bearings using adapted wavelet," *Journal of Vibration and Acoustics*, vol. 129, no. 4, pp. 495–506, 2007.

[2] Y. Lei, Z. He, and Y. Zi, "Application of a novel hybrid intelligent method to compound fault diagnosis of locomotive roller bearings," *Journal of vibration and acoustics-transactions of the Asme*, vol. 130, no. 3, pp. 569–583, 2008.

[3] R. Yan and R. X. Gao, "Rotary machine health diagnosis based on empirical mode decomposition," *Journal of Vibration and Acoustics*, vol. 130, no. 2, pp. 53–64, 2008.

[4] J. Dybala and R. Zimroz, "Rolling bearing diagnosing method based on Empirical Mode Decomposition of machine vibration signal," *Applied Acoustics*, vol. 77, pp. 195–203, 2014.

[5] H. C. Choe, Y. Wan, and A. K. Chan, "Neural Pattern Identification of railroad Wheel-Bearing Faults from Audible Acoustic Signals: Comparison of FFT, CWT, and DWT Features," in *Proceedings of the SPIE Proceedings on Wavelet Applications*, Orlando, FL, USA, April 1997.

[6] Y. Yuan, X. Zhao, J. Fei, Y. Zhao, and J. Wang, "Study on fault diagnosis of rolling bearing based on time-frequency generalized dimension," *Shock and Vibration*, vol. 2015, Article ID 808457, 11 pages, 2015.

[7] Z. Ma, W. Ruan, M. Chen, and X. Li, "An improved time-frequency analysis method for instantaneous frequency estimation of rolling bearing," *Shock and Vibration*, vol. 2018, Article ID 8710190, 18 pages, 2018.

[8] M. Zhang, X. Huang, Y. Li, H. Sun, J. Zhang, and B. Huang, "Improved continuous wavelet transform for modal parameter identification of long-span bridges," *Shock and Vibration*, vol. 2020, Article ID 4360184, 16 pages, 2020.

[9] J. E. Cline, J. R. Bilodeau, and R. L. Smith, "Acoustic Wayside Identification of Freight Car Roller Bearing Defects," in *Proceedings of the 1998 ASME/IEEE joint railroad conference*, IEEE, Philadelphia, PA, USA, April 1998.

[10] D. Barke and W. K. Chiu, "Structural health monitoring in the railway industry: a review," *Structural Health Monitoring*, vol. 4, no. 1, pp. 81–93, 2005.

[11] I. Firdausid and C. Wu, "Development and deployment of advanced wayside condition monitoring system," *Foreign Rolling Stock*, vol. 39, no. 2, pp. 39–45, 2002.

[12] L. Yu-xing and W. Long, "A novel noise reduction technique for underwater acoustic signals based on complete ensemble empirical mode decomposition with adaptive noise, minimum mean square variance criterion and least mean square adaptive filter," *Defence Technology*, vol. 16, no. 3, pp. 543–554, 2020.

[13] Q. Ni, J. C. Ji, K. Feng, and B. Halkon, "A fault information-guided variational mode decomposition (FIVMD) method for rolling element bearings diagnosis," *Mechanical Systems and Signal Processing*, vol. 164, Article ID 108216, 2022.

[14] A. Zhang, F. Hu, Q. He, C. Shen, F. Liu, and F. Kong, "Doppler shift removal based on instantaneous frequency estimation for wayside fault diagnosis of train bearings," *Journal of Vibration and Acoustics, Transactions of the Asme*, vol. 136, no. 2, 2014.

[15] X. Xu, W. Wang, J. Liu, and S. Sun, "Instantaneous frequency components separation method based on synchro-squeezed short time Fourier transform," *Journal of Vibration Engineering*, vol. 31, no. 6, pp. 1085–1092, 2018.

[16] R. A. Carmona, W. L. Hwang, and B. Torresani, "Multiridge detection and time-frequency reconstruction," *IEEE Transactions on Signal Processing*, vol. 47, no. 2, pp. 480–492, 1999.

[17] K Kailiang Xu, D Dean Ta, and W Weiqi Wang, "Multiridge-based analysis for separating individual modes from multimodal guided wave signals in long bones," *IEEE Transactions on Ultrasonics, Ferroelectrics, and Frequency Control*, vol. 57, no. 11, pp. 2480–2490, 2010.

[18] H. Li, J. D. Wen, J. Zhang, and B. C. Wen, "Research on characteristics of chaotic motion based on the wavelet ridge," *Advanced Engineering Forum*, vol. 2, pp. 765–768, 2011.

[19] X. Chen and K. Xu, "Wavelet ridge Analysis of Lamb Wav," *In Advanced Materials Research*, vol. 457, pp. 484–487, 2012.

[20] C. Dou and J. Lin, "Ridge extraction based on adaptive variable-bandwidth cost functions by edge detection of time frequency images," *Measurement Science and Technology*, vol. 31, no. 5, Article ID 55402, 2020.

[21] K. Dziedziech, W. J. Staszewski, A. Ghosh, B. Basu, and T. Uhl, "Characterisation of instantaneous dynamic parameters in vibration analysis of tuned liquid column dampers," *Nonlinear Dynamics*, vol. 90, no. 1, pp. 717–731, 2017.

[22] K. Ren, L. Du, X. Lu, Z. Zhuo, and L. Li, "Instantaneous frequency estimation based on modified kalman filter for cone-shaped target," *Remote Sensing*, vol. 12, no. 17, p. 2766, 2020.

[23] L. Meng, X. Xu, and Y. Zuo, "Fault feature extraction of logarithmic time-frequency ridge order spectrum of planetary gearbox under time-varying conditions," *Journal of Vibration and Shock*, vol. 39, no. 7, pp. 163–169, 2020.

[24] Y. Zheng, R. Fan, C. Qiu, Z. Liu, and D. Tian, "An improved algorithm for peak detection in mass spectra based on continuous wavelet transform," *International Journal of Mass Spectrometry*, vol. 409, pp. 53–58, 2016.

[25] F. Hu, C. Q. Shen, and F. R. Kong, "De-noising Method for Wayside Train Bearings Acoustic Signal Based on Doppler Shift," *Applied Mechanics and Materials*, vol. 333, pp. 504–509, 2013.

[26] C. Wang, F. Hu, Q. He, A. Zhang, F. Liu, and F. Kong, "De-noising of wayside acoustic signal from train bearings based on variable digital filtering," *Applied Acoustics*, vol. 83, pp. 127–140, 2014.

[27] Y. Lin and Y. Zhang, "Improved crazy climber algorithm and its application in obtaining frequency-hopping pattern," *Application Research of Computers*, vol. 31, no. 6, pp. 1684–1687, 2014.

[28] Y. Peng, X. Guo, Y. Xing et al., "A Method for Velocity Signal Reconstruction of AFDISAR/PDV Based on Crazy-Climber Algorithm," in *Proceedings of the AOPC 2017 Fiber Optic Sensing and Optical Communications*, SPIE, Beijing, China, October 2017.

Hindawi
Shock and Vibration
Volume 2022, Article ID 5801325, 15 pages
https://doi.org/10.1155/2022/5801325

Research Article

Static Characteristics of Finger Seal considering Contact between Fingers and Rotor

Sai Zhang,[1] **Yinghou Jiao**,[1] **Zhaobo Chen**,[1] **and Enjie Zhang**[2]

[1]*School of Mechatronics Engineering, Harbin Institute of Technology, Harbin 150001, Heilongjiang Province, China*
[2]*Shanghai Institute of Aerospace System Engineering, Shanghai 201109, China*

Correspondence should be addressed to Yinghou Jiao; jiaoyh@hit.edu.cn

Received 27 October 2021; Revised 18 January 2022; Accepted 11 February 2022; Published 14 March 2022

Academic Editor: Jiaqiang E

Finger seals are a new type of seal with good sealing performance and long service life. The noncontacting feature relies on the gas film force. However, when the seal works in an unsuitable environment or its design parameters are not reasonable, the lifting pad may not be able to generate sufficient air film force. This causes contact between the fingers and the rotor, resulting in a reduced service life of the seal. In view of this situation, this paper proposes a method that can quickly determine whether there is enough gas film force to lift the sealing finger at the design stage. The aeroelastic coupling characteristics of the noncontacting finger seal are studied in conditions where contact exists between the fingers and the rotor. The influences of various environmental and key structural parameters on the number of contact fingers, leakage, bearing force, and friction moment are studied. The results show that the pressure difference, eccentricity, and key design parameters have important effects on the number of contact fingers. The effect of rotation speed is relatively small. This paper provides a time-efficient tool for the design of noncontacting finger seals, which can quickly predict the performance of the sealing system.

1. Introduction

Gas turbines are widely used for high-power and high-efficiency applications. To ensure the proper operation of gas turbines, stringent requirements are made on their internal components. As essential components, advanced and well-designed seal equipment can effectively reduce the leakage of gas turbines. In recent years, many researchers have widely studied a new adaptive seal, namely, finger seal [1], due to its low cost and good sealing performance. A spring-mass-damper equivalent dynamic model is used to obtain the seal performance. Braun et al. [2] studied the effects of the fluid stiffness, fluid damping, and finger stiffness on the phase shift and displacement transmissibility. Chen et al. [3] studied the displacement responses, leakage clearances, and contact pressures of finger elements through a distributed mass model. The calculation results agree well with the experimental data. Experimental tests [4] show that the sealing performance of the finger seal is acceptable for engines, but the seal exhibits some hysteresis, and wear occurs at the beginning of the test. Guoqing et al. [5] experimentally studied the leakage and wear characteristics of finger seals in hot/cold states. One interesting finding is that double-laminate finger seals can achieve lower leakage in cold conditions, while triple-laminate finger seals perform better in hot conditions. A pressure-balanced finger seal [6] is proposed, which can reduce the hysteresis. To reduce wear and obtain a long-life application, a noncontacting finger seal was presented by Proctor MP and Steinetz BM [7], which has hydrodynamic lifting capabilities and a non-contacting nature.

Dynamic models have been proposed to study non-contacting finger seals. Braun et al. [8] studied the thermofluid and dynamic behavior of a two-laminate finger seal. Marie [9] provided theoretical supports for finger seal design by parametrically studying a noncontacting finger seal assembly. Du et al. [10] developed a semianalytical model that can save computation time. The dynamic properties of noncontacting finger seals were found through the model. In order to have an excellent sealing performance, the ratio of

friction force to finger stiffness and the rotor excitation amplitude should be as small as possible; the finger natural frequency should be as large as possible [11]. The fluid-solid interaction method is another commonly used way to study noncontacting finger seals. Yue et al. [12] used commercial software to analyze the leakage, the pressure distribution under lifting pads, the fluid flow through the finger seal, and the displacement of lifting pads. Braun et al. [13] developed solid models to study the deformations, stress of fingers, and lifting capabilities for a better parametric design of a finger seal. Zhang et al.[14] used a two-way fluid-structure interaction method to study the deformations of fingers and the flow field through seal assembly. The effects of different groove structure lifting pads on leakage flows and the lifting force on the finger were also studied. Studies show the possibility of fingers contacting the rotor [15]. Jia et al. [16] proposed a three-layer finger seal with grooved lifting pads. A numerical method was used to investigate the effects of the grooved structures on lifting and leakage performance. The grooved structure can significantly increase the lifting capacity of the finger seal and does not increase leakage too much. Temis et al. [17] proposed a two-way fluid-solid interaction method to calculate the seal characteristics of a noncontacting finger seal. The results of the method are very close to those obtained by finite element software. Zhao et al. [18] considered the side leakage flow into the seepage flow through a porous medium to analyze the total leakage of finger seals. Leakage is increased by 3 to 6% when considering side leakage. Fleming [19] presented an approximate solution to account for fluid inertia in gas flow through rectangular seal pads. The results show that fluid inertia has beneficial influences on noncontacting finger seals. Proctor et al. [20] tested a noncontacting finger seal with a grooved rotor, and the noncontacting operation was achieved. Smith and Braun [21] tested four-finger seal configurations whose lifting properties and structure compliance were investigated through parametric studies.

Above all, we can see that the leakage performance, lifting ability, and effects of the structure and environmental parameters of noncontacting finger seals are widely studied. However, the noncontacting feature requires specific operating conditions to be achieved because the lifting forces generated by gas films are limited. When the rotor is at high eccentricity or the seal is operating in an unsuitable working condition, the lifting forces may not be enough to keep the fingers noncontact with the rotor. It results in contact during an operating rotor system. The contact is inconsistent with the original purpose and should be avoided at the design stage. Thus, how to determine if there is contact and the effect of this contact should be studied.

In this paper, a method to determine whether there is contact between the fingers and the rotor is proposed. The effects of contact on the static characteristics of the noncontacting finger seal are studied. First, a basic analysis unit is divided to calculate the finger deformation. The formula of gas films between the lifting pads and the rotor is deduced by considering the deflection, rotation angle, and torsion of the fingers. The film forces and pressure distributions of the lifting pads are obtained through gas lubrication theory. Then, the proposed method is used to determine whether the fingers are in contact with the rotor. Based on the judgment results, the static characteristics of each finger are calculated. For fingers not in contact with the rotor, an aeroelastic model is used. For fingers in contact with the rotor, a Coulomb friction model is used. Finally, the static characteristics of the entire seal can be obtained by summing the previous results of each finger. The effects of structural parameters, working conditions, and the number of contact fingers are parametrically studied. Compared with the three-dimensional finite element method, the method presented in this paper can judge whether the designed noncontacting finger seal can achieve the noncontacting feature under specified working conditions at the design stage. Static characteristics under various operating conditions when the contact exists can be quickly calculated, thus providing a time-efficient approach for the design of noncontacting finger seals.

2. Method

2.1. Basic Analysis Units. As shown in Figure 1, the noncontacting finger seal studied in this paper consists of one high-pressure laminate, one low-pressure laminate, and one backplate with a pressure-balanced design. Uniform cuts of the laminates form flexible elements, which are called fingers. The gaps of the laminate are covered by the fingers of the other laminate. Each low-pressure laminate finger has a lifting pad to generate film force by the gas film between the lifting pad and the rotor. The film forces lift the fingers, resulting in no contact between the fingers and the rotor. However, film forces are limited, and it may not be possible to keep the finger out of contact with the rotor in some cases. For example, the fingers need a much larger film force to generate enough deformation when the rotor is under large eccentricity conditions. To better investigate the static performance of the noncontacting finger seal, the finger model and the fluid model need to be built first.

The structure of both laminates is periodically symmetrical, and the basic unit is divided according to the structural characteristic. As shown in Figure 2, each basic unit consists of two split high-pressure fingers and one low-pressure finger. During the calculation, it is assumed that there is no relative displacement between the fingers of the same basic unit. The backplate provides support for the fingers and greatly reduces their axial deformation. Thus, the axial deformations of fingers are neglected during the analysis.

2.2. Forces Calculation under Fluid Lubrication Condition. Based on the assumptions above, the deformation of the basic units can be obtained by the low-pressure finger. Figure 3 shows the schematic of a low-pressure finger under fluid lubrication. The finger is subject to three forces in the y-z plane. F_k represents the force acting on the low-pressure finger by the high-pressure finger. The direction of F_k is shown in Figure 3. The magnitude of F_k is

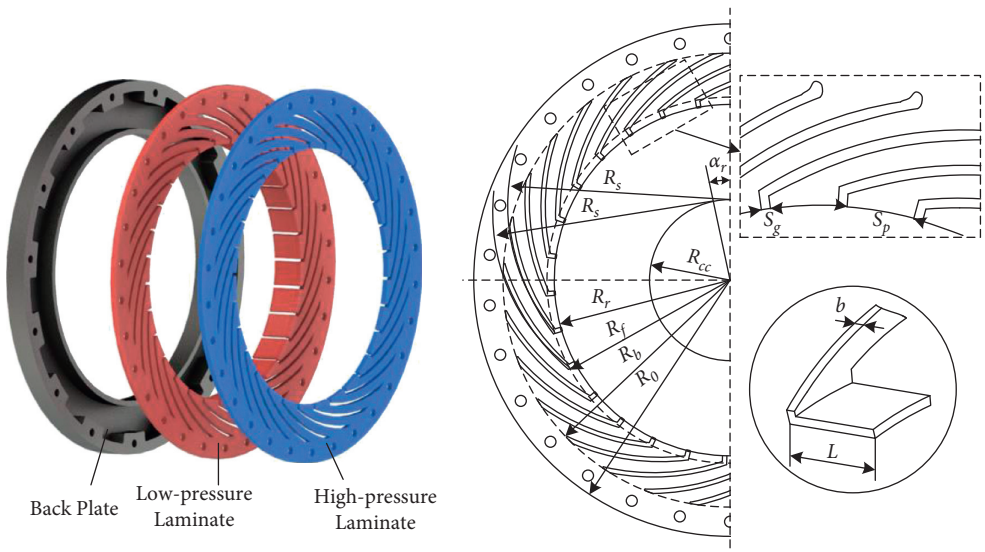

Figure 1: Structure of noncontacting finger seal.

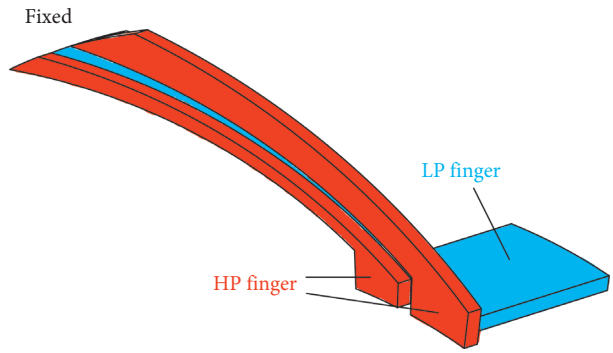

Figure 2: Basic unit of the noncontacting finger seal.

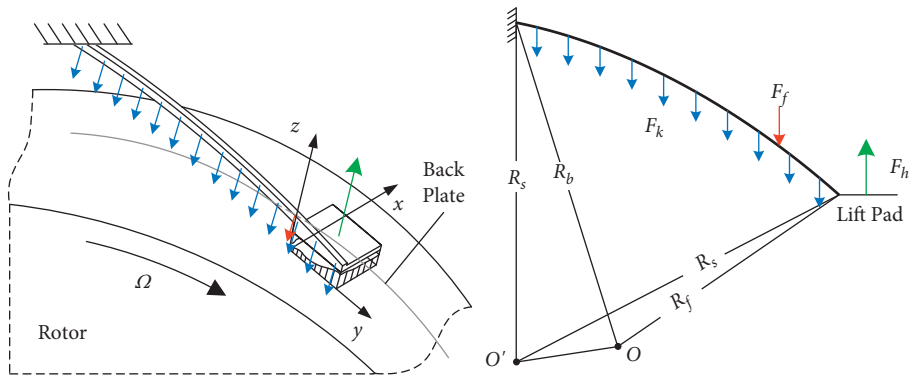

Figure 3: Schematic of the low-pressure finger.

$$F_k = k \cdot u, \tag{1}$$

where k is the stiffness of the high-pressure finger and u is the deformation of the high-pressure finger.

The stiffness of the finger can be obtained by applying a radial unit force at the end of the high-pressure finger and calculating the corresponding deformation. The deformation is calculated in the same way as the deformation of the low-pressure finger is obtained in equation (9).

F_f represents the friction force between the low-pressure finger and the backplate. It is greatly reduced by the pressure-balanced dam and is much smaller than F_k and the film force (F_h) which means it has little effect on the deformation. F_f always hinders the finger deformation. Thus, the direction

of F_f is considered downward during the calculation. The magnitudes of F_f are calculated by the following equation:

$$F_f = \mu_{lb} \cdot P_{lb} \cdot A_{lb}, \tag{2}$$

where μ_{lb} is the friction coefficient between the low-pressure fingers and backplate, P_{lb} is the pressure that pushes the finger laminate against the backplate, and A_{lb} is the contact area between the low-pressure laminate and the backplate.

F_h represents the film force generated by the film between the lifting pad and the rotor surface. The film consists of four parts: the rotor eccentricity, finger deformations, wedge shape of the lifting pad, and initial installation gap. As shown in Figure 4, the film thickness of a basic unit can be deduced:

$$h_{i_f}(\theta) = -e \cdot \cos(\theta - \phi) + T\left(u_{i_f} + h_{ri_f}(\theta) + h_w(\theta)\right) + h_{\text{init}},$$
$$\alpha_r i_f \le \theta \le \alpha_r i_f + \theta_p,\ i_f = 1, 2, 3 \ldots n_f, \tag{3}$$

where u_{if} is the finger radial deformation, e is the rotor eccentricity, φ is the attitude angle, h_{rif} is the film change due to rotation angle of fingers, h_w is the wedge under lifting pads, T is the film change due to the torsion of fingers, h_{init} is the initial installation gap, α_r is the finger repeat angle, and n_f is the number of fingers.

The wedge under each lifting pad is shown in Figure 5. The dashed line represents the original shape of the lifting pad, and $h_{w\min}$ and $h_{w\max}$ are the minimum and maximum values of the wedge, respectively.

The film force and pressure distribution under lifting pads are determined by the nonlinear compressible Reynolds equation:

$$\frac{1}{R^2}\frac{\partial}{\partial\theta}\left(h^3 p \frac{\partial p}{\partial\theta}\right) + \frac{\partial}{\partial y}\left(h^3 p \frac{\partial p}{\partial y}\right) = 6\mu\omega\frac{\partial}{\partial\theta}(ph) + 12\mu\frac{\partial}{\partial t}(ph). \tag{4}$$

The static compressible dimensionless form is as follows:

$$\frac{\partial}{\partial\theta}\left(\overline{p}\overline{h}^3\frac{\partial\overline{p}}{\partial\theta}\right) + \frac{R^2}{L^2}\frac{\partial}{\partial\overline{y}}\left(\overline{p}\overline{h}^3\frac{\partial\overline{p}}{\partial\overline{y}}\right) = \Lambda_x\frac{\partial}{\partial\theta}(\overline{p}\overline{h}), \tag{5}$$

where $\overline{p} = p/p_l$, $\overline{h} = h/C_0$, $\overline{y} = y/L$, and $\Lambda_x = 6\omega\mu_0 R^2/p_l C_0^2$.

Equation (6) is linearized by using the Newton–Raphson method [22]:

$$\begin{aligned}
&\overline{p}\overline{h}^3\frac{\partial^2\delta}{\partial\theta^2} + \frac{R^2}{L^2}\overline{p}\overline{h}^3\frac{\partial^2\delta}{\partial\overline{y}^2} \\
&\quad + \frac{\partial\delta}{\partial\theta}\left(2\overline{h}^3\frac{\partial\overline{p}}{\partial\theta} + 3\overline{p}\overline{h}^2\frac{\partial\overline{h}}{\partial\theta} - \Lambda_x\overline{h}\right) + \frac{R^2}{L^2}\frac{\partial\delta}{\partial\overline{y}}\left(2\overline{h}^3\frac{\partial\overline{p}}{\partial\overline{y}} + 3\overline{p}\overline{h}^2\frac{\partial\overline{h}}{\partial\overline{y}}\right) \\
&\quad + \delta\left[\frac{R^2}{L^2}\left(3\overline{h}^2\frac{\partial\overline{p}}{\partial\overline{y}}\frac{\partial\overline{h}}{\partial\overline{y}} + \overline{h}^3\frac{\partial^2\overline{p}}{\partial\overline{y}^2}\right) + \left(3\overline{h}^2\frac{\partial\overline{p}}{\partial\theta}\frac{\partial\overline{h}}{\partial\theta} + \overline{h}^3\frac{\partial^2\overline{p}}{\partial\theta^2}\right) - \Lambda_x\frac{\partial\overline{h}}{\partial\theta}\right] \\
&= -\overline{p}\overline{h}^3\left(\frac{\partial^2\overline{p}}{\partial\theta^2} + \frac{R^2}{L^2}\frac{\partial^2\overline{p}}{\partial\overline{y}^2}\right) - \overline{h}^3\left(\frac{\partial\overline{p}}{\partial\theta}\frac{\partial\overline{p}}{\partial\theta} + \frac{R^2}{L^2}\frac{\partial\overline{p}}{\partial\overline{y}}\frac{\partial\overline{p}}{\partial\overline{y}}\right) \\
&\quad - 3\overline{p}\overline{h}^2\left(\frac{\partial\overline{p}}{\partial\theta}\frac{\partial\overline{h}}{\partial\theta} + \frac{R^2}{L^2}\frac{\partial\overline{p}}{\partial\overline{y}}\frac{\partial\overline{h}}{\partial\overline{y}}\right) + \Lambda_x\left(\overline{h}\frac{\partial\overline{p}}{\partial\theta} + \overline{p}\frac{\partial\overline{h}}{\partial\theta}\right),
\end{aligned} \tag{6}$$

where $\delta = \overline{p}^{\xi+1} - \overline{p}^{\xi}$, $n = 0, 1, 2, \ldots$, and ξ is the number of iterations.

The finite difference method is used to discretize the linearized equation. The iterative formula can be obtained:

$$a_{i,j}\delta_{i-1,j} + b_{i,j}\delta_{i+1,j} + c_{i,j}\delta_{i,j} + d_{i,j}\delta_{i,j-1} + e_{i,j}\delta_{i,j+1} = S_{i,j}, \tag{7}$$

where i, j are indices for the grid in the circumferential and radial directions, respectively, and $a_{i,j}, b_{i,j}, c_{i,j}, d_{i,j}, e_{i,j}, S_{i,j}$ are coefficients shown in the appendix.

The boundary condition of the calculation area is defined in this way: among the four sides of the lifting pad, the pressure of the high-pressure side is related to the axial thickness of the laminate and the axial length of the lifting pad. The pressures of the other three sides are equal to the downstream pressure. The boundary conditions can be obtained as follows:

$$\begin{cases} \overline{p}(1\colon n+1, 1) = Lp_h/(b+L)p_l \\ \overline{p}(1, 2\colon m+1) = \overline{p}(n+1, 2\colon m+1) = \overline{p}(1\colon n+1, m+1) = p_l, \end{cases} \tag{8}$$

where b is the axial width of the finger laminate, L is the axial length of the lifting pad, and n and m are the numbers of grids.

Then, the deformation of the low-pressure finger is calculated by using Mohr's integrals [23], and the torsional deformation is obtained using elasticity theory:

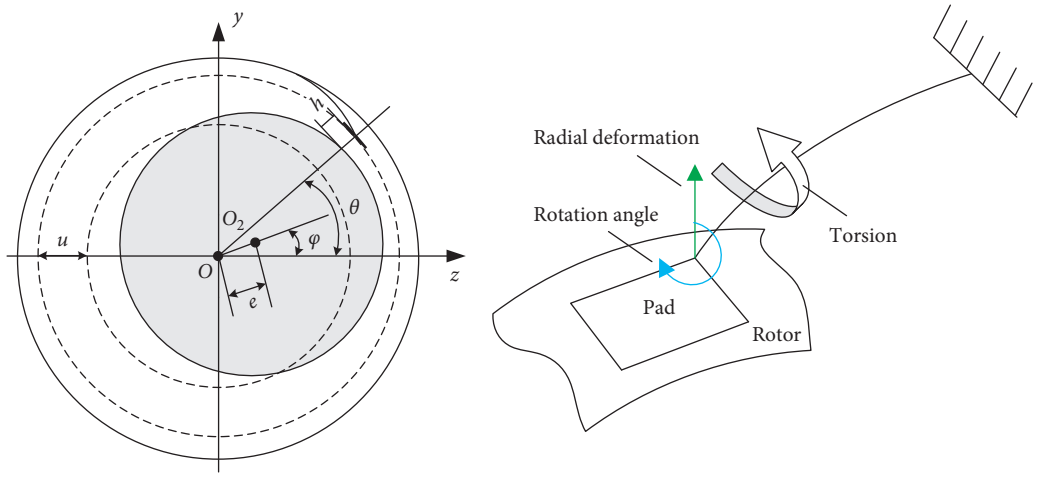

Figure 4: Schematic of the film thickness. (a) Axial schematic diagram. (b) Displacement of a finger.

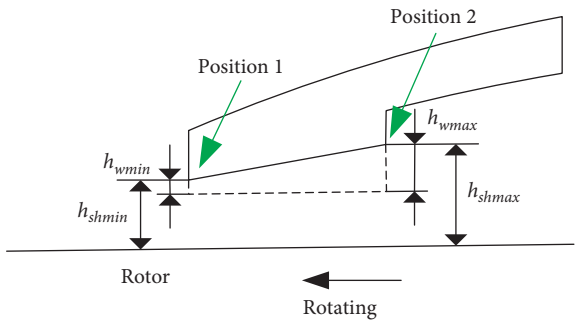

Figure 5: Wedge under the lifting pads.

$$\begin{cases} u_h = \displaystyle\int_0^{\alpha_{ul}} \left(\frac{\overline{N} N_h}{EA} + \frac{\overline{M} M_h}{EI} + \eta \frac{\overline{Q} Q_h}{GA} \right) R_s d\alpha, \\ \tau = \dfrac{M_T}{b_s h_s^3 G \beta_T}, \end{cases} \tag{9}$$

where u_h, N_h, M_h, and Q_h are finger deformation in the radial direction, the axial force, bending moment, and shear force under the fluid lubrication condition, respectively; $\overline{N}$, $\overline{M}$, and $\overline{Q}$ are the internal forces due to the unit load, and A and I are the area and moment inertia of a cross section; E and G are Young's modulus and shear modulus of elasticity, for rectangular cross section $\eta = 1.2$, α_{ul} is the curvature of the fingers, τ is the twist angle, M_T is the torque, b_s and h_s are the cross-sectional parameters, and β_T is the factor determined by b_s and h_s.

2.3. Forces Calculation under Contact Condition. When the finger is in contact with the rotor, the film force is replaced by the contact force applied by the rotor. Due to the small circumferential length of the lifting pad, the surface of the rotor can be considered a plane with respect to the lifting pad during the contact judgment. Since the axial deformation is neglected, the torsion does not affect the judgment of the contact position, which means that T in equation (3) is taken as a unit matrix in the process of judgment. Thus, it can be seen from Figure 5 that the rotor first contacts the finger at position 1 or 2.

When the rotation angle is small, it has little effect on the film thickness, which means that the first contact is at position 1. From (3), the finger deformation under this condition can be obtained:

$$u_1 = -e \cdot \cos(\theta_1 - \varphi) - h_{ri_f} - h_{w\min} - h_{\text{init}}, \tag{10}$$

where θ_1 is the angle of position 1.

Similarly, the first contact position is at position 2 when the rotation angle is large. The finger deformation is

$$u_2 = -e \cdot \cos(\theta_2 - \varphi) - h_{ri_f} - h_{w\max} - h_{\text{init}}, \tag{11}$$

where θ_2 is the angle of position 2.

The process for determining the contact position is shown in Figure 6. Take the direction of the green arrow in Figure 4 as the positive direction. For each finger, the possible deformation (u_1 or u_2) when contact occurs can be calculated by equations (10) and (11). Due to the pressure difference, the finger deformations should be positive. If u_1 and u_2 are negative, it means that the finger needs to produce a negative displacement to contact the rotor. This is inconsistent with the above conclusion. In other words, there is no contact between the finger and the rotor. If u_1 and u_2 have positive and negative values, the contact is at the position corresponding to the positive value. If both u_1 and u_2 are positive, the contact is assumed to be at position 1, and then the film thickness is calculated. If contact does occur at position 1, the film thickness at position 1 (h_1) should be less than that at position 2 (h_2). Then, contact is considered to occur at position 1; otherwise, contact occurs at position 2. The deformation of the contact finger (u_c) is obtained.

Using u_c, F_k is determined by equation (1). When there is contact between the rotor and the finger, the force acting on the finger is denoted by F_c. F_c satisfies the condition that the deformation of the finger under the forces of F_k, F_f, and F_c is

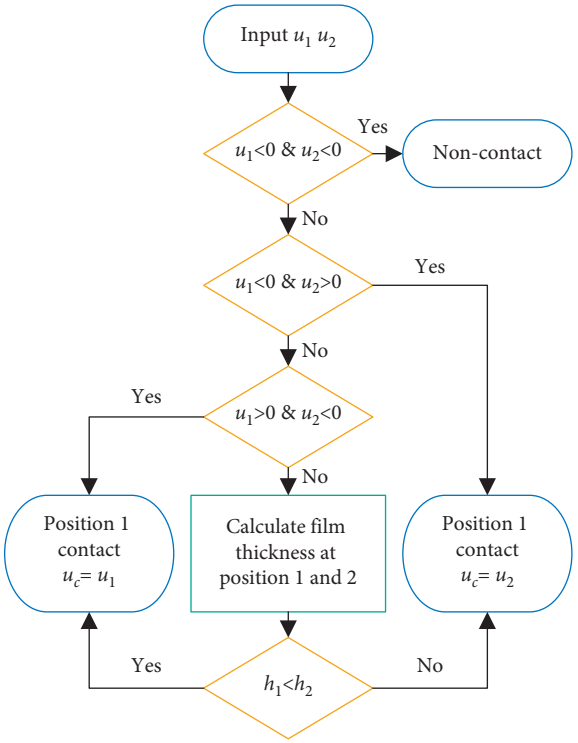

Figure 6: Flow of contact position determination.

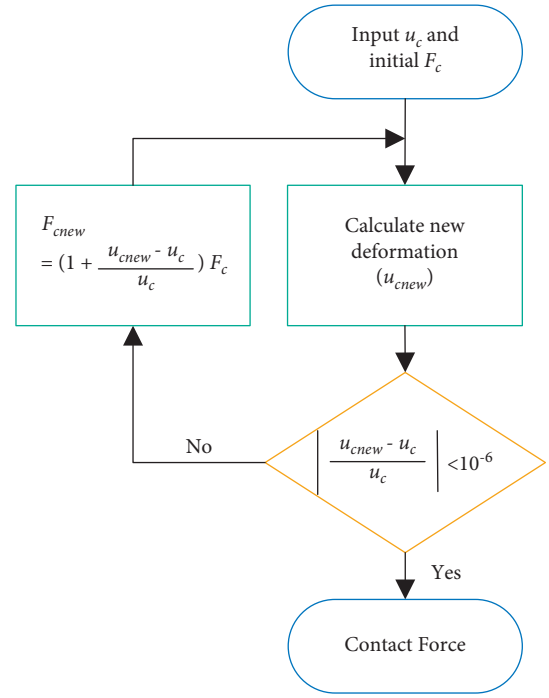

Figure 7: Calculation flow of contact force.

equal to u_c. Figure 7 shows the process of finding F_c. After entering the initial values, the finger deformation when the finger contacts the rotor (u_{cnew}) is calculated by

$$u_{cnew} = \int_0^{\alpha_{ul}} \left(\frac{\overline{N} N_c}{EA} + \frac{\overline{M} M_c}{EI} + \eta \frac{\overline{Q} Q_c}{GA} \right) R_s d\alpha, \quad (12)$$

where N_c, M_c, and Q_c are the axial force, bending moment, and shear force of the finger under the contact condition, respectively.

Compare u_c and u_{cnew}. If the absolute value of the relative error is greater than 10^{-6}, update the value of F_c according to the formula shown in Figure 7. Calculate u_{cnew} again with new F_c (F_{cnew}). This process is repeated until the relative error is less than 10^{-6}. Then, the contact force F_c is obtained.

To judge whether a finger contacts the rotor, the relationship between the film force and the film thickness should be obtained first. The film thickness ratio describes the relationship between the minimum film thickness and surface roughness [24]:

$$\gamma = \frac{h_{\min}}{\left(R_{ar}^2 + R_{ap}^2\right)^{1/2}}, \quad (13)$$

where γ is the film thickness ratio and R_{ar} and R_{ap} are the surface roughness of the rotor and the lifting pad, respectively.

When the lifting pad is not in fluid lubrication, a gas film between the lifting pad and the rotor cannot be formed, which results in contact. This paper does not consider the mixed lubrication state. The value of γ is taken as 3 to determine the minimum film thickness. As shown in Figure 8(a), the film force is larger than the contact force to the left of the dotted line, which means that the film can generate enough film force to lift this finger. As shown in Figure 8(b), the film between the lifting pad and the rotor is divergent due to the large rotation angle of the fingers. The film force increases with increasing film thickness. The contact force is always larger than the film force over the entire range of film thicknesses. The film force is not great enough to lift this finger. Thus, the finger is judged to contact the rotor.

The comparison between the previous simulation results and the results calculated using this paper's data and methods is shown in Figure 9. The figure shows the force acting on the rotor in the z-direction (shown in Figure 4) at different attitude angles of the rotor. It can be seen that the variation trend of the forces is in good agreement. When contact exists between the lifting pads and the rotor, the force acting on the rotor increases significantly.

2.4. Static Performance. This paper calculates four static characteristics of noncontacting finger seals: leakage, lift force, friction moment, and bearing force. Leakage under fluid lubrication is defined as follows:

$$Q = \sum_{i_f=1}^{n_f} \left(- \int_{\alpha i_f - \theta_p}^{\alpha i_f + \theta_p} \rho_p \frac{h_p^3}{12\mu} \frac{\partial p_p}{\partial y} R d\theta \right). \quad (14)$$

When the average axial flow velocity is larger than the local sound velocity, the gap between the lifting pad and rotor is considered chocked. The local sound velocity is used to simplify and replace the average axial velocity of gas flow. The leakage when chocked flow occurs is defined as

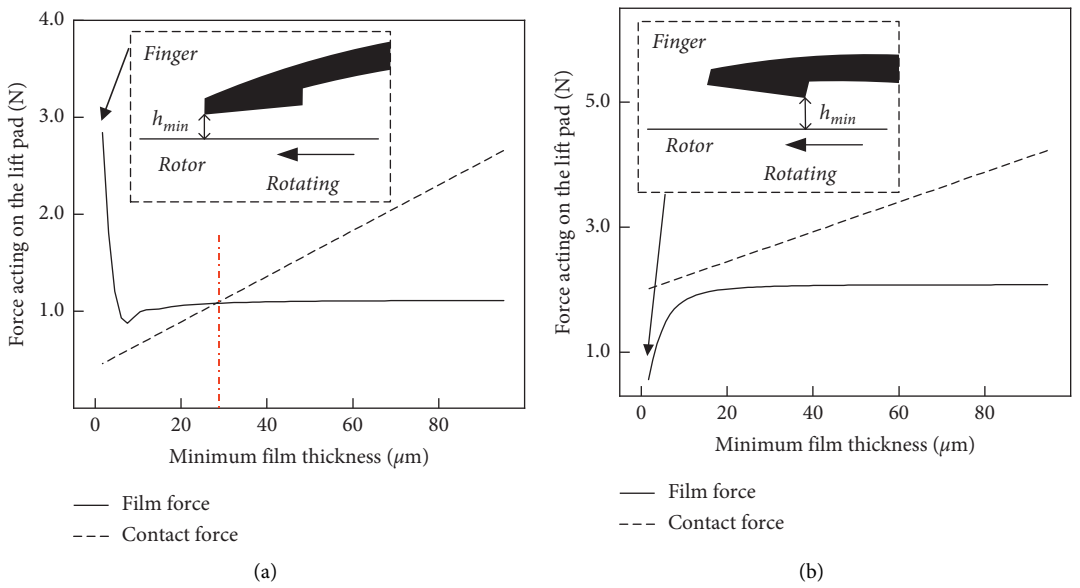

Figure 8: Relationship between the minimum film thickness and the film force. (a) The finger does not contact the rotor. (b) The finger contacts the rotor.

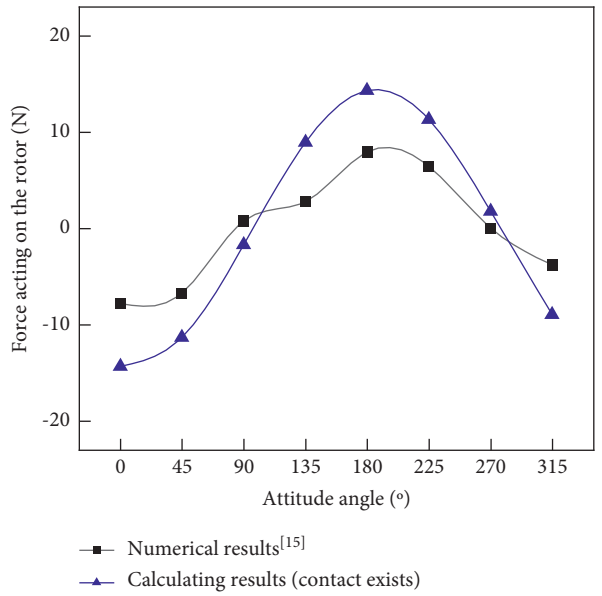

Figure 9: Force acting on the rotor in the z-direction.

$$Q = \rho V A_s, \tag{15}$$

where ρ is the density of the upstream gas, V is the average axial flow velocity, and A_s is the sectional film area.

After the finger contacts the rotor, its deformation is complex to predict. On the other hand, the thickness under the contacting finger is much smaller than that under the noncontacting finger. Thus, the leakage of the fingers under contact conditions is ignored.

The lift force of each gas film is defined as

$$F_L = \iint_{A_p} (p(\theta, y) - p_L) R \mathrm{d}\theta \mathrm{d}y, \tag{16}$$

where A_p is the area of the lifting pads and p_L is the downstream pressure.

For the fingers under fluid lubrication, the bearing force and the friction moment acting on the rotor by each finger are defined as follows:

$$\begin{cases} F_{hh} = \int_0^L \int_{\theta_{if}}^{\theta_{if}+\theta_p} (p - p_l) R_r \cos\theta \mathrm{d}\theta \mathrm{d}y, \\ F_{vh} = \int_0^L \int_{\theta_{if}}^{\theta_{if}+\theta_p} (p - p_l) R_r \sin\theta \mathrm{d}\theta\, dy, \end{cases} \tag{17}$$

$$M_{fh} = \int_0^L \int_{\theta_{if}}^{\theta_{if}+\theta_p} \left(-\frac{h(\theta)}{2R} \frac{\partial p}{\partial \theta} + \frac{\mu \omega R_r}{h(\theta)} \right) R_r \mathrm{d}\theta \mathrm{d}y.$$

For the fingers under the contact condition,

$$\begin{cases} F_{hc} = F_c \cos\theta, \\ F_{vc} = F_c \sin\theta, \\ M_{fc} = \mu_{fr} F_c R_r, \end{cases} \tag{18}$$

where μ_{fr} is the friction coefficient between the fingers and rotor.

Thus, the bearing force and friction moment acting on the rotor are

$$W = \sqrt{\left(\sum_i^{n_h}(F_{hh}) + \sum_i^{n_h}(F_{vh})\right)^2 + \left(\sum_i^{n_c}(F_{hc}) + \sum_i^{n_c}(F_{vc})\right)^2},$$
$$M_f = \sum_i^{n_h}(M_{fh}) + \sum_i^{n_c}(M_{fc}), \tag{19}$$

where n_h and n_c are the number of fingers under the fluid lubrication and contact conditions, respectively.

The aeroelastic coupling calculation flow is shown in Figure 10. The convergence conditions are as follows:

$$\begin{cases} \max\left(abs\left(\dfrac{p^{\lambda+1} - p^{\lambda}}{p^{\lambda}}\right)\right) < 1e^{-6}, \\ \max\left(abs\left(\dfrac{h^{\lambda+1} - h^{\lambda}}{h^{\lambda}}\right)\right) < 1e^{-6}, \end{cases} \tag{20}$$

where λ is the number of iterations.

3. Results

The parameters of the noncontacting finger seal in this paper are given in Table 1.

Figure 11 shows the effects of eccentricity at different pressure differences. As shown in Figure 11(a), the leakage decreases first and then increases at 50 kPa pressure difference. As the eccentricity increases, some of the clearances are reduced, resulting in a decrease in leakage. The clearances under the other lifting pads are increased, resulting in an increase in leakage. Figure 11(d) shows the leakage of each finger at different eccentricity and pressure differences (fingers 1 to 80 are numbered according to the circumferential direction). The reduced leakages through fingers 1 to 20 and 61 to 80 are less than the increased leakages through fingers 40 to 60 at 0.16 eccentricity and 50 kPa pressure difference. Thus, the total leakage is reduced. The leakages through clearances are reduced because of the contact (fingers 1 to 14 and 70 to 80) and the eccentricity (fingers 15 to 20 and 61 to 69) at 0.64 eccentricity and 150 kPa pressure difference. However, the total leakage is still greater than that at 0 eccentricity due to the increased film thickness caused by the increased eccentricity. When the pressure difference is equal to 50 kPa, a slight decrease in leakage with increasing eccentricity appears in the eccentricity range of 0.08 to 0.24. When the pressure difference is equal to 150 kPa, this change occurs in the eccentricity range of 0.32 to 0.56. This is due to the larger finger deformations and the greater clearance between the lifting pads and the rotor under the high-pressure difference.

Figures 11(b) and 11(c) show the friction moment and bearing force for various eccentricities at different pressure differences. They increase with increasing eccentricity and are greater at 50 kPa pressure difference than at 150 kPa pressure difference. This is because the film forces are smaller at low-pressure differences, resulting in more fingers in contact with the rotor. As shown in Figure 11(e), when there is no contact between the rotor and the fingers, the pressure distributions are similar for most gas films, making the bearing force, that is, the combined force acting on the rotor, small. When contact occurs between the fingers and the rotor, the contacting force is greater than the film force, resulting in a significant increase in the bearing force. The higher the eccentricity is, the higher the number of sealing fingers in contact is, and the higher the bearing force and friction moment are.

Figure 12 shows the effects of rotation speed at 100 kPa pressure difference and different eccentricities. As shown in Figure 12(a), the leakage decreases with increasing rotation speed. The rotation angles of the fingers are large at 100 kPa pressure difference, which means that the gas films are divergent. The higher the rotation speed is, the lower the film force is and the smaller the clearance is, resulting in decreased leakage. When the rotor is at high eccentricity, the decrease in the film force leads to contact between the finger and the rotor. From Figure 12(b), the friction moment increases with increasing rotation speed. At 0.2 eccentricity, the increase in friction moment is continuous because there is no contact between fingers and the rotor. Negative friction moments occur at a low rotation speed, which means that the direction of the friction moment is the same as the rotation speed. For a divergent gas film at 100 kPa pressure difference, the friction moment generated by the pressure difference is in the same direction as the rotating speed (expressed as the negative direction in this paper). When the rotating speed is low, the friction moment is mainly generated by the pressure difference. With increasing rotation speed, the friction moment generated by rotation increases, and the friction moment becomes positive (opposite to the direction of rotation). At 0.6 eccentricity, the friction moment consists of two types: the friction moment caused by contact and the friction moment caused by the gas film. The higher the rotation speed is, the bigger the number of contact fingers is and the greater the Coulomb friction of all contact fingers is. As shown in Figure 12(c), the rotation speed has no significant effect on the bearing force at 0.2 eccentricity, which means that the film force is mainly generated by the pressure difference. There is no contact between the fingers and the rotor. At 0.6 eccentricity, the bearing force increases and then does not change significantly with increasing rotation speed. This is because the increase in the number of contact fingers at 0.6 eccentricity leads to an increase in bearing force.

Figure 13 shows the effect of pressure difference. As shown in Figure 13(a), the leakage increases, and the number

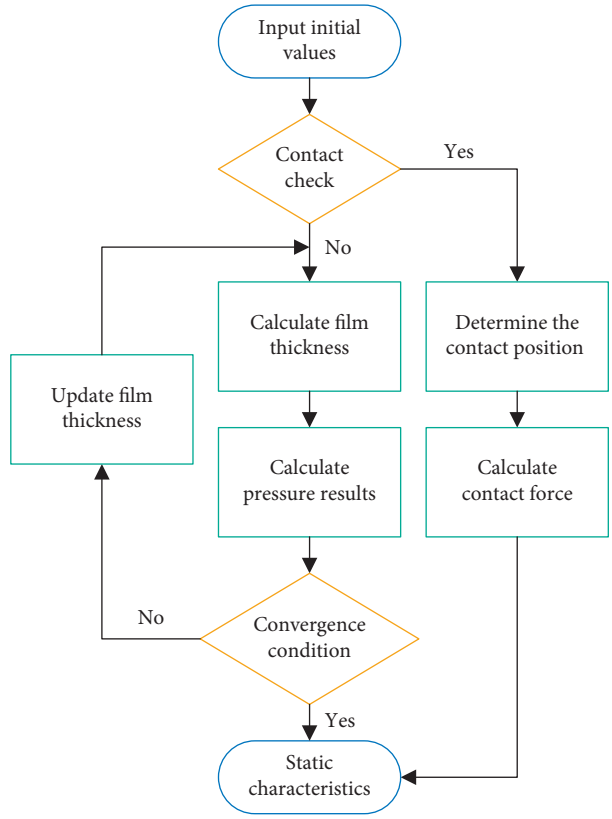

Figure 10: Calculation flow of bearing characteristic.

Table 1: Parameters of noncontacting finger seal.

Parameters	Symbol	Value	Units
Finger base radius	R_b	114.12	mm
Stick arc radius	R_s	110.00	mm
Number of fingers	N_f	80	—
Rotor radius	R_r	107.92	mm
Foot upper radius	R_f	109.22	mm
Radius of circle of centers	R_{cc}	25.20	mm
Gap width	G_p	0.38	mm
Thickness of finger laminate	b	1.00	mm
Pad axial length	B	0.64	mm
Minimum height of the wedge	$h_{w\min}$	18	μm
Maximum height of the wedge	$h_{w\max}$	36	μm
Initial installation gap	h_{init}	30	μm

of contact fingers decreases as the pressure difference increases. The increase in pressure difference results in increased film forces, which reduces the number of contact fingers. Figure 13(d) shows the leakage of each finger at different pressure differences and eccentricities. Leakage at high eccentricity is not always high, which corresponds to the discussion of eccentricity above. As shown in Figure 13(b), the friction moment decreases with increasing pressure difference. However, the reasons for the decreases are different. At 0.2 eccentricity, all the fingers are under fluid lubrication. With increasing pressure difference, the film thickness increases, which means that the friction moment caused by the rotation speed decreases. At 0.6 eccentricity, the decrease is due to the reduction in the number of contact fingers. As shown in Figure 13(c), the bearing force decreases with increasing pressure difference. This is because the forces acting on the rotor by each finger are gradually the same. This phenomenon is further illustrated in Figure 13(e), which shows each finger's force acting on the rotor at different pressure differences and eccentricities. When the pressure difference is 13 kPa, the bearing force is the combined force of the film forces at 0.2 eccentricity; the bearing force is the combined force of the film forces and the contact forces at 0.6 eccentricity. When the pressure difference is 200 kPa, the forces acting on the rotor by each finger are almost the same.

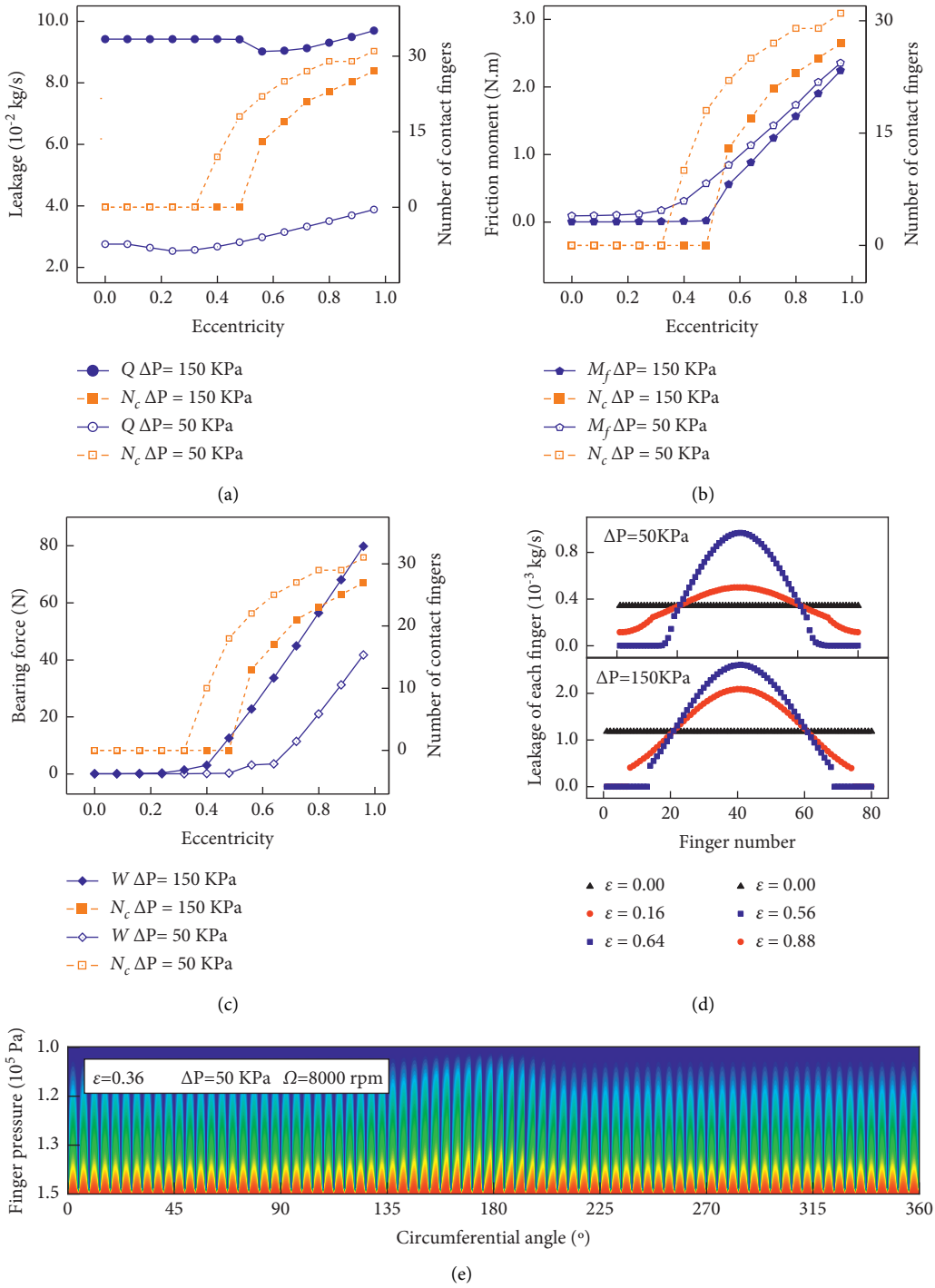

FIGURE 11: Effect of eccentricity. (a) Leakage for various eccentricities. (b) Friction moment for various eccentricities. (c) Bearing force for various eccentricities. (d) Leakage of each finger. (e) Pressure distribution of each finger.

Figure 14 shows the effect of the number of fingers at a 100 kPa pressure difference, eccentricity of 0.6, and rotation speed of 8000 rpm. The average film force decreases with an increasing number of fingers because the circumferential length of the lifting pad (B) decreases. L/B in Figure 14 represents the ratio of the axial length to the circumferential length of the lifting pads. As shown in Figure 14, the leakage increases with the number of fingers; the friction moment and bearing force decrease with the number of fingers. The leakages of the square pads (L/B = 1) are greater than those of

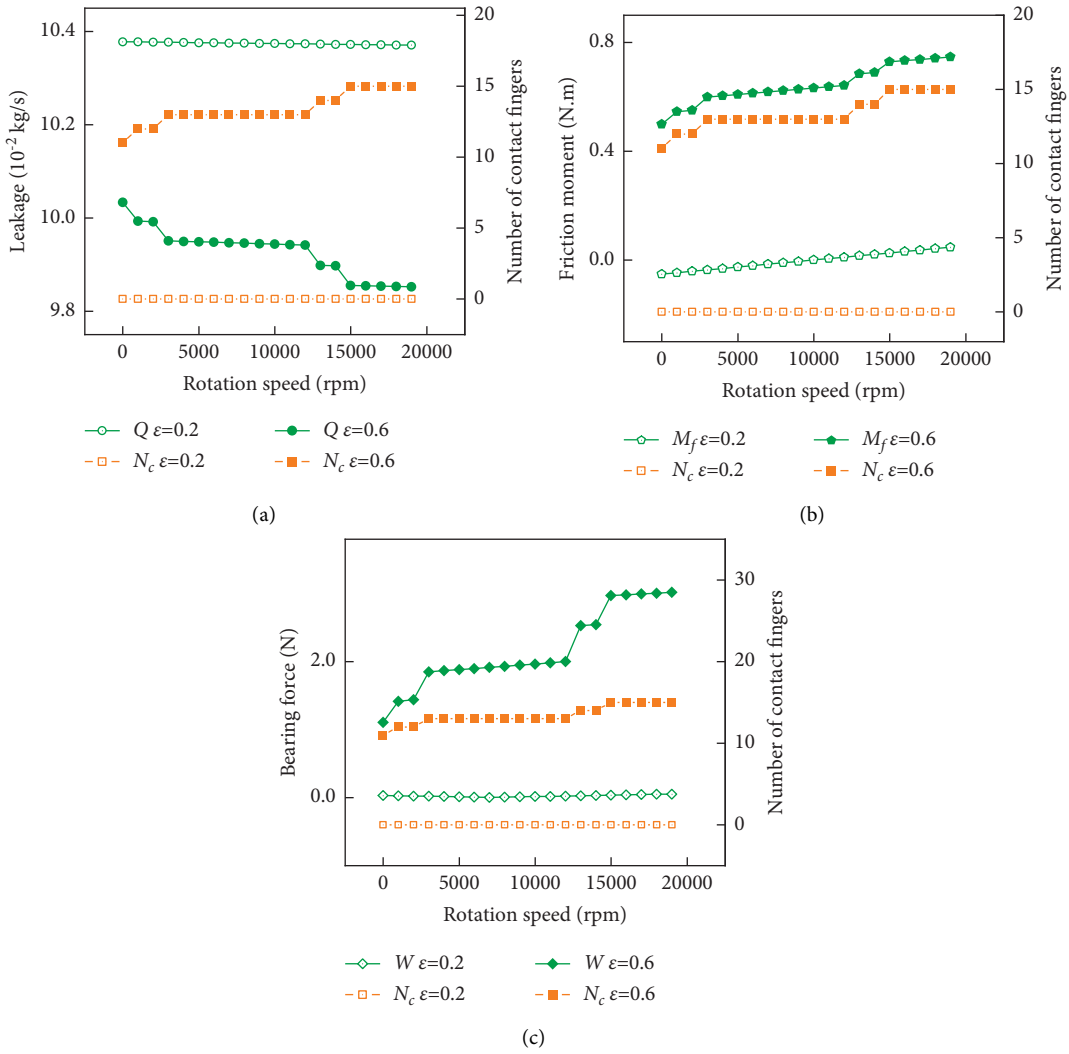

Figure 12: Effect of rotation speed. (a) Leakage for various rotation speeds. (b) Friction moment for various rotation speeds. (c) Bearing force for various rotation speeds.

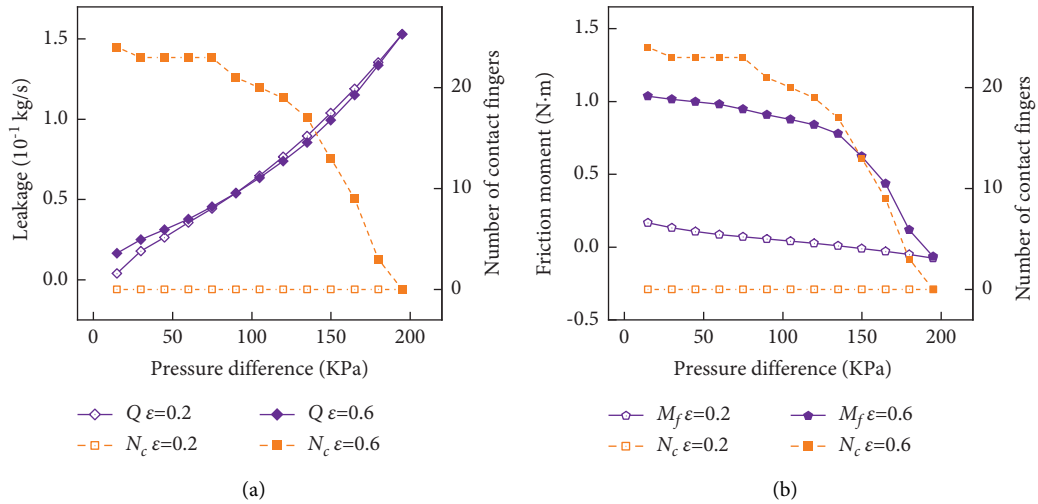

Figure 13: Continued.

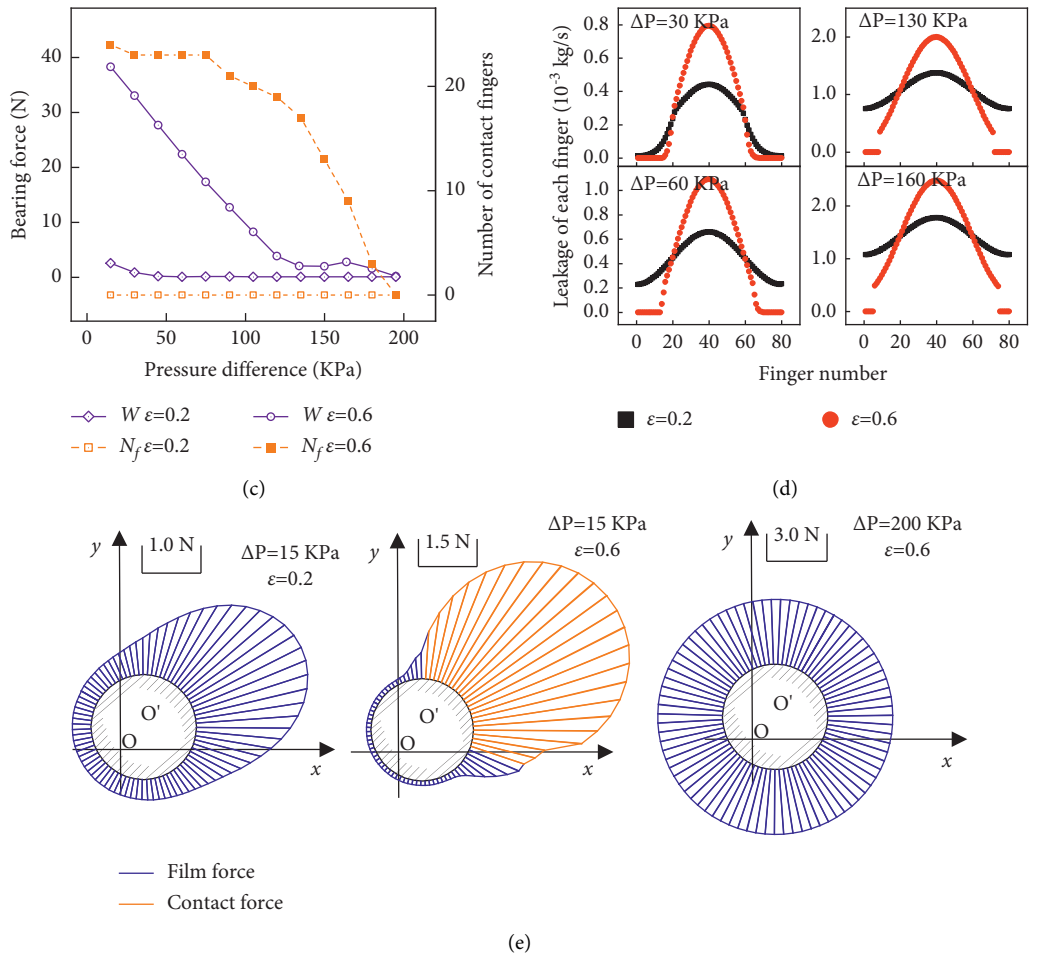

Figure 13: Effect of pressure difference. (a) Leakage for various pressure differences. (b) Friction moment for various pressure differences. (c) Bearing force for various pressure differences. (d) Leakage of each finger. (e) Force acting on the rotor by each finger.

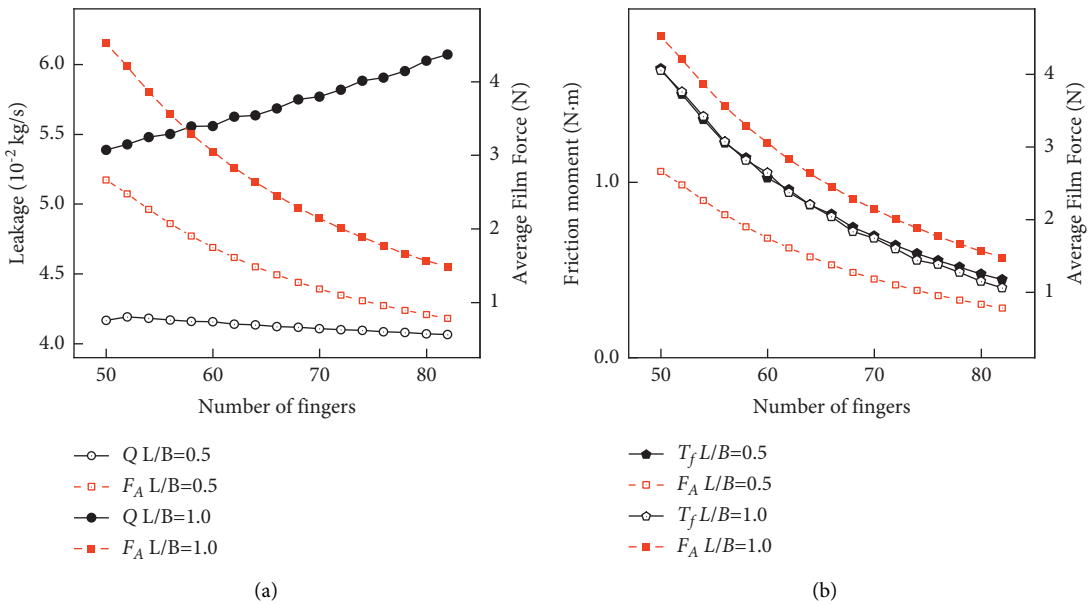

Figure 14: Continued.

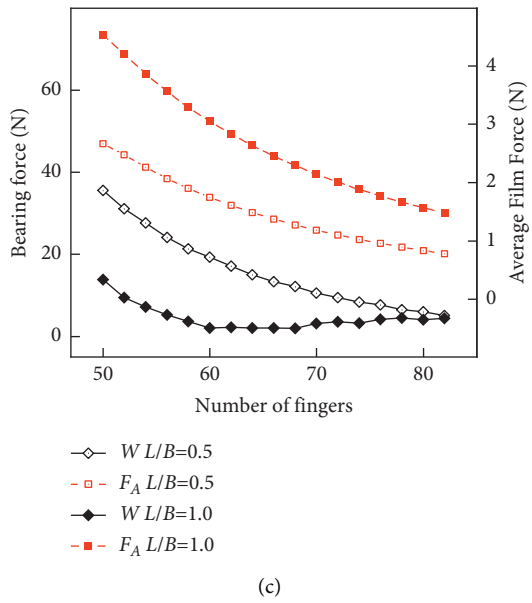

(c)

Figure 14: Effects of the number of fingers. (a) Leakages for various numbers of fingers. (b) Friction moment for various numbers of fingers. (c) Bearing force for various numbers of fingers.

the wider pads (L/B = 0.5) because the square pads can generate more film force to lift the fingers, resulting in a higher increase in the clearances. The finger stiffness decreases with the increase in the number of fingers, and the finger deformations increase with the number of fingers under the same working environment. Thus, the clearances are increased, and the pressure distributions of each finger are almost the same, which results in the increase in the leakage and the decrease in the bearing force and friction moment.

4. Conclusion

In this paper, the static characteristics of noncontacting finger seals are studied when the seal works in an inappropriate environment or its design is unreasonable, which means contact may exist between the fingers and the rotor. A method to judge whether the fingers contact the rotor is proposed. The effects of various structural and environmental parameters are studied. Detailed conclusions are summarized as follows:

(1) The contact between the fingers and the rotor reduces the leakage and significantly increases the bearing force and friction moment. This reduction or increase is proportional to the number of contact fingers.

(2) The higher the pressure difference is and the lower the eccentricity is, the less likely the finger is to contact the rotor. The effect of rotation speed on the number of contact fingers is significantly smaller than pressure difference and eccentricity. Therefore, the pressure difference and rotor vibration amplitude should be considered the main environmental parameters in the design phase.

(3) As the number of fingers increases, the film force, friction moment, and bearing force decrease, and the leakage increases. Wider pads can generate more film force than square pads. The square pads have smaller bearing forces and friction moments but have higher leakages than the wider pads. The greater the number of fingers is or the longer the axial length of the lifting pads is, the less likely the fingers come into contact with the rotor. The noncontacting feature is easier to achieve.

Abbreviations

A: Cross-sectional area
b: Axial thickness of seal laminate
e: Eccentricity distance
F_f: Friction force between low-pressure finger laminate and backplate
F_{hc}, F_{vc}: Horizontal and vertical components of contact force
F_h: Film force
h: Local film thickness
h_{if}: Film thickness of the i-th finger
h_{rif}: Film change due to rotation angle
$h_{w\min}$: Minimum pad wedge
I: Moment of inertia
L: Axial length of lifting pad
$\overline{M}$: Unit bending moment
M_h: Bending moment of noncontact finger
N: Axial force

n_f: Number of fingers
O: Diameter center of seal outer diameter
k: Stiffness of high-pressure finger
p: Pressure
p_h: Upstream pressure
R_s: Stick arc radius
R_f: Foot upper radius
R_{cc}: Radius of circle of centers
u_c: Finger deformation of contact finger
u_h: Finger deformation under fluid lubrication
α_{ul}: Curvature of the finger
μ_{fr}: Friction coefficient between finger and rotor
θ_1, θ_2: Circumferential angles of the contact position
θ: Circumferential angle
φ: Attitude angle
A_s: Sectional film area
A_{lb}: Contact area between the low-pressure laminate and the backplate
E: Young's module
W: Bearing force
F_k: Force between two laminates
F_{hh}, F_{vh}: Horizontal and vertical components of film force
F_c: Contact force
$\overline{h}$: Dimensionless film thickness
h_{init}: Initial installation gap
h_w: Wedge under lifting pad
$h_{w\max}$: Maximum pad wedge
i_f: Finger number
M: Bending moment
m: Number of circumferential grids
M_c: Bending moment of contact finger
$\overline{N}$: Unit axial force
n: Number of axial grids
O_2: Diameter center of rotor
P_{lb}: Pressure that pushes the finger laminate against the backplate
$\overline{p}$: Dimensionless pressure
p_l: Downstream pressure
R_r: Rotor radius
R_b: Finger base radius
u: Deformations of fingers
u_1, u_2: Finger deformations of positions 1 and 2
α_r: Finger repeat angle
μ: Gas viscosity
μ_{lb}: Friction coefficient between low-pressure laminate and backplate
ε: Eccentricity
θ_p: Arc degree of lifting pad
Λ_x: Compressibility number.

Appendix

The coefficients of equation (7) are as follows:

$$
\begin{aligned}
a_{i,j} &= -\frac{\overline{h}_{i,j}^3\left(\overline{p}_{i+1,j}-\overline{p}_{i-1,j}\right)}{2\Delta\theta^2}-\frac{3\overline{p}_{i,j}\overline{h}_{i,j}^2\left(\overline{h}_{i+1,j}-\overline{h}_{i-1,j}\right)}{4\Delta\theta^2}+\frac{\Lambda_x\overline{h}_{i,j}}{2\Delta\theta}+\frac{\overline{p}_{i,j}\overline{h}_{i,j}^3}{\Delta\theta^2}\\
b_{i,j} &= \frac{\overline{h}_{i,j}^3\left(\overline{p}_{i+1,j}-\overline{p}_{i-1,j}\right)}{2\Delta\theta^2}+\frac{3\overline{p}_{i,j}\overline{h}_{i,j}^2\left(\overline{h}_{i+1,j}-\overline{h}_{i-1,j}\right)}{4\Delta\theta^2}-\frac{\Lambda_x\overline{h}_{i,j}}{2\Delta\theta}+\frac{\overline{p}_{i,j}\overline{h}_{i,j}^3}{\Delta\theta^2}\\
c_{i,j} &= +\frac{3}{4}\overline{h}_{i,j}^2\left[\begin{array}{l}\dfrac{\left(\overline{p}_{i+1,j}-\overline{p}_{i-1,j}\right)\left(\overline{h}_{i+1,j}-\overline{h}_{i-1,j}\right)}{\Delta\theta^2}\\ \\ +\dfrac{R^2}{L^2}\dfrac{\left(\overline{p}_{i,j+1}-\overline{p}_{i,j-1}\right)\left(\overline{h}_{i,j+1}-\overline{h}_{i,j-1}\right)}{\Delta\overline{y}^2}\end{array}\right]\\
&\quad+\overline{h}_{i,j}^3\left(\frac{\overline{p}_{i+1,j}-2\overline{p}_{i,j}+\overline{p}_{i-1,j}}{\Delta\theta^2}+\frac{R^2}{L^2}\frac{\overline{p}_{i,j+1}-2\overline{p}_{i,j}+\overline{p}_{i,j-1}}{\Delta\overline{y}^2}\right)\\
&\quad-2\overline{h}_{i,j}^3\left(\frac{\overline{p}_{i,j}}{\Delta\theta^2}+\frac{R^2}{L^2}\frac{\overline{p}_{i,j}}{\Delta\overline{y}^2}\right)-\Lambda_x\frac{\left(\overline{h}_{i+1,j}-\overline{h}_{i-1,j}\right)}{2\Delta\theta}\\
d_{i,j} &= \frac{R^2}{L^2}\frac{\overline{p}_{i,j}\overline{h}_{i,j}^3}{\Delta\overline{y}^2}-\frac{3}{4}\frac{R^2}{L^2}\frac{\overline{p}_{i,j}\overline{h}_{i,j}^2\left(\overline{h}_{i,j+1}-\overline{h}_{i,j-1}\right)}{\Delta\overline{y}^2}\\
&\quad-\frac{R^2}{2L^2}\frac{\overline{h}_{i,j}^3\left(\overline{p}_{i,j+1}-\overline{p}_{i,j-1}\right)}{\Delta\overline{y}^2}\\
e_{i,j} &= \frac{R^2}{L^2}\frac{\overline{p}_{i,j}\overline{h}_{i,j}^3}{\Delta\overline{y}^2}+\frac{R^2}{2L^2}\frac{\overline{h}_{i,j}^3\left(\overline{p}_{i,j+1}-\overline{p}_{i,j-1}\right)}{\Delta\overline{y}^2}+\frac{3R^2}{4L^2}\frac{\overline{p}_{i,j}\overline{h}_{i,j}^2\left(\overline{h}_{i,j+1}-\overline{h}_{i,j-1}\right)}{\Delta\overline{y}^2}\\
S_{i,j} &= -\overline{p}_{i,j}\overline{h}_{i,j}^3\left(\frac{\overline{p}_{i+1,j}-2\overline{p}_{i,j}+\overline{p}_{i-1,j}}{\Delta\theta^2}+\frac{R^2}{L^2}\frac{\overline{p}_{i,j+1}-2\overline{p}_{i,j}+\overline{p}_{i,j-1}}{\Delta\overline{y}^2}\right)\\
&\quad-\overline{h}_{i,j}^3\left[\frac{\left(\overline{p}_{i+1,j}-\overline{p}_{i-1,j}\right)^2}{4\Delta\theta^2}+\frac{R^2}{L^2}\frac{\left(\overline{p}_{i,j+1}-\overline{p}_{i,j-1}\right)^2}{4\Delta\overline{y}^2}\right]\\
&\quad-\frac{3\overline{p}_{i,j}\overline{h}_{i,j}^2}{4}\left[\begin{array}{l}\dfrac{\left(\overline{p}_{i+1,j}-\overline{p}_{i-1,j}\right)\left(\overline{h}_{i+1,j}-\overline{h}_{i-1,j}\right)}{\Delta\theta^2}\\ \\ +\dfrac{R^2}{L^2}\dfrac{\left(\overline{p}_{i,j+1}-\overline{p}_{i,j-1}\right)\left(\overline{h}_{i,j+1}-\overline{h}_{i,j-1}\right)}{\Delta\overline{y}^2}\end{array}\right]\\
&\quad+\frac{\Lambda_x}{2\Delta\theta}\left[\overline{h}_{i,j}\left(\overline{p}_{i+1,j}-\overline{p}_{i-1,j}\right)+\overline{p}_{i,j}\left(\overline{h}_{i+1,j}-\overline{h}_{i-1,j}\right)\right].
\end{aligned}
\tag{A.1}
$$

Data Availability

The data calculation results used to support the findings of this study are included within the article.

Conflicts of Interest

The authors declare that they have no conflicts of interest.

Acknowledgments

This work was supported by the National Natural Science Foundation of China (Grants nos. 11972131 and 12072089) and National Science and Technology Major Project (Grant no. 2017-IV-0010-0047).

References

[1] M. C. Johnson and E. G. Medlin, "Laminated finger seal with logarithmic curvature," USA, Patent No. 5108116, 1992.

[2] M. J. Braun, F. K. Choy, and H. M. Pierson, "Structural and dynamic considerations towards the design of padded finger seals," in *Proceedings of the 39th AIAA/ASME/SAE/ASEE Joint Propulsion Conference and Exhibit*, p. 4698, Huntsville, AL, USA, 2003.

[3] G.-D. Chen, F. Lu, Q.-P. Yu, and H. Su, "Dynamic analysis of finger seal using equivalent model based on distributed mass method," *Proceedings of the Institution of Mechanical Engineers*, vol. 228, no. 16, pp. 2992–3005, 2014.

[4] M. P. Proctor, A. Kumar, and I. R. Delgado, "High-speed, high-temperature finger seal test results," *Journal of Propulsion and Power*, vol. 20, no. 2, pp. 312–318, 2004.

[5] L. Guoqing, Z. Qian, G. Lei, Y. Qiangpeng, X. Gang, and Z. Junqiang, "Leakage and wear characteristics of finger seal in hot/cold state for aero-engine," *Tribology International*, vol. 127, pp. 209–218, 2018.

[6] G. K. Arora and D. L. Glick, "Pressure balanced finger seal," USA, Patent No. 5755445, 1998.

[7] M. P. Proctor and B. M. Steinetz, "Noncontacting finger seal," USA, Patent No. 6811154, 2004.

[8] M. J. Braun, H. M. Pierson, and D. Deng, "Thermofluids considerations and the dynamic behavior of a finger seal assembly," *Tribology Transactions*, vol. 48, no. 4, pp. 531–547, 2005.

[9] H. Marie, "Dynamic simulation of finger seal-rotor interaction using variable dynamic coefficients," in *Proceedings of the 42nd AIAA/ASME/SAE/ASEE Joint Propulsion Conference & Exhibit*, p. 4931, Sacramento, FL, USA, 2006.

[10] K. Du, Y. Li, S. Suo, and Y. Wang, "Semi-analytical dynamic analysis of noncontacting finger seals," *International Journal of Structural Stability and Dynamics*, vol. 15, no. 04, Article ID 1450060, 2015.

[11] K. Du, Y. Li, S. Suo, and Y. Wang, "Dynamic leakage analysis of noncontacting finger seals based on dynamic model," *Journal of Engineering for Gas Turbines & Power*, vol. 137, no. 9, 2015.

[12] G. Yue, Q. Zheng, and R. Zhu, "Numerical simulation of a padded finger seal," in *Proceedings of the Turbo Expo: Power for Land, Sea, and Air*, pp. 263–271, Berlin, Germany, June 2008.

[13] M. J. Braun, H. M. Pierson, and V. V. Kudriavtsev, "Finger seal solid modeling design and some solid/fluid interaction considerations," *Tribology Transactions*, vol. 46, no. 4, pp. 566–575, 2003.

[14] H. Zhang, B. Chai, B. Jiang, Q. Zheng, and G. Yue, "Numerical analysis of finger seal with grooves on lifting pads," *Journal of Propulsion and Power*, vol. 31, no. 3, pp. 805–814, 2015.

[15] H. Zhang, Q. Zheng, and G. Yue, "Study on the leakage and deformation characteristics of the finger seals by using numerical simulation," in *Proceedings of the Turbo Expo: Power for Land, Sea, and Air*, pp. 1179–1190, Glasgow, UK, June 2010.

[16] X. Jia, Q. Zheng, Z. Tian, Y. Jiang, and H. Zhang, "Numerical investigations on lifting and flow performance of finger seal with grooved pad," *Aerospace Science and Technology*, vol. 81, no. OCT, pp. 225–236, 2018.

[17] J. M. Temis, A. V. Selivanov, and I. J. Dzeva, "Finger seal design based on fluid-solid interaction model," in *Proceedings of the Turbo Expo: Power for Land, Sea, and Air*, pp. V3A–V15A, American Society of Mechanical Engineers (ASME), San Antonio, Texas, USA, June 2013.

[18] H. Zhao, H. Su, and G. Chen, "Analysis of total leakage of finger seal with side leakage flow," *Tribology International*, vol. 150, Article ID 106371, 2020.

[19] D. P. Fleming, *Approximate solution for choked flow in gas seal pads*, Glenn Research Center, Cleveland, Ohio, 2004.

[20] M. Proctor and I. Delgado, "Preliminary test results of non-contacting finger seal on herringbone-grooved rotor," in *Proceedings of the 44th AIAA/ASME/SAE/ASEE Joint Propulsion Conference & Exhibit*, p. 4506, Columbus, OH, USA, 2008.

[21] I. M. Smith and M. J. Braun, "A parametric experimental investigation and performance comparison of four finger seal embodiments," in *Proceedings of the International Joint Tribology Conference*, pp. 349–351, San Diego, California, USA, October 2007.

[22] N. Wang, S. Chang, and H. Huang, "Comparison of iterative methods for the solution of compressible-fluid Reynolds equation," *Journal of Tribology*, vol. 133, no. 2, 2011.

[23] I. A. Karnovsky, *Theory of Arched Structures: Strength, Stability, Vibration*, Springer Science & Business Media, New York, NY, USA, 2011.

[24] B. J. Hamrock, B. J. Schmid, and B. O. Jacobson, *Fundamentals of Fluid Film Lubrication*, CRC Press, Florida, USA, 2004.

Hindawi
Shock and Vibration
Volume 2022, Article ID 4534103, 13 pages
https://doi.org/10.1155/2022/4534103

Research Article

Effects of Strain Node on the Actuation Performance of Multilayer Cantilevered Piezoactuator with Segmented Electrodes

Quan Bai [1,2] **and Xuejun Zheng** [1]

[1]*School of Mechanical Engineering, Xiangtan 411105, China*
[2]*Hunan Provincial Key Laboratory of Vehicle Power and Transmission System, Hunan Institute of Engineering, Xiangtan 411101, China*

Correspondence should be addressed to Xuejun Zheng; zhengxuejun@xtu.edu.cn

Received 10 December 2021; Accepted 15 January 2022; Published 3 March 2022

Academic Editor: Jiaqiang E

A model of a segmented electrode multilayer cantilever piezoelectric actuator was established to predict its actuation performance, and then, theoretical and numerical analyses of the strain nodes were performed based on normalized deflection and strain distributions. The segmented electrodes instead of the continuous electrodes are applied in a multilayer cantilever piezoelectric actuator which can avoid the modal displacement offsets at the high vibration modes, thereby enhancing the tip deflection. The theoretical analysis and simulation results show that the tip deflection of the segmented electrode at the second mode was almost 100% larger than that of the continuous electrode. At the second mode, the maximum error between the theoretical calculation value of the tip deflection and the simulation result is 6.8%. It is because the segmented electrode is optimally designed at the strain node, which avoids the modal displacement offsets of a multilayer cantilever piezoelectric actuator at the high vibration modes; meanwhile, the theoretical results are closer to the FEM simulation results. It reveals that the tip deflection of a multilayer cantilever piezoelectric actuator can be precisely estimated by the proposed model. This research can provide some useful guidance improving the actuation performance and optimizing the design of a multilayer cantilever piezoelectric actuator.

1. Introduction

Piezoactuators are widely used in microelectromechanical systems (MEMS) because of the characteristics of small size, thinness, and high displacement, such as atomic force microscopes [1], biosensors [2], microelectromechanical switches [3], and micropositioning platforms [4], etc. The actuation performance improvement and design optimization of such devices have always been the main focus of many researchers. In particular, there are many reports in the theoretical research of piezoelectric actuators. Based on the Euler model, Wang et al. [5] and Zhang et al. [6] presented the governing equations for the piezoelectric actuators with a sandwich layer. In a study conducted by Zhang et al. [7], a simple MCPAs distributed parameter model is developed to simulate the fundamental wave of piezoelectricity in thickness-extension mode. In order to reduce the poor piezoelectric effect caused by the damage of piezoelectric materials, some researchers have designed multilayer piezoelectric actuators to improve the flexibility and compactness of the structure. Afonin [8] constructed a generalized structural parameter model of nano-mechatronics multilayer electromagnetic elastic actuators. Shivashankar and Gopalakrishnan [9] reported a d33 mode surface-bondable multilayer actuator that can provide large braking force and stroke for driving large, thick, and stiffer structures. Peng et al. [10] proposed a piezoelectric multilayer actuator considering buffer layers and analyzed the dependence of the resonance frequency at the first mode and tip deflection on different layer thicknesses (buffer layer, electrode layer, and substrate layer). The contributions of the above research mainly focused on the first mode while

ignoring the other higher-frequency modes, because the tip deflection of the cantilever beam at higher modes is smaller than the tip deflection at the first mode. However, piezoelectric cantilever beams can also provide superior performance at higher modes [11], which is more common in energy harvesters [12]. Ly et al. developed a 31-effect piezoelectric bending cantilever based on the Euler-Bernoulli beam theory. Their results indicated that the voltage and bandwidth at the second mode of resonant frequency were much larger than those at the first mode [13]. Except for the first mode, the cantilevered piezoelectric energy harvester (PEH) has fixed strain nodes in other vibration modes, and there are dynamic strain distributions with opposite strain signs on both sides of the node. Theoretical and experimental results demonstrate that covering the strained nodes with continuous electrodes may lead to a strong cancelation of the electrical output [14]. In order to improve the piezoelectric performance, Zizys et al. investigated the segmentation of a vibration-shock cantilevered PEH working in higher transverse vibration modes [15]. Rafique et al. used segmented electrodes to enhance the output power of the PEH [16]. Liu et al. employed the first and second bending vibration modes to design a novel bonded-type piezoelectric actuator, which obtained higher power density than previous designs [17]. Although segmented electrodes could be applied to MCPAs at the high vibration modes, there is currently no complete electromechanical equation that can describe MCPA with segmented electrodes (MCPA-S).

In this paper, by optimizing the structure of segmented electrodes, a MCPA with segmented electrodes based on the strain nodes is designed to improve the actuation performance [18]. The strain nodes are determined by the normalized deflection and strain distribution [14]. Based on Euler-Bernoulli beam theory and piezoelectric constitutive equation, a complete electromechanical coupling model is developed for the MCPA-S. Here, the electrodes are connected in series at the first mode and in parallel at the second mode, which is different from those reported in [11]. It can prevent the displacement offset in the electric potential, increase the modal electromechanical coupling term, and improve the applied capacity. In order to understand whether segmented electrodes can eliminate the influence of strain node at higher modes, we have studied the relationship of tip deflection of segmented and continuous electrodes MCPAs with excitation frequency, excitation voltage, and beam length under different modes. In addition, the structural parameters of the MCPAs were optimized by simulating different thicknesses of the substrate, piezoelectric, and buffer layers, as well as the different Young's modulus ratios. The proposed model and prediction results can provide useful guidance for optimizing the construction and efficiency of MCPAs.

2. Design and Modeling

2.1. Design. Except for the fundamental modes, the dynamic strain distribution of the cantilevered beam changes direction at fixed strain nodes. The modal actuation capability of a cantilevered beam is closely related to the position of the piezoelectric actuators. To increase the driving force, the use of segmented actuators to control adaptive structures is proposed by avoiding the position of dynamic strain phase changes. At high modes, when the top surface of the entire piezoelectric layer was covered by continuous electrodes, the actuation capability had been significantly reduced. Therefore, we apply electrode segmentation at the nodes to a multilayer actuator (considering buffer and electrode layers), which is different from the traditional sandwich structure. This paper takes the MCPA in the second mode as an example to analyze the actuation capability. There is one strain node in the second-order mode, and the electrode is cut at the node and divided into two sections of electrodes.

Figure 1 depicts a two-dimensional schematic diagram of the MCPA-S. One end of the multilayer cantilever piezoelectric actuator is attached to the base composed of five different layers from bottom to top: the substrate, the buffer, the second electrode, the piezoelectric layer, and the first electrode as shown in Figure 1(a). The first electrode and the piezoelectric layer are cut at the strained node to form segmented electrodes for the MCPA. The contact between the second electrode and the lower surface of the piezoelectric film is continuous, but the contact between the first electrode and the upper surface of the piezoelectric layer is discontinuous. The polarization direction is reversed after passing through the strain node, and the split position is the strain node position L_1. The different electrode connections are adopted under the different modes of the cantilever beam. At the first mode, the strain distribution is in the same phase for the MCPA, because there is no strain node [10]. Here, the electrode directions in the L_1 and L_1-L regions are opposite, and the electrode wires are connected in series with the applied voltage, as shown in Figure 1(b). At the second mode, there is a strain node and the strain distributions in L_1 and L_1-L regions are 180 degrees out of phase. The connection of the electrodes is described in Figure 1(c), which is arranged in parallel to prevent modal displacement in the electric potential. And then the applied voltage should be applied on the L_1 and L_1-L regions of the cantilever beam to generate the deflection for the MCPA.

Z_1, Z_2, Z_3, and Z_4 depict the vertical coordinates of the bottom-surface of substrate, buffer, piezoelectric layer, and the first electrode, respectively. Z_i and Z_5 indicate the vertical coordinates of the top surface of buffer and the second electrode. The length and width of the cantilever beam are denoted by L and b. In Cartesian coordinate system, the x- and z-axes are consistent with the directions 1 and 3, respectively, and the z-axis represents the polarization direction of the piezoelectric layer. The coordinate origin of the x-z plane corresponds to the leftmost point of the MCPA. The mid-plane of the substrate is denoted by the dotted line. The neutral plane is located at z_0 from the mid-plane of the substrate. Moreover, h is used to describe the thickness of each layer, and its subscripts p, s, i, and e indicate the piezoelectric, substrate, buffer, and electrodes layers, respectively. The transverse deflection $w(x, t)$ of the MCPA occurs along the z-axis and is a function with the x value and time t.

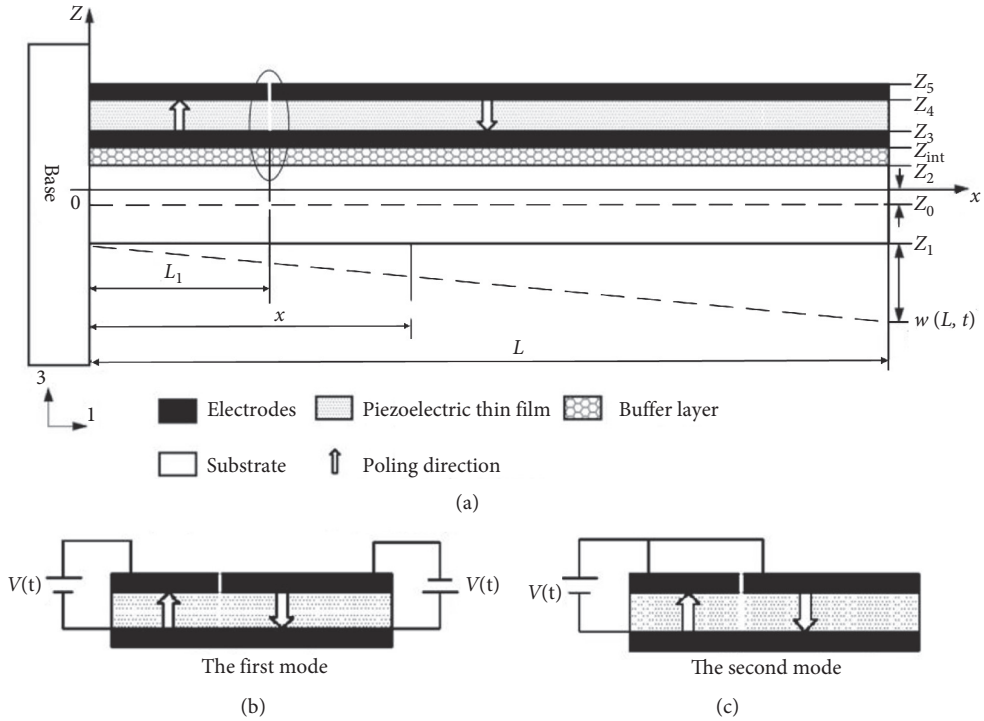

Figure 1: (a) Schematic illustration of the deflection of MCPA-S; (b) electrode wire connection at the first mode (series connection) and (c) at the second mode (parallel connection).

2.2. Modeling

2.2.1. Electromechanical Coupling Equation. The constitutive equation for piezoelectric materials can be described in the form [10]

$$T_{1,p} = c_{11,p}S_1 - e_{p31}E_3, \tag{1}$$

where stress, strain, and electric field are denoted by T, S, and E, respectively, elastic constant of the piezoelectric material is described by c, and piezoelectric coupling coefficient under steady electric field is depicted by e_p. Here, the axial strain and polarization direction are marked as subscripts 1 and 3, respectively. The elastic stiffness component can be calculated by $c_{11,p} = 1/s_{11,p}$ according to the plane-stress presumption of the MCPA. Under a constant electric field, $s_{11,p}$ denotes the elastic compliance. In addition, e_{31} can be expressed as $e_{p31} = d_{31}/s_{11,p}$ with the commonly used piezoelectric constant d_{31}. The constitutive equations applied to the substrate layer and the buffer layer can be given as [19]

$$\begin{aligned} T_{1,s} &= c_{11,s}S_1, \\ T_{1,i} &= c_{11,s}S_1. \end{aligned} \tag{2}$$

The constitutive equation for the electrode layer is [19]

$$T_{1,e} = c_{11,e}S_1, \tag{3}$$

and the axial strain S_1 at value x and time t can be obtained by [20]

$$S_1(x,t) = -z\frac{\partial^2 w(x,t)}{\partial x^2}. \tag{4}$$

According to our previous research [7], the position of the neutral plane z_0 can be given by $z_0 = [(c_{11,e}h_{e2} + c_{11,p}h_p)(2h_{e1} + 2h_i + h_s + h_p) + c_{11,e}h_{e_2} \quad (h_{e_2} + h_p)c_{11,e}h_{e_2}(h_{e_2} + h_p) + (c_{11,e}h_{e_1} + c_{11,i}h_i) \quad (h_s + h_i) + c_{11,e}h_{e_1}(h_{e_1} + h_i)]/(c_{11,s}h_s + c_{11,i}h_i + c_{11,e}h_{e_1} + c_{11,e}h_{e_2} + c_{11,p}h_p)$

According to the moment balance equation (the beam's cross section), the bending moment is given by

$$M(x,t) = -b\left(\int_{z_1}^{z_2} T_{1,s}z\mathrm{d}z + \int_{z_2}^{z_{\mathrm{int}}} T_{1,i}z\mathrm{d}z + \int_{z_{\mathrm{int}}}^{z_3} T_{1,e_1}z\mathrm{d}z + \int_{z_3}^{z_4} T_{1,p}z\mathrm{d}z + \int_{z_4}^{z_5} T_{1,e_2}z\mathrm{d}z\right). \tag{5}$$

At the first mode, the polarization and electric field are consistent along the entire beam length; thus, the uniform electric field $E_3(t)$ can be given in terms of voltage $v(t)$ across the piezoelectric layer and the thickness h_p as $E_3(t) = -v(t)/h_p$. At the second mode, the polarization direction and electric field of the two segmented piezoelectric layers are different. Therefore, for the 0-L_1 area (same direction) the electric field can be obtained by $E_3(t) = -v(t)/h_p$; and for the L-L_1 area (opposite direction), $E_3(t) = v(t)/h_p$.

By substituting equations (1)–(4) into equation (5) and integrating equation (5), it can be further simplified to

$$M(x,t) = EI\frac{\partial^2 w(x,t)}{\partial x^2} - v(t)\Gamma(x). \tag{6}$$

EI represents the bending stiffness of the composite structure's cross section, which is expressed by the following equation:

$$EI = \frac{b}{3}\left[c_{11,s}\left(z_2^3 - z_1^3\right) + c_{11,i}\left(z_i^3 - z_2^3\right) + c_{11,e}\left(z_3^3 - z_i^3\right) + c_{11,p}\left(z_4^3 - z_3^3\right) + c_{11,e}\left(z_5^3 - z_4^3\right)\right]. \tag{7}$$

$\Gamma(x)$ represents the spatial distribution of the electric potential and is related to the modes and the structure of the piezoelectric cantilever beam. For the MCPA with continuous electrodes (MCPA-C), $\Gamma(x)$ is expressed as [21]

$$\Gamma(x) = \vartheta[H(x) - H(x-L)]0 \le x \le L. \tag{8}$$

For the MCPA with segmented electrodes (Figure 1), the uniform electric fields are applied at different modes by conducting the different electrode lines. The potential spatial distribution can be regarded as the sum of the two electrode regions. At the first mode, the electric field is exerted to the segmented electrodes in series, and the $\Gamma(x)$ can be derived by

$$\Gamma(x) = \Gamma_1(x) + \Gamma_2(x) = \vartheta[H(x) + H(x-L)]. \tag{9}$$

At the second mode, the electric field is exerted to the segmented electrodes in parallel, and the $\Gamma(x)$ can be derived by

$$\Gamma(x) = \Gamma_1(x) + \Gamma_2(x) = \vartheta[H(x) + H(x-L) - 2H(x-L_1)], \tag{10}$$

where $H(x)$ denotes the Heaviside function and the coupling term ϑ is given as

$$\vartheta = \frac{be_{31}\left(z_4^2 - z_3^2\right)}{\left(2h_p\right)}. \tag{11}$$

The configurations of the microcantilever conform to the Euler-Bernoulli beam hypothesis, which have been presented in our previous research [10]. Considering viscous air (medium) damping and Kelvin-Voigt (or strain rate) damping, the governing equation of the cantilever beam can be written as [21]

$$\frac{\partial^2 M(x,t)}{\partial x^2} + c_s I\frac{\partial^5 w(x,t)}{\partial x^4 \partial t} + m\frac{\partial^2 w(x,t)}{\partial t^2} + c_a\frac{\partial w(x,t)}{\partial t} = 0. \tag{12}$$

Here, the viscous damping coefficient is denoted by c_a, the inertia moment of the cross section area is described by I, the strain rate damping term is expressed as c_sI, and the mass per unit length of the MCPA is represented by m, which is obtained by

$$m = b\left(p_s h_s + p_e h_{e1} + p_p h_p + p_e h_{e2} + p_i h_i\right), \tag{13}$$

where the uniform densities of the different layers are p_s (Si substrate), p_i (buffer), p_e (electrodes), and p_p (piezoelectric), respectively. The mass per unit length of the different layers is bp_s (Si substrate), bp_i (buffer), bp_{e1} (electrodes), bp_p (piezoelectric), and bp_{e2} (electrodes), respectively. Finally, by inserting equation (6) into equation (11), the electromechanical coupling equation of the MCPA at the first two modes can be obtained:

$$EI\frac{\partial^4 w(x,t)}{\partial x^4} + c_s I\frac{\partial^5 w(x,t)}{\partial x^4 \partial t} + m\frac{\partial^2 w(x,t)}{\partial t^2} + c_a\frac{\partial w(x,t)}{\partial t} = v(t)\frac{d^2\Gamma(x)}{dx^2}. \tag{14}$$

2.2.2. Modal Analysis. Based on the standard modal expansion approach, a series of the absolutely uniformly convergent eigenfunctions are used to describe the transverse deflection of the cantilever beam [11]:

$$w(x,t) = \sum_{r=1}^{\infty} \phi_r(x)\eta_r(t). \tag{15}$$

The mass normalized eigenfunction and modal coordinate of the clamped-free beam at the r^{th} vibration mode are, respectively, given by $\phi_r(x)$ and $\eta_r(t)$. The deflection of the cantilever beam can be exactly obtained from this equation. $\phi_r(x)$ is written as [11]

$$\phi_r(x) = \sqrt{\frac{1}{mL}}\left[\left(\cosh\frac{\lambda_r}{L}x - \cos\frac{\lambda_r}{L}x\right) - \sigma_r\left(\sinh\frac{\lambda_r}{L}x - \sin\frac{\lambda_r}{L}x\right)\right], \tag{16}$$

and it satisfies the orthogonality conditions [9].

$$\int_0^L m\phi_r(x)\phi_s(x)\mathrm{d}x = \delta_{rs},$$
$$\int_0^L EI\phi_s(x)\frac{\mathrm{d}^4\phi_r(x)}{\mathrm{d}x^4}\mathrm{d}x = \omega_r^2\delta_{rs}. \quad (17)$$

Here, λ_r (dimensionless frequency number) of the r^{th} vibration mode can be expressed as follows:

$$1 + \cos\lambda\cosh\lambda = 0, \quad (18)$$

and σ_r is given by

$$\sigma_r = \frac{\sinh\lambda_r - \sin\lambda_r}{\cosh\lambda_r + \cos\lambda_r}. \quad (19)$$

Bending strain distribution can be measured directly by the curvature eigenfunction that is the second derivative of the displacement eigenfunction (equation (16)). For a positive definite system ($\lambda_r > 0$), the positions of the strain nodes can be determined by calculating the roots of equation (20) at $0 < \overline{x} < 1$

$$(\cosh\lambda_r\overline{x} + \cos\lambda_r\overline{x}) - \sigma_r(\sinh\lambda_r\overline{x} + \sin\lambda_r\overline{x}) = 0, \quad (20)$$

where $\overline{x} = x/L$ denotes the length position (dimensionless) for the MCPA. By combining equation (20) with equations (18) and (19), the strain nodes positions (dimensionless) of the first three modes can be obtained in Table 1.

In addition, ω_r is the undamped natural frequency of the r^{th} mode, which is written as

$$\omega_r = \frac{\lambda_r^2}{L^2}\sqrt{\frac{EI}{m}}. \quad (21)$$

Equation (16) is simplified by using the orthogonal condition of equation (17) and then substituted into equation (15). The mechanical motion equation in modal coordinates can be derived as follows:

$$\frac{\mathrm{d}^2\eta_r(t)}{\mathrm{d}t^2} + 2\xi_r\omega_r\frac{\mathrm{d}\eta_r(t)}{\mathrm{d}t} + \omega_r^2\eta_r(t) - \chi_r v(t) = 0, \quad (22)$$

where ξ_r denotes the modal mechanical damping ratio. The coupling term (modal electromechanical) is defined as

$$\chi_r = \int_0^L \phi_r(x)\frac{\mathrm{d}\Gamma(x)}{\mathrm{d}x^2}\mathrm{d}x. \quad (23)$$

(23) can be further rewritten as [11]

$$\chi_r = \vartheta\int_0^L \phi_r(x)\left(\frac{\mathrm{d}\delta(x)}{\mathrm{d}x}\mathrm{d}x\right),$$
$$\chi_r = \vartheta\int_0^L \frac{\mathrm{d}\phi_r(x)}{\mathrm{d}x}\delta(x)\mathrm{d}x, \quad (24)$$

where $\delta(x)$ is the Dirac function.

By substituting equation (8) into equation (23), χ_r for the continuous electrodes can be rewritten as

$$\chi_r = \vartheta\left(\left.\frac{\mathrm{d}\phi_r(x)}{\mathrm{d}x}\right|_{x=L}\right). \quad (25)$$

For the segmented electrodes, χ_r is related to the spatial distribution of the electric potential at the vibration modes. By substituting equation (9) into equation (25), χ_r at the first mode can be expressed as

$$\chi_1 = \vartheta\left(\left.\frac{\mathrm{d}\phi_r(x)}{\mathrm{d}x}\right|_{x=L}\right). \quad (26)$$

At the second mode, it can be obtained by

$$\chi_2 = \vartheta\left(2\left.\frac{\mathrm{d}\phi_2(x)}{\mathrm{d}x}\right|_{x=L_1} - \left.\frac{\mathrm{d}\phi_2(x)}{\mathrm{d}x}\right|_{x=L}\right). \quad (27)$$

Employing the separating variables method, we record $\eta_r(t) = N_r e^{jwt}$ and $v(t) = Ve^{jwt}$, where N_r and V represent the amplitudes. By substituting them into equation (22), η_r can be calculated by

$$\eta_r(t) = \sum_{r=1}^{\infty}\frac{\chi_r\phi_r Ve^{jwt}}{\omega_r^2 - \omega^2 + j2\xi_r\omega_r\omega}. \quad (28)$$

By substituting equation (28) into equation (15), the transverse deflection can be redescribed as the following formula:

$$w(x,t) = \sum_{r=1}^{\infty}\frac{\chi_r\phi_r(x)Ve^{jwt}}{\omega_r^2 - \omega^2 + j2\xi_r\omega_r\omega}. \quad (29)$$

Finally, the tip deflection that occurred at the free end of the cantilever is expressed as

$$w(L,t) = \sum_{r=1}^{\infty}\frac{\chi_r\phi_r(L)Ve^{jwt}}{\omega_r^2 - \omega^2 + j2\xi_r\omega_r\omega}. \quad (30)$$

3. Verification by FEM Simulation

3.1. Material Properties and Structural Parameters. The MCPA finite element model consists of Si substrate, SiO_2 buffer, Pt first electrode, piezoelectric, and Pt second electrode. The geometrical dimensions of the segmented electrode MCPA include length L, width b, thicknesses h_s, h_i, h_{e1}, h_p, h_{e2}, and segmented length L_1. All dimensions are listed in Table 2. At the first and second mode, the mechanical damping ratios were $\xi_1 = 0.01$ and $\xi_2 = 0.013$, respectively. Poisson's ratio $v = 0.3$ was set in this paper, and other material property parameters are shown in Tables 3 and 4.

3.2. Strain Distribution of the Cantilevers with MCPA. In the simulations, the piezoelectric material is modeled by "solid5" composed of 3D 8-node hexahedral coupled-field elements, and the nonpiezoelectric materials are modeled by "solid45" including 8-node linear structural elements. At the beam's fixed end, the freedom degree of displacement is limited to be zero. The electrode connection of the first and second electrodes is implemented using coupling commands. For the upper surface of the second electrode layer and the lower surface of the piezoelectric layer, the voltage is coupled and constrained to be zero. The applied voltage is coupled to the upper surface of the first electrode layer. Figures 2(a), 2(b), 3(a) and 3(b) show the raw and fine mesh of the finite element (FEM); the circled area marks the position of the strain node. The strain distributions of the continuous and segmented

Table 1: Frequencies and strain node positions (dimensionless) of a cantilevered beam for the first three modes.

Mode	λ_r	Strain node positions on the *x-axis* ($\overline{x} = x/L$)	
1	1.87510407	—	—
2	4.69409113	0.2165	—
3	7.85475744	0.1323	0.4965

Table 2: The geometrical dimensions.

b (μm)	L (μm)	L_1 (μm)	h_s (μm)	h_i (μm)	h_{e1} (μm)	h_p (μm)	h_{e2} (μm)
200	1000	216	20	1	1	2	1

Table 3: Mechanical properties of the different materials.

Material	Si	SiO_2	Pt	Piezoelectric
Density (kg/m3)	2330	2200	21400	7550
Young's modulus (GPa)	170	72	168	81

electrode MCPAs at the first two modes are, respectively, presented in Figures 2(c), 2(d), 3(c), and 3(d). The black line of MCPA is the cutting position of the segmented electrode (L_1), as shown in Figure 3. It can be observed that, at the first mode, the strain of the continuous and segmented electrodes decreases monotonously from the fixed end to the free end in the strain contours of the MCPAs. However, at the second mode, there is a minimum strain magnitude at a certain region of the beam, which is much lower than at the fixed end, indicating the presence of a strain node.

4. Results and Discussion

4.1. Determination of Strain Nodes. Figure 4 shows the dependence of normalized deflection and normalized strain distribution of the MCPAs with continuous and segmented electrodes on the dimensionless position along the beam axis $\overline{x} = x/L$. Here, the normalized deflection curve is monotonically decreasing, and there is no zero point at the first mode, as shown in Figure 4(a). At the second mode there is a zero point on the normalized deflection curve, indicating the existence of strain nodes. In Figure 4(b), at the first mode, the strain distribution curve is monotonically increasing without strain node. At the second mode, there is a strain node at $\overline{x} = x/L = 0.216$, which is similar to the reported result [11]. Therefore, the existence of strain nodes at the second mode is analyzed by both the theoretical and simulation models.

4.2. Effect of Segmented Electrode Length on Tip Deflection. To verify the influence of the segmented electrode length L_1 on the tip deflection of the MCPA, the L_1-tip deflection curves under different resonance frequency were simulated when $V = 1$–5 V, $L_1 = 0$–1.0 mm, and $L = 1$ mm, as shown in Figure 5. Figure 5(a) shows that tip deflection at the first mode does not change with the increase of L_1 under constant applied voltages. Figure 5(b) indicates that, at the second mode, as L_1 increases from 0 to 0.216 mm, the tip deflection increases monotonically, but as L_1 increases from 0.216 to 1 mm, the tip deflection decreases nonmonotonically. The tip deflection increases and reaches a peak at $L_1 = 0.216$ mm (strain node); then the tip deflection decreases and reaches the lowest value at $L_1 = 0.620$ mm. Meanwhile, the maximum value of tip deflection increases as the applied voltage increases. At different modes, the electrode is segmented at the strain node and the electrodes are connected in different ways, in which the modal electromechanical coupling coefficient can reach a large value. For the modal displacement in the spatial potential, the cancelation is prevented to increase the tip deflection at the second mode. It indicates that the mechanism of the segmented electrode to avoid the modal displacement offsets at the high modes has been verified for the MCPAs. By adjusting the length of the segmented electrode and positioning segmentation location at the strain node, the larger tip deflection value can be obtained to improve the actuation performance.

4.3. Tip Deflections with the Segmented Electrode under Different Excitation Frequencies. Under different excitation frequencies, the tip deflection at the first and second modes of the MCPA with continuous and segmented electrodes is described in Figures 6 and 7. The tip deflection reaches a peak at the resonance frequency, and the peak value increases with the growth of the applied voltages, as shown in Figure 6. For continuous electrodes and segmented electrodes MCPAs, the tip deflections at the first mode are almost the same. At the second mode, the tip deflection of the MCPA-S at the second mode is almost 100% larger than that of the MCPA-C, as depicted in Figure 7. The maximum error of the tip deflection at the second mode is 6.8% between the theoretical and simulation results, and the theoretical calculation results of tip deflection are close to its simulation results. It reveals that, under different excitation frequencies, there is zero/one strain node at the first/second mode for the MCPAs, which has different degrees of influence on the tip deflection. Furthermore, the series/parallel connection is valid for MCPA-S at the first/second mode. At the second mode, the dynamic strain distribution of the beam can change the strain direction on both sides of the strain node [11]. When the strain nodes are covered by the continuous electrodes, the tip deflection of the beam is canceled. Therefore, the optimized segmented electrode is cut at the strain node, and the wires of the segmented electrodes are connected in series at the first mode and in parallel at the second mode. It can prevent the modal displacement in the electric potential from canceling out [21] and improve the actuation performance of MCPA-S.

4.4. Dependence of Tip Deflection on Applied Voltage. To perceive the dependence of tip deflection on applied voltage, theoretical calculations and simulations are carried out on the tip deflection of MCPA-C and MCPA-S under different applied voltages. Here, the tip deflection increases linearly with the increase of the applied voltage from 1 to 5 V, as indicated in Figure 8. The theoretical slope of the applied voltage-tip deflection curve at the first mode is 12.85 μm/V at 24 kHz in Figure 8(a). In Figure 8(b), at 150 kHz, the theoretical slopes of the applied voltage-tip deflection curves at

Table 4: Materials properties of the piezoelectric layer.

Piezoelectric constant d (pm V-1)	Dielectric constant	Elastic constant (GPa)
$d_{31} = -123$	$\varepsilon_{11} = 730\varepsilon_0$	$c_{11} = 139$
		$c_{12} = 77.8$
$d_{33} = 289$	$\varepsilon_{33} = 635\varepsilon_0$	$c_{13} = 74.3$
		$c_{33} = 115$
$d_{15} = 496$		$c_{44} = 25.6$
		$c_{66} = 30.6$

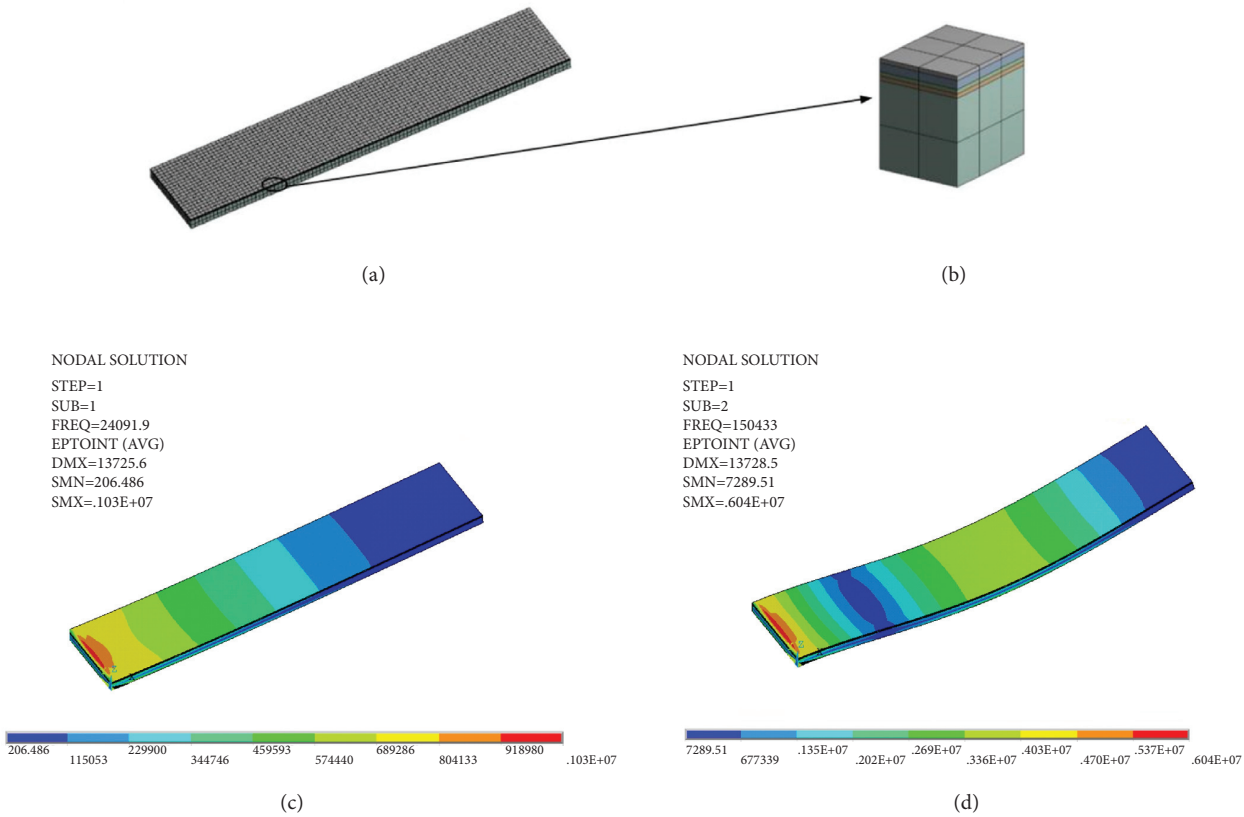

Figure 2: (a) The FEM mesh and (b) local view of the mesh at the strain node and the stress contours of the MCPA-C at the first (c) and (d) second mode.

the second mode are 0.88 μm/V and 1.73 μm/V, respectively, for MCPA-C and MCPA-S. The theoretical and simulation tip deflections of the MCPA-S are 97% larger than that of MCPA-C, and the maximum relative error is 7.8%. Obviously, the theoretical values are in good agreement with the simulation values. It shows that the presented theoretical model can correctly estimate the dynamic tip deflection of the MCPA under the applied voltage.

4.5. Dependence of the Tip Deflection on the Beam Length. In order to investigate the relationship between the tip deflection and the beam length [18], the values of tip deflection of the MCPA were obtained when $L = 0$–2.0 mm and $V = 1$–5 V. The theoretical/simulation results of the L-tip deflection curves of MCPA-C and MCPA-S at first and second mode are given in Figures 9 and 10. Under different constant voltages, as the beam length L increases from 0 to 2 mm, the tip deflections at the first and second modes increase nonlinearly, which is consistent with [22]. At the second mode, the tip deflection of the segmented electrode is obviously greater than that of the continuous electrode, as shown in Figures 10(a) and 10(b). By analyzing the relative deviations of the tip deflection when $V = 1$ V (low applied voltage), the theoretical and simulation results are expressed by lines and dots, respectively, as shown in Figure 10(c). The maximum deviations of the tip deflections between the theoretical and simulation results are 4.9% for the MCPA-S and 4.1% for the MCPA-C. It is similar to the reported results [21]. The validity of the proposed model has been verified for segmented electrode MCPA. Therefore, it is a useful strategy to improve the actuation performance by adjusting the beam length L, which can be used to drive microelectromechanical switches [3].

4.6. Dependence of Tip Deflection on the Substrate/Piezoelectric Layer Thickness Ratio. In this section, $r = E_s/E_p$ and $h = h_s/h_p$ are defined to describe Young's modulus ratio

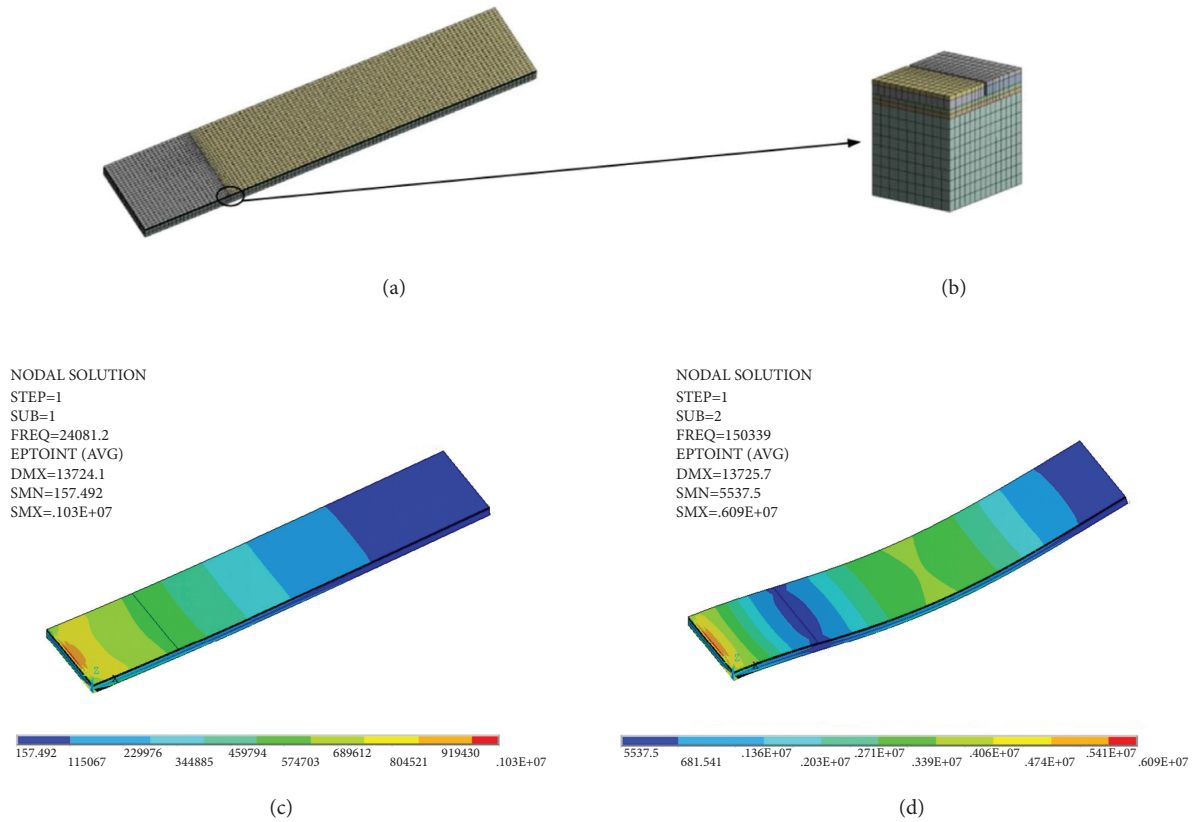

Figure 3: (a) The FEM mesh and (b) local view of the mesh at the strain node and the stress contours of the MCPA-S at the first (c) and (d) second mode.

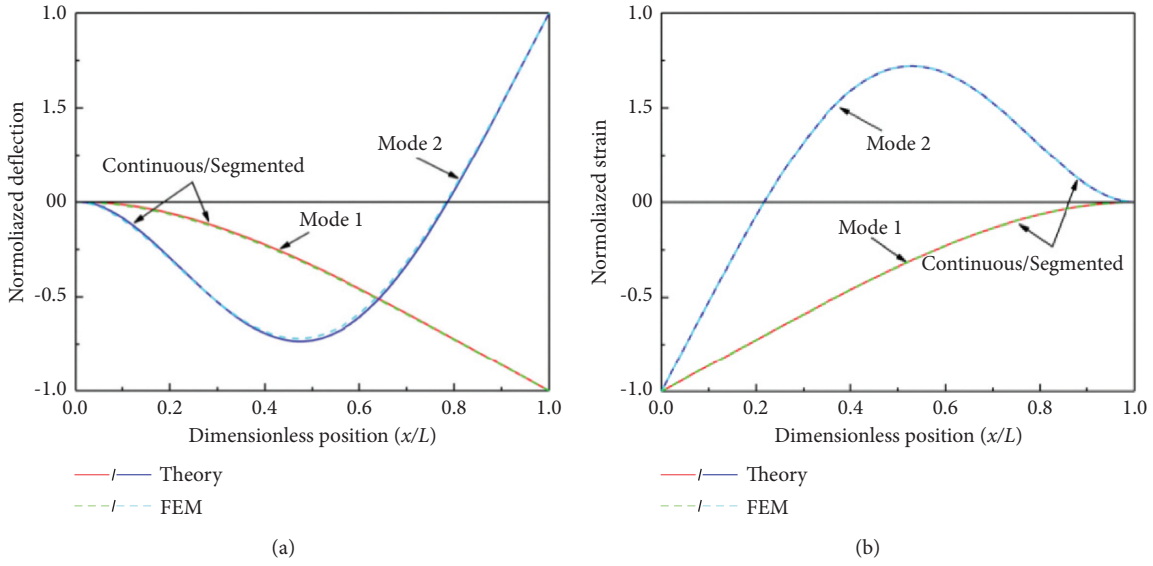

Figure 4: The (a) normalized deflection and (b) normalized strain distribution of the first two modes are simulated by MATLAB and FEM.

and thickness ratio between the substrate and the piezoelectric layer [23]. In order to investigate dependence of tip deflection on the thickness ratio between the substrate and piezoelectric layer, when $V = 1$ V, $h_e = 1\ \mu$m, $L = 1$ mm, $b = 200\ \mu$m, and $h_i = 1\ \mu$m, the h-tip deflection curves of MCPAs at the first two modes under different Young's modulus ratios were simulated and analyzed. They are shown in Figures 11 and 12. Two monotonously changing regions are formed on two sides of the maximum point of each curve. At the first and second modes, as h and r increase, the tip deflections increase/decrease in the upward/downward region. In particular, when the

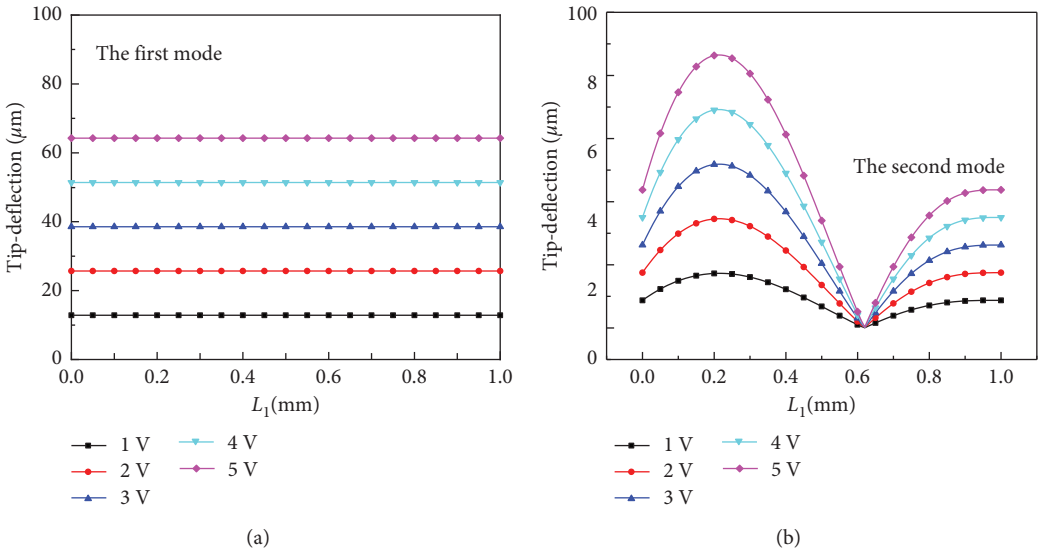

FIGURE 5: Effect of the segmented electrode length L_1 on tip deflection for the first (a) and second (b) modes under different applied voltages.

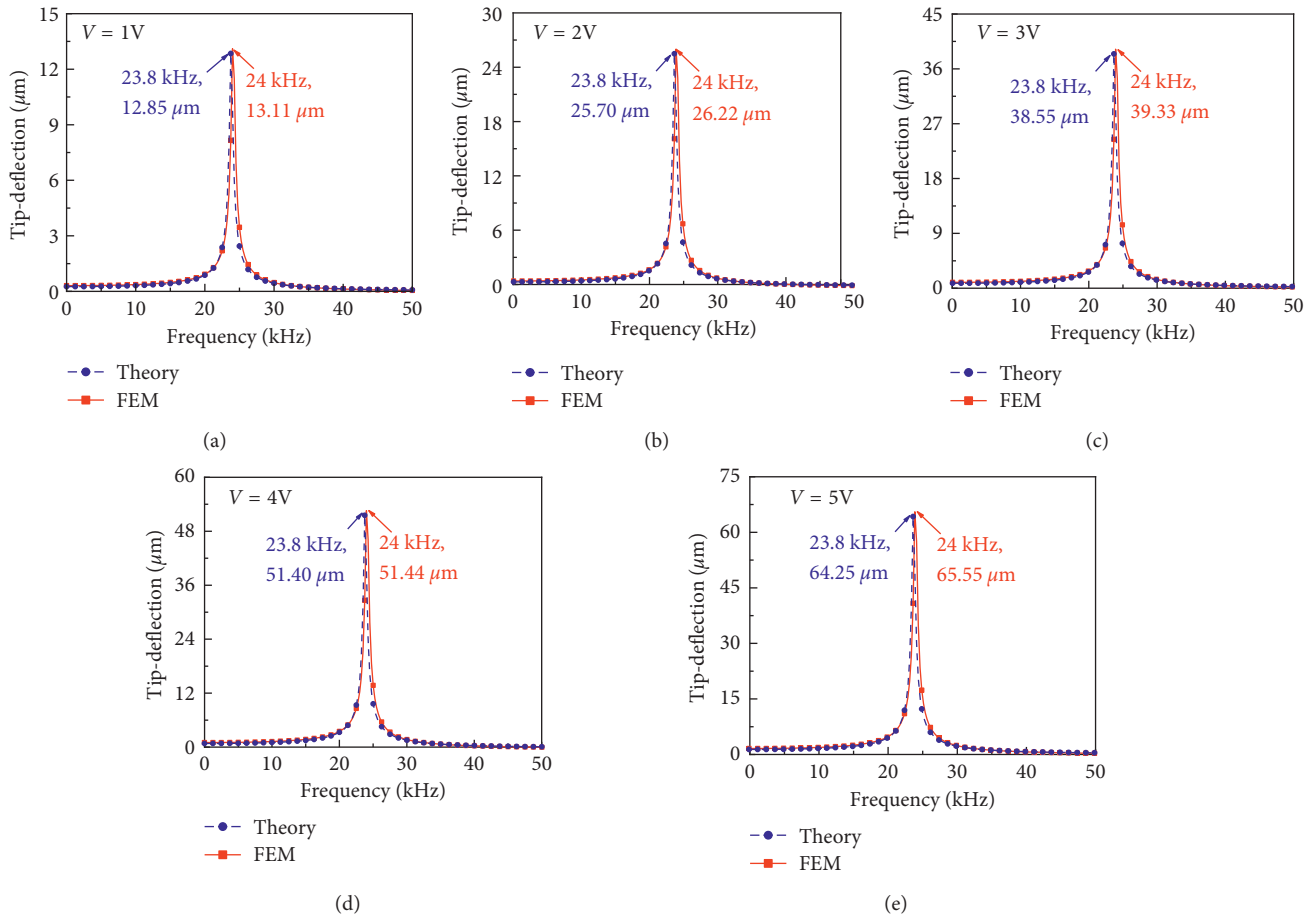

FIGURE 6: Tip deflection of the MCPA with the continuous and segmented electrodes for the first mode under different excitation frequencies at (a) $V = 1$ V, (b) $V = 2$ V, (c) $V = 3$ V, (d) $V = 4$ V, and (e) $V = 5$ V.

thickness ratio is constant ($h = 0$–2.3), the tip deflection increases with the increase of Young's modulus ($r = 0.8$–2.4). In the downward region, when h is constant ($h = 2.3$–5), the tip deflection decreases as r *increases* ($r = 0.8$–2.4). For MCPAs at the first and second mode, the change tendencies of tip deflections with h and r are

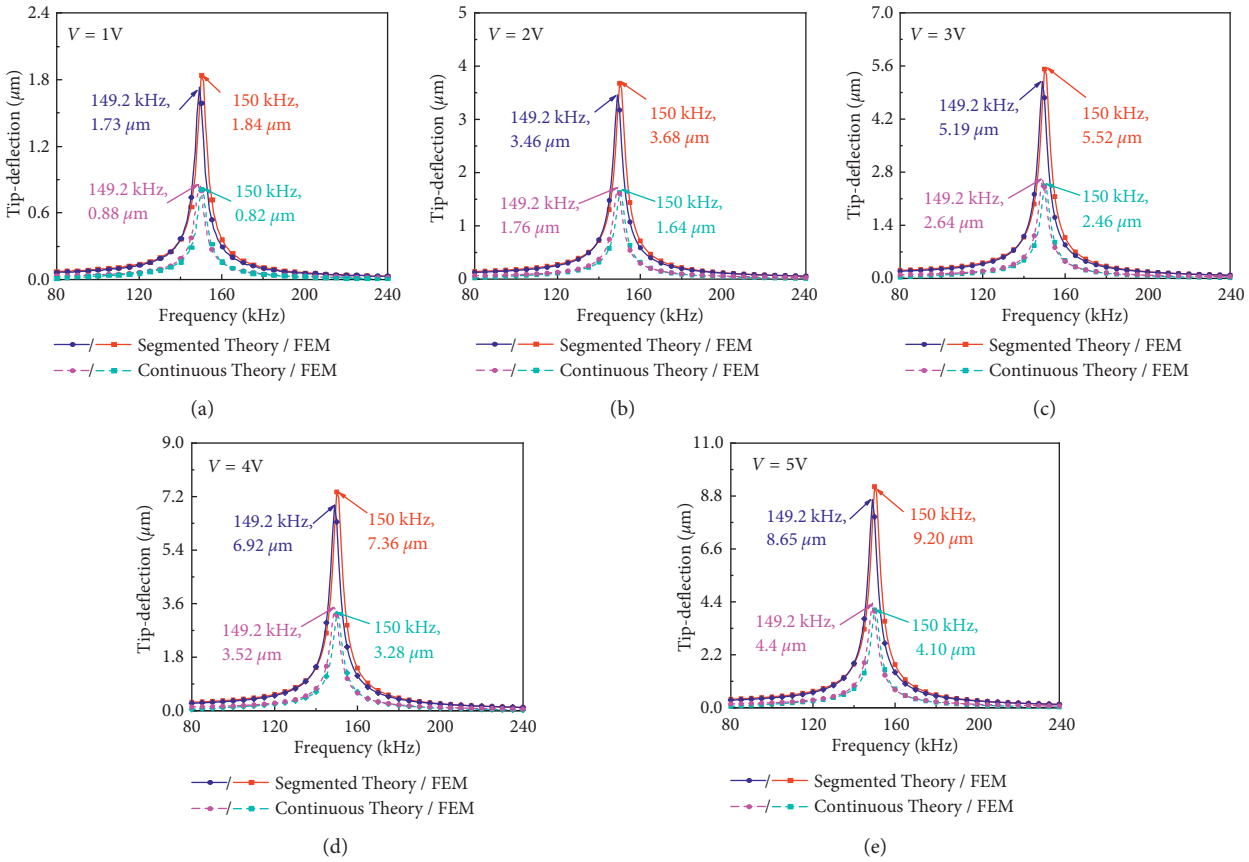

FIGURE 7: Harmonic response of the MCPA with the continuous and segmented electrodes for the second mode at (a) $V = 1$ V, (b) $V = 2$ V, (c) $V = 3$ V, (d) $V = 4$ V, and (e) $V = 5$ V.

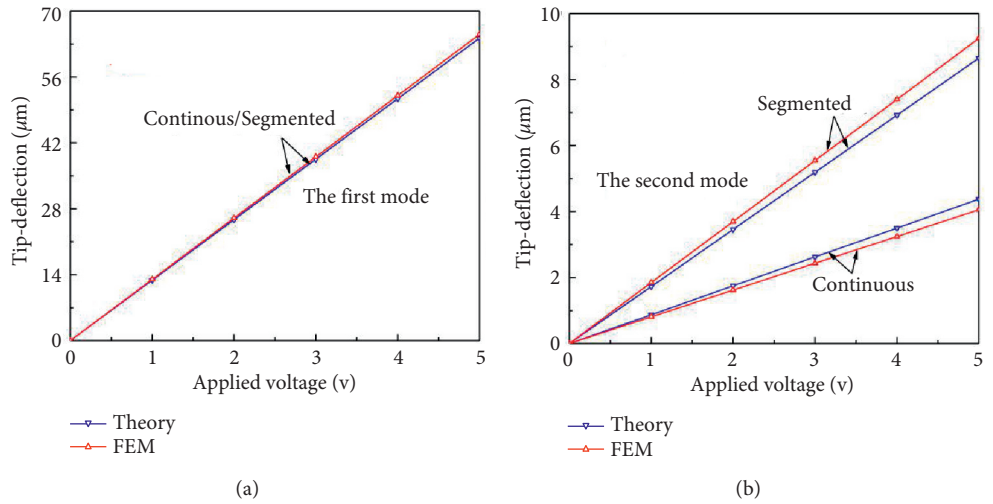

FIGURE 8: Dependence of tip deflection on applied voltage for the $L = 2$ mm beam at 24 kHz for the first mode (a) and at 150 kHz for the second mode (b).

similar through theoretical calculation and simulation. The tip deflection of MCPA-S is good with that of MCPA-C at the first mode. Obviously, with a smaller thickness ratio and a larger Young's modulus ratio, the curve in the upward region has a larger slope; i.e., in this region the tip deflection is more sensitive to the thickness change, which is beneficial for position sensing [24]. At the second mode, the slopes of the tip deflection curves for MCPA-S are significantly larger than that of the curves for MCPA-C, as shown in Figure 12. It indicates that the tip deflection of MCPA-S is more sensitive to change of thickness ratio and Young's modulus ratio. A smaller

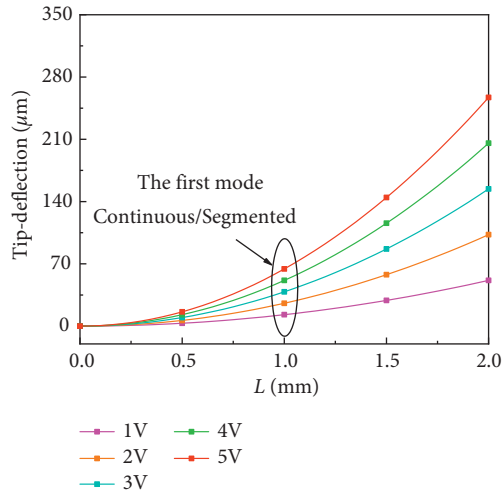

Figure 9: Theoretical and FEM simulation results of the dependence of tip deflection on beam length L at the first mode at $V = 1$–5 V.

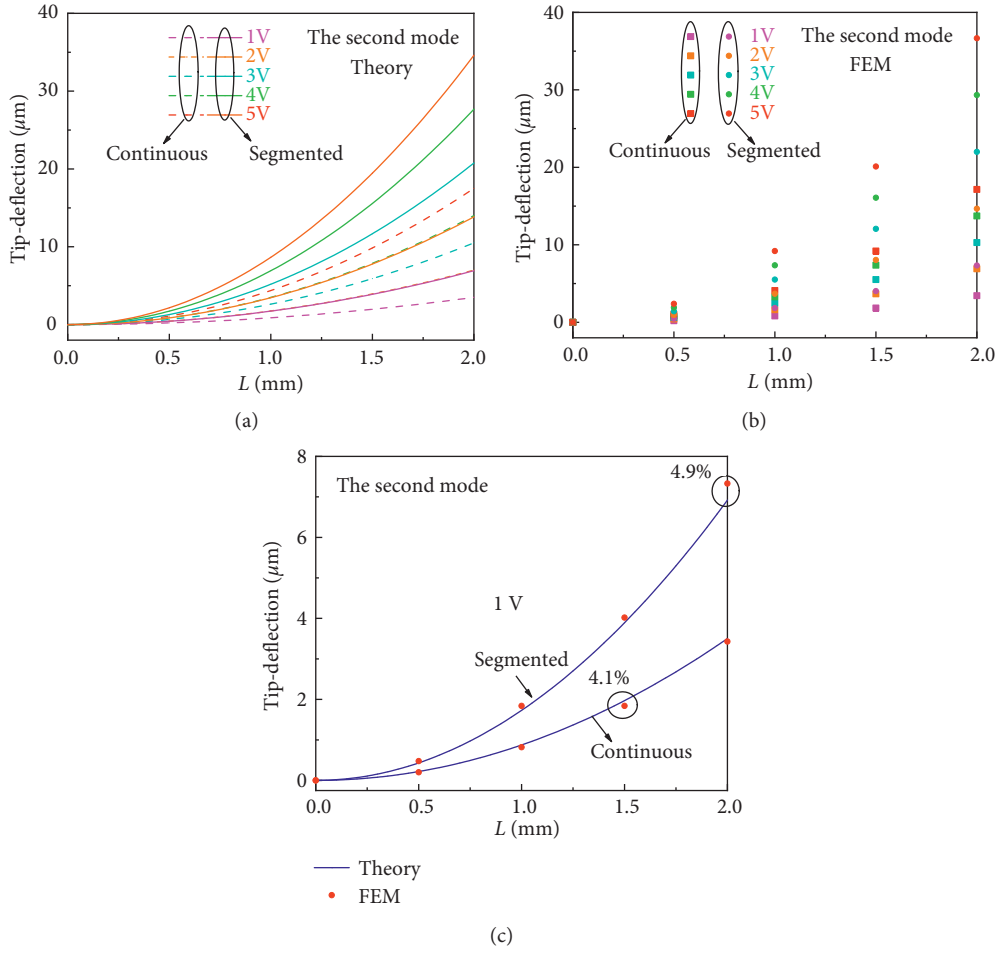

Figure 10: Theoretical (a) and FEM simulation (b) results of the dependence of tip deflection on beam length L at the second mode at $V = 1$–5 V and the theoretical and FEM simulation results at the second mode at $V = 1$ V (c).

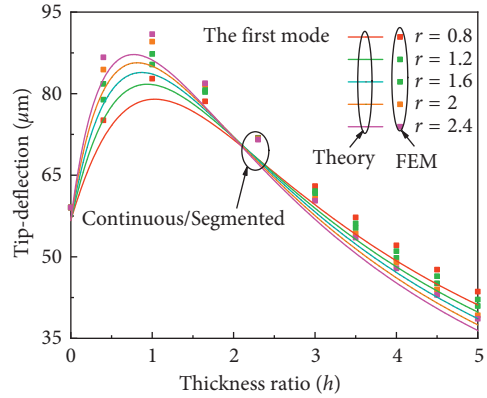

Figure 11: Theoretical and FE simulation results of the dependence of tip deflection on thickness ratio h at the first mode under different Young's modulus ratios r.

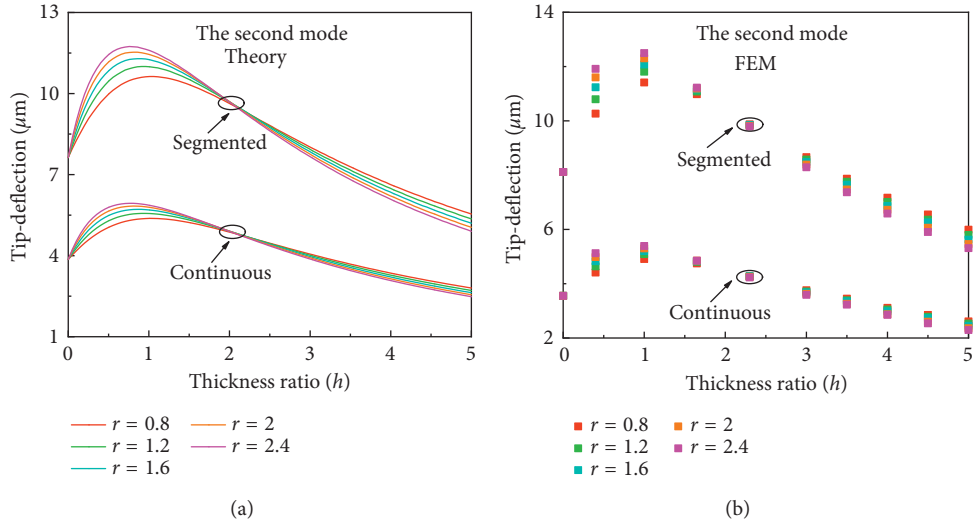

Figure 12: Theoretical (a) and FE simulation (b) results of the dependence of tip deflection on thickness ratio h at the second mode under different Young's modulus ratios r.

thickness ratio and larger Young's modulus ratio can achieve the maximum tip deflection, thereby improving the actuation performance of the MCPAs [25].

5. Conclusions

In summary, by considering the influence of the strain node on the beam at the high modes for the MCPAs, the optimal position of segmented electrode should be at the strain node. At the high modes of MCPAs, the tip deflections of the MCPA-S are larger than that of the MCPA-C, so the actuation performance can be improved. The strain node of the MCPA-S is 0.216 mm at the second mode, and the developed complete electromechanical coupling model can predict the tip deflection at the first two modes. The results of theoretical calculation and simulation indicate that the tip deflections of the MCPA-S are consistent with the MCPA-C at the first mode. The tip deflection of the MCPA-S is almost 100% larger than that of the MCPA-C at the second mode, and the tip deflection at the second mode has a maximum error of 6.8% between the theoretical and simulation results. Obviously, the theoretical values and the simulation results are relatively close, indicating that the proposed model can precisely estimate the tip deflection of MCPAs. The reliance of tip deflection on segmented electrode length, actuation frequency, voltage, beam length, substrate/piezoelectric thickness, and Young's modulus ratio are also discussed. The results indicate that, for the MCPA-S, under a certain beam length and high voltage pressure, a smaller thickness ratio and a larger Young's modulus ratio of the substrate/piezoelectric layer are beneficial to gain a larger tip deflection. The proposed model verifies the mechanism of MCPA-S to avoid the modal displacement offsets at the high modes, and predicted results can provide valuable guidance for optimizing the construction and efficiency of MCPAs.

Data Availability

The data that support the findings of this study are available from the corresponding author upon reasonable request.

Conflicts of Interest

The authors declare that there are no conflicts of interest with respect to the research, authorship, and/or publication of this article.

Acknowledgments

This work was supported by NNSF of China (11832016 and 51775471), Hunan Innovative Province Construction Special Major Landmark Innovation Demonstration Project, Changsha Zhuzhou Xiangtan Landmark Engineering Technology Project (2019XK2303 and 2020GK2014), Hefei General Machinery Research Institute Co., Ltd Project (2021ZKKF043), and Postgraduate Scientific Research Innovation Project of Hunan Province (CX20200642).

References

[1] Z. Xu, Z. Yang, K. Wang et al., "A bionic inertial piezoelectric actuator with improved frequency bandwidth," *Mechanical Systems and Signal Processing*, vol. 156, Article ID 107620, 2021.

[2] S. J. Behrouz, O. Rahmani, and S. A. Hosseini, "On nonlinear forced vibration of nano cantilever-based biosensor via couple stress theory," *Mechanical Systems and Signal Processing*, vol. 128, no. 3, pp. 19–36, 2019.

[3] Y. B. Chen and Z. Yan, "Investigation of pull-in behaviors of a nanoswitch tuned by piezoelectric and flexoelectric effects," *International Journal of Mechanical Sciences*, Article ID 107620, 2019.

[4] Q. F. Lü, X. F. Wang, K. Lu, and R. H. Huan, "Nonlinear stochastic optimal control using piezoelectric stack inertial actuator," *Shock and Vibration*, vol. 7, Article ID 5372045, 2020.

[5] R. F. Wang, L. Wang, J. M. Jin, B. T. Jia, Q. Zhang, and D. W. Wu, "Excitation method and electromechanical coupling dynamic model of a novel torsional piezoelectric actuator," *Mechanical Systems and Signal Processing*, vol. 154, Article ID 10758, 2021.

[6] V. Zhang, M. Faucher, D. Theron, C. Morelle, and L. Buchaillot, "Improved analytical modelling and finite element verification of stressed GaN microbeam resonators by piezoelectric actuation," *Journal of Micromechanics and Microengineering*, vol. 27, no. 9, Article ID 095001, 2017.

[7] Y. Zhang, T.-F. Lu, and S. Al-Sarawi, "Formulation of a simple distributed-parameter model of multilayer piezoelectric actuators," *Journal of Intelligent Material Systems and Structures*, vol. 27, no. 11, pp. 1485–1491, 2015.

[8] S. M. Afonin, "Structural-parametric model multilayer electromagnetoelastic actuator for nanomechatronics," *International Journal of Physics*, vol. 7, no. 2, pp. 50–57, 2019.

[9] P. Shivashankar and S. Gopalakrishnan, "Design, modeling and testing of d33-mode surface-bondable multilayer piezoelectric actuator," *Smart Materials and Structures*, vol. 29, pp. 0–16, 2020.

[10] S. Peng, X Zheng, J. Sun et al., "Modeling of a micro-cantilevered piezo-actuator considering the buffer layer and electrodes," *Journal of Micromechanics and Microengineering*, vol. 22, no. 6, pp. 561–566, 2012.

[11] A. Erturk and D. J. Inman, "A distributed parameter electromechanical model for cantilevered piezoelectric energy harvesters," *Journal of Vibration and Acoustics*, vol. 130, no. 4, Article ID 041002, 2008.

[12] A. Erturk and D. J. Inman, "On mechanical modeling of cantilevered piezoelectric vibration energy harvesters," *Journal of Intelligent Material Systems and Structures*, vol. 19, no. 11, pp. 1311–1325, 2008.

[13] R. Ly, M. Rguiti, S. D'Astorg, A. Hajjaji, C. Courtois, and A. Leriche, "Modeling and characterization of piezoelectric cantilever bending sensor for energy harvesting," *Sensors and Actuators A: Physical*, vol. 168, no. 1, pp. 95–100, 2011.

[14] A. Erturk, P. A. Tarazaga, and J. R. Farmer, "Effect of strain nodes and electrode configuration on piezoelectric energy harvesting from cantilevered beams," *Journal of Vibration and Acoustics*, vol. 131, no. 1, pp. 0110101–0110111, 2009.

[15] D. Zizys, R. Gaidys, R. Dauksevicius, V. Ostasevicius, and V. Daniulaitis, "Segmentation of a vibro-shock cantilever-type piezoelectric energy harvester operating in higher transverse vibration modes," *Sensors*, vol. 16, no. 1, pp. 1–14, 2016.

[16] S. Rafique and S. A. Shah, "Analysis over improving the power out of a piezoelectric energy harvester using segmented electrodes," *Mehran University Research Journal of Engineering and Technology*, vol. 36, no. 1, pp. 177–182, 2017.

[17] Y. Liu, X. Yang, W. Chen, and D. Xu, "A bonded-type piezoelectric actuator using the first and second bending vibration modes," *IEEE Transactions on Industrial Electronics*, vol. 63, no. 3, pp. 1676–1683, 2016.

[18] D. Bath and A. Salehian, "A novel 3D folded zigzag piezoelectric energy harvester; modeling and experiments," *Smart Materials and Structures*, vol. 28, Article ID 025011, 2019.

[19] J. S. Yang and H. Y. Fang, "Analysis of a rotating elastic beam with piezoelectric films as an angular rate sensor," *IEEE Transactions on Ultrasonics, Ferroelectrics, and Frequency Control*, vol. 49, no. 6, pp. 798–804, 2002.

[20] M. Brissaud, S. Ledren, and P. Gonnard, "Modelling of a cantilever non-symmetric piezoelectric bimorph," *Journal of Micromechanics and Microengineering*, vol. 13, no. 6, pp. 832–844, 2003.

[21] O. Bilgen, A. Erturk, and D. J. Inman, "Analytical and experimental characterization of macro-fiber composite actuated thin clamped-free unimorph benders," *Journal of Vibration and Acoustics*, vol. 132, no. 5, Article ID 051005, 2010.

[22] J. C. Doll, B. C. Petzold, B. Ninan, R. Mullapudi, and B. L. Pruitt, "Aluminum nitride on titanium for CMOS compatible piezoelectric transducers," *Journal of Micromechanics and Microengineering: Structures, Devices, and Systems*, vol. 20, no. 2, Article ID 25008, 2010.

[23] H. A. Tinoco and A. L. Serpa, "Voltage relations for debonding detection of piezoelectric sensors with segmented electrode," *Mechanical Systems and Signal Processing*, vol. 31, pp. 258–267, 2012.

[24] X. Cheng, X. L. Sun, Y. Liu et al., "Integrated optoelectronic position sensor for scanning micromirrors," *Sensors*, vol. 18, no. 4, Article ID 982, 2018.

[25] J. Shen, H. Wang, and S. Zheng, "Size-dependent pull-in analysis of a composite laminated micro-beam actuated by electrostatic and piezoelectric forces: generalized differential quadrature method," *International Journal of Mechanical Sciences*, vol. 135, pp. 353–361, 2018.

Hindawi
Shock and Vibration
Volume 2022, Article ID 8516971, 15 pages
https://doi.org/10.1155/2022/8516971

Research Article

Vibrations Evaluation of Functionally Graded Porous Beams in Thermal Surroundings by Generalized Differential Quadrature Method

Mahdi Khakpour,[1] Yousef Bazargan-Lari ,[1] Parham Zahedinejad,[2] and Mohammad- Javad Kazemzadeh-parsi[1]

[1]*Department of Mechanical Engineering, Shiraz Branch, Islamic Azad University, Shiraz, Iran*
[2]*Department of Mechanical and Energy Engineering, North Texas University, Denton, USA*

Correspondence should be addressed to Yousef Bazargan-Lari; bazarganlari@iaushiraz.ac.ir

Received 31 December 2021; Revised 22 January 2022; Accepted 26 January 2022; Published 23 February 2022

Academic Editor: Jiaqiang E

This study investigates how to obtain the natural frequency of functionally graded porous beams simply supported on an elastic substrate in thermal surroundings by the theory of third-order shear deformation. Temperature constantly changes in the beam thickness direction and step with the distribution of volume fraction power law of the ingredient has been affected on the material attributes. The distribution of uniform porosity at the pass phase is examined. To achieve the equations of governing, Hamilton's principle was carried out. To discretize these equations, the generalized differential quadrature method has been used. First, the approach's convergence is shown. Comparison with the results of other articles was performed for validation. Here, the impacts of numerous factors like index of power law, heat field type, temperature difference, slenderness ratio, and porosity coefficient and elastic substrate factors of a functionally graded porous beam on the natural frequencies were studied for simple boundary conditions. In addition to displaying these parameters' impact on the beam's thermomechanical evaluation, the conclusions also confirm the accuracy of the numerical technique used.

1. Introduction

Laminated composites are widely utilized in diverse equipment and structure, especially thermomechanical loads, due to their mechanical and thermal suitability. Due to the discontinuity of the material and many changes in the location of the layers, the stress concentration is created in this region, which will eventually lead to the separation of the layers from each other. In addition, many changes in the plastic in the boundary layer cause cracks and growth in the material [1]. Here, functionally graded (FG) materials are a suitable alternative to these materials. The development and expansion of FG materials in recent years have attracted the attention of engineers and researchers. These materials are used due to their multiple applications in the aerospace industry, aerospace engineering, and heat shields; therefore, it is necessary to have a detailed analysis of the dynamic behavior of FG materials. This need led to research on FG graded structures and beams and their free vibrations using various beam theories.

Several researchers like Alshorbagy et al. [2], Pradhan and Chakraverty [3], and Jin and Wang [4] have utilized the classical beam theory for FG beams with a large slenderness ratio. For FG beams with a medium slenderness ratio, this theory considers the deformation to be less than the actual value and ignores the transverse shear deformation effects and estimates the natural frequencies to be larger than the actual value. Timoshenko's theory overcomes this classical theory limitation in research by researchers, for example, Li [5], Wu et al. [6], and Katili et al. [7]. A correction parameter is required in this theory because of the zero shear stress violation at the top and bottom of the beam.

The high-order shear deformation theory is applied for better predicting the behavior of the beam and other structures. As mentioned before, this research was directed towards the analysis of the vibrations of FG beams using these theories. Wen and Zeng analyzed the vibrations of the beams utilizing the high-order finite element [8]. Şimşek evaluated the principle frequencies of FG beams making use of the theories of various high-order and different boundary conditions [9]. Kazemzadeh-Parsi et al. investigated free vibration of FG plates applying the theory of high-order shear deformation [10].

In engineering issues and applications, beams are usually supported along their length on a substrate and interact with that substrate. Studies about the impact of elastic substrate parameters on the free vibrations of isotropic beams were carried out by Chen [11] and Malekzadeh and Karami [12]. Additionally, several studies have been conducted by Aghazadeh et al. [13], Akbaş [14], and Mohseni and Shakouri [15] on the bending and free vibration of FG beams depending on one- and two-parametric elastic substrates and based on different theories and solution methods.

As we can see, there are few studies on the FG beams in thermal surroundings. Several studies were done with the thermal behavior approach for showing the advantages of FG materials. Vibrations of an FG beam located in a thermal surrounding were considered by Mahi et al. utilizing high-order shear deformation theory and analytical method [16]. An analytical technique was used by Trinh et al. for investigating the behaviors of buckling and vibration FG beams under thermal loads [17]. Thom and Kien studied the free vibrations of two-directional FG beams in thermal surroundings [18].

With rapid progression in structure technology, the latest achievements in the field of FG materials can be the porosity of these materials. Therefore, the effect of porosity is of special importance. These porous structures have interesting mechanical attributes like excessive rigidity related to very low determined weight. So far, some studies have been done about the vibrational behavior of this porous structure. Linear and nonlinear studies on vibrations of FG permeable beams depending on an elastic substrate were investigated by Wattanasakulpong and Ungbhakorn [19]. Ebrahimi and Jafari studied the temperature impact on vibrations of FG beams with two porosity types and Timoshenko's theory [20]. Ait Atmane et al. checked out the thickness and permeable effect on FG beam's mechanical responses on elastic substrates [21]. Heshmati and Daneshmand investigated the vibration analysis of nonuniform porous beams with porosity distribution in FG state [22]. Akbaş et al. presented a dynamic analysis of thick beams with porous layers in FG and viscoelastic support [23].

Often, numerical approximation methods have to be sought to solve vibration problems due to the complexity of the problems. Classical techniques such as finite element and finite difference methods are well developed and well known. These methods can provide very accurate results by using a large number of grid points; thus, they are computationally expensive. In a large number of cases, only a limited number of frequencies and mode shapes or a dynamic response at only a limited number of points needs to be found. Also, due to the difficulties with the shear deformation theory of third order, to solve the equations of governing, powerful techniques are required; therefore, the differential quadrature method (DQM) was used in this research. The DQM discretizes any derivative at a point by a weighted linear sum of functional values at its neighboring points. In the generalized differential quadrature method (GDQM), by considering the cosine division function, the number of nodes at the border increases, the calculations decrease, and the speed of convergence to the answers increases. For the free vibration analysis of FG panels, shells, plates, and beams, this method was applied by Bert and Malik [24], Farid et al. [25], Malekzadeh and Heydarpour [26], Ersoy et al. [27], Wang et al. [28], Wang et al. [29], Wang et al. [30], Al-Furjan et al. [31], Al-Furjan et al. [32], Shariati et al. [33], Huang et al. [34], Al-Furjan et al. [35], Huang et al. [34], and Al-Furjan et al. [36]. Zahedinejad investigated the free vibrations of FG beams depending on a two-parameter elastic foundation in a temperature-rise environment with DQM [37].

The novelty of this paper is the simultaneous FG porous beam analysis using the theory of third-order shear deformation on the elastic substrate in the temperature-dependent environment by GDQM. The motivation of this research is a thermomechanical analysis of thick FG porous structures under different thermal loads and also to evaluate the accuracy of GDQM. For example, hot section blades of gas turbine and plasma-facing components in divertor of a nuclear reactor are exposed to thermal loads. In this research, analysis of the free vibration FG porous beams with uniform porosity distribution is studied according to the theory of third-order shear deformation. The porosity distribution is considered through the beam thickness direction. Additionally, the effect of thermal loads and elastic substrate impact was considered on the frequency parameters. Hamilton's principle is used to obtain boundary conditions and equations of motion, and the GDQM was used to solve them. The materials attributes are a function of temperature and differ over the beam thickness direction with the distribution of power law. The behavioral convergence method was applied and the accuracy of the consequences was investigated with other solutions due to the articles. This research considered the geometric parameters impact, various temperature distributions and elastic substrate stiffness coefficients, and porosity volume fraction, according to FG porous beam natural frequencies.

2. Kinematics

Figure 1 showed uniform porosity of FG porous beam, width b, length L, and height h depending on an elastic substrate. The displacement field is selected through the beam theories of third-order shear deformation with the following assumptions: (1) Shear components and bending are components of the transverse and axial displacements. (2) The bending component of the classical beam theory and the axial displacement in this theory are similar. (3) Shear axial displacement and the third-degree variation of shear strain

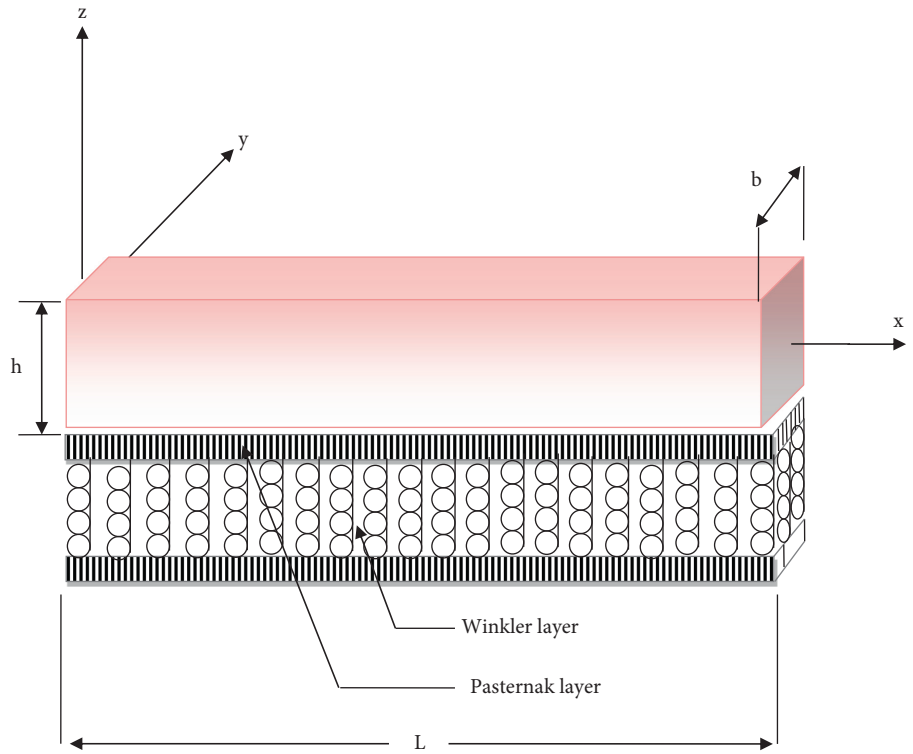

Figure 1: FG porous beam schematic depending on an elastic substrate.

in the beam depth direction are different and the shear stress in upper and lower beam planes is zero.

According to these assumptions [38], the field of the displacement is

$$\begin{aligned} u_1(x,z,t) &= u(x,t) - z\frac{\partial w_b}{\partial x} - f(z)\frac{\partial w_s}{\partial x}, \\ u_2(x,z,t) &= 0, \\ u_3(x,z,t) &= w_b(x,t) + w_s(x,t), \end{aligned} \tag{1}$$

where $u_i (i = 1, 2, 3)$, w_s, and w_b represent the axial displacement, shear, and bending components of horizontal displacement on the beam midpoint. The shear stress and the horizontal shear strain distribution at the beam depth satisfy the boundary conditions of stress-free up and low beam planes represented by the shape function $f(z)$. According to Reddy's shear deformation theory [39], this function can be shown as

$$f(z) = \frac{4z^3}{3h^2}. \tag{2}$$

The present field of displacement and Reddy's theory are different from each other. Two components of the horizontal displacement are the displacements due to bending and shear. Strains can be defined as

$$\begin{aligned} \varepsilon_{xx} &= \frac{\partial u}{\partial x} - z\frac{\partial^2 w_b}{\partial x^2} - f(z)\frac{\partial^2 w_s}{\partial x^2}, \\ \gamma_{xz} &= \left(1 - \frac{df(z)}{dz}\right)\frac{\partial w_s}{\partial x} \equiv g(z)\frac{\partial w_s}{\partial x}. \end{aligned} \tag{3}$$

3. FG Porous Materials Properties

The beam material composition changes from the metal-rich lowest surface $(z = -h/2)$ to the ceramic-rich upper surface $(z = h/2)$, following a simple power law relating to the volume fractions of the constituents; that is,

$$\begin{aligned} V_c &= \left(\frac{1}{2} + \frac{z}{h}\right)^p, \\ V_m &= 1 - V_c, \end{aligned} \tag{4}$$

where $-h/2 \le z \le h/2$ and p is the material index of power law, which is greater than or equal to zero. The case where p is equal to zero shows a completely ceramic beam, while the approaching infinity shows an almost fully metallic beam. Parameters V_m and V_c denote the fractions of the metal and ceramic volume. The main attributes P_{eff}, such as Poisson's ratio υ, Young's modulus E, and thermal expansion coefficient, are specified as

$$P_{eff}(z,T) = \left(P_c(T) - P_m(T)\right)V_c + P_m(T) - \left(P_c(T) + P_m(T)\right)\frac{a}{2}, \tag{5}$$

where a is the porosity coefficient.

FG materials are often applied in high-temperature surroundings with unavoidable changes in material attributes. Here position and temperature are important factors in the FG beam material attributes, so accurately predicting the structural response should be considered in accordance with the temperature. Material properties are stated as environmental nonlinear function at temperature $T(K)$ as

$$P(T) = P_0\left(P_{-1}T^{-1} + 1 + P_1T + P_2T^2 + P_3T^3\right), \tag{6}$$

whereas $T(z) = T_0 + \Delta T(z)$, $T_0 = 300K$, and P_0, P_{-1}, P_1, P_2, and P_3 are unique temperature-dependent coefficients for the materials of constituent. It is assumed that, in the thickness direction, the temperature varies with upper and lower surfaces temperatures being known. Due to this case, to calculate the temperature function along the thickness direction, the following steady-state heat transfer equation can be solved:

$$-\frac{d}{dz}\left[k\frac{dT}{dz}\right] = 0. \tag{7}$$

Imposing the boundary conditions solved this equation: $T = T_c$ in $z = h/2$ and $T = T_m$ in $z = -h/2$.

The equation solution in [40] is as follows:

$$T(z) = T_c - \frac{T_c - T_m}{\int_{-h/2}^{h/2} dz/k(z,T)}\int_{-h/2}^{z}\frac{dz}{k(z,T)}, \tag{8}$$

where $k(z,T)$ is thermal conductivity.

4. Equations of Governing

Hamilton's principle is determined for the FG beam equations of the motion.

$$\int_{t_1}^{t_2}\left(\delta K - \delta U - \delta V_{ef}\right)dt = 0, \tag{9}$$

where t, t_1, and t_2, respectively, are the time and the initial and end times; δK, δU, and δV_{ef} are the kinetic and the total strain energy variations and the potential energy of the elastic substrate variations. The total beam strain energy can be shown as

$$U = U_d + U_T, \tag{10}$$

where U_d and U_T are, respectively, the strain energy because of mechanical stresses and the initial stresses of the strain energy as a result of temperature rise. These strains are represented by the following equations [41]:

$$U_d = \frac{1}{2}\int_0^L\int_A\left(\sigma_{xx}\varepsilon_{xx} + \sigma_{xz}\gamma_{xz}\right)dA\mathrm{d}x,$$

$$\sigma_{xx} = E(z,T)\varepsilon_{xx}, \tag{11}$$

$$\sigma_{xz} = \frac{E(z,T)}{2(1+\upsilon(z,T))},$$

$$U_T = \frac{1}{2}\int_0^L\int_A\left(\sigma_{xx}^T d_{xx}\right)dA\mathrm{d}x, \tag{12}$$

$$d_{xx} = \left(\frac{\partial u_1}{\partial x}\right)^2 + \left(\frac{\partial u_3}{\partial x}\right)^2. \tag{13}$$

The thermal stress in (12) is presented by

$$\sigma_{xx}^T = -\frac{E(z,T)\alpha(z,T)}{1-\upsilon(z,T)}\Delta T(z). \tag{14}$$

The potential energy and the kinetic energy in the elastic substrate can be given by

$$K = \frac{1}{2}\int_0^L\int_A\rho(z)\left(\dot{u}_1^2 + \dot{u}_3^2\right)dA\mathrm{d}x, \tag{15}$$

$$V_{ef} = \frac{1}{2}\int_0^L\int_0^b\left[k_w u_3^2 + k_p\left(\frac{\partial u_3}{\partial x}\right)^2\right]\Big|_{z=0}dy\ dx, \tag{16}$$

where the Winkler and shearing-layer elastic coefficients of the substrate are k_w and k_p depending on the soil and underlayer properties, like elastic modulus, Poisson's soil ratio, and the soil length. By replacing equations (10)–(16) in (9) and integrating by components according to space and time, the motion equations of FG beam are considered as

$$\delta u:\ I_0\ddot{u} - I_1\frac{\partial\ddot{w}_b}{\partial x} - J_1\frac{\partial\ddot{w}_s}{\partial x} = \frac{\partial N}{\partial x} + \frac{\partial N^T}{\partial x}, \tag{17}$$

$$\delta w_b:\ I_0\left(\ddot{w}_b + \ddot{w}_s\right) + I_1\frac{\partial\ddot{u}}{\partial x} - I_2\frac{\partial^2\ddot{w}_b}{\partial x^2} - J_2\frac{\partial^2\ddot{w}_s}{\partial x^2} = \frac{\partial^2 M_b}{\partial x^2} + \frac{\partial^2 M_b^T}{\partial x^2} + \left(A^T + k_p\right)\left(\frac{\partial^2 w_b}{\partial x^2} + \frac{\partial^2 w_s}{\partial x^2}\right) - k_w\left(w_b + w_s\right), \tag{18}$$

$$\delta w_s:\ I_0\left(\ddot{w}_b + \ddot{w}_s\right) + J_1\frac{\partial\ddot{u}}{\partial x} - J_2\frac{\partial^2\ddot{w}_b}{\partial x^2} - K_2\frac{\partial^2\ddot{w}_s}{\partial x^2} = \frac{\partial^2 M_s}{\partial x^2} + \frac{\partial^2 M_s^T}{\partial x^2} + \left(A^T + k_p\right)\left(\frac{\partial^2 w_b}{\partial x^2} + \frac{\partial^2 w_s}{\partial x^2}\right) + \frac{\partial Q}{\partial x} - k_w\left(w_b + w_s\right), \tag{19}$$

Where N, N^T, M_b, M_b^T, M_s, M_s^T, and Q parameters are defined as

$$N = A\frac{\partial u}{\partial x} - B\frac{\partial^2 w_b}{\partial x^2} - B_s\frac{\partial^2 w_s}{\partial x^2}, \tag{20}$$

$$N^T = A^T\frac{\partial u}{\partial x} - B^T\frac{\partial^2 w_b}{\partial x^2} - B_s^T\frac{\partial^2 w_s}{\partial x^2}, \tag{21}$$

$$M_b = B\frac{\partial u}{\partial x} - D\frac{\partial^2 w_b}{\partial x^2} - D_s\frac{\partial^2 w_s}{\partial x^2}, \tag{22}$$

$$M_b^T = B^T\frac{\partial u}{\partial x} - D^T\frac{\partial^2 w_b}{\partial x^2} - D_s^T\frac{\partial^2 w_s}{\partial x^2} \tag{23}$$

$$M_s = B_s\frac{\partial u}{\partial x} - D_s\frac{\partial^2 w_b}{\partial x^2} - H_s\frac{\partial^2 w_s}{\partial x^2}, \tag{24}$$

$$M_s^T = B_s^T\frac{\partial u}{\partial x} - D_s^T\frac{\partial^2 w_b}{\partial x^2} - H_s^T\frac{\partial^2 w_s}{\partial x^2}, \tag{25}$$

$$Q = A_s\frac{\partial w_s}{\partial x}. \tag{26}$$

The estimations of coefficients are as follows:

$$\begin{aligned}
\left(I_0, I_1, J_1, I_2, J_2, K_2\right) &= \int_A \rho(z)\left(1, z, f(z), z^2, zf(z), f^2(z)\right)dA,\\
\left(A, B, B_s, D, D_s, H_s\right) &= \int_A E(z,T)\left(1, z, f(z), z^2, zf(z), f^2(z)\right)dA,\\
A_s &= \int_A \frac{E(z,T)}{2(1+\upsilon(z,T))}g^2(z)dA,\\
\left(A^T, B^T, B_s^T, D^T, D_s^T, H_s^T\right) &= \int_A \sigma_{xx}^T\left(1, z, f(z), z^2, zf(z), f^2(z)\right)dA.
\end{aligned} \tag{27}$$

The motion equations of the substation parts are estimated by replacing relations (20)–(26) with (17)–(19) as follows:

$$\delta u:\ I_0\ddot{u} - I_1\frac{\partial \ddot{w}_b}{\partial x} - J_1\frac{\partial \ddot{w}_s}{\partial x} = \left(A + A^T\right)\frac{\partial^2 u}{\partial x^2} - \left(B + B^T\right)\frac{\partial^3 w_b}{\partial x^3} - \left(B_s + B_s^T\right)\frac{\partial^3 w_s}{\partial x^3}. \tag{28}$$

$$\begin{aligned}
\delta w_b:\ I_0\left(\ddot{w}_b + \ddot{w}_s\right) + I_1\frac{\partial \ddot{u}}{\partial x} - I_2\frac{\partial^2 \ddot{w}_b}{\partial x^2} - J_2\frac{\partial^2 \ddot{w}_s}{\partial x^2} &= \left(B + B^T\right)\frac{\partial^3 u}{\partial x^3} - \left(D + D^T\right)\frac{\partial^4 w_b}{\partial x^4} - \left(D_s + D_s^T\right)\frac{\partial^4 w_s}{\partial x^4} + \left(A^T + k_p\right)\left(\frac{\partial^2 w_b}{\partial x^2} + \frac{\partial^2 w_s}{\partial x^2}\right)\\
&\quad - k_w\left(w_b + w_s\right),
\end{aligned} \tag{29}$$

$$\delta w_s: I_0\left(\ddot{w}_b+\ddot{w}_s\right)+J_1\frac{\partial\ddot{u}}{\partial x}-J_2\frac{\partial^2\ddot{w}_b}{\partial x^2}-K_2\frac{\partial^2\ddot{w}_s}{\partial x^2}=\left(B_s+B_s^T\right)\frac{\partial^3 u}{\partial x^3}-\left(D_s+D_s^T\right)\frac{\partial^4 w_b}{\partial x^4}-\left(H_s+H_s^T\right)\frac{\partial^4 w_s}{\partial x^4}+\left(A^T+k_p\right)\left(\frac{\partial^2 w_b}{\partial x^2}+\frac{\partial^2 w_s}{\partial x^2}\right)+A_s\frac{\partial^2 w_s}{\partial x^2}-k_w\left(w_b+w_s\right). \tag{30}$$

5. Conditions of Boundary

These parameters are determined due to the FG beam conditions of the boundary:

$$\left(N+N^T\right)=0 \text{ or } u=0, \tag{31}$$

$$\begin{aligned} Q_b \equiv{}& \frac{\partial M_b}{\partial x}+\frac{\partial M_b^T}{\partial x}+A^T\left(\frac{\partial w_b}{\partial x}+\frac{\partial w_s}{\partial x}\right)-I_1\ddot{u}+I_2\frac{\partial\ddot{w}_b}{\partial x}\\ &+J_2\frac{\partial\ddot{w}_s}{\partial x}=0 \text{ or } w_b\\ ={}&0, \end{aligned} \tag{32}$$

$$\begin{aligned} Q_s \equiv{}& \frac{\partial M_s}{\partial x}+\frac{\partial M_s^T}{\partial x}+A^T\left(\frac{\partial w_b}{\partial x}+\frac{\partial w_s}{\partial x}\right)+Q-J_1\ddot{u}+J_2\frac{\partial\ddot{w}_b}{\partial x}\\ &+K_2\frac{\partial\ddot{w}_s}{\partial x}=0 \text{ or } w_s\\ ={}&0, \end{aligned} \tag{33}$$

$$\begin{aligned} \left(M_b+M_b^T\right)=0 \text{ or } \frac{\partial w_b}{\partial x}\\ =0, \end{aligned} \tag{34}$$

$$\begin{aligned} \left(M_s+M_s^T\right)=0 \text{ or } \frac{\partial w_s}{\partial x}\\ =0. \end{aligned} \tag{35}$$

$x=0$ and $x=L$ are different conditions which can be obtained by combining the conditions in (30)–(35). The simple soft support conditions of boundary in this research are examined as follows:

$$\begin{gathered}\left(A+A^{T}\right)\frac{\partial u}{\partial x}-\left(B+B^{T}\right)\frac{\partial^{2} w_{b}}{\partial x^{2}}-\left(B_{s}+B_{s}^{T}\right)\frac{\partial^{2} w_{s}}{\partial x^{2}}=0 \text{ or } \left(N+N^{T}\right)=0,\\ \left(B+B^{T}\right)\frac{\partial u}{\partial x}-\left(D+D^{T}\right)\frac{\partial^{2} w_{b}}{\partial x^{2}}-\left(D_{s}+D_{s}^{T}\right)\frac{\partial^{2} w_{s}}{\partial x^{2}}=0 \text{ or } \left(M_{b}+M_{b}^{T}\right)=0,\\ \left(B_{s}+B_{s}^{T}\right)\frac{\partial u}{\partial x}-\left(D_{s}+D_{s}^{T}\right)\frac{\partial^{2} w_{b}}{\partial x^{2}}-\left(H_{s}+H_{s}^{T}\right)\frac{\partial^{2} w_{s}}{\partial x^{2}}=0 \text{ or } \left(M_{s}+M_{s}^{T}\right)=0,\\ w_{b}=0, w_{s}=0.\end{gathered} \tag{36}$$

For substitution components, these answers apply to analyze free vibrations:

$$\begin{aligned} u(x,t)&=\overline{u}(x)e^{I\omega t},\\ w_{b}(x,t)&=\overline{w}_{b}(x)e^{I\omega t},\\ w_{s}(x,t)&=\overline{w}_{s}(x)e^{I\omega t},\end{aligned} \tag{37}$$

where $I=\sqrt{-1}$ and ω is natural frequency.

6. Differential Quadrature Separation

The DQ separation rules based on Gauss-Lobatto-Chebyshev sampling points known as Generalized Differential Quadrature (GDQ) are attained to transfer the constitutive equations and related boundary conditions into algebraic equations [24].

$$x_{i}=\frac{1}{2}\left\{1-\cos\left(\frac{i-1}{N_{x}-1}\right)\pi\right\},\quad i=1,2,\ldots,N_{x}-1. \tag{38}$$

The nth-order partial derivative of f(x) with respect to x at the discrete point x_i is

$$f_{x}^{(n)}(x_{i})=\sum_{i=1}^{N_{x}}C_{ij}^{(n)}f(x_{i}), \tag{39}$$

where N_x is the number of the differential quadrature separation items in the direction of length. $C_{ij}^{(n)}$ are weighting coefficients associated with the nth-order partial derivative of $f(x)$ with respect to x at the discrete point x_i. The first one is

$$C_{ij}^{1}=\frac{M(x_{i})}{\left(x_{i}-x_{j}\right)M\left(x_{j}\right)}, \tag{40}$$

where

$$M(x_{i})=\prod_{j=1\ j\neq i}^{N_{x}}\left(x_{i}-x_{j}\right). \tag{41}$$

The weighting coefficients of higher-order derivatives can be obtained through the following recurrence relation:

$$\begin{aligned} C_{ij}^{(n)}&=n\left(C_{ij}^{(n-1)}C_{ij}^{1}-\frac{C_{ij}^{(n-1)}}{\left(x_{i}-x_{j}\right)}\right)\quad i,j=1,2,\ldots N_{x},\\ C_{ij}^{(n)}&=-\sum_{j=1\,j\neq i}^{N_{x}}C_{ij}^{n}\quad n=1,2,\ldots N_{x}-1.\end{aligned} \tag{42}$$

Based on this method, the partial derivatives of a function can be given as

$$\begin{aligned} \frac{\partial f(x,t)}{\partial x}|_{x=x_{i}}&=\sum_{j=1}^{N_{x}}A_{ij}f\left(x_{j},t\right)i=1,2,\ldots,N_{x},\\ \frac{\partial^{2} f(x,t)}{\partial x^{2}}|_{x=x_{i}}&=\sum_{j=1}^{N_{x}}B_{ij}f\left(x_{j},t\right),\\ \frac{\partial^{3} f(x,t)}{\partial x^{3}}|_{x=x_{i}}&=\sum_{j=1}^{N_{x}}C_{ij}f\left(x_{j},t\right),\\ \frac{\partial^{4} f(x,t)}{\partial x^{4}}|_{x=x_{i}}&=\sum_{j=1}^{N_{x}}D_{ij}f\left(x_{j},t\right),\end{aligned} \tag{43}$$

where A_{ij}, B_{ij}, C_{ij}, and D_{ij} are the first-, second-, third-, and fourth-order weighting coefficients of the DQM, respectively.

The conditions of boundary and the motion equations are converted to DQM as the equations related algebra. The

differential equations of governing and conditions of boundary are considered as separation use for derivatives (24) and relations (28)–(30) and (36) and DQM as follows:

$$\begin{aligned}
&\left(A + A^T\right)\sum_{j=1}^{N_x} B_{ij}\overline{u}_j - \left(B + B^T\right)\sum_{j=1}^{N_x} C_{ij}\overline{w}_{bj} - \left(B_s + B_s^T\right)\sum_{j=1}^{N_x} C_{ij}\overline{w}_{sj} + \omega^2\left(I_0\overline{u}_i - I_1\sum_{j=1}^{N_x} A_{ij}\overline{w}_{bj} - J_1\sum_{j=1}^{N_x} A_{ij}\overline{w}_{sj}\right) = 0,\\
&\left(B + B^T\right)\sum_{j=1}^{N_x} C_{ij}\overline{u}_j - \left(D + D^T\right)\sum_{j=1}^{N_x} D_{ij}\overline{w}_{bj} - \left(D_s + D_s^T\right)\sum_{j=1}^{N_x} D_{ij}\overline{w}_{sj} + \left(A^T + k_g\right)\left(\sum_{j=1}^{N_x} B_{ij}\left(\overline{w}_{bj} + \overline{w}_{sj}\right)\right) - k_w\left(\overline{w}_{bi} + \overline{w}_{si}\right)\\
&\quad + \omega^2\left(I_0\left(\overline{w}_{bi} + \overline{w}_{si}\right) + I_1\sum_{j=1}^{N_x} A_{ij}\overline{u}_j - I_2\sum_{j=1}^{N_x} B_{ij}\overline{w}_{bj} - J_2\sum_{j=1}^{N_x} B_{ij}\overline{w}_{sj}\right) = 0,\\
&\left(B_s + B_s^T\right)\sum_{j=1}^{N_x} C_{ij}\overline{u}_j - \left(D_s + D_s^T\right)\sum_{j=1}^{N_x} D_{ij}\overline{w}_{bj} - \left(H_s + H_s^T\right)\sum_{j=1}^{N_x} D_{ij}\overline{w}_{sj} + \left(A^T + k_g\right)\left(\sum_{j=1}^{N_x} B_{ij}\left(\overline{w}_{bj} + \overline{w}_{sj}\right)\right) - k_w\left(\overline{w}_{bi} + \overline{w}_{si}\right)\\
&\quad + A_s\sum_{j=1}^{N_x} B_{ij}\overline{w}_{sj} + \omega^2\left(I_0\left(\overline{w}_{bi} + \overline{w}_{si}\right) + J_1\sum_{j=1}^{N_x} A_{ij}\overline{u}_j - J_2\sum_{j=1}^{N_x} B_{ij}\overline{w}_{bj} - K_2\sum_{j=1}^{N_x} B_{ij}\overline{w}_{sj}\right) = 0,
\end{aligned} \tag{44}$$

$$\begin{aligned}
&\left(A + A^T\right)\sum_{j=1}^{N_x} A_{ij}\overline{u}_j - \left(B + B^T\right)\sum_{j=1}^{N_x} B_{ij}\overline{w}_{bj} - \left(B_s + B_s^T\right)\sum_{j=1}^{N_x} B_{ij}\overline{w}_{sj} = 0,\\
&\left(B + B^T\right)\sum_{j=1}^{N_x} A_{ij}\overline{u}_j - \left(D + D^T\right)\sum_{j=1}^{N_x} B_{ij}\overline{w}_{bj} - \left(D_s + D_s^T\right)\sum_{j=1}^{N_x} B_{ij}\overline{w}_{sj} = 0,\\
&\left(B_s + B_s^T\right)\sum_{j=1}^{N_x} A_{ij}\overline{u}_j - \left(D_s + D_s^T\right)\sum_{j=1}^{N_x} B_{ij}\overline{w}_{bj} - \left(H_s + H_s^T\right)\sum_{j=1}^{N_x} B_{ij}\overline{w}_{sj} = 0,\\
&\overline{w}_{bi} = 0, \overline{w}_{si} = 0.
\end{aligned} \tag{45}$$

Boundary conditions based on this method are written in relation (45).

The boundary degrees and domain of freedom separate parts of the freedom degrees for obtaining the eigenvalue system of equations as

$$\{d\} = \left\{\begin{array}{c}\{\overline{u}\},\\ \{\overline{w}_b\},\\ \{\overline{w}_s\},\end{array}\right\}_{\text{domain}}, \quad \{b\} = \left\{\begin{array}{c}\{\overline{u}\},\\ \{\overline{w}_b\},\\ \{\overline{w}_s\},\end{array}\right\}_{\text{boundary}}. \tag{46}$$

In the matrix form, using (46), the motion equations separated form can be arranged differently as

$$[S_{db}]\{b\} + [S_{d\,d}]\{d\} - \omega_i^2[M]\{d\} = 0. \tag{47}$$

$[M]$ is the mass matrix where $[S_{db}]$ and $[S_{d\,d}]$ are the rigid matrices. Similarly, the separated form condition of the boundary is

$$[S_{bb}]\{b\} + [S_{b\,d}]\{d\} = 0. \tag{48}$$

The rigid matrices are $[S_{bb}]$ and $[S_{b\,d}]$. For removing the freedom boundary degree $\{b\}$ from (47), (48) is applied resulting in

$$\left([S] - \omega_i^2[M]\right)\{d\} = 0, \tag{49}$$

where $[S] = [S_{d\,d}] - [S_{db}][S_{bb}]^{-1}[S_{b\,d}]$. To find the natural frequencies, the former eigenvalue equation can be solved.

7. Results and Discussion

First, the method convergence is considered for simply supported conditions of boundary. The conclusion accuracy is confirmed by comparing other available solutions. A beam containing aluminum (Al) and alumina (Al_2O_3) is considered for temperature-independent states. Table 1 shows the FG material characteristics.

A beam concluding stainless steel (SUS304) and silicon nitride (Si_3N_4) is estimated for the temperature-dependent cases. In Table 2, the temperature-dependent material attributes for some metals and ceramics are listed, according to the data given in [40].

The natural frequency of nondimensional (λ_n) are explained as

$$\lambda_n = \frac{\omega_n L^2}{h}\sqrt{\frac{\rho_m}{E_m}}. \tag{50}$$

Table 1: Properties of alumina and aluminum.

Properties	Metal (Al)	Ceramic (Al_2O_3)
E(GPa)	70	38
v	0.3	0.3
ρ(kg/m^3)	2702	3960

Table 2: The temperature-dependent coefficients in metals and ceramics.

Material	Properties	P_0	P_{-1}	P_1	P_2	P_3
Si_3N_4	E(Pa)	348.43e+9	0	−3.070e−4	2.160e−7	−8.946e−11
	α(1/K)	5.8723e−6	0	9.095e−4	0	0
	k(w/mK)	13.723	0	−1.032e−3	5.466e−7	7.876e−11
	v	0.24	0	0	0	0
	ρ(kg/m^3)	2370	0	0	0	0
SUS304	E(Pa)	201.04e+9	0	3.079e−4	−6.534e−7	0
	α(1/K)	12.330e−6	0	8.086e−4	0	0
	k(w/mK)	15.379	0	−1.264e−3	2.092e−6	−7.223e−10
	v	0.3262	0	−2.002e−4	3.797e−7	0
	ρ(kg/m^3)	8166	0	0	0	0

The metallic layer density and Young's modulus are ρ_m and E_m . Parameter values at the reference temperature of T_0 = 300K are used for temperature-dependent FG beam. The dimensionless elastic substrate constants are defined as

$$K_w = \frac{k_w L^4}{E_0 I}, \qquad K_P = \frac{k_P L^2}{\pi^2 E_0 I}. \tag{51}$$

Parameter I is defined as

$$I = \frac{bh^3}{12}. \tag{52}$$

Here, the number of differential quadrature grid points along the length was investigated for frequency convergence. However, the elastic substrate and porosity effects were ignored. Table 3 presents the natural frequency converging for simply supported conditions. In this table, it is clear that the results converged with N_x = 29.

In Table 4 the parameters of frequency were estimated and compared with those by Ebrahimi and Jafari [20] and Şimşek [9]. The good agreement was observed.

Further confirming the results obtained from the GDQM, Zahedinejad, in an article [37], investigated the isotropic beam frequencies depending on an elastic layer and in comparison with Matsunga [34]. The impacts of elastic substrate and slenderness ratio parameters are considered. The method accuracy was observed between the presented results in close agreement.

In Table 5, the first nondimensional frequency computed under the temperature-dependent environments with conditions of the simply supported boundary is compared with those by Ebrahimi and Jafari [20]. Here, three thermal states are considered: (1) uniform temperature rise (UTR), (2) linear temperature rise (LTR), and (3) nonlinear temperature rise (NLTR). There is a good agreement between the two solutions. The validity of using the GDQM is confirmed because of the above consequences comparison and the good agreement of these results and other articles. In the following, the various factors' impacts on the first frequencies are investigated.

Table 3: First three frequencies of nondimensional converging (p = 5).

L/h	n	(Nx) number of grid points						
		5	9	15	21	25	29	33
5	1	2.995	3.373	3.392	3.396	3.398	3.399	3.399
	2	19.546	11.512	11.482	11.511	11.521	11.526	11.526
	3	35.921	19.789	19.788	19.787	19.786	19.785	19.785
20	1	3.273	3.646	3.648	3.648	3.648	3.648	3.648
	2	78.673	14.558	14.364	14.369	14.370	14.372	14.372
	3	143.686	36.194	31.522	31.551	31.559	31.565	31.565

For considering the elastic substrates impact on FG beam nondimensional natural frequencies, studies were performed on both parameters of the elastic substrates. A beam with uniform porosity distribution applies a uniform thermal load. By canceling Pasternak's parameter, for porosity coefficient values, the dimensionless frequencies variation versus the Winkler's parameter can be figured in Figure 2. Also, by canceling Winkler's parameter for various porosity coefficients, these variations are plotted versus Pasternak's parameter in Figure 3. From these figures, for the porosity coefficient value, enhancing Winkler's and Pasternak's parameters causes the natural frequencies to increase. Because of enhancing both elastic substrate factors, the complete system stiffness increases, and therefore the dimensionless frequencies increase. The higher frequencies can be obtained by the larger porosity coefficient values. As

Table 4: Comparing frequency of first nondimensional FG beam simply supported conditions ($T_c = T_m = 300, a = 0, K_w = K_p = 0$).

L/h	Source and solution method		Material power law index (p)				
			0	0.2	0.5	1	2
5	Ebrahimi	Navier solution	5.152	4.808	4.410	3.990	3.626
	Şimşek	Lagrange's equations	5.152	4.806	4.408	3.990	3.634
	Present	DQM	5.149	4.804	4.407	3.988	3.624
20	Ebrahimi	Navier solution	5.460	5.081	4.651	4.205	3.836
	Şimşek	Lagrange's equations	5.460	5.082	4.651	4.205	3.836
	Present	DQM	5.460	5.081	4.651	4.205	3.836

Table 5: Comparison of the first nondimensional frequency for simply supported FG porous beam with various thermal loads and material power law index (L/h = 20).

a	Thermal loads	Reference	(p) power law index						
			0	0.1	0.2	0.5	25	29	33
ΔT = 20									
0	UTR	Ebrahimi	6.303	5.558	5.072	4.278	3.727	3.331	3.014
		Present	6.301	5.556	5.071	4.276	3.726	3.330	3.014
	LTR	Ebrahimi	6.358	5.615	5.132	4.340	3.389	3.390	3.071
		Present	6.337	5.595	5.129	4.320	3.781	3.388	3.074
	NLTR	Ebrahimi	6.358	5.616	5.134	4.343	3.792	3.394	3.074
		Present	6.346	5.609	5.131	4.341	3.791	3.393	3.073
0.1	UTR	Ebrahimi	6.889	5.911	5.308	4.369	3.744	3.308	2.968
		Present	6.880	5.907	5.303	4.366	3.741	3.306	2.966
	LTR	Ebrahimi	6.937	5.962	5.361	4.424	3.779	3.361	3.020
		Present	6.929	5.958	5.358	4.420	3.796	3.359	3.018
	NLTR	Ebrahimi	6.937	5.963	5.363	4.427	3.803	3.365	3.022
		Present	6.930	5.957	5.359	4.423	3.799	3.362	3.021
0.2	UTR	Ebrahimi	7.824	6.418	5.627	4.478	3.758	3.274	2.908
		Present	7.821	6.416	5.625	4.477	3.757	3.274	2.908
	LTR	Ebrahimi	7.865	6.463	5.675	4.527	3.807	3.321	2.953
		Present	7.859	6.458	5.670	4.523	3.805	3.319	2.953
	NLTR	Ebrahimi	7.894	6.464	5.676	4.530	3.810	3.324	2.955
		Present	7.884	6.458	5.670	4.525	3.797	3.321	2.953
ΔT = 40									
0	UTR	Ebrahimi	6.033	5.292	4.810	4.022	3.476	3.084	2.772
		Present	6.029	5.289	4.808	4.021	3.475	3.084	2.772
	LTR	Ebrahimi	6.213	5.480	5.002	4.218	3.671	3.276	2.959
		Present	6.207	5.475	4.994	4.213	3.667	3.273	2.957
	NLTR	Ebrahimi	6.213	5.482	5.006	4.224	3.678	3.283	2.964
		Present	6.205	5.475	5.001	4.219	3.675	3.280	2.962
0.1	UTR	Ebrahimi	6.641	5.671	5.073	4.140	3.521	3.090	2.755
		Present	6.638	5.669	5.070	4.137	3.519	3.088	2.753
	LTR	Ebrahimi	6.801	5.838	5.243	4.314	3.695	3.260	2.920
		Present	6.792	5.830	5.236	4.308	3.689	3.256	2.917
	NLTR	Ebrahimi	6.801	5.840	5.247	4.320	3.702	3.267	2.925
		Present	6.792	5.833	5.241	4.314	3.697	3.264	2.923
0.2	UTR	Ebrahimi	7.595	6.602	5.418	4.277	3.563	3.084	2.723
		Present	7.590	6.197	5.415	4.275	3.561	3.082	2.721
	LTR	Ebrahimi	7.736	6.349	5.568	4.430	3.715	3.232	2.867
		Present	7.728	6.334	5.564	4.426	3.711	3.229	2.865
	NLTR	Ebrahimi	7.736	6.351	5.572	4.437	3.722	3.239	2.871
		Present	7.727	6.346	5.566	4.433	3.718	3.236	2.869

shown in Figure 4, natural frequencies versus different temperature differences are in the range of 4 to 7 for different values of Winkler's parameter, and those are in the range of 25 to 40 for different values of Pasternak's parameter. Pasternak's parameter has a greater effect on natural frequencies than Winkler's parameter; also, combining both elastic substrate factors caused higher frequencies. In other words, Pasternak's parameter and combining both elastic

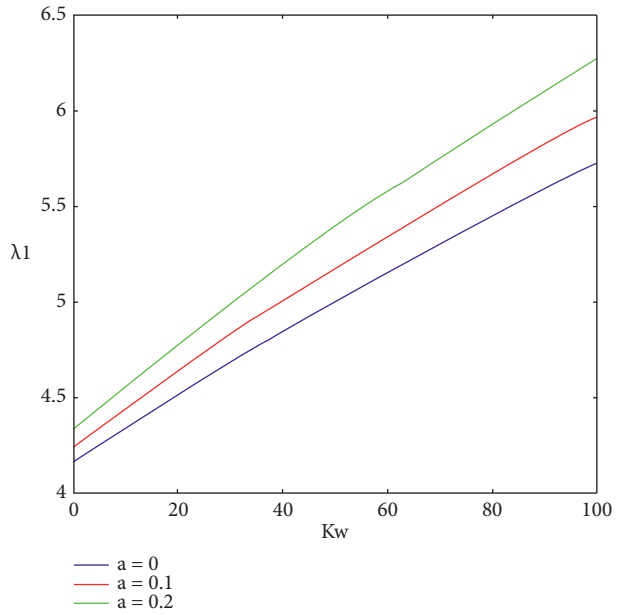

Figure 2: Winkler's parameters impact on the first nondimensional FG porous beam frequency with the simply supported condition. $p = 0.5$, $\Delta T = 100$, and $L/h = 5$.

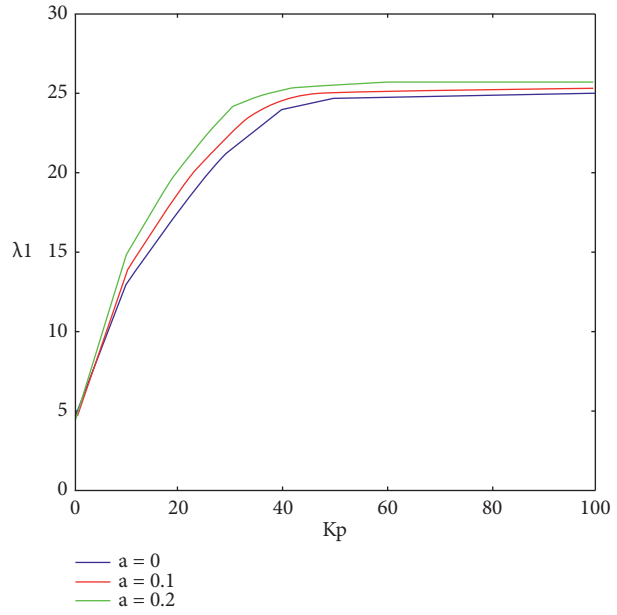

Figure 3: Pasternak's parameters impact on the first nondimensional FG porous beam frequency with the simply supported condition. $p = 0.5$, $\Delta T = 100$, and $L/h = 5$.

substrate parameters increase the stiffness and thus increase the natural frequency.

Figure 5 shows the temperature impact on frequencies, the variation of nondimensional natural frequency versus temperature for different power law indexes, and a constant slenderness ratio. A uniform temperature rise is subjected by the beam with a uniform porosity distribution. For power law indexes smaller than one, first, the natural frequency decreases with increasing temperature and then further natural frequency increases with rising temperature. But, always for indexes of power law greater than one, decreasing the natural frequencies of the beam concurred with increasing temperature. In the case of porous beams, given the modulus of elasticity, density, coefficients of inertia, and other mechanical properties in addition to the observance of temperature and porosity, it can also be affected by the power law index. The natural frequency with increasing temperature depending on the value of the power law index and porosity coefficient has been down to a point, and, from there, with the predominance of the effects of the power law

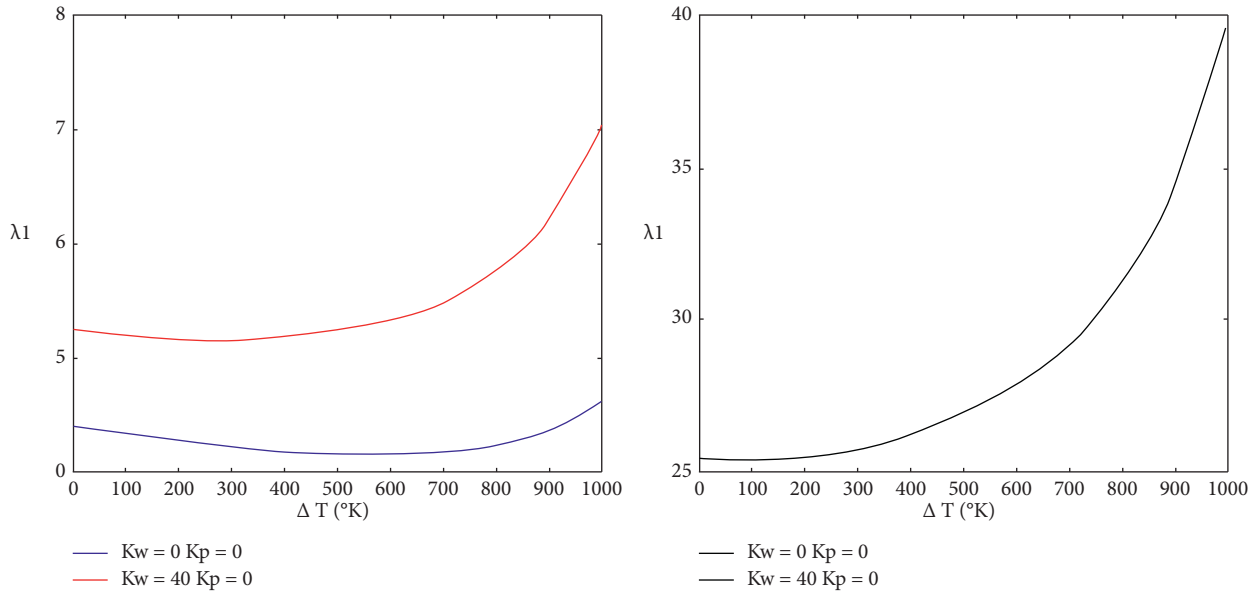

Figure 4: Winkler's and Pasternak's parameters impact on the first nondimensional FG porous beam frequency with the rise in uniform temperature with the simply supported condition. $p = 0.5$, $a = 0.2$, and $L/h = 5$.

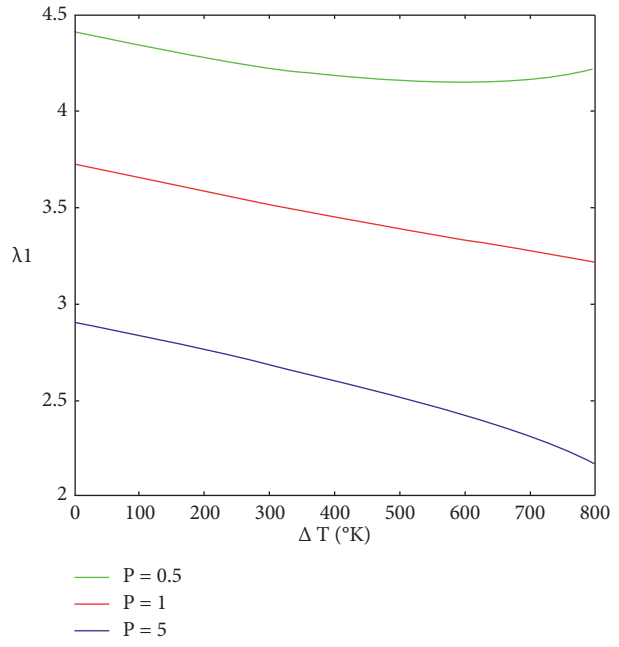

Figure 5: Various temperatures differences impact on the first nondimensional FG porous beam frequency with the simply supported condition. $a = 0.2$ and $L/h = 5$.

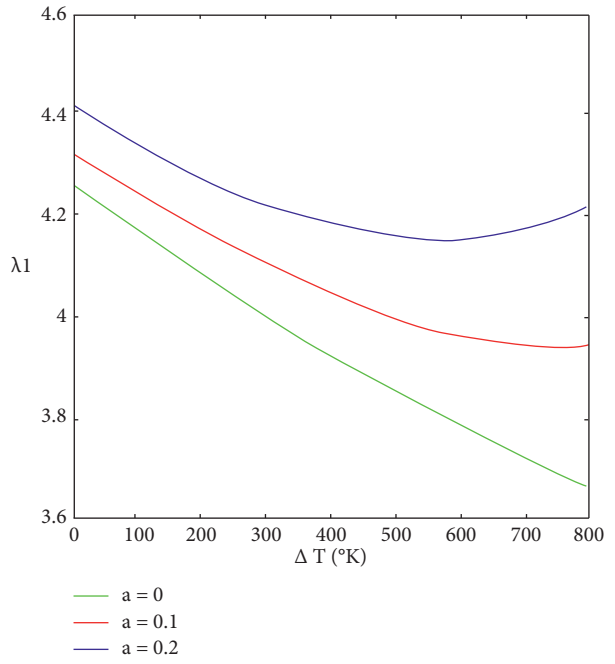

Figure 6: Porosity index impact on the first nondimensional FG porous beam frequency with the simply supported condition and various temperatures differences. $p = 0.5$ and $L/h = 5$.

index and the porosity coefficient, this trend will increase. In this case, by approaching the ceramic material, this issue will be more evident. Also, with enhancing the power law index, the frequency decreases for a certain temperature variation.

Figure 6 shows the frequency consequences contrary to the different porosity parameters temperature at fixed values of the slenderness ratio and index of power law to display the porosity coefficient impact with a uniform porosity distribution on the natural frequency. Higher natural frequencies are required for a higher value of the porosity coefficient. As shown in Figure 6, for the nonporosity mode, with increasing temperature variation for a thick beam, the natural frequency decreases because of the change in beam stiffness and greater flexibility with increasing temperature. In the case of porous beams, given that porosity can affect all the elasticity modulus, coefficients of inertia density, and other mechanical attributes with observing temperature and

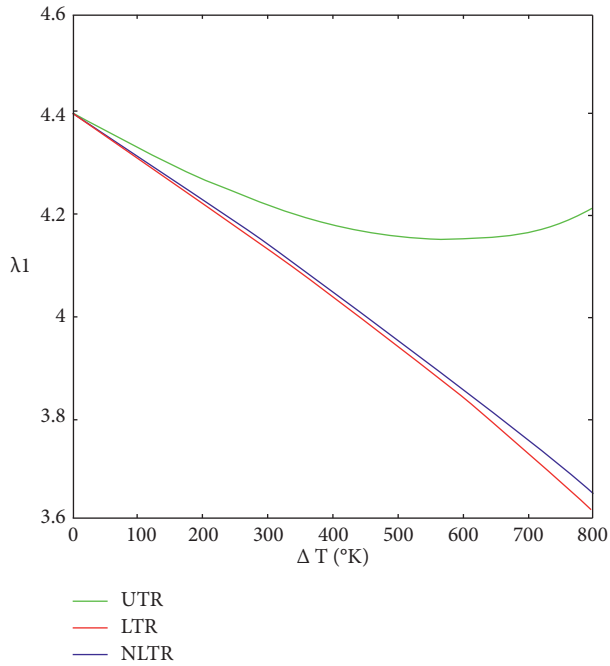

Figure 7: Thermal field type impact on the first nondimensional FG porous beam frequency with the simply supported condition and various temperatures differences. $p = 0.5$, $a = 0.2$, and $L/h = 5$.

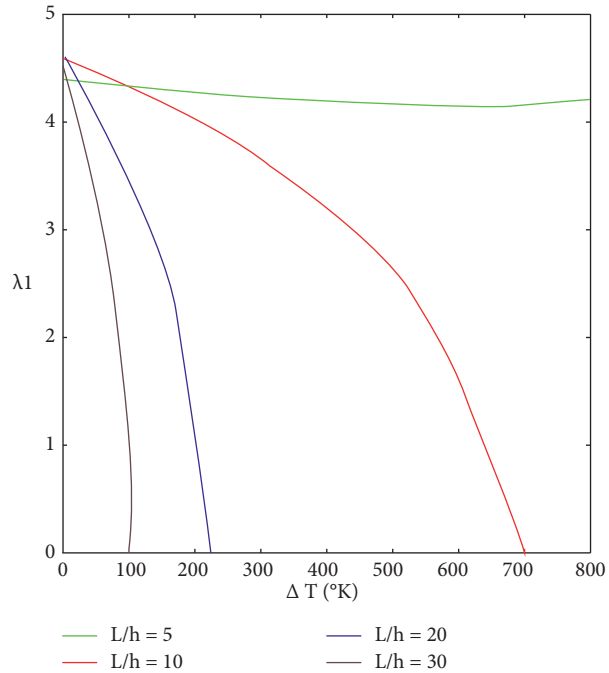

Figure 8: Slenderness ratio effect on the first nondimensional FG porous beam frequency with the simply supported condition and various temperatures difference. $p = 0.5$ and $a = 0.2$.

power law index, the natural frequency with increasing temperature depending on the power law index value and coefficient of porosity to a point and, from there, with the predominance of the index of power law impact and the coefficient of porosity, can cause this trend increase. For a larger porosity coefficient, this will occur at lower temperature differences.

In Figure 7, the thermal load's effect on frequencies is presented. The uniform porosity distribution of the beam is displayed in three uniform, linear, and nonlinear thermal loads for fixed values coefficient of porosity, slenderness ratio, and index of power law. The frequencies are higher than the other two states for the uniform temperature distribution with various temperatures differences, and the slope of the frequency decreasing variations is smaller. This is due to the greater flexibility of the beam due to the higher temperature of different points in the beam thickness direction.

For different slenderness ratio values and constant values coefficient of the porosity and the index of power law, the differences of the dimensionless natural frequencies of FG beam with the temperature versus a uniform porosity distribution are presented in Figure 8. The beam is exposed in a uniform temperature rise. As shown in the figure, at a high slenderness ratio, thermal buckling occurs at a lower temperature difference. Therefore, the comparison of frequencies should be made below the critical temperature. It is clear, in the figure, that the natural frequencies were higher at a given temperature difference for a smaller slenderness ratio, and this is due to the greater geometric stiffness of the beam with a smaller slenderness ratio.

8. Conclusion

This research studies functionally graded beams dynamic behavior with an elastic substrate of two parameters in a temperature-dependent environment and uniform porosity. Temperature-dependent and constant variation in the direction of the beam thickness and the distribution of power law of the material constituents' volume fraction are the material attributes. Uniform, linear, and nonlinear thermal loads are carried out in the direction of beam thickness. For considering the thick beam's vibrational behavior, the theory of third-order shear deformation is used. For the motion equations, Hamilton's principle was administered. For solving the equations of governing, generalized differential quadrature method has been used. The impacts of power law index, type of thermal load porosity coefficient, and beam slenderness ratio on natural beam frequencies were investigated. We can conclude the numerical consequences as follows:

(i) the decrease in frequency, there is an increase in the material index (p).

(ii) The shorter (or thicker) beam has a higher natural frequency.

(iii) the increase in temperature, there is a decrease in natural frequency for nonporous beam, because high temperatures can reduce the material stiffness with fixed mass.

(iv) In the case of porous beams, given the modulus of elasticity, density, coefficients of inertia, and other

mechanical properties in addition to the observance of temperature and power law index, it can also be affected by porosity. The natural frequency with increasing temperature depending on the value of the power law index and porosity coefficient has been down to a point, and, from there, with the predominance of the effects of the power law index and the porosity coefficient, this trend will increase.

(v) The natural frequency under the uniform increase in temperature for thick functionally graded porous beam is greater than those under the linear and nonlinear increase in temperature.

(vi) The porosity increase will enhance the natural frequency in the distribution of uniform porosity and a certain thermal variation.

(vii) There is a significant effect on the natural frequency by changes in the elastic substrate rigidity. The total system stiffness and, accordingly, the natural frequency are enhanced by increasing both elastic substrate factors. In other words, combining both elastic substrate parameters increases the stiffness and thus increases the natural frequency.

(viii) The presented numerical method is in good agreement with the solution methods in other articles. In other words, generalized differential quadrature method provides very accurate results, and, with fewer divisions, the answer can be reached faster.

Data Availability

The manuscript is a mathematical method; therefore, no data were used to support this study.

Conflicts of Interest

The authors declare that they have no conflicts of interest.

References

[1] Y. Tomota, K. Kuroki, T. Mori, and I. Tamura, "Tensile deformation of two-ductile-phase alloys: flow curves of α-γ Fe□Cr□Ni alloys," *Materials Science and Engineering*, vol. 24, no. 1, pp. 85–94, 1976.

[2] A. E. Alshorbagy, M. A. Eltaher, and F. F. Mahmoud, "Free vibration characteristics of a functionally graded beam by finite element method," *Applied Mathematical Modelling*, vol. 35, no. 1, pp. 412–425, 2011.

[3] K. K. Pradhan and S. Chakraverty, "Free vibration of Euler and Timoshenko functionally graded beams by Rayleigh-Ritz method," *Composites Part B: Engineering*, vol. 51, pp. 175–184, 2013.

[4] C. Jin and X. Wang, "Accurate free vibration analysis of Euler functionally graded beams by the weak form quadrature element method," *Composite Structures*, vol. 125, pp. 41–50, 2015, þ.

[5] X.-F. Li, "A unified approach for analyzing static and dynamic behaviors of functionally graded Timoshenko and Euler–Bernoulli beams," *Journal of Sound and Vibration*, vol. 318, no. 4-5, pp. 1210–1229, 2008.

[6] H. Wu, S. Kitipornchai, and J. Yang, "Free vibration and buckling analysis of sandwich beams with functionally graded carbon nanotube-reinforced composite face sheets," *International Journal of Structural Stability and Dynamics*, vol. 15, no. 7, Article ID 1540011, 2015.

[7] I. Katili, T. Syahril, and A. M. Katili, "Static and free vibration analysis of FGM beam based on unified and integrated of Timoshenko's theory," *Composite Structures*, vol. 242, 2020 þ, Article ID 112130.

[8] Y. Wen and Q. Y. Zeng, "A high-order finite element formulation for vibration analysis OF beam-type structures," *International Journal of Structural Stability and Dynamics*, vol. 9, no. 4, pp. 649–660, 2009.

[9] M. Şimşek, "Fundamental frequency analysis of functionally graded beams by using different higher-order beam theories," *Nuclear Engineering and Design*, vol. 240, no. 4, pp. 697–705, 2010.

[10] M.-J. Kazemzadeh-Parsi, F. Chinesta, and A. Ammar, "Proper generalized decomposition for parametric study and material distribution design of multi-directional functionally graded plates based on 3D elasticity solution," *Materials*, vol. 14, no. 21, p. 6660, 2021.

[11] C.-N. Chen, "DQEM vibration analyses of nonprismatic beams resting on elastic foundations," *International Journal of Structural Stability and Dynamics*, vol. 2, no. 1, pp. 99–115, 2002.

[12] P. Malekzadeh and G. Karami, "A mixed differential quadrature and finite element free vibration and buckling analysis of thick beams on two-parameter elastic foundations," *Applied Mathematical Modelling*, vol. 32, no. 7, pp. 1381–1394, 2008.

[13] R. Aghazadeh, E. Cigeroglu, and S. Dag, "Static and free vibration analyses of small-scale functionally graded beams possessing a variable length scale parameter using different beam theories," *European Journal of Mechanics - A: Solids*, vol. 46, pp. 1–11, 2014.

[14] Ş. D. Akbaş, "Free vibration and bending of functionally graded beams resting on elastic foundation," *Research on Engineering Structures and Materials*, vol. 1, no. 1, pp. 25–37, 2015.

[15] A. Mohseni and M. Shakouri, "Vibration and stability analysis of functionally graded CNT-reinforced composite beams with variable thickness on elastic foundation," *Proceedings of the Institution of Mechanical Engineers - Part L: Journal of Materials: Design and Applications*, vol. 233, no. 12, pp. 2478–2489, 2019.

[16] A. Mahi, E. A. Adda Bedia, A. Tounsi, and I. Mechab, "An analytical method for temperature-dependent free vibration analysis of functionally graded beams with general boundary conditions," *Composite Structures*, vol. 92, no. 8, pp. 1877–1887, 2010.

[17] L. C. Trinh, T. P. Vo, H.-T. Thai, and T.-K. Nguyen, "An analytical method for the vibration and buckling of functionally graded beams under mechanical and thermal loads," *Composites Part B: Engineering*, vol. 100, pp. 152–163, 2016.

[18] T. T. Thom and N. D. Kien, "Free vibration analysis of 2-D FGM beams in thermal environment based on a new third-order shear deformation theory," *Vietnam Journal of Mathematics*, vol. 40, no. 2, pp. 121–140, 2018.

[19] N. Wattanasakulpong and V. Ungbhakorn, "Linear and nonlinear vibration analysis of elastically restrained ends FGM beams with porosities," *Aerospace Science and Technology*, vol. 32, no. 1, pp. 111–120, 2014.

[20] F. Ebrahimi and A. Jafari, "A higher-order thermomechanical vibration analysis of temperature-dependent FGM beams with porosities," *Journal of Engineering*, vol. 2016, Article ID 9561504, 20 pages, 2016.

[21] H. Ait Atmane, A. Tounsi, and F. Bernard, "Effect of thickness stretching and porosity on mechanical response of a functionally graded beams resting on elastic foundations," *International Journal of Mechanics and Materials in Design*, vol. 13, no. 1, pp. 71–84, 2017.

[22] M. Heshmati and F. Daneshmand, "Vibration analysis of non-uniform porous beams with functionally graded porosity distribution," *Proceedings of the Institution of Mechanical Engineers - Part L: Journal of Materials: Design and Applications*, vol. 233, no. 8, pp. 1678–1697, 2019, þ.

[23] Ş. D. Akbaş, A. H. Bashiri, A. E. Assie, and M. A. Eltaher, "Dynamic analysis of thick beams with functionally graded porous layers and viscoelastic support," *Journal of Vibration and Control*, vol. 27, 2020.

[24] C. W. Bert and M. Malik, "Differential quadrature method in computational mechanics: a review," *Applied Mechanics Reviews*, vol. 49, 1996.

[25] M. Farid, P. Zahedinejad, and P. Malekzadeh, "Three-dimensional temperature dependent free vibration analysis of functionally graded material curved panels resting on two-parameter elastic foundation using a hybrid semi-analytic, differential quadrature method," *Materials & Design*, vol. 31, no. 1, pp. 2–13, 2010.

[26] P. Malekzadeh and Y. Heydarpour, "Free vibration analysis of rotating functionally graded cylindrical shells in thermal environment," *Composite Structures*, vol. 94, no. 9, pp. 2971–2981, 2012.

[27] H. Ersoy, K. Mercan, and Ö. Civalek, "Frequencies of FGM shells and annular plates by the methods of discrete singular convolution and differential quadrature methods," *Composite Structures*, vol. 183, pp. 7–20, 2018.

[28] Y. Wang, C. Feng, X. Wang, Z. Zhao, C. S. Romero, and J. Yang, "Nonlinear free vibration of graphene platelets (GPLs)/polymer dielectric beam," *Smart Materials and Structures*, vol. 28, no. 5, Article ID 055013, 2019.

[29] Y. Wang, C. Feng, J. Yang, D. Zhou, and S. Wang, "Nonlinear vibration of FG-GPLRC dielectric plate with active tuning using differential quadrature method," *Computer Methods in Applied Mechanics and Engineering*, vol. 379, Article ID 113761, 2021.

[30] Y. Wang, Y. Zhou, C. Feng, J. Yang, D. Zhou, and S. Wang, "Numerical analysis on stability of functionally graded graphene platelets (GPLs) reinforced dielectric composite plate," *Applied Mathematical Modelling*, vol. 101, pp. 239–258, 2022.

[31] MS. Al-Furjan, M. Habibi, J. Ni, D. won Jung, and A. Tounsi, "Frequency simulation of viscoelastic multi-phase reinforced fully symmetric systems," *Engineering with Computers*, pp. 1–7, 2020.

[32] MS. Al-Furjan, M. Habibi, G. Chen, H. Safarpour, M. Safarpour, and A. Tounsi, "Chaotic simulation of the multi-phase reinforced thermo-elastic disk using GDQM," *Engineering with Computers*, pp. 1–24, 2020.

[33] A. Shariati, M. Habibi, A. Tounsi, H. Safarpour, and M. Safa, "Application of exact continuum size-dependent theory for stability and frequency analysis of a curved cantilevered microtubule by considering viscoelastic properties," *Engineering with Computers*, vol. 37, no. 4, pp. 3629–3648, 2021.

[34] X. Huang, H. Hao, K. Oslub, M. Habibi, and A. Tounsi, "Dynamic stability/instability simulation of the rotary size-dependent functionally graded microsystem," *Engineering with Computers*, pp. 1–7, 2021.

[35] M. S. H. Al-Furjan, A. hatami, M. Habibi, and L. Shan, "On the vibrations of the imperfect sandwich higher-order disk with a lactic core using generalize differential quadrature method," *Composite Structures*, vol. 257, Article ID 113150, 2021.

[36] MS. Al-Furjan, M. Habibi, A. Ghabussi, H. Safarpour, M. Safarpour, and A. Tounsi, "Non-polynomial framework for stress and strain response of the FG-GPLRC disk using three-dimensional refined higher-order theory," *Engineering Structures*, vol. 228, Article ID 111496, 2021.

[37] P. Zahedinejad, "Free vibration analysis of functionally graded beams resting on elastic foundation in thermal environment," *International Journal of Structural Stability and Dynamics*, vol. 16, no. 7, Article ID 1550029, 2016.

[38] H.-T. Thai and T. P. Vo, "Bending and free vibration of functionally graded beams using various higher-order shear deformation beam theories," *International Journal of Mechanical Sciences*, vol. 62, no. 1, pp. 57–66, 2012.

[39] J. N. Reddy, "A simple higher-order theory for laminated composite plates," *Journal of Applied Mechanics*, vol. 51, 1984.

[40] H.-S. Shen and Z.-X. Wang, "Nonlinear analysis of shear deformable FGM beams resting on elastic foundations in thermal environments," *International Journal of Mechanical Sciences*, vol. 81, pp. 195–206, 2014.

[41] Y.-W. Kim, "Temperature dependent vibration analysis of functionally graded rectangular plates," *Journal of Sound and Vibration*, vol. 284, no. 3-5, pp. 531–549, 2005.

Hindawi
Shock and Vibration
Volume 2022, Article ID 8148337, 13 pages
https://doi.org/10.1155/2022/8148337

Research Article

Improved Empirical Modal Decomposition Coupled with Interwoven Fourier Decomposition for Building Vibration Signal Denoising

Xi Luo[1] **and Shitu Abubakar**[2]

[1]*School of Architecture and Art, Central South University, Changsha 410083, China*
[2]*Department of Mechanical Engineering, Ahmadu Bello University, Zaria 810107, Nigeria*

Correspondence should be addressed to Shitu Abubakar; abubakarshitu88@gmail.com

Received 28 December 2021; Accepted 22 January 2022; Published 10 February 2022

Academic Editor: Jiaqiang E

The precise detection of building vibration signals is a crucial problem for the identification of building vibration sources and characteristics. However, the building vibration signal is usually accompanied by complex high-frequency noise. The present study proposed a novel building vibration signal denoising method based on improved empirical modal decomposition coupled with interwoven Fourier decomposition (IEMD-IWFD). The noise-embed building vibration signal is first decomposed by the IEMD-IWFD. Then, the intrinsic mode function (IMF) components with useful information are extracted from the original building vibration signal using the energy criterion of the autocorrelation function. After that, the building vibration signal is formed by reconstructing the IMF component using the Hilbert transform. Based on the comparison of similarity coefficient and mean square error between the reconstructed signal from IEMD-IWFDM and EMD and target signal, it is indicated that the IEMD-IWFDM exhibits a better denoising performance for the simulated building vibration signal induced by trains.

1. Introduction

Building vibration signal processing is an indispensable part of vibration source identification and feature extraction. Poston et al. [1] reported on measurements from an instrumented, public building and examined the viability of conventional localization algorithms for locating persons moving within a building. Field measurements of vibration and noise on the ground and inside a nearby 3-story building subjected to moving subway trains were conducted by Zou et al. [2]. A general synthesis of identification and vibration control of building structures under unknown excitations was proposed by Lei et al. [3], which has been proven to be cost-effective and beneficial for developing smart building structures.

The key role of signal processing is to extract the desired section of the signal and remove the high-frequency noise. Some time, frequency and time-frequency domain-based methods have been proposed to suppress interference during vibration signal collection [4]. Traditional averaging approaches in the time domain are more suited to periodic signals [5]. Their denoising performance is limited to vibration signals with varying frequency and amplitude. Frequency domain methods such as Butterworth filtering and homomorphic filtering provide a better insight into the stability of a system, which can remove noise within the frequency band of interest [6]. The model frequency and its changing range caused by the variation of working conditions and surroundings are required when using frequency domain methods. Therefore, their application is limited [7]. Since characteristics such as time and frequency are taken into account, wavelet transform and other time-frequency domain techniques can be used on both static and nonstatic signals [8]. Nonetheless, some proper thresholds and optimal parameters should be manually selected and adjusted to avoid the elimination of useful information [9]. Other

denoising methods based on global projection [10], artificial neural network [11], and singular value decomposition [12] have also been proposed to carry out the denoising tasks. Among the methods mentioned above for denoising vibration signals, the denoising performance depends on the selection and optimization of key parameters, which heavily rely on the researchers' empirical experiences.

Empirical mode decomposition (EMD) is an interesting and paramount direction in the field of signal processing. Lots of the works in the existing literature focus on nonlinear unsmooth signal analysis. For instance, a novel data-driven technique for the detection and isolation of faults was built upon pseudo-fault signal (PFS)-assisted EMD [13]. Ahn et al. [14] investigated fault detection of a roller bearing system using a wavelet denoising scheme and proper orthogonal values of an intrinsic mode function covariance matrix. Liu et al. [15] applied EMD-entropy to extract characteristic parameters from vibration signals of high voltage circuit breakers. EMD has been widely used in the engineering field owing to its adaptability. As the key point of the EMD, the screening process has a major influence on signal decomposition. The upper and lower envelopes, on the other hand, generated from cubic spline interpolation (CSI) in the EMD always lead to undershoots [16], overshoots [17], and edge effects [18], hence yielding unsatisfactory results. Li et al. [19] proposed an improved empirical modal decomposition (IEMD) algorithm. The latter is based on the modification of the envelope algorithm by repacking the CSI with C2 piecewise rational cubic spline interpolation (PRCSI) and C2 monotonic piecewise rational cubic spline interpolation (MPRCSI), which presented the superiority, especially for those nonlinear and unstable signals. However, the IEMD algorithm is not good when decomposing those signals with the overlapped spectra [20]. As an auxiliary measure to the IEMD, interwoven Fourier decomposition (IWFD) can extract signals by optimizing bandwidths in the frequency domain. The IWFD is a digital information time-frequency analytical technique that is adaptable. Quasi-bandpass filters with zero phase are used to decompose the signal into a few Fourier intrinsic band functions guaranteeing the signal's complete rebuilding in the IWFD [21].

As mentioned above, although extensive investigations have been conducted in the field of building vibration signals, research report in the denoising of building vibration signals, which remains a challenging task, is limited. Moreover, it becomes more difficult when signals disturbed by noise have nonlinear and nonsteady characteristics. Therefore, the authors of this study evaluated the denoising performance for the building vibration signal using the IEMD coupled with the IWFD (referred to as IEMD-IWFD).

2. Strategy for Building Vibration Signal Denoising

Figure 1 shows the procedure flowchart for building vibration signal denoising. The IEMD-IWFD is employed to decompose the real building vibration signal into intrinsic mode functions (IMFs). After that, the IMFs are extracted using the energy criterion of the autocorrelation function (ACF). After the determination of IMFs, the target building vibration signal is formed by IMFs reconstruction by the Hilbert transform. The details of the algorithms used in the current denoising method are described as follows.

2.1. Description of IEMD-IWFD

2.1.1. IEMD Algorithm. Many researchers have employed the EMD method, which is an adaptive algorithm to perform the reconstruction [22], classification [23], and denoising [24] of a signal. However, the use of CSI to generate peak and lowest envelopes has some disadvantages such as overtones and subtones. EMD encountered difficulties in fitting signals with the local extremum of CSI. Some methods have been proposed to improve the adaptability of cubic spline [25]. One of these methods is the Hermite cubic spline with a shape controlling parameter developed by Li et al. [19]. The shape controlling parameter is more flexible than the CSI, but it still cannot satisfy the flexibility and smoothness simultaneously. There has been lots of research on the C2 cubic spline, which can interpolate the monotone, positive, and convex data [25].

For a given dataset $((xi, fi),\ i = 0,\ 1,\ \ldots,\ n)$ with $x0 < x1 < \ldots < xn$, let $hi = xi + 1 - \mathrm{xi}$, $\Delta i = (fi + 1 - \mathrm{fi})/\mathrm{hi}$ and $\theta = (x - xi)/hi\ \ (0 < \theta < 1)$. A well-advised cubic spline for interpolating $Ii = [xi,\ xi + 1]$ is defined as follows:

$$S_i(x) = \frac{M_i(x)}{N_i(x)} = \frac{P_{i0}(1-\theta)^3 + P_{i1}\theta(1-\theta)^2 + P_{i2}\theta^2(1-\theta) + P_{i3}\theta^3}{(1-\theta)^2\alpha_i + \theta(1-\theta)(2\alpha_i\beta_i + \gamma_i) + \theta^2\beta_i}. \tag{1}$$

An unknown P_{ik} $(k = 0,\ 1,\ \ldots,\ n)$ has the following form:

$$\begin{cases} P_{i0} = \alpha_i f_i, \\ P_{i1} = (2\alpha_i\beta_i + \alpha_i + \gamma_i) f_i + \alpha_i h_i d_i, \\ P_{i2} = (2\alpha_i\beta_i + \beta_i + \gamma_i) f_{i+1} - \beta_i h_i d_i, \\ P_{i3} = \beta_i f_{i+1}, \end{cases} \tag{2}$$

where the parameters $\alpha_i > 0$, $\beta_{\mathrm{i}} > 0$, and $\gamma_i \geq 0$ are used to adjust the interpolation curve shape. For instance, the data range, monotonicity, positivity, and convexity over the complete gap can be controlled. Based on the C2 continuity, the following linear system can be described:

$$a_i d_{i-1} + b_i d_i + c_i d_{i+1} = e_i, i = 1, 2, \ldots, n-1, \tag{3}$$

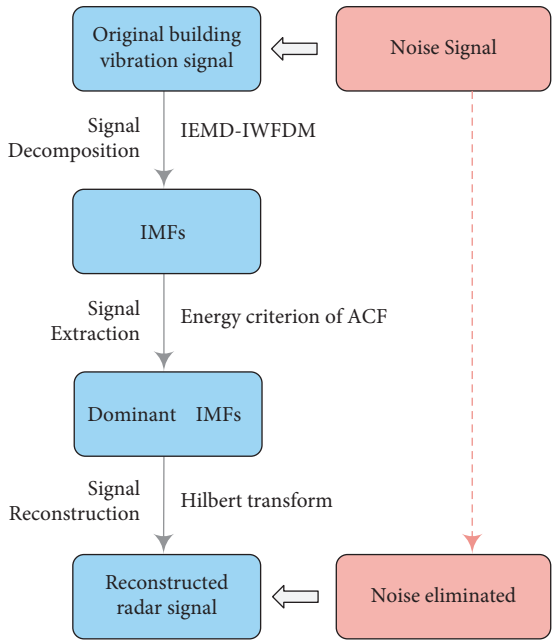

Figure 1: Procedure flowchart of building vibration signal denoising.

where

$$\begin{cases} a_i = h_i\alpha_{i-1}\alpha_i, \\ b_i = h_i\alpha_i(\gamma_{i-1} + 2\alpha_{i-1}\beta_{i-1}) + h_{i-1}\beta_{i-1}(\gamma_i + 2\alpha_i\beta_i), \\ c_i = h_{i-1}\beta_{i-1}\beta_i, \\ e_i = h_i\alpha_i(\gamma_{i-1} + \alpha_{i-1} + 2\alpha_{i-1}\beta_{i-1})\Delta_{i-1} + h_{i-1}\beta_{i-1}(\gamma_i + \beta_i + 2\alpha_i\beta_i)\Delta_i, \end{cases} \tag{4}$$

Clearly, the first derivative variable d_i can be calculated with good approximation based on the aforementioned linear system and coupled with two more equations such as $s(t)\ (x0) = d0$ and $s(t)\ (xn) = dn$, and the first derivative parameter d_i can be calculated through a unique solution from this linear system. Two options for end-point derivatives were explored by Karim and Pang [25], d_0 and d_n. There is only one option in this case, which takes into account the equation.

$$d_0 = \Delta_0 + (\Delta_0 - \Delta_1)\left(\frac{h_0}{h_0 + h_1}\right) \text{ and } d_n = \Delta_{n-1} + (\Delta_{n-1} - \Delta_{n-2})\left(\frac{h_{n-1}}{h_{n-1} + h_{n-2}}\right). \tag{5}$$

For the choice of the parameters, they have tested some cases to guarantee the smoothness of curves with different interpolation shapes, and the C2 PRCSI has been extensively validated. In the comparison between the simulated results from [25, 26], it is proved that the performance of the C2 cubic spline performed well. Nevertheless, there is no useful information mentioned for the monotonicity, and thus, a monotone version for the C2 PRCSI will be further introduced.

Abbas et al. [26] investigated the shape-preserving C2 PRCSI for monotone data. It can be seen that it appears with the original form of C2 PRCSI at every span $Ii = [xi, xi + 1]$.

$$S_i(x) = \frac{P_i(\theta)}{Q_i(\theta)}, \tag{6}$$

where

$$P_i(\theta) = \alpha_i f_i (1-\theta)^3 + \left(f_i(2\alpha_i + \beta_i + \gamma_i) + \alpha_i h_i d_i\right)\theta(1-\theta)^2 + \left(f_{i+1}(\alpha_i + 2\beta_i + \gamma_i) - \beta_i h_i d_{i+1}\right)\theta^2(1-\theta) + \beta_i f_{i+1}\theta^3,$$
$$Q_i(\theta) = (1-\theta)^2\alpha_i + \theta(1-\theta)(\gamma_i + \alpha_i + \beta_i) + \theta^2\beta_i. \tag{7}$$

At the same boundary conditions as mentioned above, such as the variables that keep the shape of $\alpha_i > 0$, $\beta_i > 0$, $\gamma_i \geq 0$ and the dataset $((xi, fi), i = 0,1, \ldots, n)$ with $xi < xi + 1$ and $fi < fi + 1$, etc., two cases for the monotonical series are presented as follows.

Case 1. $\Delta_i = 0$, $d_i = d_{i+1} = 0$ and $S_i(x) = f_i, \forall x \in I_i$, $i = 0, 1, \ldots, n-1$;

Case 2. $\Delta_i > 0$, $S_i^{(1)}(x) = \sum_{k=0}^{4} (1-\theta)^{4-k}\theta^k M_{ki}/(q_i(\theta))^2$, where

$$\begin{cases} M_{0i} = \alpha_i^2 d_i, \\ M_{1i} = 2\alpha_i\left((\alpha_i + 2\beta_i + \gamma_i)\Delta_i - \beta_i d_{i+1}\right), \\ M_{2i} = M_{1i} + M_{3i} - (M_{0i} + M_{4i}) + \gamma_i(\alpha_i + \beta_i + \gamma_i)\Delta_i - 2\alpha_i\beta_i(d_i + d_{i+1}), \\ M_{3i} = 2\beta_i\left((2\alpha_i + \beta_i + \gamma_i)\Delta_i - \alpha_i d_i\right), \\ M_{4i} = \beta_i^2 d_{i+1}. \end{cases} \tag{8}$$

The C2 curve for monotone data is preserved by the rational cubic function when the shape parameters meet the following requirements:

$$\begin{cases} \alpha_i > 0, \\ \beta_i > 0, \\ \gamma_i = m_i + \max\left\{0, \dfrac{(d_{i+1}\beta_i - \Delta_i(\alpha_i + 2\beta_i))}{\Delta_i}, \dfrac{(d_i\alpha_i - \Delta_i(2\alpha_i + \beta_i))}{\Delta_i}\right\}, \end{cases} \tag{9}$$

where m_i is a constant larger than 0,

The interpolation error was investigated in [18], whereby the minimum interpolation error is lower than 0.064. Compared to other alternative approaches, it is very diminutive, and this implies that the C2 MPRCSI with the parameter choice schemes presented in [26] is computationally economical and pictorially appealing in comparison with the local and global schemes [27] and the scheme developed in Ref. [28].

2.1.2. IWFD Algorithm. The Fourier decomposition algorithm with adaptability characteristics is an adaptive data-driven signal decomposition technique that generates the signal's analytic illustration and Hilbert transform [29]. Compared to the EMD algorithm, the main advantage of the Fourier decomposition algorithm is that it has more detailed mathematical expressions. As a result, there is no need to predefine the parameters such as iterations, window lengths, and termination criteria. When using the Fourier decomposition algorithm, a signal can be considered as a series of zero-mean orthosecting functions known as analytical Fourier intrinsic band functions.

In the Fourier decomposition algorithm, a real-valued N-point signal x[n] is represented by the weighted sum of Fourier bases based on the discrete Fourier transform (DFT):

$$x[n] = \sum_{k=0}^{N-1} X[k]W_N^{-kn}, \tag{10}$$

where $W_N = e - j(2\pi/\mathrm{N})$ and $x[k]$ denotes the N-point DFT coefficients of the signal $x[n]$. These coefficients can be achieved in a numerically effective way using fast Fourier transform (FFT) techniques.

The N-point signal $x[n]$ can be rewritten by the following two forms:

$$x[n] = X[0] + \sum_{k=1}^{N/2-1} X[k]W_N^{-kn} + X\left[\frac{N}{2}\right]W_N^{-Nn/2} + \sum_{k=N/2+1}^{N-1} X[k]W_N^{-kn}, \tag{11}$$

$$x[n] = X[0] + \sum_{k=1}^{(N-1)/2} X[k]W_N^{-kn} + \sum_{k=(N-1)/2+1}^{N-1} X[k]W_N^{-kn}. \tag{12}$$

Due to x(n) being a real-valued signal, $\sum_{k=1}^{N/2-1} X[k]W_N^{-kn}$ and $\sum_{k=N/2+1}^{N-1} X[k]W_N^{-kn}$ are a pair of complex conjugates. The same holds true for $\sum_{k=1}^{(N-1)/2} X[k]W_N^{-kv}$ and $\sum_{k=(N-1)/2+1}^{N-1} X[k]W_N^{-k}$ in equation (12). Two definitions are made as follows:

$$z[n] \triangleq 2\sum_{k=1}^{N/2-1} X[k]W_N^{-kn}, \tag{13}$$

$$v[n] \triangleq 2\sum_{k=1}^{(N-1)/2} X[k]W_N^{-kn}. \tag{14}$$

The N-point signal $x[n]$ can be expressed in a simpler form as

$$x[n] = \begin{cases} X[0] + \mathrm{Re}\{z[n]\} + (-1)^n X[N/2], & N\text{: even}, \\ X[0] + \mathrm{Re}\{v[n]\}, & N\text{: odd}, \end{cases} \tag{15}$$

where the real parts of $z[n]$ and $v[n]$ signals are stated by Re($z[n]$) and Re($v[n]$), respectively. To reduce the complexity in Fourier decomposition equations, signals with even values of N are only considered. The $z[n]$ signal is factorizable as in

$$2\sum_{k=1}^{N/2-1} X[k]W_N^{-kv} = \sum_{i=1}^{M} a_i[n]e^{j\phi_i[n]}, \tag{16}$$

where $\varphi_i[n]$ and $ai[n]$ are the real-time scenario and instantaneous frequency, respectively, and M is the total number.

Equation (16) expressed the decomposition process which can be performed under the following conditions for each analytic Fourier intrinsic band function:

$$f_i[n] = \frac{1}{2\pi}\left(\phi_i[n+1] - \phi_i[n]\right) \geq 0, \tag{17}$$

$$a_i[n] \geq 0, n = 0, 1, 2, \ldots\ldots N-1, \tag{18}$$

where f_i[n] is the instantaneous frequency of the analytic Fourier intrinsic band function.

In a forward search, i.e., the scanning from low to high frequency, the decomposition process in equation (17) is carried out by [29]

$$a_i[n]e^{j\phi_i[n]} = 2\sum_{k=N_i-1+1}^{N_i} X[k]W_N^{-kn}, \tag{19}$$

where $N_0 = 0$ and N_M=N/2–1. In a backward search, i.e., the scanning from high to low frequency, the decomposition process in equation (17) is carried out by

$$a_i[n]e^{j\phi[n]} = 2\sum_{k=N_i}^{N_{i-1}-1} X[k]W_N^{-kn}. \tag{20}$$

The key points of (19) and (20) aim to confirm the frequency $N_1, N_2, \ldots, N_{M-1}$. When the N_i is used, the right-hand side of equation (15) and its corresponding instantaneous phase and instantaneous frequencies are calculated for $n = 0, 1, \ldots, N-1$. The minimum amount of possible N_i for all n is determined by the frequency index N_i.

2.1.3. IEMD Coupled with IWFD. The envelope algorithm based on C2 piecewise rational cubic spline interpolation (PRCSI) and C2 monotone piecewise rational cubic spline interpolation (MPRCSI) was employed to decompose the building vibration signal corrupted by noise. The zero-phase nonrectangular bandpass filters contained in the IWFD were coupled into the IEMD to analyze signals with multiple components and intersecting instantaneous frequencies. We first structured the upper envelope and lower envelope using the C2-PRCSI method. Considering the presence of undershoots, we further iteratively modified the original envelope using C2 MPRCSI technology to eliminate undershoots as accurately as possible. With the assistance of IWFD, filter parameters were evaluated in order to ensure that the sum of all Fourier intrinsic band functions can reconstruct the entire signal, which effectively improves the compatibility of multicomponent building vibration signal processing. Figure 2 presents the construction flowchart of the IEMD-IWFD method. As it can be noticed and based on the traditional EMD method, modified cubic spline interpolations are inserted to optimize the envelopes of the original building vibration signal. This is done so that a relatively high accuracy and efficiency decomposition for the extremely nonlinear and nonstationary building vibration signals is achieved. The determination of the IFM signal refers to the decomposition process of the original signals in IWFD. In a bid to analyze the signals of intersecting instantaneous frequencies, the zero-phase nonrectangular bandpass filters referred from IWFD were employed to assist the IEMD method. The features of these filters are determinate, and as a result, the sum of all FIBFs ensures a full rebuilding of the signal. When compared with EMD, the IEMD-IWFD is expected to be more competitive for the

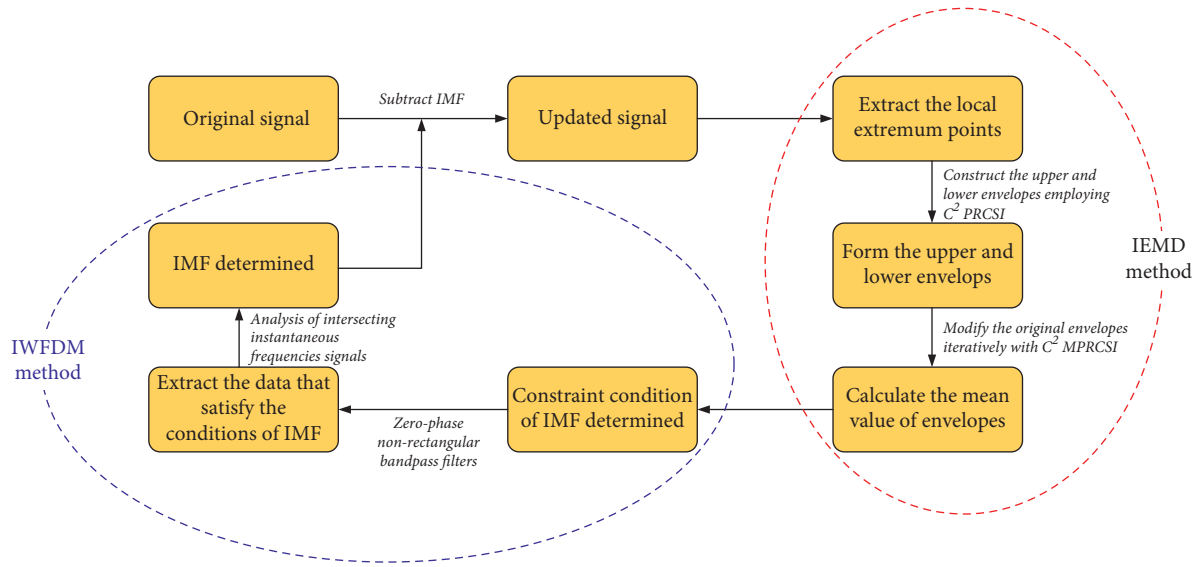

Figure 2: Procedure of IEMD-IWFD construction.

denoising of nonlinear and nonstationary building vibration signals and more compatible for analyzing the intersecting instantaneous frequencies of building vibration signals.

2.2. Description of Energy Criterion of ACF. The correlation function is an average measure of signal time-domain characteristics, which describes the similarity degree between signals at different times. The time average-based ACF is calculated as follows:

$$R_x(m) = \frac{1}{N - |m|} \sum_{n=0}^{N-1-|\tau|} x_N(n) x_N(n+m), \tag{21}$$

where m represents the time delay. In order to ensure the consistency between the sequence length of ACF and the length of signal $xN(n)$, the time delay m should satisfy $(-N/2) - 1 < m < N/2$. This sequence energy is expressed as follows:

$$E(n) = \sum_{n=0}^{N-1} x^2(n). \tag{22}$$

The ACF of each component of the decomposed signal can be calculated, and the distribution characteristics of the ACF can be obtained. Due to weak correlation and strong randomness at each moment of the random noise, the ACF reaches its maximum value at the zero point, while the value of the ACF rapidly decreases to a small value at other points. Since there is a correlation between general signals at different times, the autocorrelation function value outside of zero cannot quickly decay to very small values, but changes with the varying time difference, especially for the periodic signal. The ACF is still a periodic signal and its change law is different from the changing rule of the noise ACF obviously. The dominant IMFs can be determined according to the ACF characteristics of each component.

2.3. Description of Signal Reconstruction Based on Hilbert Transform. The IMFs of the original signal can be regarded as a set of multidimensional components closely related to the information of the source signal. By calculating the correlation between time-frequency characteristics, the original signal can be recovered from these components. Based on the signal decomposition, the basic flowchart of target signal recovery is shown in Figure 3. The Hilbert transformation is used in multichannel IMFs to solve the instantaneous frequency of signal components and obtain the time-frequency characteristics of the signal. The noise and/or invalid signals can be filtered out based on the time-frequency distribution of signal components. Based on IMF'[n] and coefficient matrix A, the source signal S in the mixed signal is separated, which can be expressed as

$$\mathrm{A} \cdot \mathrm{IMF}'[n] = \mathrm{S}. \tag{23}$$

To explore the time-frequency behavior of each IMF component, the Hilbert spectrum analysis was used in this study to process the signals. Unlike FFT time-frequency analysis, the Hilbert spectrum analysis is performed without using the basic variable frequency to represent the behavior of the signal. It analyzes the signal from the perspective of instantaneous frequency and expands the signal into a time-frequency plane. The Hilbert spectrum analysis is derived by applying Hilbert transform to any signal $x(t)$, $t \in (-\infty, +\infty)$, stated as

$$y(t) = H[x(t)] = \int_{-\infty}^{+\infty} \frac{x(\tau)}{\pi(t-\tau)} d\tau. \tag{24}$$

Due to the integral singularity $\tau = t$, the formula expressed by Cauchy principal value integrals is given as

$$y(t) = H[x(t)] = \frac{1}{\pi} \mathrm{P.V} \int_{-\infty}^{+\infty} \frac{x(\tau)}{t-\tau} d\tau, \tag{25}$$

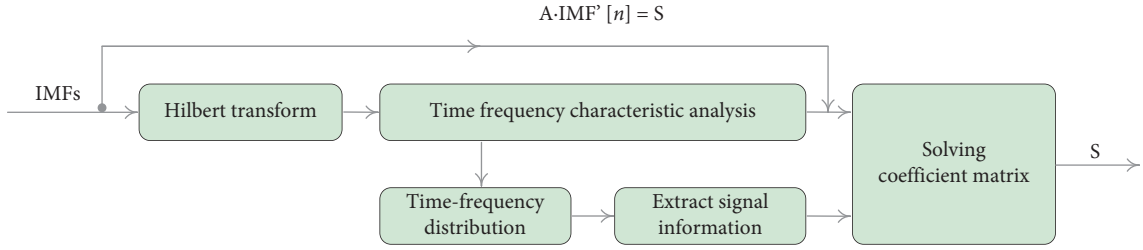

Figure 3: Procedure of target signal recovery.

where P.V represents the generalized Cauchy principal valued integral.

Considering $y(t)$ is the convolution of signal $x(t)$ and $1/\pi t$, the above relationship also exists as

$$y(t) = x(t) \cdot \frac{1}{t\pi}. \tag{26}$$

It is known by the property of Fourier transform that

$$F(y) = F[1/t\pi]F[x(t)], \tag{27}$$

$$F[1/t\pi] = -j\mathrm{sgn}(f) = \begin{cases} -j, f > 0 \\ j, f < 0 \end{cases} = \begin{cases} e^{-j\frac{\pi}{2}}, f > 0. \\ e^{j\frac{\pi}{2}}, f < 0. \end{cases} \tag{28}$$

To understand the meaning of the Hilbert transform, expressed as type

$$z(t) = x(t) + jy(t) = a(t)e^{j\theta(t)}, \tag{29}$$

where $a(t)$=$(x2 + y2)1/2$ is the amplitude of the signal and $\theta(t) = \tan^{-1}(y/x)$ is the instantaneous response signal.

The frequency at any instance is expressed as

$$\omega(t) = \frac{d\theta(t)}{dt}. \tag{30}$$

The instantaneous frequency of the signal represents the aggregation degree of signal energy in a certain frequency band. Based on the Hilbert transform on IMF components, the original signal is given as

$$x(\omega, t) = \sum_{j=1}^{n} a_j(t)\exp\left(i\int \omega_j dt\right). \tag{31}$$

After the transformation in the above steps, the amplitude and frequency of the original signal are given as a function of time. If the signal is represented on the time-frequency-energy three-dimensional distribution, the Hilbert spectrum $H(\omega, t)$ of the signal can be obtained as

$$H(\omega, t) = \sum H_i(\omega, t). \tag{32}$$

3. Results and Discussion

A model was proposed by Rossi and Nicolini [30] to predict the building vibration induced by trains, as shown in equation (3), in which the train's quality and velocity, the rail's displacement, the soil's characteristics, and the sleeper's spacing were considered as

$$P_{\max} = \int_{-T/2}^{T/2} \frac{Mgsv_tKe^{-\alpha\sqrt{x^2+d^2}}}{T2\pi i\sqrt{x^2+d^2}}dx, \tag{33}$$

$$L_v = 20\log\left(\frac{\sqrt{P_{\max}/\rho_s c_R}}{v_{ref}}\right), \tag{34}$$

where $P_{\max}$ is the largest time-average power, M the total train mass, s the longest vertical rail displacement, vt the velocity of train, K the constant depended on model calibration, α the dissipation constant of soil, d the distance between power and train, T the length of train, i the spacing between adjoining sleepers, L_v the level of vibration, ρ_s the surface density of soil, and c_R the velocity of wave's propagation, and v_{ref} equals $2.54 \times 10{-}8$ m/s.

Developing a reliable prediction model for noise is necessary to prevent the interference of environmental noise. Some noise prediction models have been developed and codified into industrial standards based on test conditions and industrial circumstances. A model was proposed by Nassiri et al. [31] to assess the noise induced by the train, which is related to the velocity of the train, vt, and the distance between power and train d, as shown in equation (35). However, the impact of the curve, joint, and turnout of the train were not considered, and thus, this model can only be used to predict the noise caused in the testing line.

$$L_n = L_0 - K_l\lg\left(\frac{d}{d_0}\right) + K_s\lg\left(\frac{v}{v_0}\right), \tag{35}$$

where L_n is the equivalent sound level, K_l and K_s are the correction factors of length and speed, and L_0, d_0, and v_0 are the reference values of sound level, distance, and speed, respectively.

The simulated building vibration signal without and with the noise are given in Figures 4(a) and 4(b), respectively.

The denoising of building vibration signals requires signal decomposition first. Figure 5 shows the decomposed IMF components based on the method of IEMD-IWFD. The synthetic building vibration signal is decomposed into 7 IMFs, which are ordered according to frequency. IMF1 and IMF2 are obviously high-frequency components, while IMF5–IMF7 are relatively low-frequency components.

The decomposed results of synthetic building vibration using the EMD are presented in Figure 6. As can be seen, two fewer IMF components are obtained from the EMD

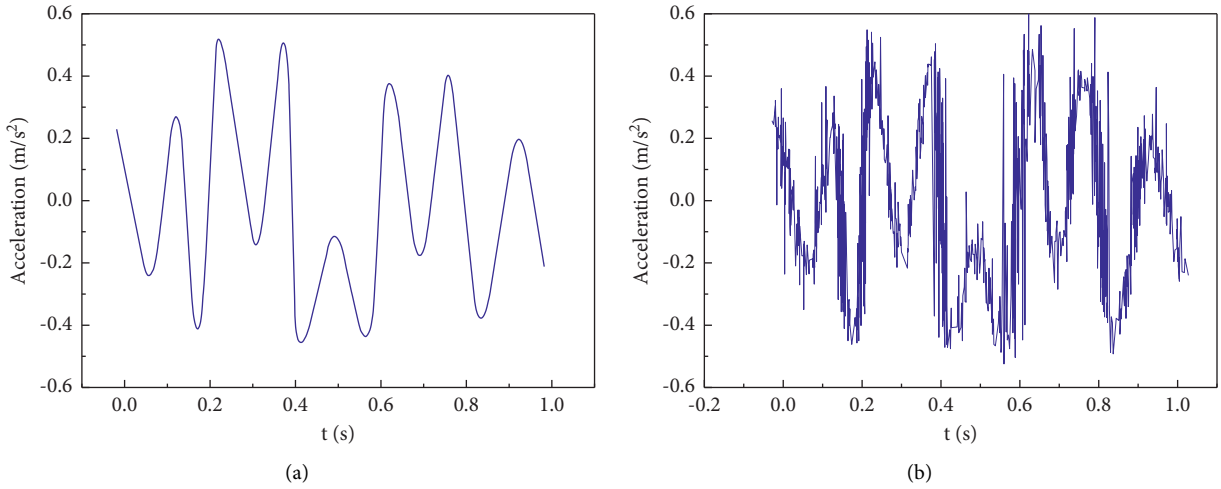

Figure 4: Simulated building vibration signal without and with noise.

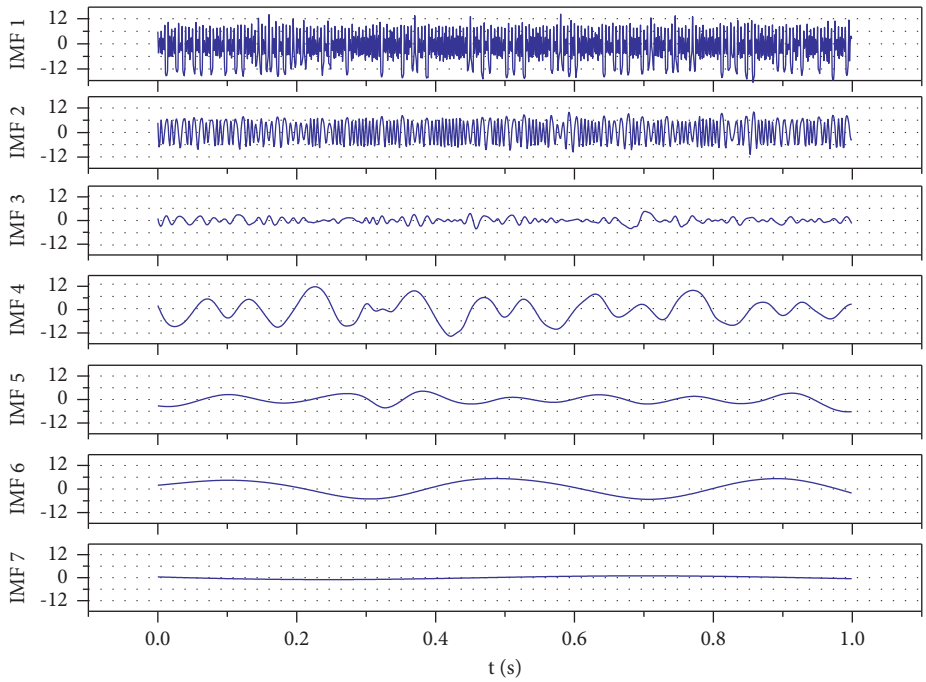

Figure 5: IMFs decomposed from building vibration signal using IEMD-IWFD.

compared to the IEMD-IWFD. And the frequency change in IMFs is distinct: high-frequency IMF components are mainly concentrated in IMF1, while IMF2 and IMF3 show relatively high-frequency signals.

Many experimental studies revealed many statistical characteristics of noise after decomposition. In fact, each IMF component complies with the normal distribution. After the signal mixed with noise is decomposed, the IMF component with a small ordinal number mainly contains the highest frequency part of the noise, while the IMF component with a large ordinal number mainly contains the lowest frequency part of the noise. The frequency-domain characteristic of noise is destroyed. The noise in each IMF component is no longer the real noise, but still has the statistical features of noise. With the similar distribution of the general noise autocorrelation function, the autocorrelation function of the noise in each IMF component reaches its maximum value at zero and rapidly decays to zero at other points.

Figure 7 shows the autocorrelation function calculated for the decomposed IMFs by IEMD-IWFD. According to the distribution characteristics of the signal autocorrelation function, the high frequency part of the noise, useful information components, and low frequency part of the noise are mainly contained in IMF1-3, IMF4-5, and IMF6-7, respectively. The energy variation curve of the autocorrelation function calculated by IMFs obtained by EMD decomposition is shown in Figure 8. It can be seen that the

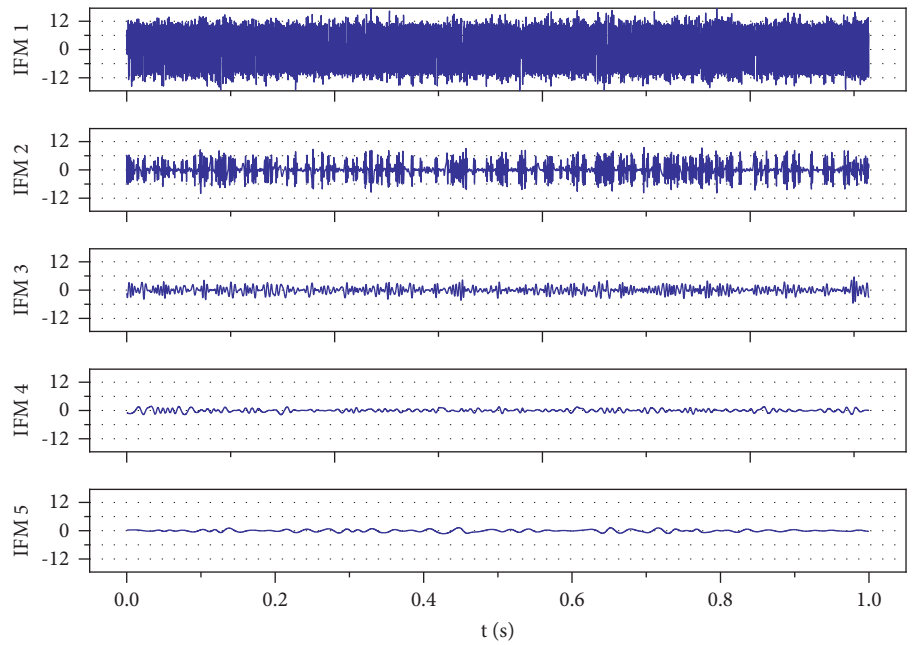

Figure 6: IMFs decomposed from building vibration signals using EMD.

autocorrelation function of IMF1-2 has low energy, while the autocorrelation function of IMF3-4 has high energy. Thus, it is indicated that the decomposed IMFs dominated by useful information by IEMD-IWFD and EMD are IMF4-5 and IMF3-4 components, respectively.

After obtaining the IMF components dominated by useful information, their weight coefficients were obtained by solving the coefficient matrix based on the Hilbert transform, and the target signal was reconstructed as follows. The transformation process of signal extraction time-frequency characteristics is represented by $F[\cdot]$, and the relationship between the mixed signal and an IMF part is represented as

$$\begin{aligned} \mathrm{A} \cdot F[IMF] &= F[\widehat{S}], \\ F[IMF] &= \mathrm{A}^{-1} \cdot F[\widehat{S}], \end{aligned} \tag{36}$$

where A is the coefficient matrix related to the time change and $\widehat{S}$ represents the time domain estimate of the source signal. By applying the Hilbert transform to both sides of the equation, the time-frequency relationship of the signal can be transformed into the relationship between time and energy, which can be expressed as

$$H^{-1}[F[IMF]] = H^{-1}\left[A^{-1} \cdot F[\widehat{S}]\right]. \tag{37}$$

In the process of using the time-frequency behavior of each IMF component to reconstruct the time-frequency characteristics of the source signal, the coefficient matrix A essentially represents the weight value of each component at each time node, i.e., the component with the larger A corresponds to the larger correlation with the reference value.

The reconstructed building vibration signal based on IEMD-IWFDM and EMD is shown in Figure 9. It is clear from Figure 9(a) that the reconstructed building vibration signal recovers well which benefits from the good separation of the synthetic building vibration signal. And the signal amplitude slightly changes after the reconstruction because the building vibration signal mainly uses frequency modulation, which leads to the amplitude changes having a relatively small impact on the separation performance. However, it is observable in Figure 9(b) that the noise interference was not exhaustively eliminated in the reconstructed building vibration signal, which indicates that the signal decomposition method of EMD has poorer performance on building vibration signal denoising compared with IEMD-IWFDM.

Figure 10 shows an experimental building vibration signal collected from the high-speed rail station of Changsha, in which the abscissa and ordinate represent frequency and sound level, respectively. The setup was built to maintain the working of train and staff. The vibration of buildings mainly comes from the running of trains. The noise from rails, aerodynamic, and machinery are the major noise sources.

Figure 11 shows the denoised building vibration signal by EMD and the IEMD-IWFD methods. The signal is reconstructed after removing the recognized high-frequency IMF component, which is regarded as a noise signal. As seen, the denoised signal by the conventional EMD method has a serious distortion. Especially at the distance from 0 to 1 km, the signal cannot be effectively recovered. The denoised data from 1 to 6 km is similar to the original echo signal, but still has large fluctuations. The denoised result obtained by the IEMD-IWFD method is much better than the EMD method since the noise can be effectively separated and eliminated and the signal details can be kept to a certain extent.

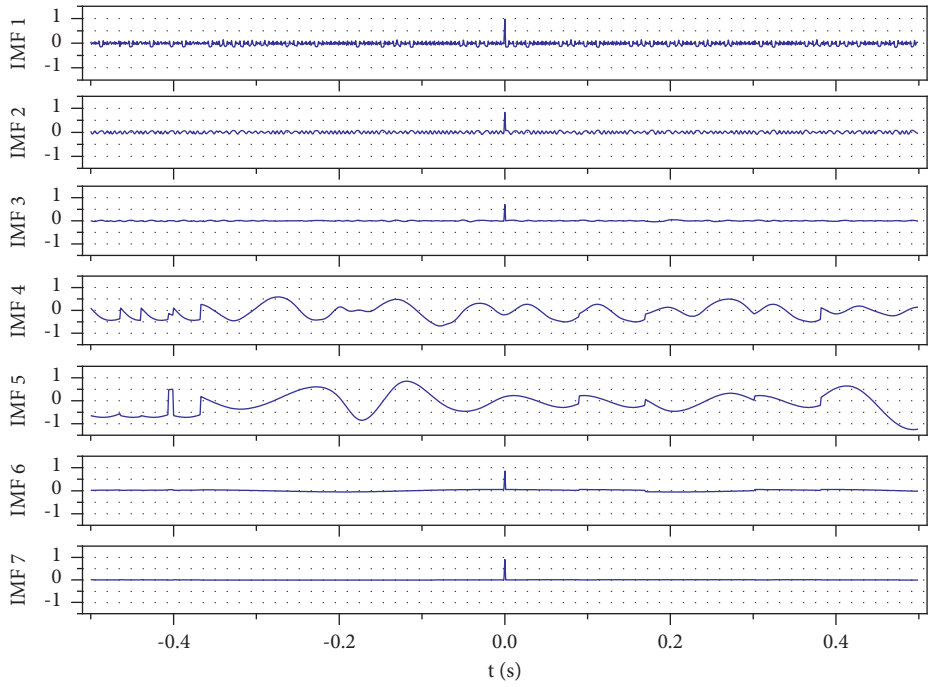

Figure 7: ACF of each IMF by IEMD-IWFD.

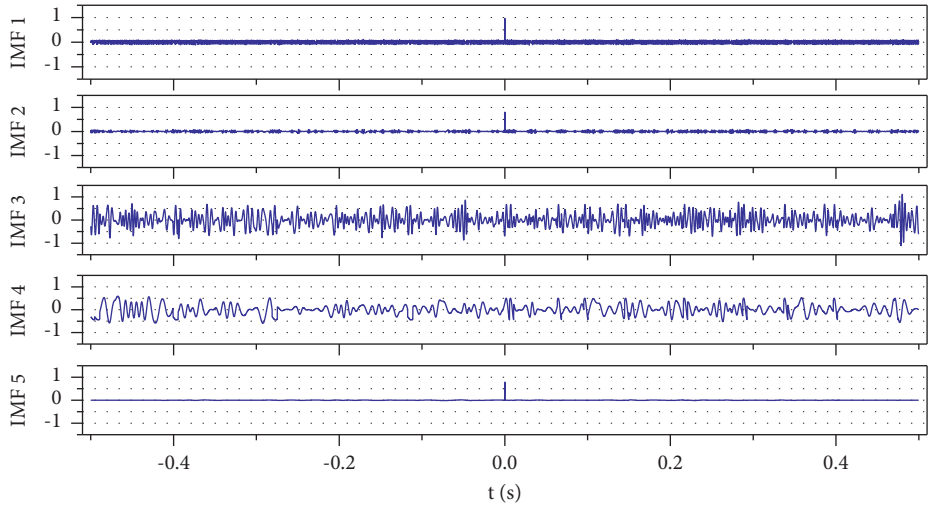

Figure 8: ACF of each IMF by EMD.

The similarity coefficient and the mean square error have been used to assess the degree of denoising performance of the mixed signal based on IEMD-IWFD and EMD.

The similarity coefficient is defined as

$$\varepsilon_i = \frac{\left|\sum_{n=1}^{N} s_i(n) y_i(n)\right|}{\sqrt{\sum_{n=1}^{N} s_i^2(n) \sum_{n=1}^{N} y_i^2(n)}}, \tag{38}$$

where $s(n)$ represents the target signal, i.e., the reference value, and $y(n)$ represents the restricted signal, i.e., the comparison value.

The mean square error of signal is defined as

$$\sigma_i = \sqrt{\frac{1}{N} \sum_{n=1}^{N} \left|z_i(n) - s_i(n)\right|^2}. \tag{39}$$

The similarity coefficient, mean square error, and time-consuming between the reconstructed signal based on IEMD-IWFDM and EMD and the target signal are enumerated in Table 1. The similarity coefficient and mean square error for the IEMD-IWFDM are higher and lower compared to those for the EMD, respectively, which reveals that the target signal can be effectively separated from the building vibration signal corrupted by noise based on the

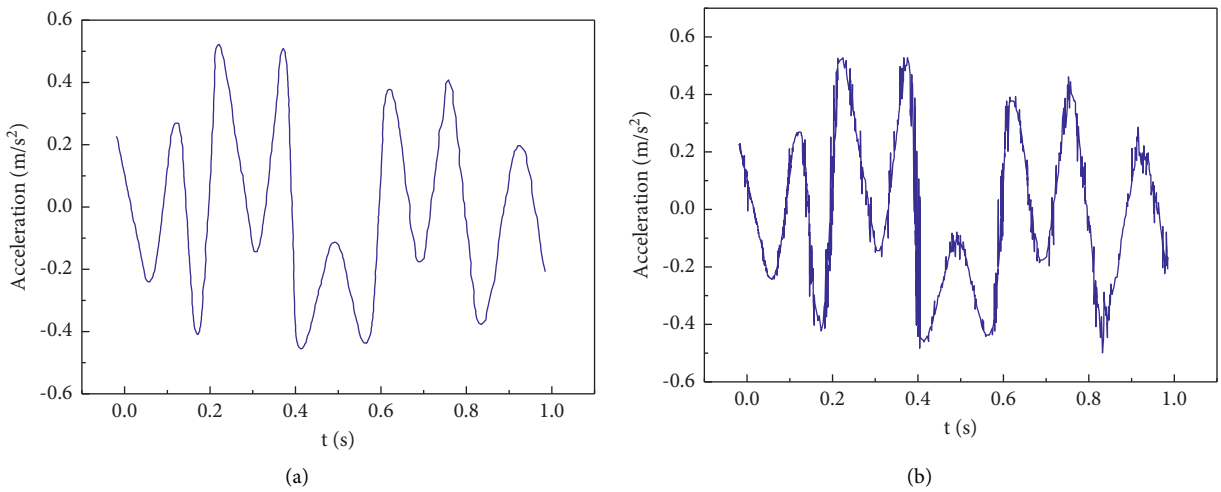

Figure 9: Reconstructed building vibration signal based on decomposed IMFs by IEMD-IWFD and EMD.

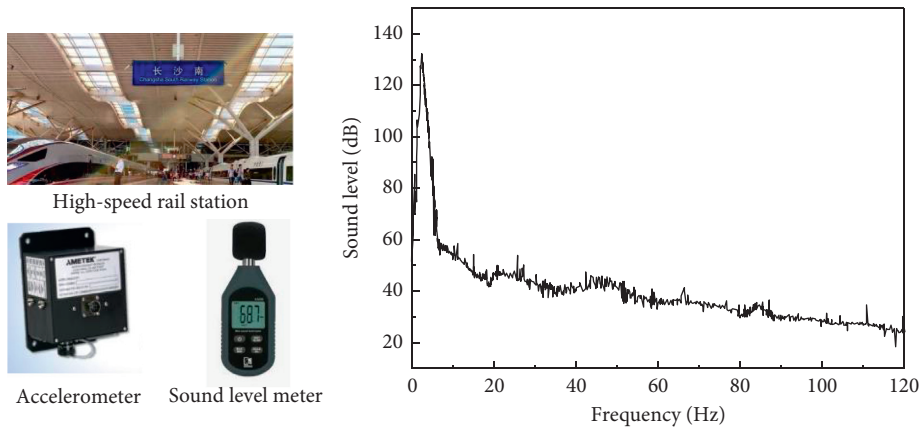

Figure 10: Building vibration signal at a high-speed rail station

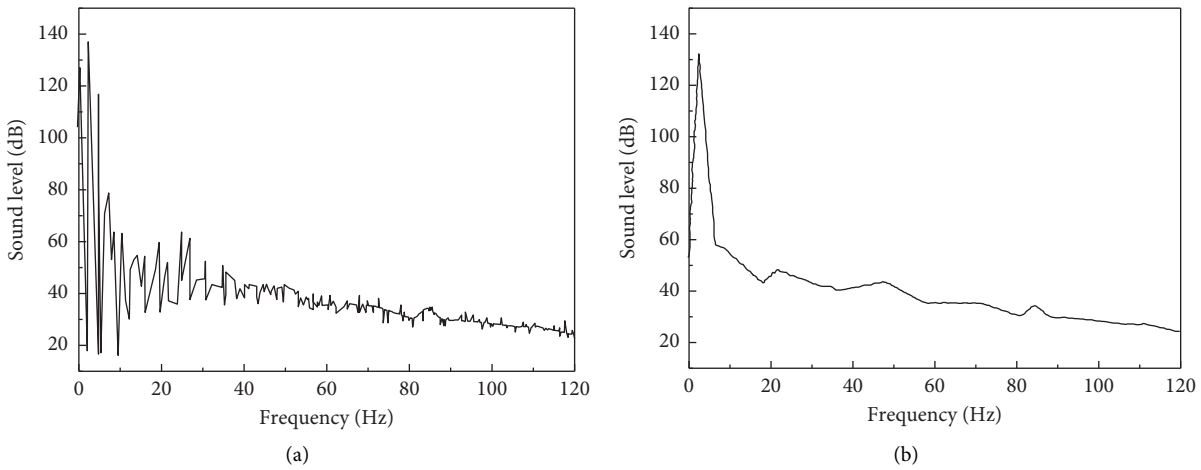

Figure 11: Denoised building vibration signal by EMD and IEMD-IWFD methods.

IEMD-IWFD. The time-consuming performances of EMD and IEMD-IWFDM methods are compared for computational complexity assessment. Obviously, the total CPU time of those methods depends on "the number of extrema points, the length of the signal, the number of IMFs decomposed, and other system setup expenses," which are

Table 1: Evaluation of denoising performance for real building vibration signal.

Parameters	IEMD-IWFDM	EMD
Mean square error	0.06	0.26
Similarity coefficient	0.97	0.62
Times (s)	0.28	0.23

set as the same value to keep the comparability in the simulation. It can be seen from Table 1 that the IEMD-IWFDM is slightly slower than the EMD, but it can achieve a more complete decomposition than the EMD.

4. Conclusion

In this study, a novel signal decomposition method was proposed by coupling the algorithms of IEMD and IWFD, which can be used in the denoising of building vibration signals. A synthetic building vibration was simulated by the combination of a target building vibration signal and a noise signal. It was first decomposed into some IMF components using the novel IEMD-IWFD and traditional EMD methods. The energy criterion of ACF was then employed to determine the IMFs dominated by useful information. Subsequently, the weight coefficient of each useful IMF was obtained by solving the coefficient matrix through the Hilbert transform. And the building vibration signal denoising was finally carried out by reconstructing the useful IMFs. The denoising effects for the IEMD-IWFD and EMD methods were compared by calculating the mean square error and similarity coefficient. The findings portrayed that the new method (IEMD-IWFD) can effectively extract the target signal from the signal corrupted by noise and achieve a better building vibration signal denoising performance. Next, we can make use of these clean signals to carry out statistical classification of feature information extracted from different types and scales and to realize multisource and multiparameter diagnoses of building vibration signals.

Data Availability

All data used to support the findings of this study are included within the article.

Conflicts of Interest

The authors declare that there are no conflicts of interest regarding the publication of this study.

Acknowledgments

The present research was supported by National Natural Science Foundation of China (Grant no. 51478470).

References

[1] J. D. Poston, J. Schloemann, R. M. Buehrer, and P. A. Tarazaga, "Towards indoor localization of pedestrians via smart building vibration sensing," in *Proceedings of the 2015 international conference on localization and GNSS (ICL-GNSS)*, pp. 1–6, IEEE, Gothenburg, Sweden, June 2015.

[2] C. Zou, Y. Wang, P. Wang, and J. Guo, "Measurement of ground and nearby building vibration and noise induced by trains in a metro depot," *The Science of the Total Environment*, vol. 536, pp. 761–773, 2015.

[3] Y. Lei, J. Lu, J. Huang, and S. Chen, "A general synthesis of identification and vibration control of building structures under unknown excitations," *Mechanical Systems and Signal Processing*, vol. 143, p. 106803, 2020.

[4] Q. He, X. Wang, and Q. Zhou, "Vibration sensor data denoising using a time-frequency manifold for machinery fault diagnosis," *Sensors*, vol. 14, pp. 382–402, 2014.

[5] S. Braun, "The synchronous (time domain) average revisited," *Mechanical Systems and Signal Processing*, vol. 25, no. 4, pp. 1087–1102, 2011.

[6] J.-B. Poullet, D. M. Sima, and S. Van Huffel, "MRS signal quantitation: a review of time- and frequency-domain methods," *Journal of Magnetic Resonance*, vol. 195, no. 2, pp. 134–144, 2008.

[7] M. S. McMullen and A. Jameson, "The computational efficiency of non-linear frequency domain methods," *Journal of Computational Physics*, vol. 212, no. 2, pp. 637–661, 2006.

[8] E. Sejdić, K. A. Lowry, J. Bellanca, M. S. Redfern, and J. S. Brach, "A comprehensive assessment of gait accelerometry signals in time, frequency and time-frequency domains," *IEEE Transactions on Neural Systems and Rehabilitation Engineering*, vol. 22, pp. 603–612, 2013.

[9] S. N. Chegini, A. Bagheri, and F. Najafi, "Application of a new EWT-based denoising technique in bearing fault diagnosis," *Measurement*, vol. 144, pp. 275–297, 2019.

[10] S. Hou, M. Liang, and Y. Li, "An optimal global projection denoising algorithm and its application to shaft orbit purification," *Structural Health Monitoring*, vol. 10, no. 6, pp. 603–616, 2011.

[11] G. Fan, J. Li, and H. Hao, "Vibration signal denoising for structural health monitoring by residual convolutional neural networks," *Measurement*, vol. 157, p. 107651, 2020.

[12] M. Zhao and X. Jia, "A novel strategy for signal denoising using reweighted SVD and its applications to weak fault feature enhancement of rotating machinery," *Mechanical Systems and Signal Processing*, vol. 94, pp. 129–147, 2017.

[13] D. S. Singh and Q. Zhao, "Pseudo-fault signal assisted EMD for fault detection and isolation in rotating machines," *Mechanical Systems and Signal Processing*, vol. 81, pp. 202–218, 2016.

[14] J.-H. Ahn, D.-H. Kwak, and B.-H. Koh, "Fault detection of a roller-bearing system through the EMD of a wavelet denoised signal," *Sensors*, vol. 14, no. 8, pp. 15022–15038, 2014.

[15] M. Liu, K. Wang, L. Sun, and J. Zhen, "Applying empirical mode decomposition (EMD) and entropy to diagnose circuit breaker faults," *Optik*, vol. 126, pp. 2338–2342, 2015.

[16] R. Sharma and S. R. Mahadeva Prasanna, "A better decomposition of speech obtained using modified empirical mode decomposition," *Digital Signal Processing*, vol. 58, pp. 26–39, 2016.

[17] O. Niang, É. Delechelle, and J. Lemoine, "A spectral approach for sifting process in empirical mode decomposition," *IEEE Transactions on Signal Processing*, vol. 58, no. 11, pp. 5612–5623, 2010.

[18] Y. B. Li, M. Q. Xu, Y. Wei, and W. H. Huang, "Diagnostics of reciprocating compressor fault based on a new envelope algorithm of empirical mode decomposition," *Journal of Vibroengineering*, vol. 16, pp. 2269–2286, 2014.

[19] H. Li, L. Li, and D. Zhao, "An improved EMD method with modified envelope algorithm based on C2 piecewise rational cubic spline interpolation for EMI signal decomposition," *Applied Mathematics and Computation*, vol. 335, pp. 112–123, 2018.

[20] J. Gilles, "Empirical wavelet transform," *IEEE Transactions on Signal Processing*, vol. 61, pp. 3999–4010, 2013.

[21] B. Boashash and S. Ouelha, "Efficient software platform TFSAP 7.1 and Matlab package to compute Time–Frequency Distributions and related Time-Scale methods with extraction of signal characteristics," *Software*, vol. 8, pp. 48–52, 2018.

[22] H. Li, L. Li, D. Zhao, J. Chen, and P. Wang, "Reconstruction and basis function construction of electromagnetic interference source signals based on Toeplitz-based singular value decomposition," *IET Signal Processing*, vol. 11, pp. 59–65, 2016.

[23] M. Salgarello, G. Visconti, and L. Barone-Adesi, "Interlocking circumareolar suture with undyed polyamide thread: a personal experience," *Aesthetic Plastic Surgery*, vol. 37, pp. 1061-1062, 2013.

[24] H. Ji, J. Long, Y. Fu, Z. Huang, B. Wang, and H. Li, "Flow pattern identification based on EMD and LS-SVM for gas–liquid two-phase flow in a minichannel," *IEEE Transactions on Instrumentation and Measurement*, vol. 60, pp. 1917–1924, 2011.

[25] S. A. Abdul Karim and K. Voon Pang, "Shape preserving interpolation using rational cubic spline," *Journal of Applied Mathematics*, vol. 8, no. 2, pp. 167–178, 2016.

[26] M. Abbas, A. A. Majid, and J. M. Ali, "Monotonicity-preserving C2 rational cubic spline for monotone data," *Applied Mathematics and Computation*, vol. 219, pp. 2885–2895, 2012.

[27] P. Lamberti and C. Manni, "Shape-preserving C2 functional interpolation via parametric cubics," *Numerical Algorithms*, vol. 28, pp. 229–254, 2001.

[28] R. G. Andrzejak, K. Schindler, and C. Rummel, "Nonrandomness, nonlinear dependence, and nonstationarity of electroencephalographic recordings from epilepsy patients," *Physical Review*, vol. 86, p. 046206, 2012.

[29] P. Singh, S. D. Joshi, R. K. Patney, and K. Saha, "The Fourier decomposition method for nonlinear and non-stationary time series analysis," *Proceedings of the Royal Society A: Mathematical, Physical & Engineering Sciences*, vol. 473, p. 20160871, 2017.

[30] F. Rossi and A. Nicolini, "A simple model to predict train-induced vibration: theoretical formulation and experimental validation," *Environmental Impact Assessment Review*, vol. 23, pp. 305–329, 2003.

[31] P. Nassiri, M. Abbaspour, M. Mahmoodi, and S. Givargis, "A rail noise prediction model for the Tehran-Karaj commuter train," *Applied Acoustics*, vol. 68, pp. 326–333, 2007.

Hindawi
Shock and Vibration
Volume 2021, Article ID 4469251, 10 pages
https://doi.org/10.1155/2021/4469251

Research Article

Analysis and Experimental Investigation of Vibration Characteristics of Rotary Platform of Hydraulic Excavator under Complex Working Conditions

Tinghao Li,[1,2] Fuxiu Liu,[1] Zhaojun Li,[1] Mingjin Lu,[1] and Qiulu He[1]

[1]*College of Mechanical Engineering, Guangxi University, Nanning 530004, China*
[2]*Institute of Systems Engineering, Macau University of Science and Technology, Macau 999078, China*

Correspondence should be addressed to Zhaojun Li; lizhaojun@gxu.edu.cn

Received 7 September 2021; Revised 19 October 2021; Accepted 6 November 2021; Published 3 December 2021

Academic Editor: Jiaqiang E.

The rotary platform is the load-bearing substrate of a hydraulic excavator. The dynamic characteristics of the rotary platform directly affect the reliability and safety of the whole machine of a hydraulic excavator. In this work, the characteristics of the main external excitations acting on the hydraulic excavator such as the engine excitation, pressure pulsation excitation of the piston pump, inertial excitation of the working device, and road excitation are analyzed. The vibration transmission paths under the action of external excitations are ascertained. A vibration test method for the rotary platform of the hydraulic excavator is proposed. The vibration characteristics of the rotary platform under complex working conditions are researched, and the internal relationships between the vibration characteristics of the rotary platform and the engine excitation, pressure pulsation excitation of the piston pump, and road excitation are analyzed experimentally. The results show that the rotary platform is subjected to different excitations when it is under different working conditions. Moreover, the internal relationships between the dynamic characteristics of the rotary platform and the external excitation characteristics can be discovered by analyzing the vibration signals of the rotary platform, and the dynamic characteristics of the whole machine of the hydraulic excavator can be deeply studied based on the vibration characteristics of the rotary platform.

1. Introduction

Hydraulic excavators are widely used in many fields and play a very important role in reducing manual labor and improving labor production efficiency [1]. They are not only used in the field of mining [2] but also in earthwork construction, such as farmland transformation and demolition [3]. The hydraulic excavator is mainly composed of the rotary platform, cab, working device, engine, hydraulic system, and walking device. The main components are installed on the rotary platform of the hydraulic excavator, which means that the rotary platform is not only the load-bearing substrate of the hydraulic excavator but also an indispensable intermediate link in the vibration transmission path. Obviously, there is a coupling relationship between the rotating platform and the main devices of the hydraulic excavator, such as the power device, working device, and walking device. Thus, the dynamic performance of the rotary platform can effectively reflect the internal relationships between the rotary platform and other devices within the hydraulic excavator. Therefore, to ensure the safe and reliable operation of the hydraulic excavator, it is necessary to analyze the vibration characteristics of the rotary platform.

At present, research works on the dynamics of the rotary platform of hydraulic excavators have mainly focused on theoretical and simulation studies. For example, Li et al. [4] calculated the natural frequencies and mode shapes of the rotary platform of the hydraulic excavator and proposed a method to avoid the resonance of the rotary platform by modifying its structure. The result showed that the root mean square value of the vibration acceleration of the improved prototype cab is 0.12 m/s^2, which is lower than the value of 0.25 m/s^2 before improvement. Zhang et al. [5]

found the weak points of the structure of the rotary platform of the hydraulic excavator using the finite element method, allowing its stability and overall performance to be enhanced. The result showed that the maximum composite stress in the fatigue failure area under all working conditions decreased from 172.46 MPa to 123.82 MPa. Yang et al. [6] established a coupled lateral-torsional vibration model of the rotary mechanism of the hydraulic excavator by considering the rotary platform as an equivalent rotational inertia unit. Jovanović et al. [7] developed software to enable the determination and detailed analysis of the slewing bearing load in the entire working range of the excavator. Qin et al. [8] proposed a hydraulic-electric hybrid excavator swing drive system. They verified that the energy consumption of the proposed system was reduced by 37.26%~53.29% within a swing working cycle compared with the original system, and the backswing phenomenon of the swing system is suppressed. However, there have been few theoretical research studies on the vibration response of the rotary platform of a hydraulic excavator under complex working conditions.

Experimental investigations are an important method for studying the dynamic characteristics of mechanical structures. Therefore, increasing attention has focused on experimental research studies. For example, Wei et al. [9] undertook experiments to investigate the vibration response performances of a rotating beam with respect to the intensity of the electric field, rotation speed, and acceleration. They found that the vibration of the beam caused by the rotating motion at different rotating speeds and acceleration could be quickly suppressed by applying the electric field to the ER beam and evaluated the feasibility of ER fluid in attenuating the vibration of rotating beams. Zheng et al. [10] dealt with the modeling and analysis of random vibration tests with six degrees of freedom, involving an advanced multi-input/multioutput system in which three translational and three rotational motions could be simultaneously controlled. Jiang et al. [11] provided an alternative method for testing the low-frequency vibration of a huge bucket-wheel excavator and obtained accurate estimates of the low natural frequencies of the bucket-wheel excavator. Hydraulic excavators are a complex vibration system; therefore, experimental investigations are important to reveal their vibration characteristics. At present, experimental investigations of the vibration characteristics of hydraulic excavators are mainly focused on the vibration characteristics of the cab. For example, Alphin et al. [12] regarded whole-body vibration to be a major health hazard among operators, so they conducted field measurements of the whole-body vibration in tracked excavators with a breaker by using a standard vibration measurement system. The experimental result showed that the vibration dose value recorded was 17.6–62.72 m/s$^{1.75}$, and whole-body vibration exposure of the breaker operator was much higher and lies beyond the upper limit as given in ISO 2631-1. Lu and Zhou [13] processed the measured seat vibration responses of a hydraulic excavator and identified the vibration signals corresponding to different excitation sources through the time-frequency analysis method combined with ensemble empirical mode decomposition and a continuous wavelet transform. Wang et al. [14] proposed measures to improve the vibration characteristics of the cab following vibration testing of hydraulic excavators. The result showed that the vibration isolation performance of the improved prototype cab was obviously improved below 40 Hz and above 200 Hz. Pang et al. [15] built an operational transfer path analysis model of vibration from the engine to the cab seat using the vibration test data of an excavator under working conditions. The result showed that the frequency-domain features of the synthesized output signal agree well with those of the test output signal; thus, the model is proved valid. Dąbrowski and Dziurdź [16] present the proposition of a simple estimation of noise and vibration propagation paths of the machine and verify the effectiveness of a proposed procedure on the basis of the analysis of hydraulic excavator. They found that this procedure helped to minimize the transfer of vibrations of power units in selected frequency ranges that led to the change of overall noise level in operator's cab about 5 dB. However, few experimental studies have investigated the vibration characteristics of the rotary platform under complex working conditions.

In this study, the vibration characteristics of the rotary platform of a hydraulic excavator are tested and studied under complex working conditions. The aim of this study is to comprehensively analyze the influence of various excitations on the dynamic characteristics of the rotary platform and to provide a useful basis for discovering the coupling relationships between the rotary platform and other related devices of the hydraulic excavator.

The CLG906D tracked hydraulic excavator is taken as the research object in this study, as shown in Figure 1.

2. Analysis of Vibration Characteristics of Rotary Platform

2.1. Vibration Characteristic. Using the finite element method, the dynamic equation of the rotary platform of the hydraulic excavator can be established in the form:

$$\mathbf{M}\ddot{\mathbf{U}} + \mathbf{C}\dot{\mathbf{U}} + \mathrm{K}\mathbf{U} = \mathbf{F}, \tag{1}$$

where **M**, **K,** and **C** are the mass matrix, stiffness matrix, and damping matrix of the rotary platform of hydraulic excavator, respectively; $\ddot{\mathbf{U}}$, $\dot{\mathbf{U}}$, and **U** are the generalized acceleration vector, generalized velocity vector, and generalized displacement vector, respectively; **F** is the excitation acting on the hydraulic excavator, including the engine excitation, pressure pulsation excitation of the piston pump, inertial excitation of the working device, and road excitation [17].

According to the dynamic equation (1), the frequency equation of the rotary platform of the hydraulic excavator can be expressed as

$$\left|\mathbf{K} - \omega^2\mathbf{M}\right| = 0, \tag{2}$$

where ω is the natural frequency of the rotary platform of hydraulic excavator.

According to equation (2), the natural frequencies of the rotary platform of the hydraulic excavator can be calculated and the modes of the rotary platform of the hydraulic excavator can also be determined.

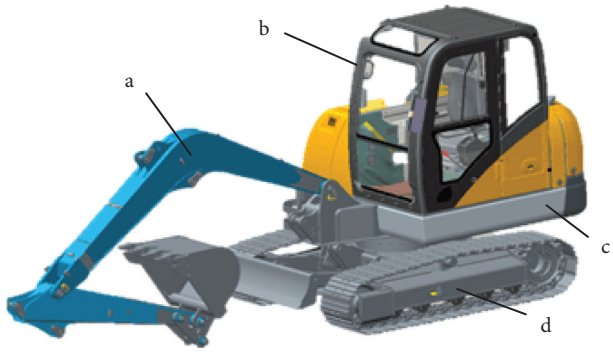

Figure 1: CLG906D tracked hydraulic excavator. (a) Working device. (b) Cab. (c) Rotary platform. (d) Walking device.

According to the dynamic equation (1), the dynamic response of the rotary platform is calculated by the modal superposition method, which can be expressed as

$$\mathbf{U} = \sum_{i=1}^{N} \eta_i(t)\boldsymbol{\varphi}^{(i)}, \tag{3}$$

where $\boldsymbol{\varphi}^{(i)}$ is the i-th order modal vector of the regular modal matrix; $\eta_i(t)$ is the response of the rotary platform under the i-th canonical coordinate; and N is the number of degrees of freedom of the rotary platform.

2.2. Analysis of Main Excitations. Under complex working conditions, the excitations affecting a hydraulic excavator are very complicated. The excitations that impact a hydraulic excavator mainly include the following: the engine excitation, the pressure pulsation excitation of the piston pump, the inertial excitation of the working device, and the road excitation.

2.2.1. Engine Excitation. The engine excitation of a hydraulic excavator mainly comes from the internal cylinder gas pressure during engine operation and the unbalanced inertia forces and moments of inertia caused by the moving mass. For an in-line four-cylinder Yanmar engine, as is often used in hydraulic excavators, the second-order unbalanced inertia force F_1 can be expressed as [18]

$$F_1 = -4m_b\lambda R_w(\pi f_{F1})^2\cos(f_{F1}t), \tag{4}$$

where m_b is the mass of the moving parts; R_w is the crank radius; $\lambda = R_w/l$, l is the rod length; t is the time; and f_{F1} is the frequency of the engine excitation (Hz) and can be expressed as

$$f_{F1} = \frac{n_F}{30}, \tag{5}$$

where n_F is the engine speed.

2.2.2. Pressure Pulsation Excitation of Piston Pump. The piston pump is an important part of the hydraulic system of hydraulic excavator. When a piston pump operates, the pressure pulsation excitation occurs [19]. This is one of the main sources of vibration and noise for the hydraulic excavator. According to the working principle of the piston pump, the pressure pulsation excitation of the piston pump F_2 can be expressed as [20]

$$F_2 = A_K\left(B_0 + \sum_{n=1}^{\infty} B_n\sin(nf_{F2}t + \psi_n)\right), \tag{6}$$

where A_K is the area of the bottom surface of the plunger, B_0 is the pressure pulsation constant term of the piston pump, B_n is the pressure pulsation amplitude of the piston pump, ψ_n is the pressure pulsation phase angle of the piston pump, and B_0, B_n, and ψ_n are related to the structural parameters and material parameters of the piston pump, which can be obtained from reference [20]; f_{F2} is the pressure pulsation excitation frequency of the piston pump (Hz) and can be expressed as

$$f_{F2} = \frac{zn_F}{60}, \tag{7}$$

where z is the number of pistons in the piston pump.

2.2.3. Inertial Excitation of Working Device. In the working process of the hydraulic excavator, the working device often starts and stops. Thus, the working device will generate inertial excitations [21]. As the working device is installed on the rotary platform of the hydraulic excavator, the inertial excitation of the working device is transmitted to the rotary platform through the fixed devices. According to reference [22], the inertial excitation of the working device F_3 can be expressed as

$$F_3 = m_c\frac{\Delta v}{T_c}(1+\tau)(1-\cos f_{F3}t), \tag{8}$$

where m_c is the mass of the working device in the excitation process; Δv is the velocity variation in the excitation process; T_c is the excitation time; τ is the excitation recovery coefficient; and f_{F3} is the inertial excitation frequency of the working device (Hz) and can be expressed as

$$f_{F3} = \frac{2\pi}{T_c}. \tag{9}$$

2.2.4. Road Excitation. The excavator considered in this study is a tracked hydraulic excavator. When the tracked hydraulic excavator moves along an uneven road, the road excitation produces a large low-frequency vibration. Thus, it is necessary to analyze the influence of road excitation on the vibration characteristics of the tracked hydraulic excavator [23].

Let $Z(x)$ be the pavement unevenness function for a pavement length of x. When the tracked hydraulic excavator is traveling at a speed of v, the road excitation can be expressed as [24]

$$s(t) = Z(vt), \tag{10}$$

where $x = vt$ and t is the time; the vertical road excitation frequencies are mainly distributed in the range 8–10 Hz and integer multipliers of this frequency range [24].

2.3. Analysis of Vibration Transmission Path. The essence of vibration transfer is the transfer of energy [25]. To distinguish the vibration characteristics under different excitations, it is necessary to analyze the vibration transmission paths under different excitation types.

The engine is the power source of the hydraulic excavator and the piston pump. The engine output shaft end and the piston pump input shaft end are connected by a rigid coupling, so the engine and the piston pump can be taken as a single system when analyzing the vibration transmission paths. The system composed of the engine and the piston pump is named the engine-piston pump system. The engine-piston pump system has two excitations, namely, engine excitation and pressure pulsation excitation of the piston pump. According to the working principle and structural characteristics of the hydraulic excavator, the engine is fixed on the rotary platform by the connecting bolts. One end of the piston pump shaft is connected to the engine output shaft by the coupling, and the other end of the piston pump shaft is joined by the pipe joint to the hydraulic hoses that are linked with the hydraulic components and the fixed devices [26], that is, the hydraulic components and the fixed devices are directly or indirectly connected with the rotary platform. Therefore, the engine excitation and the pressure pulsation excitation of the piston pump produced by the engine-piston pump system are transmitted to the rotary platform through two paths: (i) the engine excitation and the pressure pulsation excitation of the piston pump are transmitted to the rotary platform through the engine connecting bolts; (ii) the excitations are transmitted to the rotary platform through the hydraulic components and the fixed devices.

When the working device starts and stops, the inertial excitation of the working device can be transmitted to the rotary platform through the fixed devices. This is because the working device is installed on the rotary platform of the hydraulic excavator by the fixed devices. Similarly, according to the structural characteristics of the hydraulic excavator, when the tracked hydraulic excavator moves along an uneven road, the road excitation is transmitted to the rotary platform through the guide wheel, support wheel, driving wheel, and so on. In summary, the main vibration transmission paths of the rotary platform of the hydraulic excavator are shown in Figure 2.

2.4. Analysis of Vibration Transfer Characteristics. Using equation (1), the vibration characteristics of the rotary platform of the hydraulic excavator can be studied. By the Fourier transform of dynamic equation (1), the corresponding displacement frequency response function can be obtained [27]. The rotary platform of the hydraulic excavator is generally a steel structure. For steel structures, the amplitudes of the frequency response function decrease as the distance from the source increases. The location of the excitation source is recorded as x_0, and the amplitude of the frequency response function at the excitation source is recorded as $U(x_0)$. Thus, the amplitude of the frequency response function at a distance of x from the excitation source can be expressed as [28]

$$U(x) = U(x_0)e^{-\beta x}, \tag{11}$$

where β is the attenuation coefficient.

Equation (11) implies that increasing the distance between the measuring point on the rotary platform and the excitation source will produce a smaller amplitude of the frequency response function and enhance the amplitude of vibration attenuation.

2.5. Modal Simulation. The vibration modes of the rotary platform of the hydraulic excavator can be analyzed by using the ANSYS Workbench software. The three-dimensional model of the rotary platform is shown in Figure 3. Here, the first four modes of the rotary platform are analyzed by simulation. The simulation results of the first four-order natural frequencies of the rotary platform are listed in Table 1.

3. Vibration Test of Rotary Platform

3.1. Vibration Test System. Electric measurement methods have many advantages, such as a wide range of testing frequencies and high sensitivity [29]. Thus, an electric measurement method was adopted to collect the vibration signals of the rotary platform. The vibration test site is shown in Figure 4. The instruments used in the vibration test include an ICP three-way acceleration sensor, LMS Test.LAB signal collector, and a notebook computer.

3.2. Measuring Points. The vibration characteristics of measuring point 1 and measuring point 2 on the rotary platform were analyzed experimentally. Measuring point 1 is located at the connection between the engine and the rotary platform, and measuring point 2 is located below the left-hand door of the cab, as shown in Figure 5. Obviously, measuring point 2 is farther away from the engine-piston pump system (the excitation source) than measuring point 1.

3.3. Vibration Signal Acquisition and Processing. In this study, the vibration signals of the rotary platform were collected by an ICP three-way acceleration sensor. According to the sampling theorem, the sampling frequency is selected to be 2,000 Hz because the vibration signals of the rotary platform are generally concentrated below 1,000 Hz.

The frequency-domain analysis method is often used for vibration signal processing because the frequency-domain signals are more intuitive than time-domain signals [30]. As the vibration signals acquired by the acceleration sensor are usually time-domain signals, the FFT transformation function in the LMS Test.Lab system was used to convert the acquired time-domain signals into frequency-domain signals for the analysis of the vibration characteristics.

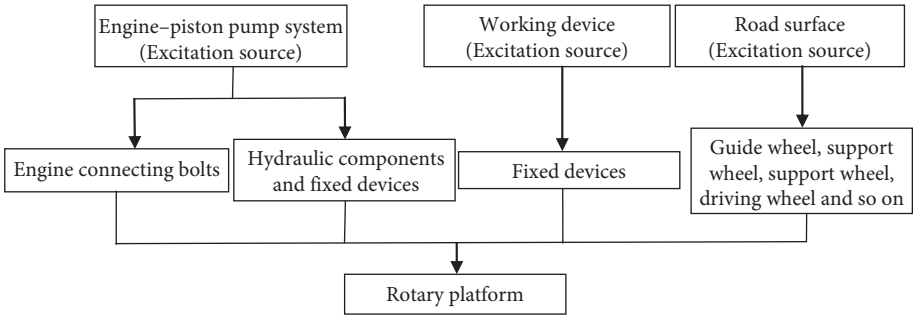

Figure 2: Vibration transmission paths of the rotary platform of hydraulic excavator.

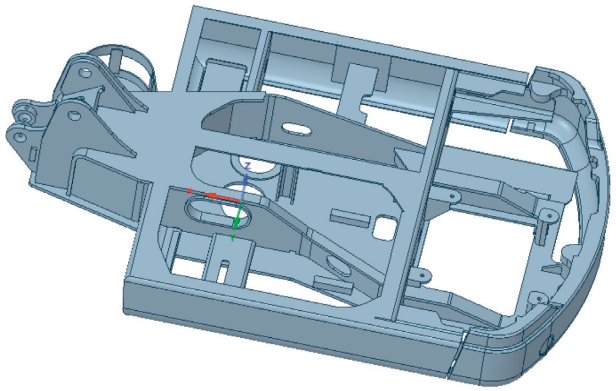

Figure 3: Three-dimensional model of the rotary platform.

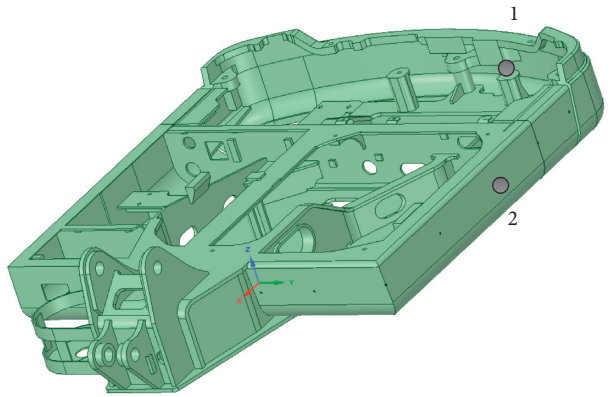

Figure 5: Measuring point positions on the rotary platform.

Table 1: Simulation results of the first four-order natural frequencies of the rotary platform.

Order	Frequency (Hz)	Mode shape
1	10.06	Bending
2	15.43	Torsion
3	16.52	Torsion
4	26.21	Bending

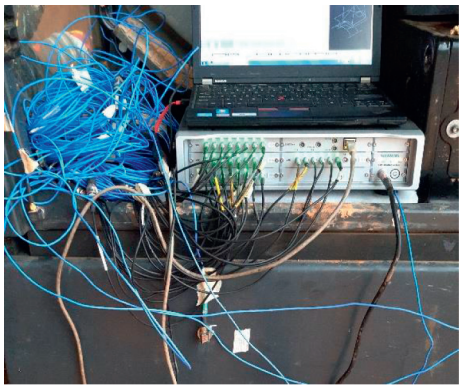

Figure 4: Vibration test site diagram.

4. Analysis of Vibration Test Results of Rotary Platform

4.1. Vibration Test under Fixed Collecting Bucket Condition. The fixed collecting bucket condition provides a modal test of the rotary platform of the hydraulic excavator. Under the fixed collecting bucket condition, the working device of the hydraulic excavator is taken back and the collecting bucket test is carried out. As the working device is installed on the rotary platform of the hydraulic excavator, the rotary platform will be impacted by the inertial excitation of the working device as it retracts, which means that the rotary platform is subjected to a hammer excitation. Therefore, the impact on the rotary platform due to the retraction of the working device is equivalent to a swept-sine vibration test of the rotary platform. In this case, the vibration test under the fixed collecting bucket condition can be regarded as a modal test of the rotary platform.

According to the test data, the first four-order natural frequencies of the rotary platform are obtained as shown in Table 2. By comparing the test results of the first four-order natural frequencies of the rotary platform with the simulation results of the first four natural frequencies of the rotary platform (see Table 1), it can be seen that the modal simulation results are basically consistent with the test results. Therefore, it is feasible to obtain the modal of the rotary platform by experiments under the fixed collecting bucket condition. This provides a novel idea for testing the modal of the rotary platform of hydraulic excavator.

4.2. Vibration Test under Fixed Idle Speed Condition. According to the working principle and structural characteristics of the hydraulic excavator, when it is under the fixed idle speed condition, the engine is in the working state while the hydraulic system is not working. Thus, the excitation

Table 2: Test results of the first four-order natural frequencies of the rotary platform.

Order	Frequency (Hz)	Mode shape
1	10.16	Bending
2	15.31	Torsion
3	16.23	Torsion
4	26.06	Bending

acting on the hydraulic excavator is mainly engine excitation, and the excitation source is the engine-piston pump system.

In Figure 5, measuring point 1 is located between the engine and the rotary platform, and measuring point 2 is the point on the rotary platform located below the left-hand door of the cab. Measuring point 2 is farther away from the engine-piston pump system (the excitation source) than measuring point 1. Therefore, according to the vibration characteristics of measuring points 1 and 2, the vibration characteristics of the rotary platform excited by the engine excitation can be studied and the vibration transmission characteristics of the rotary platform can be analyzed.

Under the fixed idle speed condition, the engine speed is $n_F = 1050$ r/min, and according to equation (5), the engine excitation frequency is $f_{F1} = 35$ Hz. The vibration signals along the direction perpendicular to the rotary platform were obtained under the fixed idle speed condition. The experimental frequency-domain dynamic response characteristic curves of measuring points 1 and 2 under the fixed idle speed condition are shown in Figures 6 and 7, respectively. It can be seen from Figures 6 and 7 that there are obvious vibration peaks at the engine excitation frequency (35 Hz). The experimental results show that the rotary platform is excited by the engine excitation under the fixed idle speed condition, which is consistent with the theoretical analysis.

According to the experimental frequency-domain dynamic response characteristic curves in Figures 6 and 7, the values of the vibration peaks corresponding to the engine excitation frequency at measuring points 1 and 2 are listed in Table 3. It can be seen from Table 3 that the vibration peak value at measuring point 2 is 2.12% of that at measuring point 1. The main reason why the vibration peak value at measuring point 2 is smaller than that at measuring point 1 is that measuring point 2 is farther away from the engine-piston pump system than measuring point 1. According to the vibration transmission characteristics, measuring points farther away from the excitation source will observe greater vibration attenuation.

The above results showed that the vibration signals of the rotary platform revealed the inherent relationship between the vibration characteristics of the rotary platform and the engine excitation under the fixed idle speed condition. Thus, the dynamic characteristics of other related devices of the hydraulic excavator can be analyzed based on the vibration characteristics of the rotary platform because the rotary platform is the indispensable intermediate link in the vibration transmission path of a hydraulic excavator.

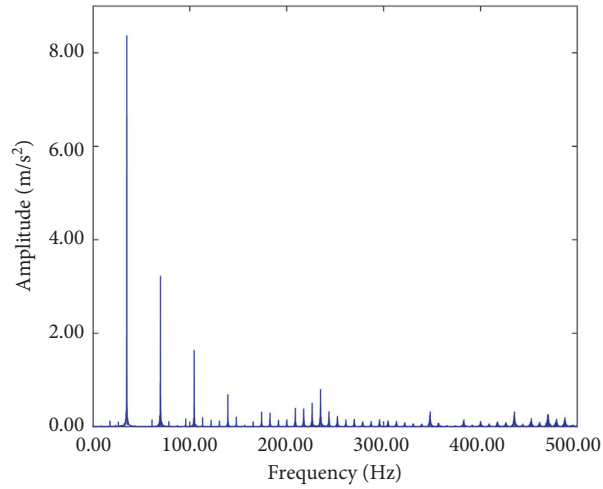

Figure 6: Experimental frequency-domain dynamic response characteristic curves of measuring point 1 in the vertical direction.

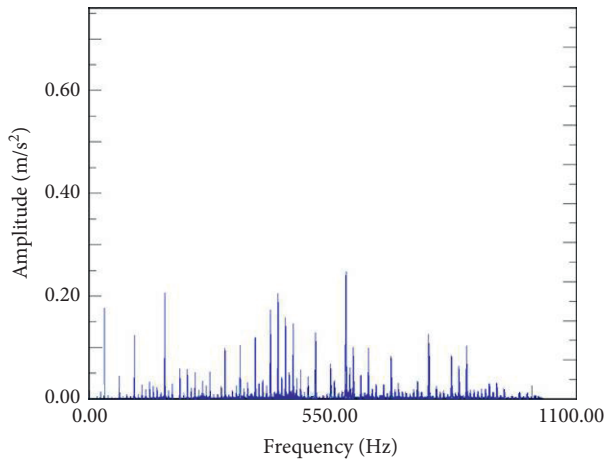

Figure 7: Experimental frequency-domain dynamic response characteristic curves of measuring point 2 in the vertical direction.

4.3. Vibration Test under Fixed Working Condition. According to the working principle and structural characteristics of the hydraulic excavator, under the fixed working condition, both the engine and the hydraulic system are in the working state. Therefore, the excitations acting on the hydraulic excavator are mainly the engine excitation and the pressure pulsation excitation of the piston pump under the fixed working condition, that is, the sources of excitations are all from the engine-piston pump system.

In Figure 5, measuring points 1 and 2 are on the rotary platform of the hydraulic excavator, and measuring point 2 is farther away from the excitation source than measuring point 1. Therefore, based on the vibration characteristics of measuring points 1 and 2, the vibration characteristics of the rotary platform simultaneously excited by the engine excitation and the pressure pulsation excitation of the piston pump can be studied and the vibration transmission characteristics of the rotary platform can be analyzed.

Under the fixed working condition, the engine speed is $n_F = 2250$ r/min; according to equation (5), the engine

Table 3: Comparative analysis of vibration test results under fixed idle speed condition.

Measuring point	Frequency corresponding to vibration peak (Hz)	Vibration peak value (m/s^2)
1	34.81	8.51
2	35.46	0.18

excitation frequency is $f_{F1} = 75$ Hz. As the number of pistons in the plunger pump is $z = 10$, equation (7) implies that the pressure pulsation excitation frequency of the piston pump is $f_{F2} = 375$ Hz.

The vibration signals along the direction perpendicular to the rotary platform were obtained by the experiments under the fixed working condition. The experimental frequency-domain dynamic response characteristic curves of measuring points 1 and 2 under the fixed working condition of constant speed rotation are shown in Figures 8 and 9, respectively. It can be seen from Figures 8 and 9 that there are obvious vibration peaks at the pressure pulsation excitation frequency (375 Hz) and the engine excitation frequency (75 Hz). The experimental results show that the rotary platform is simultaneously excited by the engine excitation and the pressure pulsation excitation under the fixed working condition, which is consistent with the theoretical analysis results.

According to the experimental frequency-domain dynamic response characteristic curves in Figures 8 and 9, the values of vibration peaks corresponding to the pressure pulsation excitation frequency (375 Hz) and the engine excitation frequency (75 Hz) at measuring points 1 and 2 are listed in Table 4. It can be seen from Table 4 that the vibration peak value corresponding to the pressure pulsation excitation frequency (375 Hz) at measuring point 2 is 67.13% of that at measuring point 1, that is, when the vibration excited by the pressure pulsation excitation of the piston pump is transmitted from measuring point 1 to measuring point 2, the vibration amplitude suffers an attenuation of 32.87%. Moreover, the vibration peak value corresponding to the engine excitation frequency (75 Hz) at measuring point 2 is 22.92% of that at measuring point 1, that is, the vibration excited by the engine excitation suffers an attenuation of 77.08% from measuring point 1 to measuring point 2.

According to the above results, the rotary platform is simultaneously excited by the engine excitation and the pressure pulsation excitation under the fixed working condition. When different excitations are acting on the rotary platform, the vibration characteristics and the vibration transfer characteristics of the rotary platform are not identical. Moreover, the above results also showed that the vibration signals of the rotary platform revealed the inherent relationship between the vibration characteristics of the rotary platform and the engine excitation and pressure pulsation excitation of the piston pump under the fixed working condition. Because the rotary platform is the load-bearing substrate of the hydraulic excavator, the dynamic characteristics of other related devices can be studied by analyzing both the vibration characteristics of the rotary platform and the coupling relationship between the rotating platform and other devices of the hydraulic excavator.

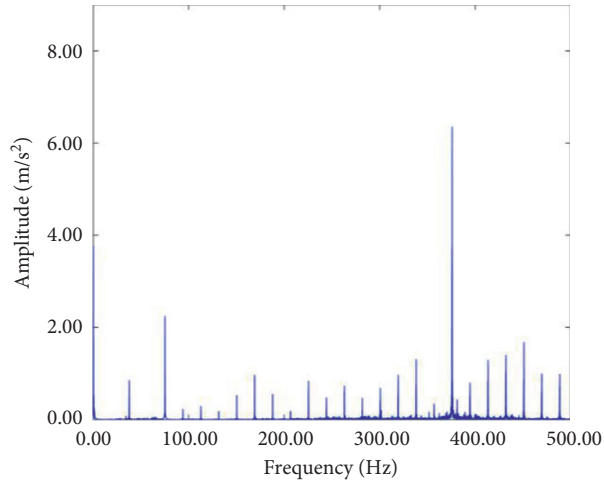

Figure 8: Experimental frequency-domain dynamic response characteristic curves of measuring point 1 in the vertical direction.

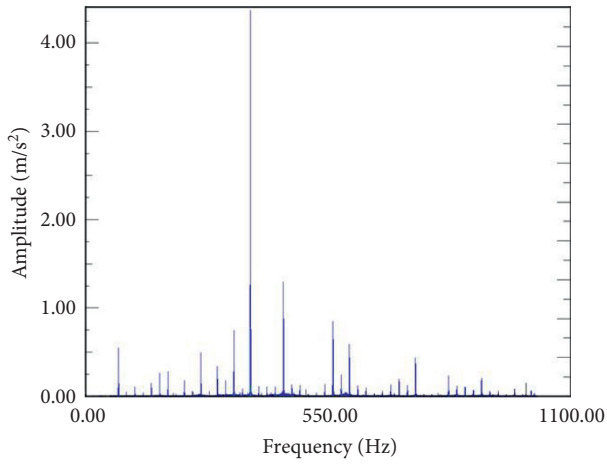

Figure 9: Experimental frequency-domain dynamic response characteristic curves of measuring point 2 in the vertical direction.

4.4. Vibration Test under Walking Condition. According to the working principle and structural characteristics of the hydraulic excavator, when the hydraulic excavator is under the walking condition, both the engine and the hydraulic system are in the working state, that is, under the walking condition, the hydraulic excavator is not only subject to the road excitation but also receives the engine excitation and the pressure pulsation excitation of the piston pump. Thus, the vibration characteristics of the rotary platform will be very complicated.

The vibration transmission characteristics of the rotary platform of the hydraulic excavator have been analyzed in Sections 4.2 and Sections 4.3 under the fixed idling conditions and the fixed working conditions, respectively. Here,

Table 4: Comparative analysis of vibration test results under fixed working condition.

Measuring point	Frequency corresponding to vibration peak (Hz)	Vibration peak value (m/s^2)
1	375.86	6.51
	75.14	2.40
2	374.49	4.37
	74.99	0.55

based on the experimental vibration signals at measuring point 2, the vibration characteristics of the rotary platform are analyzed when the rotary platform is simultaneously excited by the road excitation, the engine excitation, and the pressure pulsation excitation of the piston pump.

Under the walking condition, the engine speed is $n_F = 2250$ r/min; according to equation (5), the engine excitation frequency is $f_{F1} = 75$ Hz. As the number of pistons in the piston pump is $z = 10$, equation (7) gives the pressure pulsation excitation frequency to be $f_{F2} = 375$ Hz. Moreover, the road excitation must be considered when the hydraulic excavator is under the walking condition. According to equation (10) and reference [24], the road excitation frequencies are mainly distributed in the range 8–10 Hz and its integer multipliers.

The vibration signals along the direction perpendicular to the rotary platform were obtained by experiments under the walking condition. The experimental frequency-domain dynamic response characteristic curves of measuring point 2 under the rabbit speed walking condition is shown in Figure 10. It can be seen that there is an obvious vibration peak near the pressure pulsation excitation frequency (375 Hz), where the peak value is 1.77 m/s^2, and there is a vibration peak near the engine excitation frequency (75 Hz), where the peak value is 0.68 m/s^2, that is, the rotary platform of the hydraulic excavator is affected by the pressure pulsation excitation of the piston pump and the engine excitation. Figure 10 also indicates that there are very dense frequencies in the low-frequency range of the vibration signal, and these are mainly caused by road excitation. According to these results, it is clear that under the walking condition, the hydraulic excavator is not only excited by the road excitation but also by the engine excitation and the pressure pulsation excitation of the piston pump. Moreover, the above results also showed that the vibration signals of the rotary platform revealed the inherent relationship between the vibration characteristics of the rotary platform and the engine excitation, pressure pulsation excitation of the piston pump, and road excitation under the walking condition. Thus, according to the vibration characteristics of the rotary platform, the dynamic characteristics of other related devices can also be analyzed.

In summary, under complex working conditions such as a fixed idle speed, fixed working conditions, and walking conditions, the internal relationships between the vibration characteristics of the rotary platform and the external excitation characteristics can be analyzed by observing the vibration signals of the rotary platform. As the rotary platform is the indispensable intermediate link in the vibration transmission path of a hydraulic excavator, the dynamic characteristics of the whole machine of the hydraulic excavator can be effectively analyzed based on the vibration characteristics of the rotary platform. This provides a new idea for deeply studying the dynamic characteristics of the whole machine of the hydraulic excavator under complex working conditions.

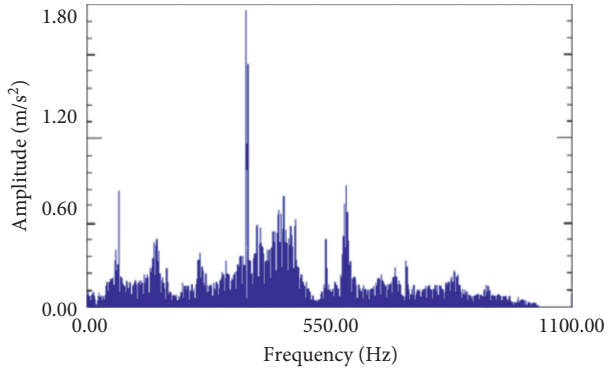

Figure 10: Experimental frequency-domain dynamic response characteristic curves of measuring point 2 in the vertical direction.

5. Conclusions

The hydraulic excavator was taken as the research object in this study. The vibration characteristics of the rotary platform of the hydraulic excavator were studied theoretically and experimentally. The studies show that

(1) The vibration of the rotary platform can be excited effectively by the inertial excitation of the working device as it retracts, which is equivalent to a swept-sine vibration test of the rotary platform. By the vibration test, the first four natural frequencies of the rotary platform are obtained, and the results are verified by the corresponding simulation results. It is found that the vibration test under the fixed collecting bucket condition can provide a novel and effective method for testing the modal of the rotary platform.

(2) The vibration signals of the rotary platform revealed the inherent relationship between the vibration characteristics of the rotary platform and the main excitations under complex working conditions. Moreover, the dynamic characteristics of other related devices can be studied by analyzing both the vibration characteristics of the rotary platform and the coupling relationship between the rotating platform and other devices of the hydraulic excavator.

(3) Under the fixed working condition, the vibration peak values at measuring points 1 and 2 that are

excited by the pressure pulsation excitation of the piston pump are 6.51 m/s^2 and 4.37 m/s^2, respectively, and the corresponding vibration peak values that are excited by the engine excitation are 2.40 m/s^2 and 0.55 m/s^2, respectively. The results show that the influence of the pressure pulsation excitation of the piston pump on the dynamic characteristics of the rotary platform is much greater than that of engine excitation under the fixed working condition.

Data Availability

The data used to support the findings of this study are available from the corresponding author upon request.

Conflicts of Interest

The authors declare that they have no conflicts of interest.

Acknowledgments

This research was supported by the National Natural Science Foundation of China under grant no. 51465001.

References

[1] H. Ding, L. Han, W. Yang, and C. Wu, "Kinematics and dynamics analyses of a new type face-shovel hydraulic excavator," *Proceedings of the Institution of Mechanical Engineers, Part C: Journal of Mechanical Engineering Science*, vol. 231, no. 5, pp. 909–924, 2017.

[2] Y. Li, X. Mu, and R. Fan, "Multi-objective optimization and simulation of novel working mechanism for face-shovel excavator," *International Journal of Intelligent Robotics and Applications*, vol. 5, no. 1, pp. 1–9, 2021.

[3] F. Morosi, M. Rossoni, and G. Caruso, "Coordinated control paradigm for hydraulic excavator with haptic device," *Automation in Construction*, vol. 105, Article ID 102848, 2019.

[4] Z. Li, W. P. Ding, W. Ding, R. Song, and X. C. Xu, "NVH improvement of hydraulic excavator based on modal analysis of rotary platform," *Coal Mine Machinery*, vol. 33, no. 1, pp. 191–193, 2012.

[5] W. Zhang, Q. He, and H. B. Wang, "Finite element analysis and improvement of the revolving platform of hydraulic excavator," *Journal of Xuzhou Institute of Technology (Natural Sciences Edition)*, vol. 28, no. 3, pp. 64–68, 2013.

[6] X. J. Yang, G. H. Xu, Z. J. Li, and R. G. Wang, "Dynamic modeling and response analysis of lateral-torsional coupling vibration of the slewing mechanism of a hydraulic excavator," *Advanced Materials Research*, vol. 753-755, pp. 1755–1759, 2013.

[7] V. Jovanović, D. Janošević, and N. Petrović, "Analysis of slewing bearing load of a rotating platform drive in hydraulic excavators," *Technical Gazette*, vol. 21, no. 2, pp. 263–270, 2014.

[8] T. Qin, L. Ge, W. N. Huang, and L. You, "Operation characteristics and energy efficiency of swing drive system of hydraulic-electric hybrid excavator," *Machine Tool & Hydraulics*, vol. 49, no. 8, pp. 111–116, 2021.

[9] K. Wei, G. Meng, S. Zhou, and J. Liu, "Vibration control of variable speed/acceleration rotating beams using smart materials," *Journal of Sound and Vibration*, vol. 298, no. 4-5, pp. 1150–1158, 2006.

[10] R. Zheng, H. Chen, A. Angeli, and D. Vandepitte, "A simplified modelling and analysis of six degree of freedom random vibration test," *Mechanical Systems and Signal Processing*, vol. 150, Article ID 107304, 2021.

[11] Y. Z. Jiang, C. J. Liu, X. J. Li, K. F. He, and D. M. Xiao, "Low-frequency vibration testing of huge bucket wheel excavator based on step-decay signals," *Shock and Vibration*, vol. 2018, Article ID 6182156, 7 pages, 2018.

[12] M. S. Alphin, K. Sankaranarayanasamy, and S. P. Sivapirakasam, "Experimental evaluation of whole body vibration exposure from tracked excavators with hydraulic breaker attachment in rock breaking operations," *Journal of Low Frequency Noise, Vibration and Active Control*, vol. 29, no. 2, pp. 101–110, 2010.

[13] D. Lu and Y. Q. Zhou, "Vibration analysis of excavator seat based on EEMD and CWT," *Journal of Shandong University (Engineering Science)*, vol. 45, no. 3, pp. 58–64, 2015.

[14] F. Wang, D. Q. Wang, and Y. Liu, "Hydraulic excavator cab vibration testing and research of vibration reduction," *Construction Mechanization*, vol. 35, no. 1, pp. 49–51, 2014.

[15] X. K. Pang, Y. Q. Zhou, W. Tang, L. Wang, and Y. Z. Mi, "Excavator seat vibration investigation based on operational transfer path analysis," *Journal of Vibration and Shock*, vol. 34, no. 9, pp. 171–176, 2015.

[16] Z. Dąbrowski and J. Dziurdź, "Simultaneous analysis of vibrations and noise in the task of minimizing vibroacoustic activity of machines," *Archives of Acoustics*, vol. 41, no. 2, pp. 303–308, 2016.

[17] Z. J. Li, T. Mao, S. X. Liu, and G. H. Liang, "Dynamic equations of hydraulic excavator slewing transmission mechanism–working device system," *Equipment Manufacturing Technology*, vol. 19, no. 2, pp. 1–5, 2012.

[18] G. R. Zhang, D. J. Yu, L. Y. Yao, and X. G. Zang, "Study on automotive interior structural noise excited by engines," *Noise and Vibration Control*, vol. 30, no. 1, pp. 44–47, 2010.

[19] P. Casoli, M. Pastori, F. Scolari, and M. Rundo, "Active pressure ripple control in axial piston pumps through high-frequency swash plate oscillations-A theoretical analysis," *Energies*, vol. 12, no. 7, p. 1377, 2019.

[20] Z. J. Li, Y. Y. Huang, and Y. Sun, "Effect of the piston pump pressure pulsation on the vibration characteristics of the hydraulic excavator," *Chinese Hydraulics & Pneumatics*, vol. 45, no. 2, pp. 77–84, 2021.

[21] J. Chen, F. Qing, and X. Pang, "Mechanism optimal design of backhoe hydraulic excavator working device based on digging paths," *Journal of Mechanical Science and Technology*, vol. 28, no. 1, pp. 213–222, 2014.

[22] B. V. Chapnik, G. R. Heppler, and J. D. Aplevich, "Modeling impact on a one-link flexible robotic arm," *IEEE Transactions on Robotics and Automation*, vol. 7, no. 4, pp. 479–488, 1991.

[23] J. F. Jia, J. Q. Zhang, J. Zhang, Y. L. Liu, Y. Q. Gao, and J. Yue, "Ride comfort simulation of tracked vehicles from stochastic excitation based on road surface spectrum," *Journal of System Simulation*, vol. 24, no. 6, pp. 1350–1354, 2012.

[24] Y. Sun, *Study on Vibration Mechanism and Vibration Control Method of Excavator Cab*, Guangxi University, Nanning, China, 2018.

[25] A. Bedotti, M. Pastori, and P. Casoli, "Modelling and energy comparison of system layouts for a hydraulic excavator," *Energy Procedia*, vol. 148, pp. 26–33, 2018.

[26] X. F. Liu, W. Zhang, J. L. Liu, and L. P. Liu, "Design and research on selection for seal of hydraulic system and oil inlet of pipe joint," *Chinese Hydraulics & Pneumatics*, vol. 42, no. 12, pp. 97–101, 2018.

[27] Z. H. Liu, Q. H. Gao, Z. Liu, and X. Wang, "In-plane rigid-elastic coupling dynamic modeling and vibration response prediction of heavy duty radial tire," *Acta Armamentarii*, vol. 39, no. 2, pp. 224–233, 2018.
[28] X. Zhang, X. Li, C. X. Hao et al., "Experimentation on vibration transmission characteristics of modern tram tracks," *Journal of Southwest Jiaotong University*, vol. 56, no. 1, pp. 75–83, 2021.
[29] G. Y. Ji and C. S. Zhao, "Summary of vibration testing and analysis," *Machine Building & Automation*, vol. 39, no. 3, pp. 1–5, 2010.
[30] L. G. Chen, J. G. Wang, and J. Zhang, "Vibration test and signal analysis of RV reducer," *Journal of Mechanical Transmission*, vol. 42, no. 3, pp. 80–84, 2018.

Hindawi
Shock and Vibration
Volume 2021, Article ID 8699218, 23 pages
https://doi.org/10.1155/2021/8699218

Research Article

Nonlinear Dynamics of Cutting Process considering Higher-Order Deformation of Composite Cutting Tool

Donghui Yao, Yongsheng Ren, Yuhuan Zhang, and Bole Ma

College of Mechanical and Electronic Engineering, Shandong University of Science and Technology, Qingdao 266590, China

Correspondence should be addressed to Yongsheng Ren; renys@sdust.edu.cn

Received 8 September 2021; Revised 28 October 2021; Accepted 10 November 2021; Published 2 December 2021

Academic Editor: Marta Berardengo

In this paper, the nonlinear dynamic analysis of the cutting process of composite cutting tool is performed. The cutting tool is simplified to a nonplanar bending rotating shaft. The higher-order bending deformation, structural damping, and gyroscopic effect of cutting tool are considered. It is assumed that cutting tool is subjected to a regenerative two-dimensional cutting force containing the first and second harmonic components. Based on the Hamilton principle, the motion equation of nonlinear chatter of the cutting system is derived. The nonlinear ordinary differential equations in the generalized coordinates are obtained by Galerkin method. In order to analyze the nonlinear dynamic response of cutting process, the multiscale method is used to derive the analytical approximate solution of the forced response for the cutting system under periodic cutting forces. In the forced response analysis, four cases including primary resonance and superharmonic resonance, i.e., $\overline{\Omega} = \omega_1$, $\overline{\Omega} = \omega_2$, $2\overline{\Omega} = \omega_1$, and $2\overline{\Omega} = \omega_2$, are considered. The influences of ratio of length to diameter, structural damping, cutting force, and ply angle on primary resonance and superharmonic resonance are investigated. The results show that nonlinearity due to higher-order bending deformation significantly affects the dynamic behavior of the milling process and that the effective nonlinearity of the cutting system is of hard type. Multivalued resonance curves and jump phenomenon are presented. The influences of various factors, such as ratio of length to diameter, ply angle, structural damping, cutting force, and rotating speed, are thoroughly discussed.

1. Introduction

As a high-efficiency, high-quality, low-cost machining method, high-speed cutting technology has been widely used in aerospace and mold manufacturing. However, chatter reduces the cutting stability during machining operations, causes a decrease in the machining quality and cutting efficiency of the workpiece, damages the tool, and shortens the service life of the machine.

The passive chatter control methods are mainly based on various types of dynamic vibration absorbers [1, 2] and impact dampers [3]. However, composite materials are known to have higher static stiffness, damping, and specific stiffness. It has been found that the dynamic stiffness and fundamental natural frequency of cutter bar may be improved simultaneously if composite is employed [4–6]. This is very beneficial for the stability of high rotational speed machining for deep holes.

Within the framework of linear chatter theories and based on different theories, several of chatter phenomena as well as their stability boundary in different cutting processes were discovered [7–14]. Tobias [8] introduced the time-delay instability in the cutting force and proposed the regeneration theory, which is considered to provide a complete explanation of the chatter phenomenon so far.

However, because linear theory cannot predict some important dynamic behaviors of cutting process, nonlinear modeling of cutting systems has received more attention. The nonlinearity in cutting systems is mainly caused by structural nonlinearity, delayed nonlinearity of cutting force, etc. [15–18]. Hanna and Tobias [15] first proposed a time-delay nonlinear model with quadratic and cubic structural stiffness and cutting forces, which has inspired great interest in analyzing the global dynamics of the cutting system. The effective mathematical methods for the nonlinear theory of cutting systems include center manifold theory, bifurcation

theory, perturbation analysis, phase portraits, and Poincaré sections.

Pratt [19] used the multiscale method, harmonic balance method, and Floquet theory to study the models of Hanna and Tobias [18]. The results showed that subcritical Hopf bifurcation may occur due to the existence of cubic structural nonlinearity. Moradi et al. [20] studied the existence of different types of bifurcation in the cutting process considering the tool wear and process damping. They developed a 2-dof linear model of the tool and a polynomial nonlinear model of the cutting force. In addition, the multiscale method was used to obtain the approximation analysis solution of primary resonance. Moradi et al. [21] used a model similar to that in literature [20] to analyze the forced vibration of the milling process. In the study, not only the primary resonance but also the superharmonic resonance and the internal resonance were investigated. Moradi et al. [22] investigated the internal resonance and regenerative chatter of the milling process considering both the cutting force and the structural nonlinearity.

However, in the above studies, the tool structure was simulated with 1-dof or 2-dof vibration system, in which the concentration parameters such as mass and stiffness were obtained through experiments or empirical method. There is no obvious correlation between these simplified models and the continuous system equations of the tool.

In order to investigate the dynamic characteristics of cutting system and the stability mechanism of machining process, it is necessary to conduct a comprehensive analysis on various influencing factors. In this case, if the empirical method is used to establish the model of the tool structure, a large number of repetitive tests are needed to obtain the dynamic parameters of the tool structure of different sizes, geometries, and materials, which is very time consuming and of low effectiveness. Therefore, as a more effective modeling method for cutting tool, the continuous parameter dynamics modeling of cutting tool based on analytical method, has received great attention [23–33].

However, in most of the existing continuous system dynamics models, the influence of the nonlinearity of the tool structure has not been considered. Therefore, the existing dynamic model is only suitable for analyzing the linear dynamics of the natural frequency, chatter frequency, dynamic deformation, and chatter stability of the cutting system. In addition, the current continuous system dynamic studies are mainly focused on the tool structure made of isotropic metal materials. Nevertheless, there is no research about the nonlinear dynamics of the process with anisotropy composite tool structures.

The structural nonlinearity is essentially arisen by the flexible nature of the cutting tools with small diameter or long extension part. The structural nonlinearity of the cutting tools may be described using higher-order large deformations [34] or geometric nonlinearity [35].

In this paper, the nonlinear dynamics of the cutting process with a composite cutting tool are investigated. The composite tool structure is simplified to a nonplanar cantilever rotating shaft. The structural nonlinearity is introduced by considering the higher-order deformation of cutting tool. It is assumed that the cutting tool is subjected to a regenerative cutting force containing harmonic components. Based on the Hamilton principle, the nonlinear chatter equation of the cutting system is derived. The Galerkin method is used to obtain the nonlinear ordinary differential equations in the generalized coordinates. The multiscale method is used to obtain the approximate solution of the forced vibration response of the cutting process subjected to periodic cutting forces. Nonlinear dynamics of the system are studied for four cases of primary and superharmonic resonances; i.e., $\overline{\Omega} = \omega_1$, $\overline{\Omega} = \omega_2$, $2\overline{\Omega} = \omega_1$, and $2\overline{\Omega} = \omega_2$ are studied. The numerical calculation is conducted to investigate the effect of various parameters on the frequency response of the cutting system.

2. Mathematical Model and Solution

2.1. Kinetic Energy and Potential Energy. The structural sketch of composite cutting tool with nonplanar bending is shown in Figure 1. The kinetic energy of the rotating cutting tool without considering torsional deformation is as follows:

$$T = \frac{1}{2}\int_0^l \left[\rho A\left(\dot{v}^2 + \dot{w}^2\right) + \rho I\left(\dot{\psi}_y^2 + \dot{\psi}_z^2\right) - 4\Omega\rho I\psi_z\dot{\psi}_y\right]dx, \tag{1}$$

where v and w represent the displacement at any point on the neutral axis along the y and z directions, respectively. ψ_z and ψ_y represent bending rotation angles of the cross section around the y and z axes, respectively. ρA represents the mass per unit length, and ρI represents the mass moment of inertia of the cross section. The superposed dots represent derivatives with respect to the time t.

Using the expression of the displacement fields for Euler–Bernoulli beam and the stress-strain displacement relations of the composite cutting tool, as shown in Appendix A, one can obtain the following expression for the potential energy of the rotating composite cutting tool with the higher-order deformation:

$$U = \frac{1}{2}\int_0^L \iint_A \overline{Q}_{11}\left(z^2\left(\frac{\partial\psi_y}{\partial x}\right)^2 + y^2\left(\frac{\partial\psi_z}{\partial x}\right)^2 - 2yz\frac{\partial\psi_y}{\partial x}\frac{\partial\psi_z}{\partial x} + \frac{1}{4}\psi_y^4 + \frac{1}{4}\psi_z^4 + \frac{1}{2}\psi_y^2\psi_z^2 - 2\left(z\frac{\partial\psi_y}{\partial x} + y\frac{\partial\psi_z}{\partial x}\right)\left(\frac{1}{2}\psi_y^2 + \frac{1}{2}\psi_z^2\right)\right)^2 dAdx, \tag{2}$$

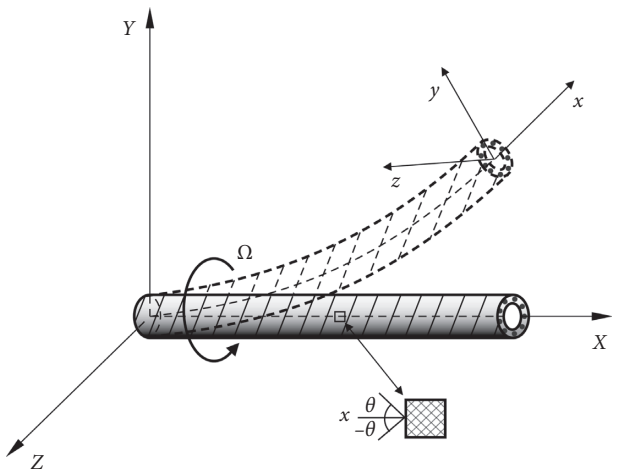

Figure 1: Composite cutting tool with nonplanar bending.

where $\overline{Q}_{11}$ refers to the off-axis stiffness coefficient of the kth layer for the composite cutting tool.

Regardless of the influence of shear deformation, based on the Euler–Bernoulli beam theory, the bending rotation angles and the displacements have the following relationship:

$$\psi_z = -\frac{\partial w}{\partial x}, \psi_y = \frac{\partial v}{\partial x}. \tag{3}$$

2.2. Damping Dissipative Energy Function and Virtual Work of Cutting Force. Rayleigh dissipative energy function of the cutting tool can be expressed as follows:

$$W_c = \frac{1}{2}\int_0^L c\left(\dot{v}^2 + \dot{w}^2\right)dx, \tag{4}$$

where c is structural damping coefficient.

The virtual work of the cutting force δW can be expressed as

$$\delta W = \int_0^L \left(L_v \delta v + L_w \delta w\right)dx, \tag{5}$$

where $L_v = F_y\delta_D(x-L)$, $L_w = F_z\delta_D(x-L)$, and $\delta_D(x-L)$ is the delta function.

The linear regenerative cutting forces F_y and F_z can be obtained by [20]

$$\begin{aligned} F_y &= -\frac{N}{2\pi}\left[\alpha_0(v-v_\tau) + \beta_0(w-w_\tau) + \gamma_0\right] + \frac{c_f}{2}\left[\varsigma_1\cos(2\Omega t - \pi/2) - \eta_1\cos 2\Omega t + \eta_1\right] + \left[\eta_2\cos(\Omega t - \pi/2) + \varsigma_2\cos\Omega t\right], \\ F_z &= \frac{N}{2\pi}\left[\alpha_0'(v-v_\tau) + \beta_0'(w-w_\tau) + \gamma_0'\right] + \frac{c_f}{2}\left[\eta_1\cos(2\Omega t - \pi/2) + \varsigma_1\cos 2\Omega t - \varsigma_1\right] + \left[\varsigma_2\cos(\Omega t - \pi/2) - \eta_2\cos\Omega t\right], \end{aligned} \tag{6}$$

where

$$\begin{aligned} &\alpha_0 = 0.5\varsigma_1 + 0.25\pi\eta_1, \beta_0 = 0.5\eta_1 + 0.25\pi\varsigma_1, \\ &\alpha_0' = -0.5\eta_1 + 0.25\pi\varsigma_1, \beta_0' = 0.5\varsigma_1 - 0.25\pi\eta_1, \\ &\gamma_0 = \eta_2 + \varsigma_2, \gamma_0' = \varsigma_2 - \eta_2, \\ &\varsigma_1 = K_{tc}a, \varsigma_2 = K_{te}a, \\ &\eta_1 = K_{rc}a, \eta_2 = K_{re}a, \\ &v = v(x,t), v_\tau = v(x,t-\tau), w = w(x,t), w_\tau = w(x,t-\tau), \end{aligned} \tag{7}$$

in which $\tau = 2\pi/N\Omega$ is the delay time of milling process; N is the number of teeth; (K_{tc}, K_{te}) and (K_{rc}, K_{re}) are the cutting force coefficients in the tangential and radial directions, respectively; a is the axial cutting depth; and c_f is the feed per tooth per revolution.

2.3. Dynamic Model of Milling Process. In order to obtain the equation of motion of the cutting system, the principle of Hamilton is used as follows:

$$\int_{t_1}^{t_2}\left(\delta U + \delta W_c - \delta T - \delta W\right)dt = 0. \tag{8}$$

Substituting (1), (2), (4), and (5) into (8), the equations of motion in both y and z directions can be obtained:

$$\begin{aligned} &(m)_{\text{equiv}}\ddot{v} + c\dot{v} - 2(\rho I)_{\text{equiv}}\Omega\dot{w}'' - (\rho I)_{\text{equiv}}\ddot{v}'' + (EI)_{\text{equiv}}\frac{\partial^4 v}{\partial x^4} + \frac{(EA)_{\text{equiv}}}{2}\left[\left(v'^2 + w'^2\right)v'\right]' = F_y\delta_D(x-L), \\ &(m)_{\text{equiv}}\ddot{w} + c\dot{w} + 2(\rho I)_{\text{equiv}}\Omega\dot{v}'' - (\rho I)_{\text{equiv}}\ddot{w}'' + (EI)_{\text{equiv}}\frac{\partial^4 w}{\partial x^4} + \frac{(EA)_{\text{equiv}}}{2}\left[\left(v'^2 + w'^2\right)w'\right]' = F_z\delta_D(x-L), \end{aligned} \tag{9}$$

where

$$
\begin{aligned}
(m)_{\text{equiv}} &= (\rho A)_{\text{equiv}} = \pi \sum_{k=1}^{N} \rho_k \left(r_{k+1}^2 - r_k^2\right),\\
(\rho I)_{\text{equiv}} &= \frac{\pi}{4} \sum_{k=1}^{N} \rho_k \left(r_{k+1}^4 - r_k^4\right),\\
(EI)_{\text{equiv}} &= \frac{\pi}{4} \sum_{k=1}^{N} \overline{Q}_{11} \left(r_{k+1}^4 - r_k^4\right),\\
(EA)_{\text{equiv}} &= \pi \sum_{k=1}^{N} \overline{Q}_{11} \left(r_{k+1}^2 - r_k^2\right).
\end{aligned}
\tag{10}
$$

Here, $(EI)_{\text{equiv}}$ and $(EA)_{\text{equiv}}$ represent the equivalent bending and tensile stiffness of the cutting tool, respectively; $(\rho I)_{\text{equiv}}$ and $(m)_{\text{equiv}}$ represent the equivalent diametrical mass moment of inertia and the equivalent mass per unit length, respectively; ρ_k represents the density of the kth layer; and r_{k} and $r_{\text{k+1}}$ represent the inner diameter and outer diameter of the kth layer, respectively. The detailed expression of $\overline{Q}_{11}$ can be found in Appendix B. In (9), the primes denote differentiation with respect to x.

The following nondimensional quantities are defined:

$$
\begin{aligned}
&\overline{x} = \frac{x}{L}, \overline{v} = \frac{v}{L}, \overline{w} = \frac{w}{L}, \overline{t} = \sqrt{\frac{(EI)_{\text{equiv}}}{(m)_{\text{equiv}} L^4}} t = \gamma t, \overline{\tau} = \gamma \tau, \overline{c} = \frac{cL^2}{\sqrt{(m)_{\text{equiv}} (EI)_{\text{equiv}}}},\\
&\overline{\rho I} = \frac{(\rho I)_{\text{equiv}}}{\left((m)_{\text{equiv}} L^2\right)}, \overline{\Omega} = \sqrt{\frac{(m)_{\text{equiv}} L^4}{(EI)_{\text{equiv}}}} \Omega, \lambda = \frac{(EA)_{\text{equiv}} L^2}{2 (EI)_{\text{equiv}}},\\
&\overline{\alpha}_0 = \frac{L^3 \alpha_0}{(EI)_{\text{equiv}}}, \overline{\beta}_0 = \frac{L^3 \beta_0}{(EI)_{\text{equiv}}}, \overline{\gamma}_0 = \frac{L^2 \gamma_0}{(EI)_{\text{equiv}}}, c_{f\varsigma_1} = \frac{L^2 c_f}{(EI)_{\text{equiv}}} \varsigma_1, c_{f\eta_1} = \frac{L^2 c_f}{(EI)_{\text{equiv}}} \eta_1,\\
&\overline{\alpha}_0' = \frac{L^3 \alpha_0'}{(EI)_{\text{equiv}}}, \overline{\beta}_0' = \frac{L^3 \beta_0'}{(EI)_{\text{equiv}}}, \overline{\gamma}_0' = \frac{L^2 \gamma_0'}{(EI)_{\text{equiv}}}, \overline{\varsigma}_2 = \frac{L^2 \varsigma_2}{(EI)_{\text{equiv}}}, \overline{\eta}_2 = \frac{L^2 \eta_2}{(EI)_{\text{equiv}}}.
\end{aligned}
\tag{11}
$$

Using the above dimensionless variables, (9) is rewritten as

$$
\begin{aligned}
&\ddot{v} + \overline{c}\dot{v} - 2\overline{\rho} I \overline{\Omega} \dot{w}'' - \overline{\rho} I \ddot{v}'' + \frac{\partial^4 v}{\partial x^4} + \lambda \left[\left(v'^2 + w'^2\right) w'\right]' = \overline{F}_y \delta_D (x - 1),\\
&\ddot{w} + \overline{c}\dot{w} + 2\overline{\rho} I \overline{\Omega} \dot{v}'' - \overline{\rho} I \ddot{w}'' + \frac{\partial^4 w}{\partial x^4} + \lambda \left[\left(v'^2 + w'^2\right) w'\right]' = \overline{F}_z \delta_D (x - 1),
\end{aligned}
\tag{12}
$$

where

$$
\begin{aligned}
\overline{F}_y &= -\frac{N}{2\pi} \left[\overline{\alpha}_0 (v - v_\tau) + \overline{\beta}_0 (w - w_\tau) + \overline{\gamma}_0\right] + \frac{1}{2} \left[c_{f\varsigma_1} \cos (2\overline{\Omega}\overline{t} - \pi/2) - c_{f\eta_1} \cos 2\overline{\Omega}\overline{t} + c_{f\eta_1}\right] + \left[\overline{\eta}_2 \cos (2\overline{\Omega}\overline{t} - \pi/2) + \overline{\varsigma}_2 \cos \overline{\Omega}\overline{t}\right],\\
\overline{F}_z &= \frac{N}{2\pi} \left[\overline{\alpha}_0' (v - v_\tau) + \overline{\beta}' (w - w_\tau) + \gamma_0'\right] - \frac{1}{2} \left[c_{f\eta_1} \cos (2\overline{\Omega}\overline{t} - \pi/2) + c_{f\varsigma_1} \cos 2\overline{\Omega}\overline{t} - c_{f\varsigma_1}\right] + \left[\overline{\varsigma}_2 \cos (2\overline{\Omega}\overline{t} - \pi/2) - \overline{\eta}_2 \cos \overline{\Omega}\overline{t}\right].
\end{aligned}
\tag{13}
$$

In (12), the primes denote differentiation with respect to $\overline{x}$, and the superposed dots denote derivatives with respect to the time $\overline{t}$.

The solution of (12) can be written as

$$v(\overline{x},\overline{t}) = \phi_1(\overline{x})V(\overline{t}), w(\overline{x},\overline{t}) = \phi_1(\overline{x})W(\overline{t}). \tag{14}$$

For cantilever beams, $\phi_1(\overline{x})$ has to meet the following boundary conditions:

$$\phi_1(0) = \phi_1'(0) = \phi_1''(1) = \phi_1'''(1) = 0. \tag{15}$$

The mode function that satisfies the boundary condition in (12) can be expressed as follows:

$$\phi_1(\overline{x}) = \cos\beta_1 L\overline{x} - \cosh\beta_1 L\overline{x} - \frac{\cos\beta_1 L + \cosh\beta_1 L}{\sin\beta_1 L + \sinh\beta_1 L}\left(\sin\beta_1 L\overline{x} - \sinh\beta_1 L\overline{x}\right), \overline{x} \in (0,1), \tag{16}$$

where $\beta_1 L = 1.875$.

Substituting (14) into (9), simplifying the equation by the Galerkin method, and dropping the constant cutting force terms, the following ordinary differential equations can be obtained.

$$\begin{aligned}
\overline{A}_1\ddot{V} + \overline{A}_2\dot{V} - \overline{A}_3\dot{W} + \overline{A}_4 V + \overline{A}_5 V\left(V^2 + W^2\right) &= -\frac{N}{2\pi}\left[\overline{\alpha}_0(V - V_\tau) + \overline{\beta}_0(W - W_\tau)\right]\phi_1^2(1) + \overline{F}_{y2}\phi_1(1),\\
\overline{A}_1\ddot{W} + \overline{A}_2\dot{W} + \overline{A}_3\dot{V} + \overline{A}_4 W + \overline{A}_5 W\left(V^2 + W^2\right) &= \frac{N}{2\pi}\left[\overline{\alpha}_0'(V - V_\tau) + \overline{\beta}_0'(W - W_\tau)\right]\phi_1^2(1) + \overline{F}_{z2}\phi_1(1),
\end{aligned} \tag{17}$$

where

$$\begin{aligned}
&\overline{A}_1 = \int_0^1 \phi_1^2(\overline{x})d\overline{x} - \overline{\rho}\overline{I}\int_0^1 \phi_1(\nu)\phi_1''(\overline{x})d\overline{x}, \overline{A}_2 = \overline{c}\int_0^1 \phi_1^2(\overline{x})d\overline{x}, \overline{A}_3 = 2\overline{\rho}\overline{I}\overline{\Omega}\int_0^1 \phi_1(\overline{x})\phi_1''(\overline{x})d\overline{x},\\
&\overline{A}_4 = \int_0^1 \phi_1(\overline{x})\phi_1^{(4)}(\overline{x})d\overline{x}, \overline{A}_5 = \lambda\int_0^1 \left(\phi_1'(\overline{x})^3\right)'\phi_1 d\overline{x}.
\end{aligned} \tag{18}$$

Here, the superscript (4) means the fourth-order partial derivative of $\overline{x}$.

2.4. Perturbation Analysis of Milling Process Using Multiple Scales Method. In order to solve (17) using the multiscale method, the structural damping and nonlinear and exciting force terms are scaled using small parameters ε as follows:

$$\overline{A}_2 \Rightarrow \varepsilon^2\overline{A}_2, \frac{N}{2\pi}\overline{\alpha}_0 \Rightarrow \varepsilon^2\frac{N}{2\pi}\overline{\alpha}_0, \frac{N}{2\pi}\overline{\beta}_0 \Rightarrow \varepsilon^2\frac{N}{2\pi}\overline{\beta}_0, \frac{N}{2\pi}\overline{\alpha}_0' \Rightarrow \varepsilon^2\frac{N}{2\pi}\overline{\alpha}_0',$$

$$\frac{N}{2\pi}\overline{\beta}_0' \Rightarrow \varepsilon^2\frac{N}{2\pi}\overline{\beta}_0', \overline{\overline{F}}_{y2} \Rightarrow \varepsilon^3\overline{\overline{F}}_{y2}, \overline{\overline{F}}_{z2} \Rightarrow \varepsilon^3\overline{\overline{F}}_{z2}. \tag{19}$$

$V(\overline{t})$ and $W(\overline{t})$ are expanded in the form

$$\begin{aligned}
V(\overline{t}) &= \varepsilon V_1(T_0, T_2) + \varepsilon^3 V_3(T_0, T_2) + \cdots,\\
W(\overline{t}) &= \varepsilon W_1(T_0, T_2) + \varepsilon^3 W_3(T_0, T_2) + \cdots,
\end{aligned} \tag{20}$$

where $T_0 = \overline{t}, T_2 = \varepsilon^2\overline{t}$.

Taking the derivative of (20), one obtains the following equations:

$$\begin{aligned}
\dot{V} &= \varepsilon\frac{\partial V_1}{\partial T_0} + \varepsilon^3\left(\frac{\partial V_3}{\partial T_0} + \frac{\partial V_1}{\partial T_2}\right) + \cdots,\\
\ddot{V} &= \varepsilon\frac{\partial^2 V_1}{\partial T_0^2} + \varepsilon^3\left(\frac{\partial^2 V_3}{\partial T_0^2} + 2\frac{\partial^2 V_1}{\partial T_0\partial T_2}\right) + \cdots,\\
\dot{W} &= \varepsilon\frac{\partial W_1}{\partial T_0} + \varepsilon^3\left(\frac{\partial W_3}{\partial T_0} + \frac{\partial W_1}{\partial T_2}\right) + \cdots,\\
\ddot{W} &= \varepsilon\frac{\partial^2 W_1}{\partial T_0^2} + \varepsilon^3\left(\frac{\partial^2 W_3}{\partial T_0^2} + 2\frac{\partial^2 W_1}{\partial T_0\partial T_2}\right) + \cdots.
\end{aligned} \tag{21}$$

Substituting (20) and (21) into (17) and considering (19), one can obtain the following equations by comparing the coefficients of ε and ε^3:

O(ε):

$$\begin{aligned}
\overline{A}_1\frac{\partial^2 V_1}{\partial T_0^2} - \overline{A}_3\frac{\partial W_1}{\partial T_0} + \overline{A}_4 V_1 &= 0,\\
\overline{A}_1\frac{\partial^2 W_1}{\partial T_0^2} + \overline{A}_3\frac{\partial V_1}{\partial T_0} + \overline{A}_4 W_1 &= 0.
\end{aligned} \tag{22}$$

$O(\varepsilon^3)$:

$$\begin{aligned}
&\overline{A}_1\frac{\partial^2 V_3}{\partial T_0^2}-\overline{A}_3\frac{\partial W_3}{\partial T_0}+\overline{A}_4 V_3=-2\overline{A}_1\frac{\partial^2 V_1}{\partial T_0\partial T_2}-\overline{A}_2\frac{\partial V_1}{\partial T_0}+\overline{A}_3\frac{\partial W_1}{\partial T_2}-\overline{A}_5 V_1\left(V_1^2+W_1^2\right)-\frac{N}{2\pi}\left[\overline{\alpha}_0\left(V_1-V_{1\tau}\right)+\overline{\beta}_0\left(W_1-W_{1\tau}\right)\right]\\
&\quad\phi_1^2(1)+\lambda_V+\overline{F}_{y2}\phi_1(1),\\
&\overline{A}_1\frac{\partial^2 W_3}{\partial T_0^2}+\overline{A}_3\frac{\partial V_3}{\partial T_0}+\overline{A}_4 W_3=-2\overline{A}_1\frac{\partial^2 W_1}{\partial T_0\partial T_2}-\overline{A}_2\frac{\partial W_1}{\partial T_0}-\overline{A}_3\frac{\partial V_1}{\partial T_2}-\overline{A}_5 W_1\left(V_1^2+W_1^2\right)+\frac{N}{2\pi}\left[\overline{\alpha}_0'\left(V_1-V_{1\tau}\right)+\overline{\beta}_0'\left(W_1-W_{1\tau}\right)\right]\\
&\quad\phi_1^2(1)+\lambda_W+\overline{F}_{z2}\phi_1(1).
\end{aligned}\tag{23}$$

Assume the solution of (22) is as follows:

$$\begin{aligned}
V_1(T_0,T_2)&=F_1(T_2)e^{i\omega_1 T_0}+F_2(T_2)e^{i\omega_2 T_0}+\overline{F}_1(T_2)e^{-i\omega_1 T_0}+\overline{F}_2(T_2)e^{-i\omega_2 T_0},\\
W_1(T_0,T_2)&=-iF_1(T_2)e^{i\omega_1 T_0}+iF_2(T_2)e^{i\omega_2 T_0}+i\overline{F}_1(T_2)e^{-i\omega_1 T_0}-i\overline{F}_2(T_2)e^{-i\omega_2 T_0},\\
V_{1\tau}(T_0,T_2)&=F_1(T_2)e^{i\omega_1\left(T_0-\overline{\tau}\right)}+F_2(T_2)e^{i\omega_2\left(T_0-\overline{\tau}\right)}+\overline{F}_1(T_2)e^{-i\omega_1\left(T_0-\overline{\tau}\right)}+\overline{F}_2(T_2)e^{-i\omega_2\left(T_0-\overline{\tau}\right)},\\
W_{1\tau}(T_0,T_2)&=-iF_1(T_2)e^{i\omega_1\left(T_0-\overline{\tau}\right)}+iF_2(T_2)e^{i\omega_2\left(T_0-\overline{\tau}\right)}+i\overline{F}_1(T_2)e^{-i\omega_1\left(T_0-\overline{\tau}\right)}-i\overline{F}_2(T_2)e^{-i\omega_2\left(T_0-\overline{\tau}\right)},
\end{aligned}\tag{24}$$

where $i=\sqrt{-1}$ represents the imaginary unit, $F_1(T_2)$ and $F_2(T_2)$ are the complex functions to be determined, and $\overline{F}_1(T_2)$ and $\overline{F}_2(T_2)$ represent the complex conjugate. ω_1 and ω_2 refer to the forward and backward whirling frequencies, respectively, which are expressed as follows:

$$\omega_1=\frac{\overline{A}_3+\sqrt{\overline{A}_3^2+4\overline{A}_1\overline{A}_4}}{2\overline{A}_1},\omega_2=\frac{-\overline{A}_3+\sqrt{\overline{A}_3^2+4\overline{A}_1\overline{A}_4}}{2\overline{A}_1}.\tag{25}$$

Substituting (24) into (23) and dropping the constant terms λ_V and λ_W, one obtains the following equations:

$$\begin{aligned}
&\overline{A}_1\frac{\partial^2 V_3}{\partial T_0^2}-\overline{A}_3\frac{\partial W_3}{\partial T_0}+\overline{A}_4 V_3=P_3e^{i\omega_1 T_0}+Q_3e^{i\omega_2 T_0}+\overline{\overline{F}}_{y2},\\
&\overline{A}_1\frac{\partial^2 W_3}{\partial T_0^2}+\overline{A}_3\frac{\partial V_3}{\partial T_0}+\overline{A}_4 W_3=P_4e^{i\omega_1 T_0}+Q_4e^{i\omega_2 T_0}+\overline{\overline{F}}_{z2}
\end{aligned},\tag{26}$$

where

$$\begin{aligned}
P_3&=\Gamma_1-i\Lambda_1F_1'-i\overline{A}_2\omega_1F_1-\phi_1^2(1)\frac{N}{2\pi}\left(\overline{\overline{\alpha}}_0-i\overline{\overline{\beta}}_0\right)\left(1-e^{-i\omega_1\overline{\tau}}\right)F_1,\\
Q_3&=\Gamma_2-i\Lambda_2F_2'-i\overline{A}_2\omega_2F_2-\phi_1^2(1)\frac{N}{2\pi}\left(\overline{\overline{\alpha}}_0+i\overline{\overline{\beta}}_0\right)\left(1-e^{-i\omega_2\overline{\tau}}\right)F_2,\\
P_4&=-i\Gamma_1-\Lambda_1F_1'-\overline{A}_2\omega_1F_1+\phi_1^2(1)\frac{N}{2\pi}\left(\overline{\overline{\alpha}}_0'-i\overline{\overline{\beta}}_0'\right)\left(1-e^{-i\omega_1\overline{\tau}}\right)F_1,\\
Q_4&=i\Gamma_2+\Lambda_2F_2'+\overline{A}_2\omega_2F_2+\phi_1^2(1)\frac{N}{2\pi}\left(\overline{\overline{\alpha}}_0'+i\overline{\overline{\beta}}_0'\right)\left(1-e^{-i\omega_2\overline{\tau}}\right)F_2,\\
\Lambda_1&=2\overline{A}_1\omega_1+\overline{A}_3,\Gamma_1=-4\overline{A}_5\left(F_1^2\overline{F}_1+2F_1F_2\overline{F}_2\right),\\
\Lambda_2&=2\overline{A}_1\omega_2-\overline{A}_3,\Gamma_2=-4\overline{A}_5\left(F_2^2\overline{F}_2+2F_1F_2\overline{F}_1\right),\\
\overline{\overline{F}}_{y_2}&=\overline{F}_{y_2}\phi_1(1),\\
\overline{\overline{F}}_{z_2}&=\overline{F}_{z_2}\phi_1(1).
\end{aligned}\tag{27}$$

In this paper, four cases of primary and superharmonic resonances, i.e., case I: $\overline{\Omega} = \omega_1$, case II: $\overline{\Omega} = \omega_2$, case III: $2\overline{\Omega} = \omega_1$, and case IV: $2\overline{\Omega} = \omega_2$, are studied.

2.4.1. Case I: Primary Resonance ($\overline{\Omega} = \omega_1$). Assume

$$\overline{\Omega} = \omega_1 + \varepsilon^2\sigma, \tag{28}$$

where σ represents the detuning parameter.

Substituting (24) into (26), one can obtain the following equations:

$$\begin{aligned}
&\overline{A}_1\frac{\partial^2 V_3}{\partial T_0^2} - \overline{A}_3\frac{\partial W_3}{\partial T_0} + \overline{A}_4 V_3 = \overline{P}_3 e^{i\omega_1 T_0} + \overline{Q}_3 e^{i\omega_2 T_0},\\
&\overline{A}_1\frac{\partial^2 W_3}{\partial T_0^2} + \overline{A}_3\frac{\partial V_3}{\partial T_0} + \overline{A}_4 W_3 = \overline{P}_4 e^{i\omega_1 T_0} + \overline{Q}_4 e^{i\omega_2 T_0},
\end{aligned} \tag{29}$$

where

$$\begin{aligned}
\overline{P}_3 &= P_3 + \phi_1(1)\overline{q}_1 e^{i\sigma T_2},\\
\overline{P}_4 &= P_4 - i\phi_1(1)\overline{q}_1 e^{i\sigma T_2},\\
\overline{Q}_3 &= Q_3,\\
\overline{Q}_4 &= Q_4,
\end{aligned} \tag{30}$$

where $\overline{q}_1 = (\overline{\varsigma}_2 - i\overline{\eta}_2)/2$.

The particular solutions of (29) are

$$\begin{aligned}
V_3(T_0, T_2) &= F_{11}(T_2)e^{i\omega_1 T_0} + F_{12}(T_2)e^{i\omega_2 T_0},\\
W_3(T_0, T_2) &= F_{21}(T_2)e^{i\omega_1 T_0} + F_{22}(T_2)e^{i\omega_2 T_0}.
\end{aligned} \tag{31}$$

Substituting (31) into (29) and equating the coefficient of $e^{i\omega_1 T_0}$ and $e^{i\omega_2 T_0}$ in both sides of (29), one has

$$\begin{aligned}
\left(\overline{A}_4 - \overline{A}_1\omega_1^2\right)F_{11} - i\overline{A}_3\omega_1 F_{21} &= \overline{P}_3,\\
i\overline{A}_3\omega_1 F_{11} + \left(\overline{A}_4 - \overline{A}_1\omega_1^2\right)F_{21} &= \overline{P}_4.
\end{aligned} \tag{32}$$

$$\begin{aligned}
\left(\overline{A}_4 - \overline{A}_1\omega_2^2\right)F_{12} - i\overline{A}_3\omega_2 F_{22} &= \overline{Q}_3,\\
i\overline{A}_3\omega_2 F_{12} + \left(\overline{A}_4 - \overline{A}_1\omega_2^2\right)F_{22} &= \overline{Q}_4.
\end{aligned} \tag{33}$$

Equations (32) and (33) constitute systems of two inhomogeneous algebraic equations for F_{11}, F_{21} and F_{12}, F_{22}, respectively. Their homogeneous parts have a nontrivial solution. Then their solvability conditions can be written as [36]

$$\begin{aligned}
&\begin{vmatrix} \overline{P}_3 & -i\overline{A}_3\omega_1 \\ \overline{P}_4 & \overline{A}_4 - \overline{A}_1\omega_1^2 \end{vmatrix} = 0,\\
&\begin{vmatrix} \overline{A}_4 - \overline{A}_1\omega_1^2 & \overline{P}_3 \\ i\overline{A}_3\omega_1 & \overline{P}_4 \end{vmatrix} = 0.
\end{aligned} \tag{34}$$

$$\begin{aligned}
&\begin{vmatrix} \overline{Q}_3 & -i\overline{A}_3\omega_2 \\ \overline{Q}_4 & \overline{A}_4 - \overline{A}_1\omega_2^2 \end{vmatrix} = 0,\\
&\begin{vmatrix} \overline{A}_4 - \overline{A}_1\omega_2^2 & \overline{Q}_3 \\ i\overline{A}_3\omega_2 & \overline{Q}_4 \end{vmatrix} = 0.
\end{aligned} \tag{35}$$

After simplification, the solvability conditions are reduced to two independent governing equations in the following form:

$$\begin{aligned}
&4\overline{A}_5\left(F_1^2\overline{F}_1 + 2F_1F_2\overline{F}_2\right) - i\Lambda_1 F_1' - i\overline{A}_2\omega_1 F_1 + \phi_1^2(1)\frac{N}{4\pi}\\
&\left[\overline{\beta}_0' - \overline{\alpha}_0 + i\left(\overline{\alpha}_0' + \overline{\beta}_0\right)\right]\left(1 - e^{-i\omega_1\overline{\tau}}\right)F_1 + \phi_1(1)\overline{q}_1 e^{i\sigma T_2} = 0,
\end{aligned} \tag{36}$$

$$\begin{aligned}
&4\overline{A}_5\left(F_2^2\overline{F}_2 + 2F_1F_2\overline{F}_1\right) - i\Lambda_2 F_2' - i\overline{A}_2\omega_2 F_2 - \frac{1}{2}\phi_1^2(1)\frac{N}{2\pi}\\
&\left[\overline{\alpha}_0 + \overline{\beta}_0' + i\left(\overline{\alpha}_0' - \overline{\beta}_0\right)\right]\left(1 - e^{-i\omega_1\overline{\tau}}\right)F_2 = 0.
\end{aligned} \tag{37}$$

Assume that the solutions of (36) and (37) are

$$\begin{aligned}
F_1 &= \frac{1}{2}a_1(T_2)e^{i\theta_1(T_2)},\\
F_2 &= \frac{1}{2}a_2(T_2)e^{i\theta_2(T_2)},
\end{aligned} \tag{38}$$

where $a_j(T_2)$ and $\theta_j(T_2)$ $(j = 1,2)$ refer to the amplitudes and phase angles of the response, respectively.

Substituting (38) into (36) and (37), separating the real and the imaginary parts, one can obtain the following equations:

$$\begin{aligned}
\Lambda_1 a_1' &= -\overline{A}_2\omega_1 a_1 + \phi_1^2(1)\frac{N}{4\pi}\left(\left(\overline{\alpha}_0' + \overline{\beta}_0\right)(1 - \cos\omega_1\overline{\tau}) + \left(\overline{\beta}_0' - \overline{\alpha}_0\right)\sin\omega_1\overline{\tau}\right)a_1 + \phi_1(1)\left(\overline{\varsigma}_2\sin\psi_1 - \overline{\eta}_2\cos\psi_1\right),\\
\Lambda_1 a_1\psi_1' &= \Lambda_1\sigma a_1 - \overline{A}_5\left(a_1^3 + 2a_1a_2^2\right) + \phi_1^2(1)\frac{N}{4\pi}\left(\left(\overline{\beta}_0' - \overline{\alpha}_0\right)(1 - \cos\omega_1\overline{\tau}) - \left(\overline{\alpha}_0' + \overline{\beta}_0\right)\sin\omega_1\overline{\tau}\right)a_1 + \phi_1(1)\left(\overline{\eta}_2\sin\psi_1 + \overline{\varsigma}_2\cos\psi_1\right).
\end{aligned} \tag{39}$$

$$\begin{aligned}
\Lambda_2 a_2' &= -\overline{A}_2\omega_2 a_2 - \phi_1^2(1)\frac{N}{4\pi}\left(\left(\overline{\alpha}_0' + \overline{\beta}_0\right)(1 - \cos\omega_2\overline{\tau}) + \left(\overline{\alpha}_0 - \overline{\beta}_0'\right)\sin\omega_2\overline{\tau}\right)a_2,\\
\Lambda_2\psi_2' a_2 &= -\overline{A}_5\left(a_2^3 + 2a_1^2a_2\right) - \phi_1^2(1)\frac{N}{4\pi}\left(\left(\overline{\alpha}_0 - \overline{\beta}_0'\right)(1 - \cos\omega_2\overline{\tau}) - \left(\overline{\alpha}_0' + \overline{\beta}_0\right)\sin\omega_2\overline{\tau}\right)a_2,
\end{aligned} \tag{40}$$

where $\sigma T_2 - \theta_j = \psi_j$ $(j = 1,2)$.

To determine the steady-state forced response, the time derivatives in (39) and (40) are set to zero. It can be immediately concluded from (40) that only solution for a_2 is zero. This shows that under the primary resonance $\Omega \approx \omega_1$, only the first mode, i.e., the forward mode, can be excited, while the second mode, i.e., the backward mode, does not participate in the primary resonance and remains stationary.

Substituting $a_2 = 0$ into (39) and solving for σ, one obtains

$$\sigma = -\phi_1^2(1)\frac{N}{4\pi\Lambda_1}\left[\left(\overline{\beta}_0' - \overline{\alpha}_0\right)(1-\cos\omega_1\overline{\tau}) - \left(\overline{\alpha}_0' + \overline{\beta}_0\right)\sin\omega_1\overline{\tau}\right] + \frac{\overline{A}_5}{\Lambda_1}a_1^2 \pm \frac{1}{\Lambda_1}\sqrt{\frac{\phi_1^2(1)\left(\overline{\varsigma}_2^2 + \overline{\eta}_2^2\right)}{a_1^2} - \left[\overline{A}_2\omega_1 - \phi_1^2(1)\frac{N}{4\pi}\left[\left(\overline{\alpha}_0' + \overline{\beta}_0\right)(1-\cos\omega_1\overline{\tau}) + \left(\overline{\beta}_0' - \overline{\alpha}_0\right)\sin\omega_1\overline{\tau}\right]\right]^2}. \tag{41}$$

To study the stability of the steady-state response of case I, the nature of steady-state response can be investigated numerically by linearizing (39) (with $a_2 = 0$) around (a_0, ψ_0).

2.4.2. Case II: Primary Resonance ($\overline{\Omega} = \omega_2$). According to (26), under such conditions, one introduces detuning parameters as

$$\overline{\Omega} = \omega_2 + \varepsilon^2\sigma. \tag{42}$$

Using their solvability conditions (which are not shown) and (38) leads to

$$\begin{aligned}
\Lambda_1 a_1' &= -\overline{A}_2\omega_1 a_1 + \phi_1^2(1)\frac{N}{4\pi}\left(\left(\overline{\alpha}_0' + \overline{\beta}_0\right)(1-\cos\omega_1\overline{\tau}) + \left(\overline{\beta}_0' - \overline{\alpha}_0\right)\sin\omega_1\overline{\tau}\right)a_1,\\
\Lambda_1 a_1\psi_1' &= \Lambda_1\sigma a_1 - \overline{A}_5\left(a_1^3 + 2a_1a_2^2\right) + \phi_1^2(1)\frac{N}{4\pi}\left(\left(\overline{\beta}_0' - \overline{\alpha}_0\right)(1-\cos\omega_1\overline{\tau}) - \left(\overline{\alpha}_0' + \overline{\beta}_0\right)\sin\omega_1\overline{\tau}\right)a_1,\\
\Lambda_2 a_2' &= -\overline{A}_2\omega_2 a_2 - \phi_1^2(1)\frac{N}{4\pi}\left(\left(\overline{\alpha}_0' + \overline{\beta}_0\right)(1-\cos\omega_2\overline{\tau}) + \left(\overline{\alpha}_0 - \overline{\beta}_0'\right)\sin\omega_2\overline{\tau}\right)a_2 - \phi_1(1)\left(\overline{\varsigma}_2\sin\psi_2 - \overline{\eta}_2\cos\psi_2\right),\\
\Lambda_2\psi_2' a_2 &= -\overline{A}_5\left(a_2^3 + 2a_1^2a_2\right) - \phi_1^2(1)\frac{N}{4\pi}\left(\left(\overline{\alpha}_0 - \overline{\beta}_0'\right)(1-\cos\omega_2\overline{\tau}) - \left(\overline{\alpha}_0' + \overline{\beta}_0\right)\sin\omega_2\overline{\tau}\right)a_2 - \phi_1(1)\left(\overline{\varsigma}_2\cos\psi_2 + \overline{\eta}_2\sin\psi_2\right).
\end{aligned} \tag{43}$$

By using steady-state condition (i.e., set $a_1' = 0$, $\psi_1' = 0$, $a_2' = 0$, and $\psi_2' = 0$), the following steady-state response of case II can be obtained:

$$\sigma = \phi_1^2(1)\frac{N}{4\pi\Lambda_2}\left[\left(\overline{\alpha}_0 - \overline{\beta}_0'\right)(1-\cos\omega_2\overline{\tau}) - \left(\overline{\alpha}_0' + \overline{\beta}_0\right)\sin\omega_2\overline{\tau}\right] + \frac{\overline{A}_5}{\Lambda_2}a_2^2 \pm \frac{1}{\Lambda_2}\sqrt{\frac{\phi_1^2(1)\left(\overline{\varsigma}_2^2 + \overline{\eta}_2^2\right)}{a_2^2} - \left[\frac{2}{A}\omega_2 + \phi_1^2(1)\frac{N}{4\pi}\left[\left(\overline{\alpha}_0' + \overline{\beta}_0\right)(1-\cos\omega_2\overline{\tau}) + \left(\overline{\alpha}_0 - \overline{\beta}_0'\right)\sin\omega_2\overline{\tau}\right]\right]^2}. \tag{44}$$

From (44), it can be seen that $a_1 = 0$ and $a_2 \neq 0$, indicating that only the forced vibration response of backward mode is excited, while forward mode remains stationary.

2.4.3. Case III: Superharmonic Resonance ($2\overline{\Omega} = \omega_1$). For this case, the formulation of steady-state response is the same as case I, but in (41), $\overline{\varsigma}_2$ and $\overline{\eta}_2$ are replaced with $c_{f\varsigma_1}/2$ and $c_{f\eta_1}/2$, respectively.

2.4.4. Case IV: Superharmonic Resonance ($2\overline{\Omega} = \omega_2$). For this case, the formulation of steady-state response is the same as case II, but in (43), $\overline{\varsigma}_2$ and $\overline{\eta}_2$ are replaced with $c_{f\varsigma_1}/2$ and $c_{f\eta_1}/2$, respectively.

3. Numerical Results and Discussions

In this study, the composite material of carbon fiber/epoxy resin is selected as the material of the cutting tool. The mechanical properties of the material are shown in Table 1. Coefficients of cutting forces for simulation are given in Table 2. The cutting tool has a hollow structure, the outer diameter of the cross section is $D = 8$ mm, the inner diameter is $D = 4$ mm, the thickness of the section is $h = 2$ mm, and the length L is determined by the given ratio of length to diameter. The composite cutting tool has 16 layers with identical thickness, and the stack sequence is $[\pm\theta]_8$. In all cases, $\overline{\Omega} = 200$, except where other values are mentioned.

Figure 2 shows the natural frequency versus rotating speed, which is generally known as a Campbell diagram. In vibration of gyroscopic systems, there are two natural frequencies associated with forward and backward whirling motions. In forward natural frequency, the natural frequency is measured when the rotating cutting tool whirls in direction of the rotation. However, in backward natural frequency, the natural frequency is measured when the cutting tool whirls in the opposite direction of the rotation. The forward natural frequency (black solid line) increases with the increase of the rotating speed, while the backward natural frequency (blue dashed line) decreases with the increase of the rotating speed. The intersections of the curves related to the natural frequencies with the straight line $\omega_n = \overline{\Omega}$ determine the critical rotating speeds of the rotating cutting tool.

3.1. Stability Lobe Diagram. By removing the nonlinear term and the harmonic cutting force in the right-side term of (17), the stability of the cutting system can be investigated. Figure 3 shows a stability lobe diagram where the Ω versus a_{lim} curve separates the space into two regions. Any (Ω, a_{lim}) pair that appears above the collective boundary indicates unstable milling process where regenerative chatter or self-excited vibration occurs, while any pair below the boundary is a stable milling process.

3.2. Primary Resonance Response

3.2.1. Case I. The numerical solutions for the forced vibration responses of the cutting system with composite cutting tool are presented in Figure 4. As shown in Figure 4, by increasing detuning parameters at point A, the amplitude a_1 gradually increases until reaching point B. a_1 jumps downward from point B to point C. Afterward, a_1 gradually drops to point D while continuing increasing the detuning parameter. On the other hand, as the detuning parameter decreases from point D to point E, a_1 increases and jumps upward from point E to point F. As the detuning parameter further decreases, a_1 drops until arriving at point A. By considering the nonlinearity of higher-order bending deformation, the forced response curve of the cutting system deviates toward the right, suggesting hard spring vibration

Table 1: Mechanical properties of carbon fiber/epoxy composite [37].

ρ(kg/m^3)	E_{11} (GPa)	E_{22} (GPa)	G_{12} (GPa)	G_{23} (GPa)	ν_{12}
1672	25.8	8.7	3.5	3.5	0.34

Table 2: Coefficients of cutting forces [21].

C_f (mm/rev-tooth)	$\overline{\overline{\varsigma}}_1$ (N/mm)	$\overline{\overline{\eta}}_1$ (N)	$\overline{\overline{\varsigma}}_2$ (N/mm)	$\overline{\overline{\eta}}_2$ (N)	a_c (mm)	N
0.2	620	208	43	52	3	4

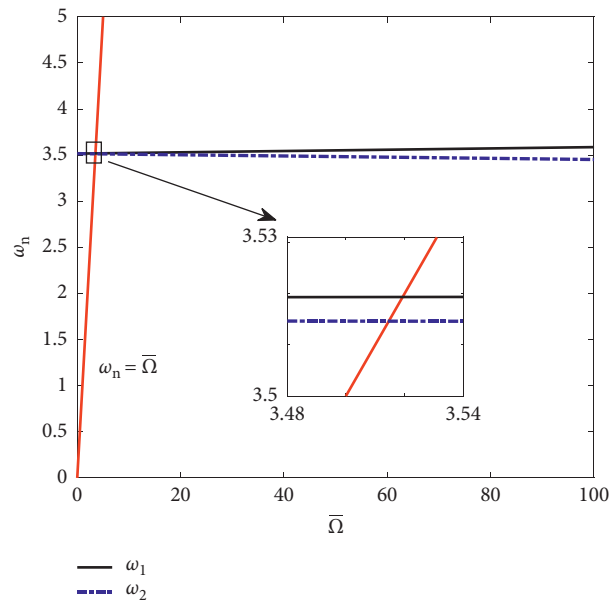

Figure 2: Natural frequency versus rotational speed (L/d = 10, $\theta = 0^\circ$).

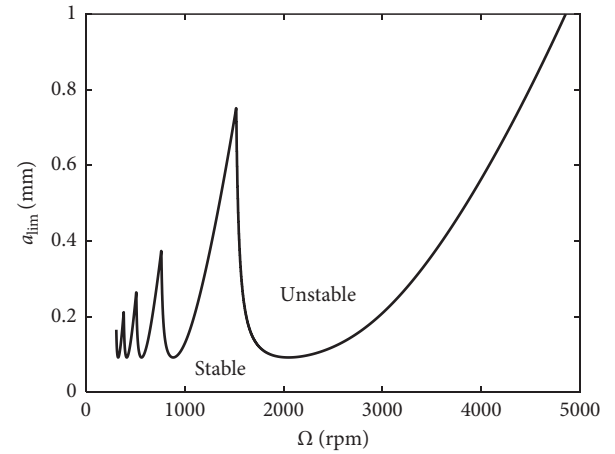

Figure 3: Stability lobe diagram of the cutting system with composite cutting tool (L/d = 10, $\overline{c} = 0.3$, $\theta = 0^\circ$).

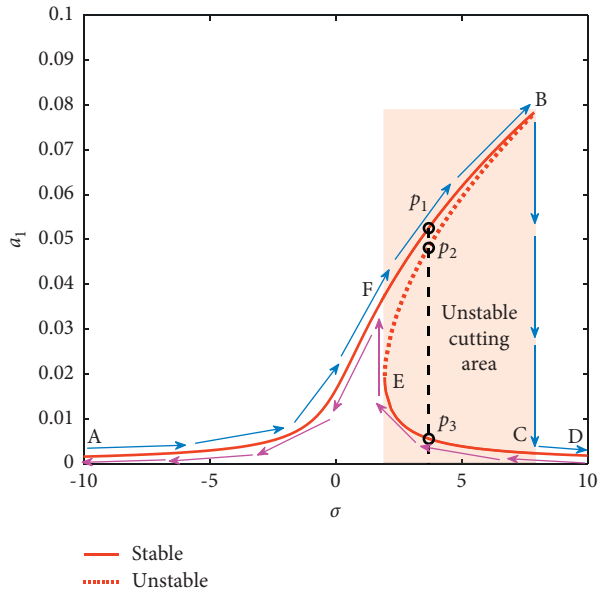

Figure 4: Frequency response curve in case I.

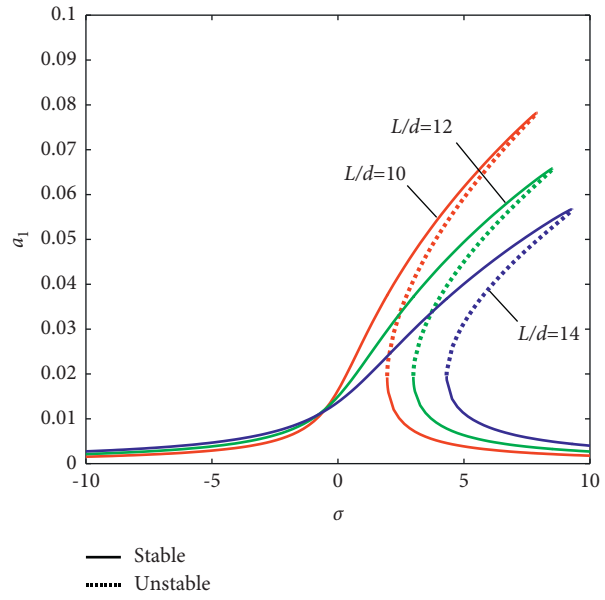

Figure 5: The effect of ratio of length to diameter on frequency response curve ($\bar{c} = 0.01$, $\theta = 0^\circ$, case I).

behavior of Duffing type oscillator. As the detuning parameter varies between σ_F and σ_B, the cutting system has three steady-state vibration amplitudes, p_1, p_2, and p_3, among which p_1 and p_3 are stable and p_2 is unstable. This means that the cutting system works in an unstable cutting state. Therefore, cutting conditions and consequently initial conditions should be adjusted such that the stable branch with less vibration amplitudes is realized in practice.

Figures 5–9 show the effects of ratio of length to diameter, structural damping, cutting force, ply angle, and rotating speed on frequency response curve, respectively, for the case $\overline{\Omega} = \omega_1$. As shown in Figure 5, when ratio of length to diameter increases, vibration amplitudes decrease and frequency response curve bends more strongly toward left. This is physically expected, because the nonlinear stiffness coefficient $\lambda = (EA)_{\text{equiv}} L^2/2(EI)_{\text{equiv}}$ is proportional to ratio of length to diameter according to (12). As is observed and physically expected from Figure 6, the increase in the structural damping leads to the decrease in vibration amplitudes. In order to study the effect of cutting force coefficients, we define $\varsigma_2 = K_f \bar{\bar{\varsigma}}_2$, $\eta_2 = K_f \bar{\bar{\eta}}_2$, with the parameters $\bar{\bar{\varsigma}}_2$ and $\bar{\bar{\eta}}_2$ given in Table 2. As is shown in Figure 7, by increasing cutting forces, vibration amplitudes increase. Figure 8 shows that the primary resonance amplitude increases with the increase of the ply angle because the elastic modulus E_{11} along the longitudinal direction of the fiber is significantly larger than the transverse elastic modulus E_{22} (as shown in Table 1). Therefore, as the ply angle is greater, the equivalent bending stiffness $(\text{EI})_{\text{equiv}}$ of the composite cutting tool is smaller; thus, the nondimensional cutting force coefficients are greater (as shown in (11)). As a result, the amplitude of the primary resonance response is larger.

Figure 9 shows that vibration amplitudes decrease with the decrease of rotating speed. This is physically expected, because the equivalent damping of the cutting system (which will be introduced in the subsequent section) increases with

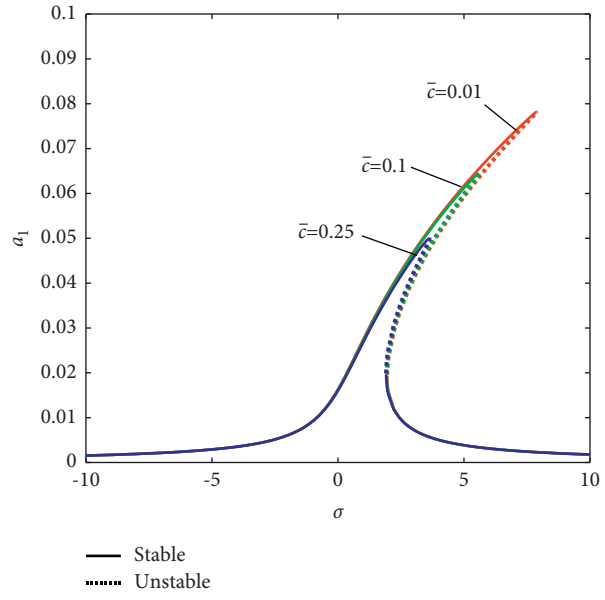

Figure 6: The effect of structural damping on frequency response curve (L/d = 10, $\theta = 0^\circ$, case I).

the decrease of rotating speed due to the damping effect from regenerative chatter mechanism.

Figures 10–14 show the amplitude versus damping coefficient with different ratios of length to diameter, detuning parameter values, cutting force coefficients, ply angles, and rotating speeds, respectively, for the case $\overline{\Omega} = \omega_1$. From these figures, it can be seen that for some values of L/d, σ, K_f, or θ, there are multivalued curves. For example, when $L/d = 10$ and $\bar{c} < 0.45$, as is shown in Figure 10, the system has two stable and one unstable branches, but for $L/d = 10$ and $\bar{c} > 0.45$, there exists only

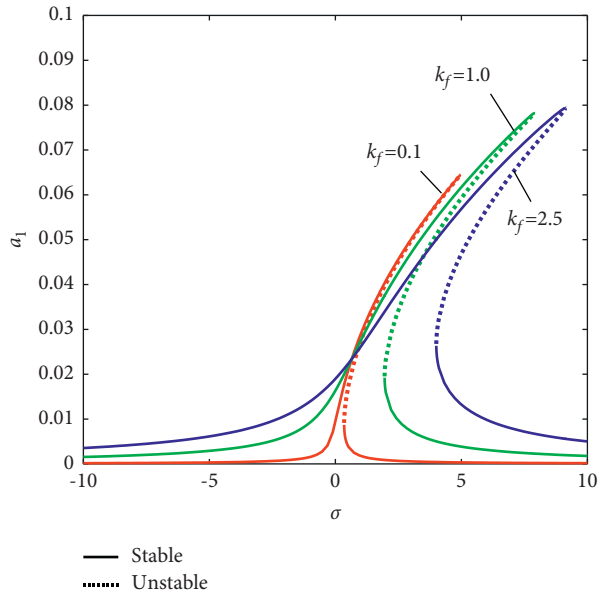

FIGURE 7: The effect of cutting force coefficient on frequency response curve (L/d = 10, $\bar{c}$ = 0.01, θ = 0°, case I).

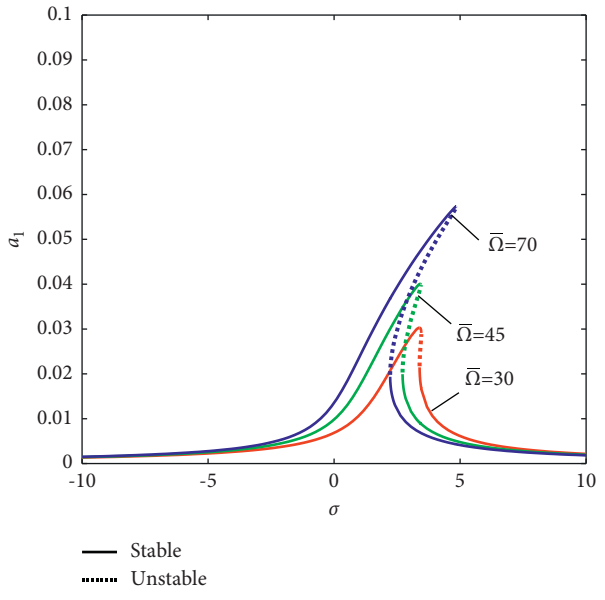

FIGURE 9: The effect of rotating speed on frequency response curve (L/d = 10, $\bar{c}$ = 0.01, θ = 0°, case I).

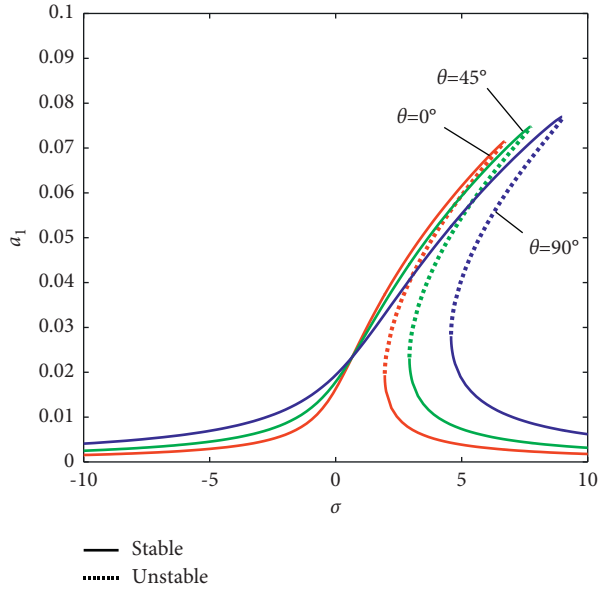

FIGURE 8: The effect of ply angle on frequency response curve (L/d = 10, $\bar{c}$ = 0.01, case I).

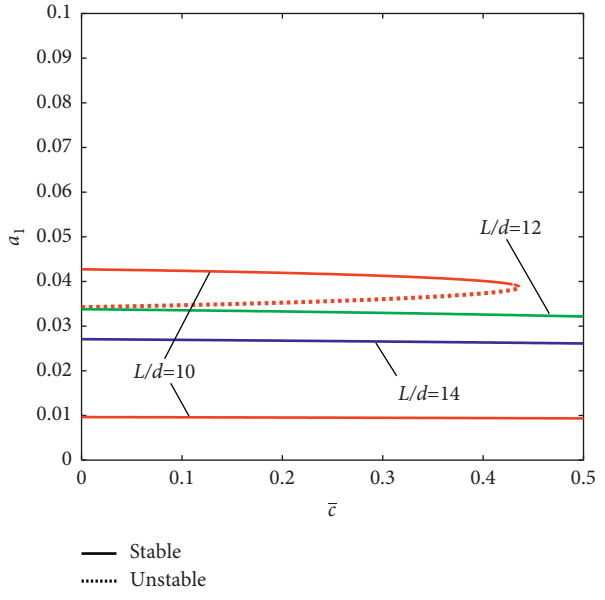

FIGURE 10: Amplitude versus damping coefficient with different ratios of length to diameter (σ = 2, $\bar{c}$ = 0.01, θ = 0°, case I).

one stable branch. For large values of $\bar{c}$ and large values of L/d, curves are always single-valued.

Figures 15–19 show the amplitude versus ply angle with different ratios of length to diameter, detuning parameter values, cutting force coefficients, damping coefficients, and rotating speeds, respectively ($\overline{\Omega} = \omega_1$). Similar to the cases in Figure 10 ~ 14, again, for some values of L/d, σ, K_f, or $\bar{c}$, multivalued curves can be observed.

Figures 20–24 show the amplitude versus cutting force coefficient with different ratios of length to diameter, detuning parameter values, ply angle, damping coefficients, and rotating speeds, respectively. Again, when cutting force coefficient is less than the specified value, multivalued curves can be obtained for some values of L/d, σ, θ, $\bar{c}$, or $\overline{\Omega}$.

Figures 25–27 show the effects of ply sequences (see Table 3) on the frequency response curve, the amplitude versus dumping coefficient, and the amplitude versus cutting force coefficient, respectively. It can be seen from Figure 25 that the configuration A leads to the largest vibration amplitude, while the configuration C leads to the smallest vibration amplitude. This phenomenon can also be found in Figure 8 where the vibration amplitude increases with the

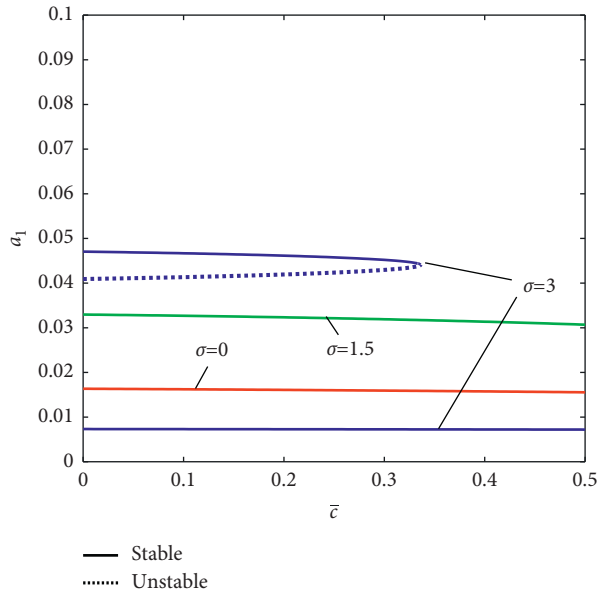

FIGURE 11: Amplitude versus damping coefficient with different detuning parameter values (L/d = 10, $\bar{c}$ = 0.01, θ = 0°, case I).

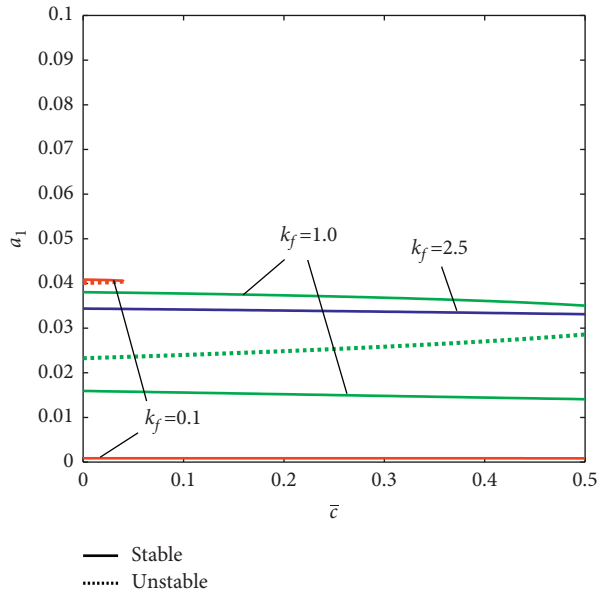

FIGURE 12: Amplitude versus damping coefficient with different cutting force coefficients (L/d = 10, σ = 2, θ = 0°, case I).

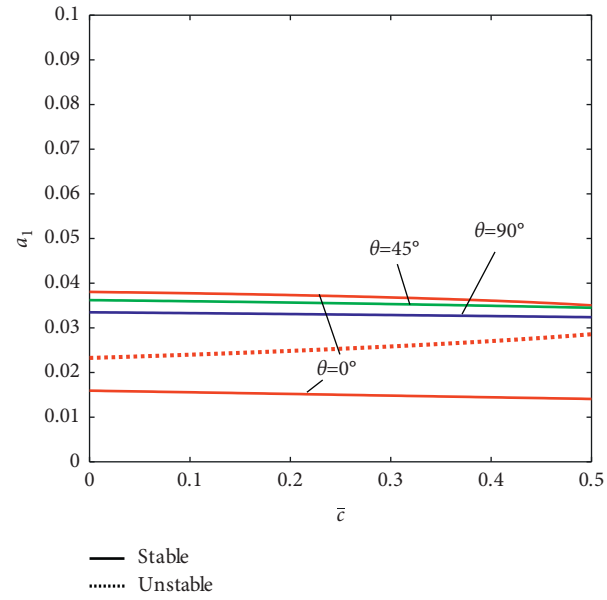

FIGURE 13: Amplitude versus damping coefficient with different ply angles (L/d = 10, σ = 2, case I).

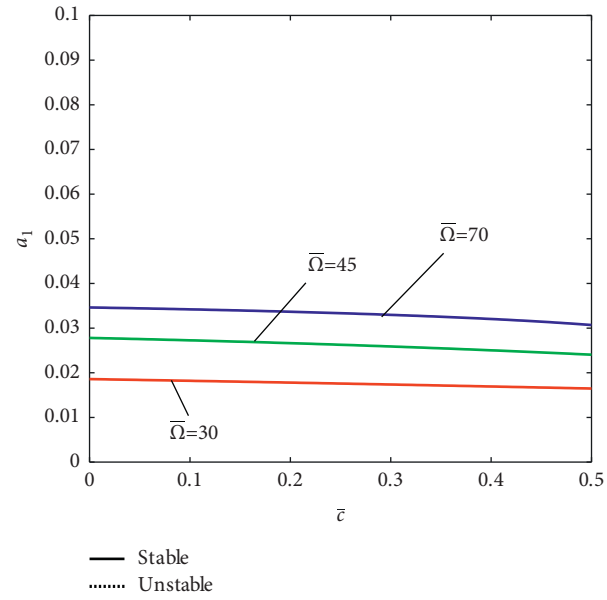

FIGURE 14: Amplitude versus damping coefficient with different rotating speed (L/d = 10, σ = 2, case I).

ply angle when using the same configuration. Again, it can be seen from Figures 26 and 27 that multivalued curves can be observed for some values of L/d, σ, K_f, or $\bar{c}$.

3.2.2. Case II. Figures 28–33 show the effects of ratio of length to diameter, structural damping, cutting force, ply angle, ply sequence, and rotating speed on frequency response curve, respectively, for the case $\overline{\Omega} = \omega_2$. As is observed, the frequency responses and effect of various parameters for the cutting system are similar to those in case I; as ratio of length to diameter and structural damping increase, vibration amplitudes decrease. Furthermore, as cutting force coefficient, ply angle, and rotating speed increase, vibration amplitudes increase. However, for this case, vibration amplitudes are less than those of case I.

It should be noted that the equivalent damping of the cutting system is composed of the structural damping and the damping from regenerative chatter mechanism. The equivalent damping coefficient of case I can be expressed as

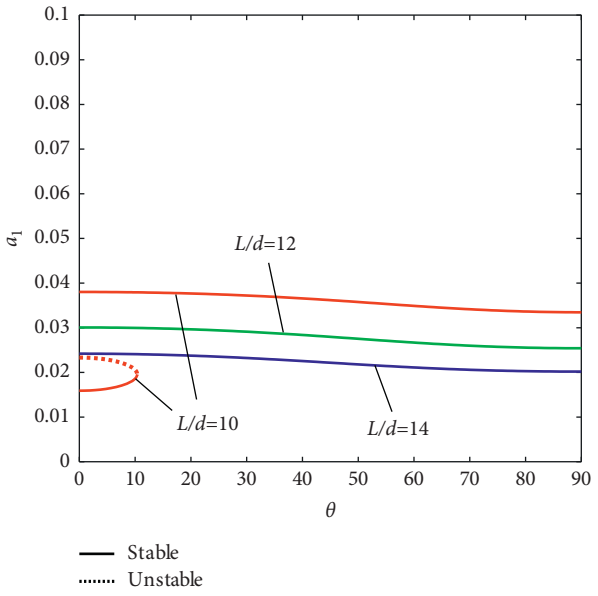

Figure 15: Amplitude versus ply angle with different ratios of length to diameter ($\bar{c}$ = 0.01, σ = -1.5, case I).

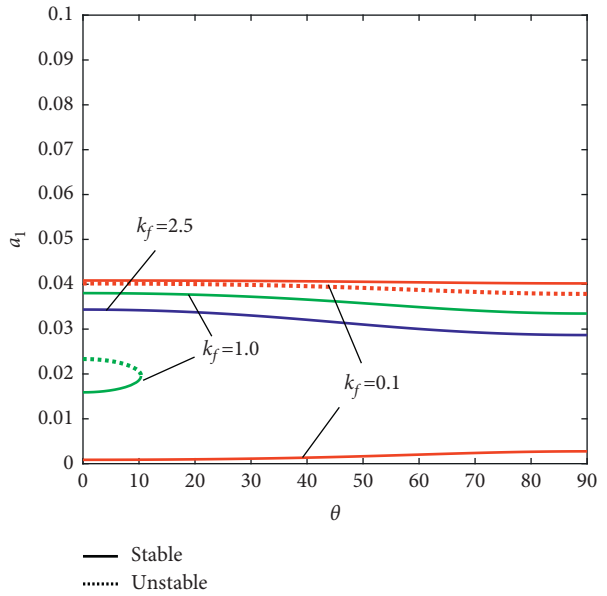

Figure 17: Amplitude versus ply angle with different cutting force coefficients (L/d = 10, $\bar{c}$ = 0.01, σ = 2, case I).

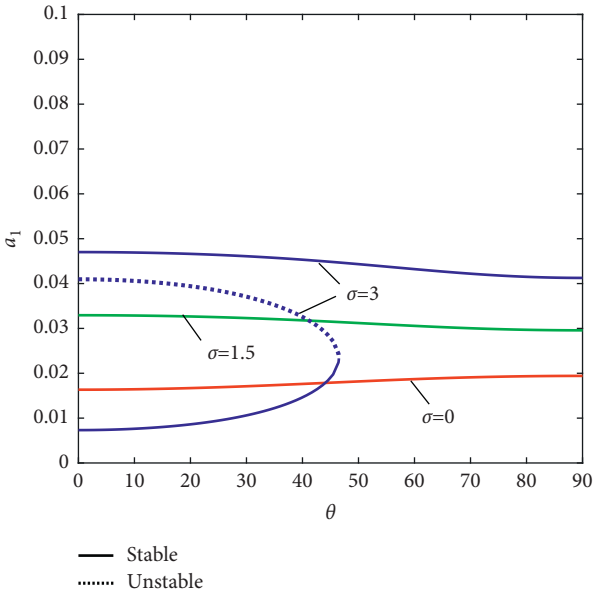

Figure 16: Amplitude versus ply angle with different detuning parameter values (L/d = 10, $\bar{c}$ = 0.01, case I).

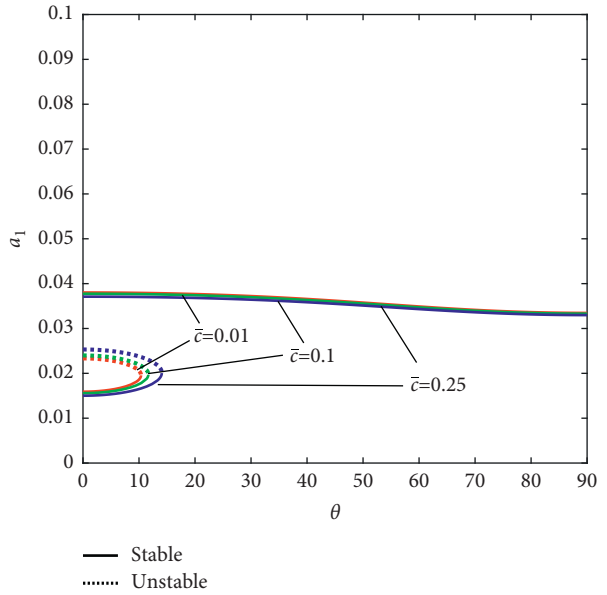

Figure 18: Amplitude versus ply angle with different damping coefficients (L/d = 10, σ = 2, case I).

$$c_{equiv1} = \bar{c} - \phi_1^2(1)\frac{N}{4\pi}\left[\left(\bar{\alpha}_0' + \bar{\beta}_0\right)\left(1 - \cos\omega_1\bar{\tau}\right) + \left(\bar{\beta}_0' - \bar{\alpha}_0\right)\sin\omega_1\bar{\tau}\right] \Big/ \left[\omega_1\int_0^1 \phi_1^2(x)dx\right]. \tag{45}$$

In addition, the equivalent damping coefficient of case II can be expressed as

$$c_{equiv2} = \bar{c} + \phi_1^2(1)\frac{N}{4\pi}\left[\left(\bar{\alpha}_0' + \bar{\beta}_0\right)\left(1 - \cos\omega_2\bar{\tau}\right) + \left(\bar{\alpha}_0 - \bar{\beta}_0'\right)\sin\omega_2\bar{\tau}\right] \Big/ \left[\omega_2\int_0^1 \phi_1^2(x)dx\right]. \tag{46}$$

Figures 34–38 show the effect of different parameters on the equivalent damping coefficients. As is observed, the

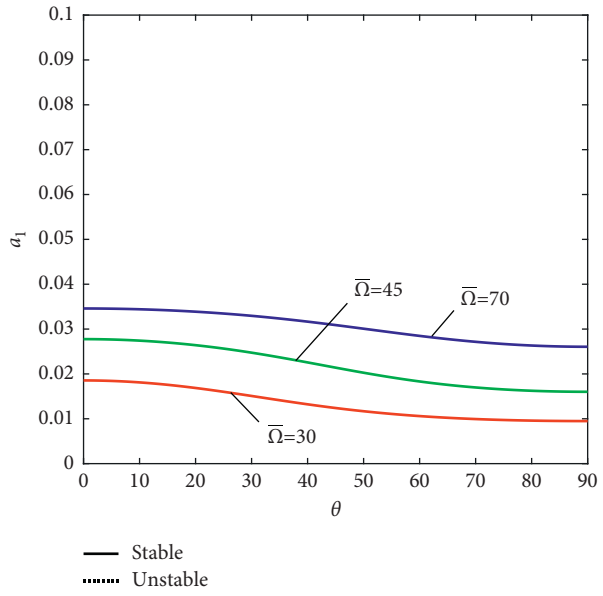

FIGURE 19: Amplitude versus ply angle with different rotating speeds (L/d = 10, $\overline{c}$ = 0.01, σ = 2, case I).

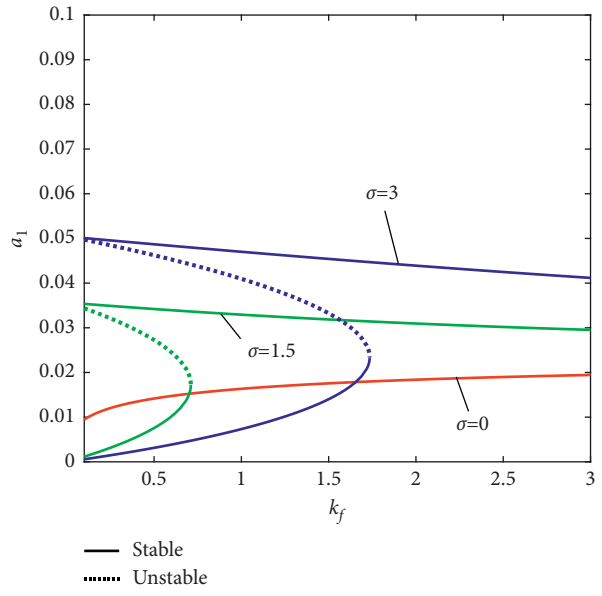

FIGURE 21: Amplitude versus cutting force coefficient with different detuning parameter values (θ = 0°, $\overline{c}$ = 0.01, L/d = 10, case I).

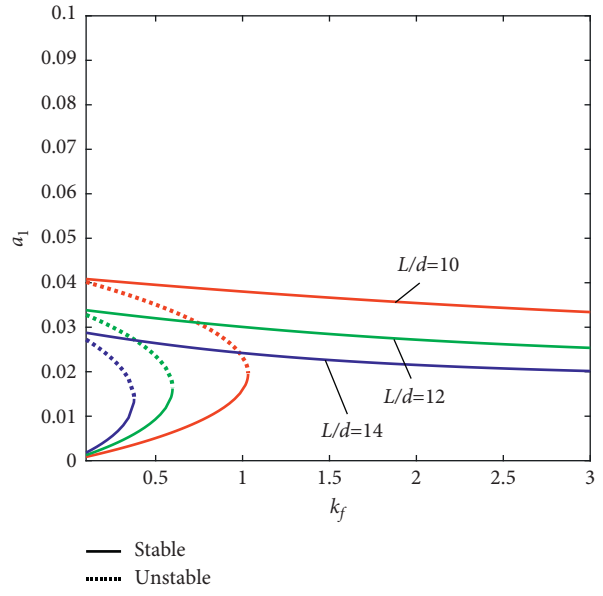

FIGURE 20: Amplitude versus cutting force coefficient with different ratios of length to diameter (θ = 0°, $\overline{c}$ = 0.01, σ = 2, case I).

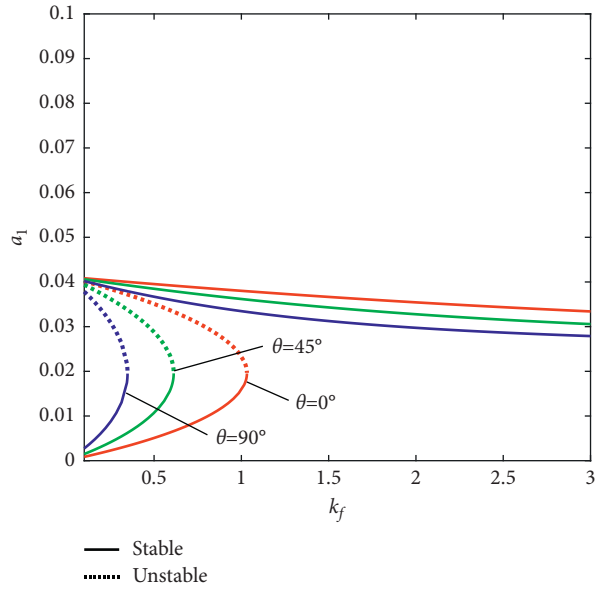

FIGURE 22: Amplitude versus cutting force coefficient with different ply angles (σ = 2, $\overline{c}$ = 0.01, L/d = 10, case I).

equivalent damping coefficients of case I are always larger than those of case II. This explains the reason why vibration amplitudes of case I are larger than those of case II. It can be also seen that the equivalent damping coefficients increase with ratio of length to diameter, ply angle, cutting force, and structural damping but decrease with rotating speed. Therefore, the increase of rotating speed leads to large vibration amplitudes, as shown in Figures 9 and 32. When rotating speed approaches infinity, the equivalent damping coefficient approaches the structural damping $\overline{c}$ (see Figure 38).

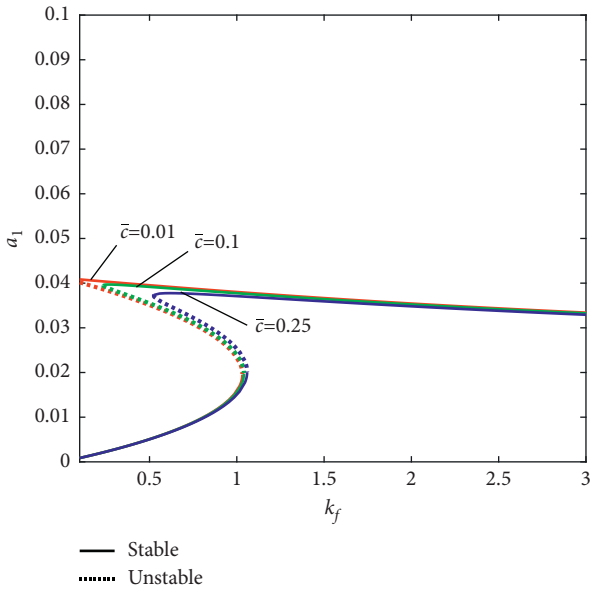

FIGURE 23: Amplitude versus cutting force coefficient with different damping coefficients ($\sigma = 2$, $\theta = 0^\circ$, L/d = 10, case I).

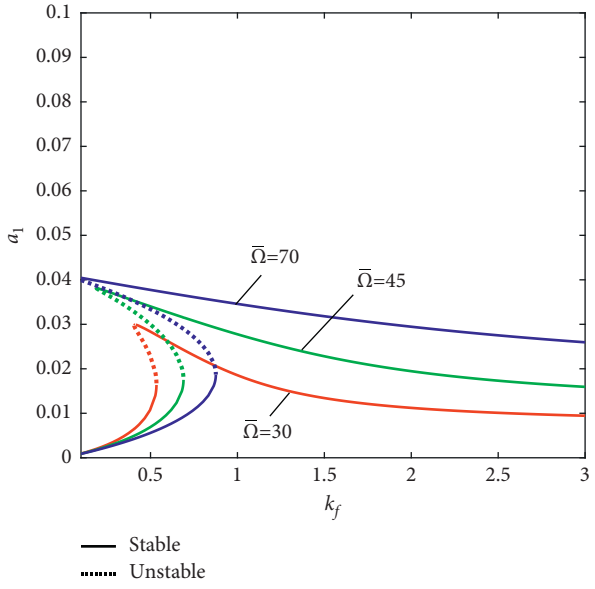

FIGURE 24: Amplitude versus cutting force coefficient with different rotating speeds ($\sigma = 2$, $\bar{c} = 0.01$, $\theta = 0^\circ$,L/d = 10, case I).

Moreover, for some values of L/d, σ, K_f, $\bar{c}$, θ, or $\bar{\Omega}$, multivalued solutions can be found from the amplitude versus damping coefficient with different ratios of length to diameter, detuning parameter values, cutting force coefficients, ply angles, and rotating speeds, respectively (not shown).

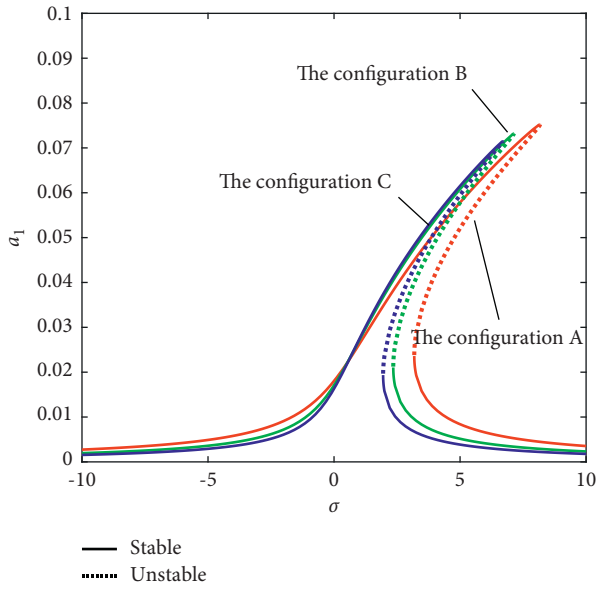

FIGURE 25: The frequency response curve with different ply sequences ($\bar{c} = 0.05$, L/d = 10, case I).

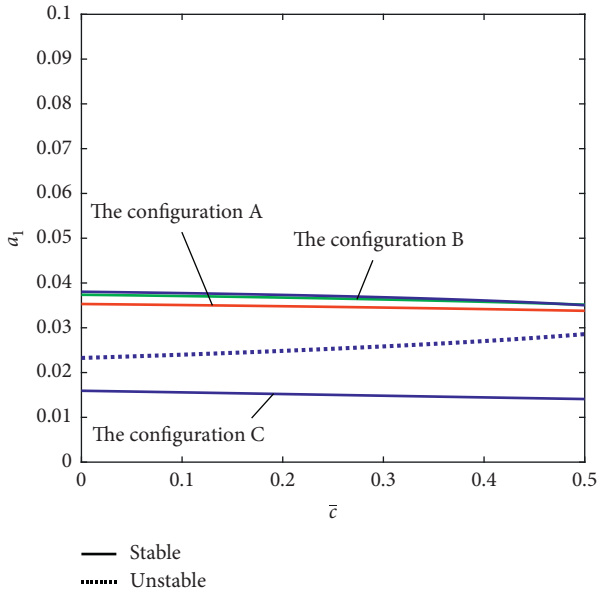

FIGURE 26: Amplitude versus dumping coefficient with different ply sequences ($\sigma = 2$, L/d = 10, case I).

TABLE 3: Configuration of composite.

Configuration	Sequence
A	$[90^\circ/90^\circ/0^\circ]_s$
B	$[0^\circ/90^\circ/0^\circ/0^\circ/90^\circ/0^\circ]$
C	$[0^\circ]_6$

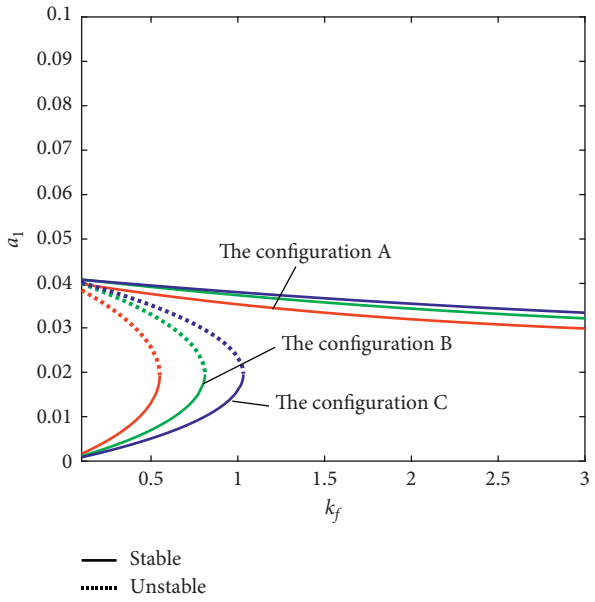

Figure 27: Amplitude versus cutting force coefficient with different ply sequences ($\bar{c} = 0.01$, $\sigma = 2$, L/d = 10, case I).

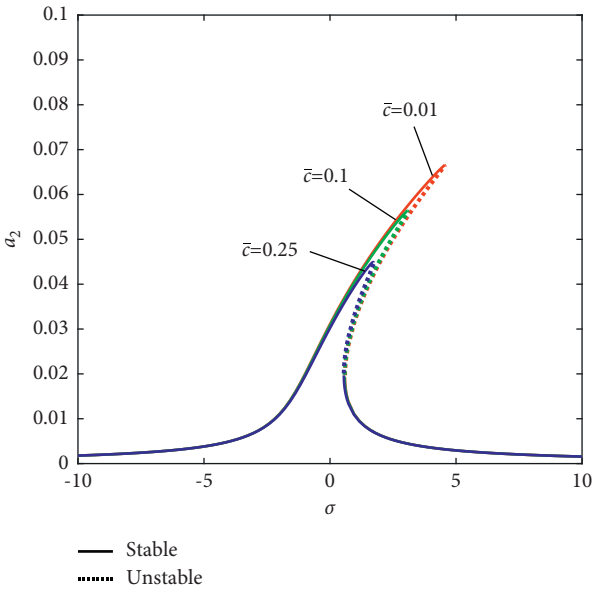

Figure 29: The effect of structural damping on frequency response curve (L/d = 10, $\theta = 0^\circ$, case II).

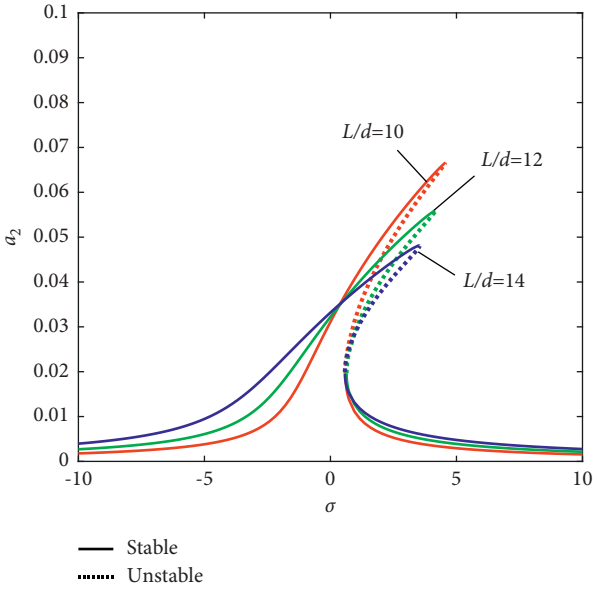

Figure 28: The effect of ratio of length to diameter on frequency response curve ($\theta = 0^\circ$, $\bar{c} = 0.01$, case II).

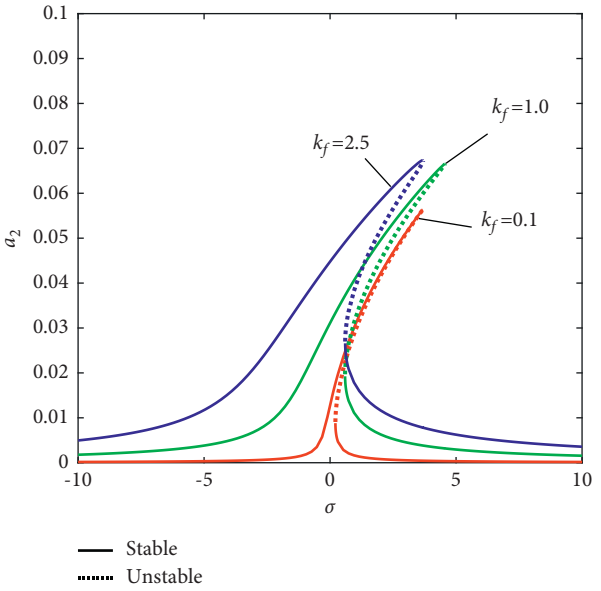

Figure 30: The effect of cutting force coefficient on frequency response curve (L/d = 10, $\theta = 0^\circ$, $\bar{c} = 0.01$, case II).

Figure 39 shows the frequency response curve for the four cases. As is observed, the curves of cases I and III are very similar, except that the amplitude in case I is larger than that in case III. Likewise, the curves of cases II and IV are very similar, except that the amplitude in case II is larger than that in case IV.

3.2.3. Case III. For this case, the equivalent coefficient is identical with that in case I, but the amplitude of excitation force $(c^2_{f\varsigma_1} + c^2_{f\eta_1})/4$ in this case is lower than $(\bar{\varsigma}_2^2 + \bar{\eta}_2^2)$ in case I (e.g., using the same parameters L/d = 10, $\theta = 90^\circ$, and $K_f = 3$, the amplitudes of excitation force are 0.2695 and 0.2532 for cases I and III, respectively). Therefore, generally,

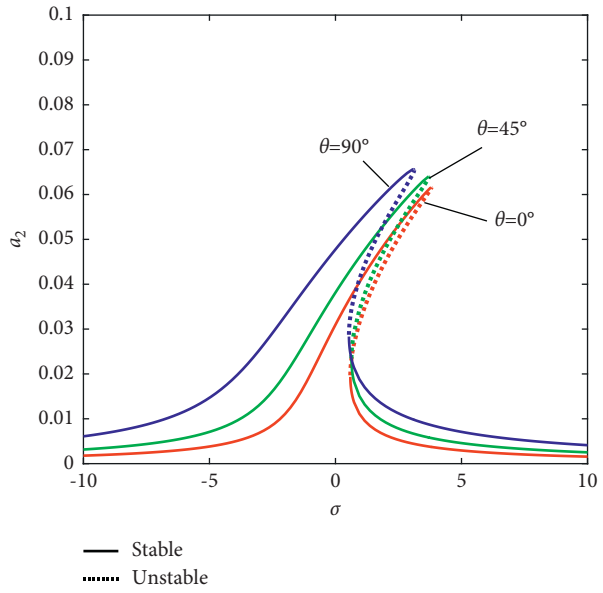

Figure 31: The effect of ply angle on frequency response curve (L/d = 10, $\bar{c}$ = 0.01, case II).

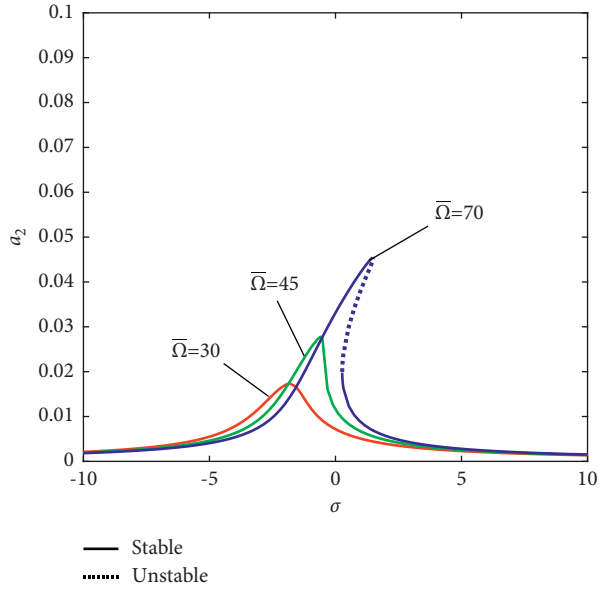

Figure 32: The effect of rotating speed on frequency response curve (L/d = 10, $\bar{c}$ = 0.01, case II).

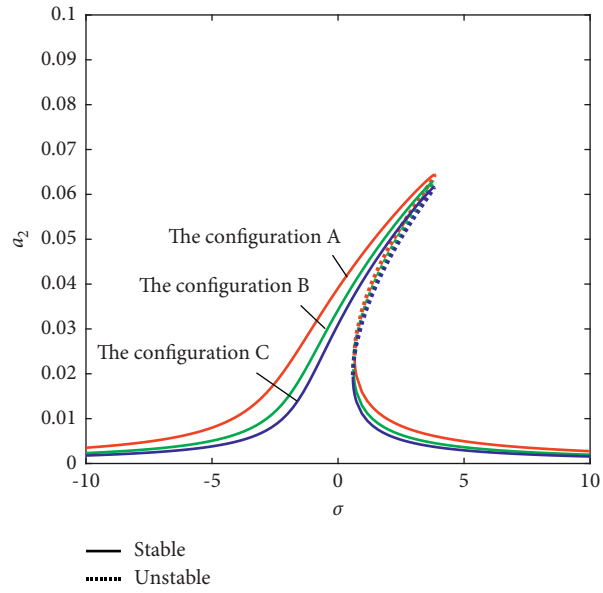

Figure 33: Frequency response curve with different ply configurations ($\bar{c}$ = 0.05, L/d = 10, case II).

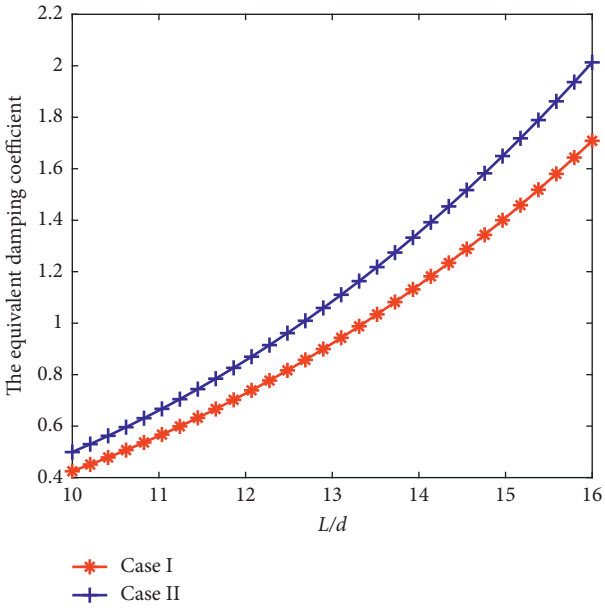

Figure 34: The equivalent damping coefficients versus ratio of length to diameter for cases I and II.

the behavior of nonlinear forced vibration in this case (see Figure 39) is similar to case I, despite having less vibration amplitudes compared with case I.

3.2.4. Case IV. For this case, the equivalent coefficient is identical with that in case II, and the amplitude of excitation force in this case is lower than that in in case II. Thus, under the same conditions, vibration amplitudes are generally lower than those in case II. The results of case IV are not shown to save space.

In order to validate the calculated approximate solution using multiscale method, the numerical simulation results according to (17) are also displayed in Figures 40 and 41. These two calculated results using different methods are in good consistency.

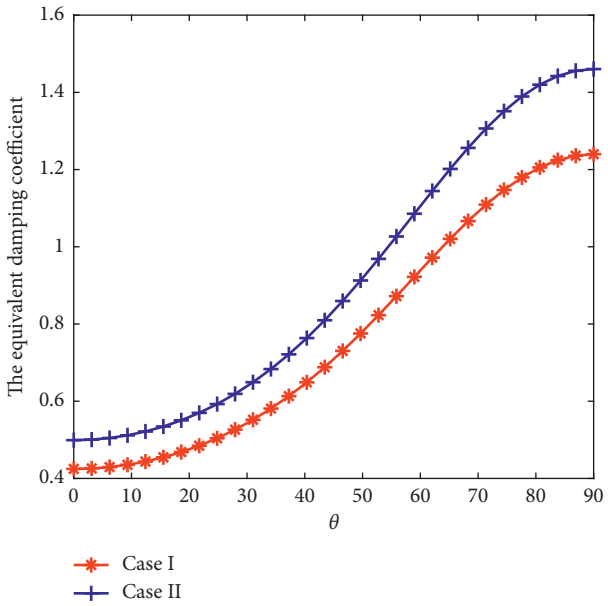

Figure 35: The equivalent damping coefficients versus ply angle for cases I and II.

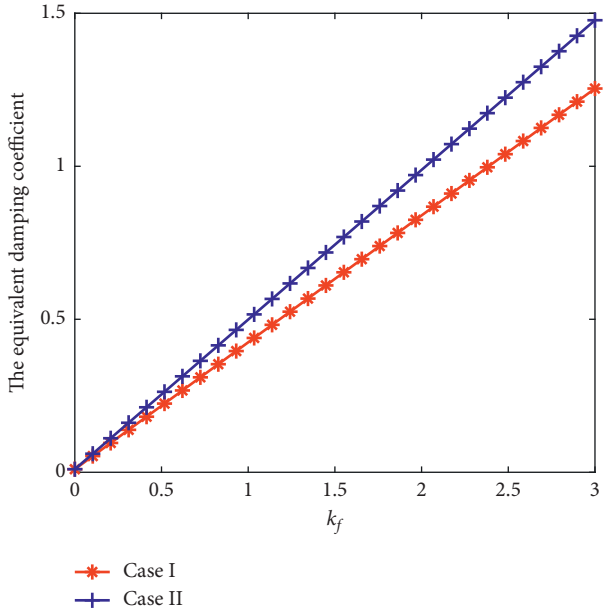

Figure 36: The equivalent damping coefficients versus cutting force for cases I and II.

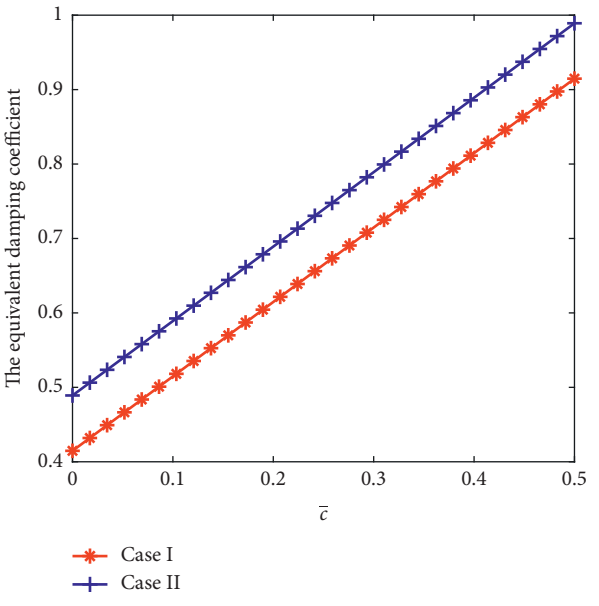

Figure 37: The equivalent damping coefficients versus structural damping for cases I and II.

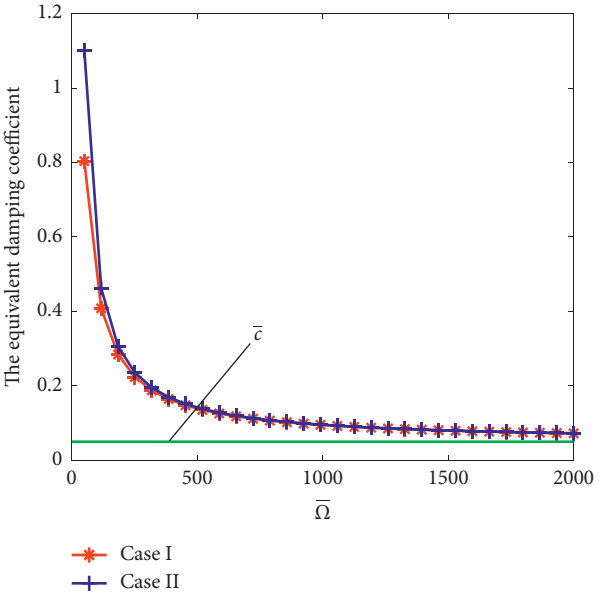

Figure 38: The equivalent damping coefficients versus rotating speed for cases I and II.

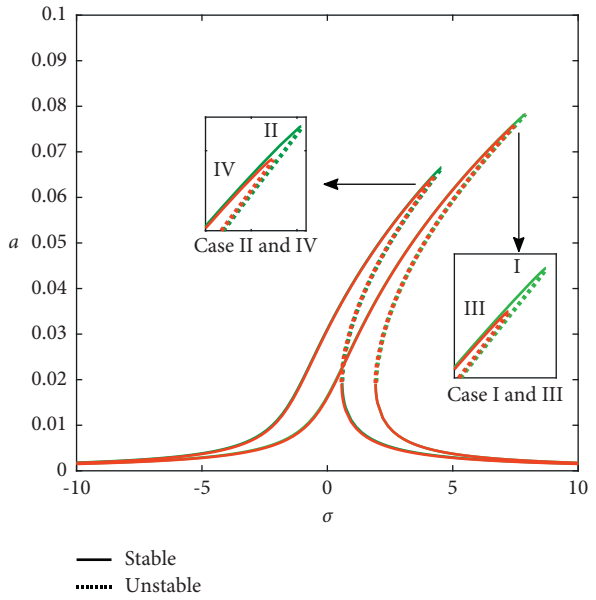

Figure 39: The frequency response curve for the four cases (L/d = 10, $\bar{c} = 0.01$, $\theta = 0^{\circ}$, $\overline{\Omega} = 100$).

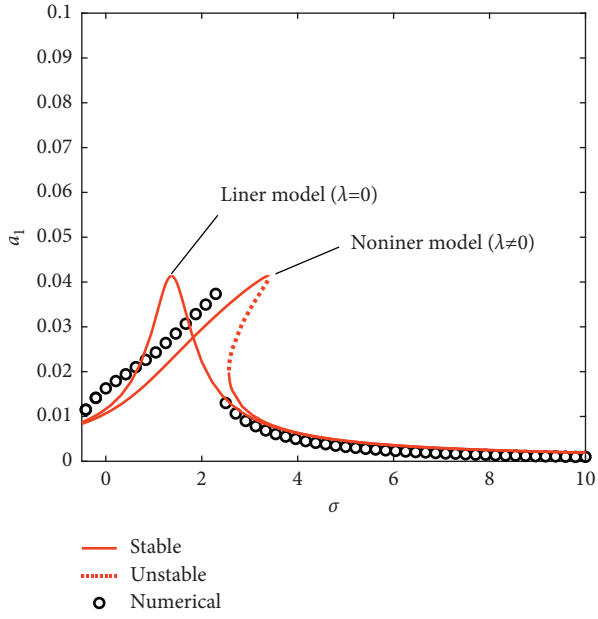

Figure 40: Comparison of results between the method of multiple scales and the numerical simulation (case I, L/d = 10, $\bar{c} = 0.03$, $\theta = 0^{\circ}$, $\overline{\Omega} = 50$, $K_f = 1$).

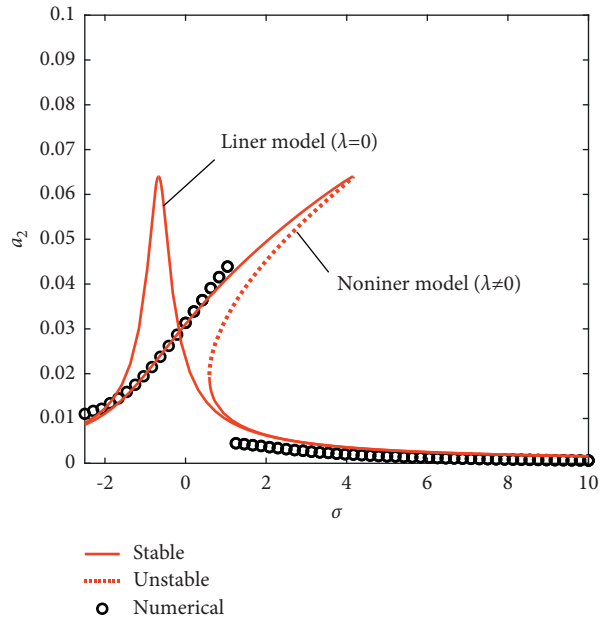

FIGURE 41: Comparison of results between the method of multiple scales and the numerical simulation (case II, L/d = 10, $\bar{c} = 0.03$, $\theta = 0^\circ$, $\overline{\Omega} = 100$, $K_f = 1$).

4. Conclusions

In this paper, a nonlinear dynamic model of the milling process with composite rotational cutting tool is presented. The cutting tool is simplified to a nonplanar bending Euler–Bernoulli beam, and the structural nonlinearity is attributed to the higher-order bending deformation of the cutting tool. A linear cutting force model considering regenerative mechanism, which includes time-delay terms and the first and second harmonic terms, is used. In addition, structural damping and gyroscopic effect are also considered. Nonlinear ordinary differential equations in the generalized coordinates are derived using the Hamilton principle and the Galerkin method. The lobe diagram of the cutting system is obtained. The multiscale method is used to construct the analytical approximate solutions of the forced vibration frequency response. It is found that, for all cases of primary resonance and superharmonic resonance, excitation of the forward (backward) mode does not produce the vibration responses in the backward (forward) mode because of not taking into account internal resonance in the proposed model. For primary and superharmonic resonance conditions, the effective nonlinearity of the cutting system with higher-order bending deformation rotating composite cutting tool is of a hard type. Jump phenomenon and multivalued solutions can be observed.

The influence of higher-order bending deformation causes the frequency response curve to bend more strongly toward right when ratio of length to diameter increases. The study also finds that the vibration amplitudes of the cutting tool increase with cutting force or ply angle. It can be seen that the damping of the cutting system has a significant influence on the vibration amplitude of the composite cutting tool. The damping capacities of the cutting system can be measured by the two different equivalent damping coefficients c_{equiv1} and c_{equiv2} which include the structural damping and the damping from regenerative chatter mechanism. Cases I and III have the same equivalent damping coefficient c_{equiv1}, and cases II and IV have the same equivalent damping coefficient c_{equiv2}. It has been found that c_{equiv2} is larger than c_{equiv1}, so the vibration amplitudes of case I are larger than those of case II. In addition, for all resonant cases, as rotating speed decreases or structural damping increases, the equivalent damping coefficient is strengthened, and consequently less vibration amplitudes are observed. Therefore, from this point of view, low rotating speeds are preferable to keep vibration amplitudes small. [38].

Abbreviations

T:	Kinetic energy
L:	Length of the cutting tool
t:	Time
ρ:	Density
A:	Cross-sectional area
I:	Second moment of area of the beam cross section
v, w:	Transverse deflections of the shaft element
x, y, z:	Variable coordinates
ψ_y, ψ_z:	Rotation angles of the cross section around the y and z axes
Ω:	Rotating speed of the shaft
$\overline{Q}_{11}$:	Off-axis stiffness coefficient of the kth layer for the composite cutting tool
U:	Potential energy
W_c:	Rayleigh dissipative energy function of the cutting tool
c:	Structural damping coefficient
δ:	Variational operator

δW: Virtual work of the cutting force
F_y, F_z: Linear regenerative cutting forces
τ: Delay time of milling process
N: The number of teeth
K_{tc}: Cutting force coefficients in the tangential directions
K_{te}: Edge force coefficients in the tangential directions
K_{rc}: Cutting force coefficients in the radial directions
K_{re}: Edge force coefficients in the radial directions
a: Axial cutting depth
c_f: Feed per tooth per revolution
$(EI)_{equiv}$, $(EA)_{equiv}$: Equivalent bending and tensile stiffness of the cutting tool
$(\rho I)_{equiv}$, $(m)_{equiv}$: Equivalent diametrical mass moment of inertia and equivalent mass per unit length
ρ_k: Density of the kth layer
r_k, r_{k+1}: Inner diameter and outer diameter of the kth layer
$\phi_1(\overline{x})$: Mode function
ω_1, ω_2: Forward and backward whirling frequencies
ε: Small parameter
i: $\sqrt{-1}$.

Appendix

A. The Stain Energy of the Composite Cutting Tool

If the torsional deformation is negligible, the bending displacements of the composite cutting tool in x, y, and z directions are as follows:

$$u_x = -z\psi_y + y\psi_z, u_y = v, u_z = w. \tag{A.1}$$

The strain in the x direction is

$$\varepsilon_{xx} = \varepsilon_l + \varepsilon_{nl}, \tag{A.2}$$

where

$$\varepsilon_l = -z\frac{\partial \psi_y}{\partial x} + y\frac{\partial \psi_z}{\partial x}, \varepsilon_{nl} = \frac{1}{2}\psi_y^2 + \frac{1}{2}\psi_z^2, \tag{A.3}$$

where ε_l and ε_{nl} are the linear strain and the nonlinear strain generated in high-order bending deformation, respectively.

Bending energy for the composite cutting tool can be expressed as

$$U = \frac{1}{2}\int_0^L \iint_A (\sigma_{xx}\varepsilon_{xx})\mathrm{d}A\mathrm{d}x. \tag{A.4}$$

The elastic stress-strain relations of the laminate cutting tool can be expressed as

$$\sigma_{xx} = \overline{Q}_{11}\varepsilon_{xx}. \tag{A.5}$$

Employing (A.2), (A.3), and (A.5), (A.4) can be rewritten as

$$U = \frac{1}{2}\int_0^L \iint_A \overline{Q}_{11}\left(z^2\left(\frac{\partial \psi_y}{\partial x}\right)^2 + y^2\left(\frac{\partial \psi_z}{\partial x}\right)^2 - 2yz\frac{\partial \psi_y}{\partial x}\frac{\partial \psi_z}{\partial x} + \frac{1}{4}\psi_y^4 + \frac{1}{4}\psi_z^4 + \frac{1}{2}\psi_y^2\psi_z^2 - 2\left(z\frac{\partial \psi_y}{\partial x} + y\frac{\partial \psi_z}{\partial x}\right)\left(\frac{1}{2}\psi_y^2 + \frac{1}{2}\psi_z^2\right)\right)^2 dAdx. \tag{A.6}$$

Due to the symmetry of the cross section, the third and seventh terms in the above equation are equal to zero.

Therefore, the strain energy of the composite cutting tool can be reduced as follows:

$$U = \frac{(EI)_{equiv}}{2}\int_0^L \left(\left(\frac{\partial \psi_y}{\partial x}\right)^2 + \left(\frac{\partial \psi_z}{\partial x}\right)^2\right)dx + \frac{(EA)_{equiv}}{2}\int_0^L \left(\frac{1}{4}\psi_y^4 + \frac{1}{4}\psi_z^4 + \frac{1}{2}\psi_y^2\psi_z^2\right)dx. \tag{A.7}$$

B. The Expression of the Off-Axis Stiffness Coefficient

The off-axis stiffness coefficient of the kth layer for the composite cutting tool is defined as

$$\overline{Q}_{11} = C_{11}\cos^4\theta^{(k)} + C_{22}\sin^4\theta^{(k)} + 2(C_{12} + 2C_{66})\sin^2\theta^{(k)}\cos^2\theta^{(k)}, \tag{B.1}$$

where $\theta^{(k)}$ is the layer angle of each layer of the material.

The expressions of C_{11}, C_{12}, C_{22}, and C_{66} are as follows:

$$C_{11} = \frac{E_{11}}{1-\nu_{12}\nu_{21}}, C_{12} = \frac{\nu_{12}E_{11}}{1-\nu_{12}\nu_{21}} = \frac{\nu_{21}E_{22}}{1-\nu_{12}\nu_{21}}, C_{22} = \frac{E_{22}}{1-\nu_{12}\nu_{21}}, C_{66} = C_{12}, \tag{B.2}$$

where

$$\nu_{21} = \frac{\nu_{12} E_{11}}{E_{22}}. \quad \text{(B.3)}$$

Data Availability

The data used to support the findings of this study are included within the article.

Conflicts of Interest

The authors declare that they have no conflicts of interest.

Acknowledgments

The research was funded by the https://doi.org/10.13039/501100001809National Natural Science Foundation of China (Grant No. 11672166).

References

[1] K. Seto and N. Tominari, "Effect of a variable stiffness-type dynamic damper on machine tools with long overhung ram," *Bulletin of JSME*, vol. 19, no. 137, pp. 1270–1277, 1976.

[2] D. J. P. Hartog, *Mechanical Vibrations*, McGraw-Hill, New York, 1956.

[3] S. Ema and E. Marui, "Suppression of chatter vibration of boring tools using impact dampers.International," *Journal of Machine Tools and Manufacture*, vol. 40, no. 8, pp. 1141–1156, 2008.

[4] S. Nagano, T. Koizumi, T. Fujii, N. Tsujiuchi, H. Ueda, and S. Kobe, "Development of a composite boring bar. Compos Structures," *Composite Structures*, vol. 38, pp. 531–539, 1997.

[5] D. G. Lee, H. Y. Hwang, and J. K. Kim, "Design and manufacture of a carbon fiber epoxy rotating boring bar," *Composite Structures*, vol. 60, pp. 115–124, 2003.

[6] S. Ghorbani, V. A. Rogov, A. Carluccio, and P. S. Belov, "The effect of composite boring bars on vibration in machining process," *International Journal of Advanced Manufacturing Technology*, vol. 105, no. 1-4, pp. 1157–1174, 2019.

[7] F. Taylor, "On the art of cutting metals," *Trans. ASME*, vol. 28, pp. 31–350, 1907.

[8] S. A. Tobias and W. Fishnick, "The chatter of lathe tools under orthogonal cutting conditions," *Transactions of the American Society of Mechanical Engineers*, vol. 80, pp. 1079–1086, 1958.

[9] H. E. Merritt, "Theory of self-excited machine tool chatter, condition to machine tool chatter research-1," *Transactions of the American Society of Mechanical Engineers, Journal of Engineering for Industry*, vol. 87, pp. 447–454, 1965.

[10] S. Kato and E. Marui, "On the cause of regenerative chatter due to workpiece deflection," *Transactions of the American Society of Mechanical Engineers, Journal of Engineering for Industry*, vol. 96, pp. 179–186, 1974.

[11] D. W. Wu and C. R. Li, "An analytical model of cutting dynamics," *Transactions of the American Society of Mechanical Engineers, Journal of Engineering for Industry*, vol. 107, pp. 107–188, 1985.

[12] Y. Altintas, *Manufacturing Automation, Metal Cutting Mechanics, Machine Tool Vibrations, and CNC Design*, Cambridge University Press, New York, 2000.

[13] E. Budak and Y. Altintas, "Analytical prediction of chatter stability in milling. Part I: general formulation," *Trans. ASME, Journal of Dynamic Systems, Measurement, and Control*, vol. 120, pp. 22–30, 1998.

[14] E. Budak and Y. Altintas, "Analytical prediction of chatter stability in milling. Part II: application of the general formulation to common milling systems," *Trans. ASME, Journal of Dynamic Systems, Measurement, and Control*, vol. 120, pp. 31–36, 1998.

[15] N. H. Hanna and S. A. Tobias, "A theory of nonlinear regenerative chatter," *Transactions of American Society of Mechanical Engineers, Journal of Engineering for Industry*, vol. 96, pp. 247–255, 1974.

[16] L. Vela-Martinez, J. C. Jáuregui-Correa, O. M. González-Brambila, and H. R. Gilberto, "Instability conditions due to structural nonlinearities in regenerative chatter," *Nonlinear Dynamics*, vol. 56, pp. 415–427, 2009.

[17] N. Deshpande and M. S. Fofana, "Nonlinear regenerative chatter in turning," *International Journal of Computer Integrated Manufacturing*, vol. 17, pp. 107–112, 2001.

[18] G. Stepan, T. Insperger, and R. Szalai, "Delay, parametric excitation, and the nonlinear dynamics of cutting process," *International Journal of Bifurcation and Chaos*, vol. 15, no. 9, pp. 2783–2798, 2005.

[19] J. R. Pratt, *Vibration Control for Chatter Suppression*, Ph.D. Thesis, Virginia Polytechnic Institute and State University, Blacksburg, VA, 1997.

[20] H. Moradi, M. R. Movahhedy, and G. Vossoughi, "Bifurcation analysis of milling process with tool wear and process damping: regenerative chatter with primary resonance," *Nonlinear Dynamics*, vol. 70, no. 1, pp. 481–509, 2012.

[21] H. Moradi, G. Vossoughi, M. R. Movahhedy, and T. A. Mohammad, "Forced vibration analysis of the milling process with structural nonlinearity, internal resonance, tool wear and process damping effects," *International Journal of Non-linear Mechanics*, vol. 54, pp. 22–34, 2013.

[22] H. Moradi, M. R. Movahhedy, and G. Vossoughi, "Dynamics of regenerative chatter and internal resonance in milling process with structural and cutting force nonlinearities," *Journal of Sound and Vibration*, vol. 331, pp. 3844–3865, 2012.

[23] P. N. Rao, U. R. K. Rao, and J. S. Rao, "Towards improved design of boring bars part 1: dynamic cutting force model with continuous system analysis for the boring bar," *Journal of Machine Tools Manufacture*, vol. 28, no. 1, pp. 33–44, 1988.

[24] L. Andren, L. Hakansson, A. Brandt, and I. Claesson, "Identification of dynamic properties of boring bar vibrations in a continuous boring operation," *Journal of Mechanical Systems and Signal Processing*, vol. 18, no. 4, pp. 869–901, 2004.

[25] L. Andren, L. Hakansson, A. Brandt, and I. Claesson, "Identification of motion of cutting tool vibration in a continuous boring operation-correlation to structural properties," *Journal of Mechanical Systems and Signal Processing*, vol. 18, pp. 903–927, 2004.

[26] B. Moetakef-Imani and N. Z. Yussefian, "Dynamic simulation of boring process," *International Journal of Machine Tools and Manufacture*, vol. 49, pp. 1096–1103, 2009.

[27] M. Sortino, G. N. Totis, and F. Prosperi, "Modeling the dynamic properties of conventional and high-damping boring bars," *Mechanical Systems and Signal Processing*, vol. 34, pp. 340–352, 2013.

[28] B. Huang, "The drilling vibration behavior of a twisted microdrill," *ASME, Journal of Manufacturing Science and Engineering*, vol. 126, pp. 719–726, 2004.

[29] S. Filiz and O. B. Ozdoganlar, "Micro-end mill dynamics including the actual fluted geometry and setup errors-part I:

model development and numerical solution," *ASME, Journal of Manufacturing Science and Engineering*, vol. 130, no. 03, pp. 11–19, 2008.

[30] M. R. Movahhedy and P. Mosaddegh, "Prediction of chatter in high speed milling including gyroscopic effects," *International Journal of Machine Tools and Manufacture*, vol. 46, no. 9, pp. 996–1001, 2005.

[31] S. A. Tajalli, M. R. Movahhedy, and J. Akbari, "Chatter instability analysis of spinning micro-end mill with process damping effect via semi-discretization approach," *Acta Mechanics*, vol. 225, pp. 715–734, 2014.

[32] C. J. Li, A. G. Ulsoy, and W. J. Endres, "The effect of flexible-tool rotation on regenerative instability in machining," *Journal of Manufacturing Science and Engineering*, vol. 125, no. 1, pp. 39–47, 2003.

[33] W. Kim, A. Argento, and R. A. Scott, "Forced vibration and dynamic stability of a rotating tapered composite Timoshenko shaft: bending motions in end-milling operations," *Journal of Sound and Vibration*, vol. 246, no. 4, pp. 583–600, 2001.

[34] M. R. Shad, G. Michon, and A. Berlioz, "Modeling and analysis of nonlinear rotordynamics due to higher order deformation in bending," *Applied Mathematical Modelling*, vol. 35, pp. 2145–2159, 2011.

[35] A. H. Nayfeh and P. F. Pai, *Linear and Nonlinear Structural Mechanics*, John Wiley & Sons, New York, 2004.

[36] A. H. Nayfeh, *Introduction to Perturbation Techniques*, Wiley-Interscience, New York, 1981.

[37] D. A. Saravanos, D. Varelis, T. S. Plagianakos, and N. Chrysochoidis, "A shear beam finite element for the damping analysis of tubular laminated composite beams," *Journal of Sound and Vibration*, vol. 291, pp. 802–823, 2006.

[38] G. Tlusty, *Manufacturing Process and Equipment*, Prentice-Hall, Englewood, 2000.

Hindawi
Shock and Vibration
Volume 2021, Article ID 6793351, 10 pages
https://doi.org/10.1155/2021/6793351

Research Article

Generation and Evolution Conditions of Polygonal Wear of High-Speed Wheel

Yahong Dong [1,2,3] **and Shuqian Cao** [2,3]

[1]*School of Mechanical and Electrical Engineering, Lanzhou Jiaotong University, Lanzhou, Gansu, China*
[2]*Department of Mechanics, School of Mechanical Engineering, Tianjin University, Tianjin, China*
[3]*Tianjin Key Laboratory of Nonlinear Dynamics and Control, Tianjin, China*

Correspondence should be addressed to Shuqian Cao; sqcao@tju.edu.cn

Received 17 September 2021; Accepted 20 October 2021; Published 20 November 2021

Academic Editor: Jiaqiang E

Wheel polygonal wear has long been a problem that confused the safety of railway operation which has important theoretical value and research significance. In this paper, the conditions of polygonal wear of high-speed wheel are analyzed based on the wear model and verified by the field measured data. Considering the wheel track interaction caused by rotation, a finite element model of wheelset rotor dynamics is established. The effects of rotor speed, mass eccentricity, wheelset, and track flexibility on the vibration characteristics of wheelset rotor system and wheel polygonal wear characteristics are analyzed by beam element and solid element, respectively. The results show that the wheel longitudinal vibration is the main reason of wheel polygonal wear, and the wheel polygonal wear follows the law of "constant frequency and divisible." Its "constant frequency" comes from the wheel track contact vibration, which stimulates the third-order vertical bending vibration of wheelset and the eighth-order coupled bending vibration of track, and the order is equal to the ratio of "constant frequency" to the wheelset rotation frequency.

1. Introduction

Polygonal wear of high-speed wheel has long troubled the safe operation of railway [1]. It not only arouses harmful vibration to the vehicle track system, causing damage or failure of vehicle and track components, but also increases vibration and noise during operation which can reduce the comfort of passengers and disturb the lives of residents along the line. At present, researchers have carried out relevant research on the wheel polygon problem by means of simulation or field test.

Meywerk [2] established a flexible wheelset model running on a flexible track, considering wheel track vibration in simulation. It was found that the first and second bending modes of the wheelset played an important role in the growth of polygon. Johansson and Andersson [3] found through a large number of field tests and numerical simulation that the fixed wavelength range of noncircular wheels is the vertical resonance zone of the vehicle track coupled system, which has high dynamic track stiffness. Wu et al. [4] established the multibody dynamics model of vehicle/track coupled and found that the high frequency vibration of wheel track contact may be the main reason for the generation of wheel polygon, and the main reason for the high frequency vibration in the frequency range of 500–800 Hz is the bending vibration modes of the track segment of two wheelsets. Ye et al. [5] pointed out that the wheel defects can cause or exacerbate wheel polygonization. Torstensson et al. [6] established the structural dynamics model of rotating flexible wheelsets considering the inertia effect of wheel rotation and found that more accurate results could be obtained by using the flexible rotating wheelset model to study high frequency contact forces. Brommundt [7] proposed that the evolution mechanism of wheel out of round is the result of interaction between initial wheel OOR (out of round) and the moment of inertia. Meinke [8] adopted the elastic beam element as the axle to establish a wheelset dynamics model with 40 degrees of freedom connecting the

rigid wheel and brake disc and proposed that the dynamics of high-speed wheelset is determined by the gyroscopic moment and the inertial moment, which is different from the traditional wheelset. Jin et al. [9] made statistics on the polygonal wear test results of hundreds of wheels shortly after rotary cutting and found that eccentric wear occurred in 96% of wheels, and the proportion of other harmonic wear was 69% of 11th order, 58% of 6th order, and 35% of 3rd order, respectively.

Most of the existing studies are based on statistical analysis of field measured data or theoretical simulation from the perspective of wheel track or vehicle track coupled dynamics, and some conclusions related to wheelset bending or track bending modes have been found. However, the polygonal problem of wheel is prominent under high-speed operation increasingly, so the essence of the problem should be in the structure or characteristics of wheelset itself. Literature [6–8] all had put forward the necessity of considering flexible rotation to study wheel OOR, but few studies have been carried out based on rotor dynamics theory. The factors that affect the generation and development of polygon are very complicated, and there is no consistent understanding so far.

Therefore, this paper studies the generation and evolution mechanism of high order polygon wear of high-speed railway. Based on the wear model, the conditions of polygon wear of wheels were analyzed by theoretical analysis and field data verification. The finite element model of wheel-rotor dynamics considering mass eccentricity was established. Through the simulation and verification of beam element and solid element, the evolution law of "constant frequency and integer multiple" was found. The influence of wheel speed and wheel track flexibility on the generation and evolution of polygonal wear of wheels was studied. It provides an innovative perspective and theoretical basis for understanding the mechanism of generation and evolution of polygonal wear.

2. Theoretical Analysis and Verification

Firstly, based on the measured data of polygonal wear of wheel and the material wear model of wheel, the circular wear depth model of wheel was determined, from which the generation conditions of polygonal wear of wheel were found. Then, the wheelset rotor dynamic model was established to verify the vibration characteristics of polygonal wear of wheel, and combined with the established circumferential wear depth model, the evolution conditions and influencing factors of polygonal wear of wheel were studied. Figure 1 shows the research process of the generation and evolution conditions of wheel polygonal wear.

2.1. Circumferential Wear Model of the Wheel. Archard model and work model are usually used in polygonal wear prediction. The research shows that the trend of wheel polygonal generation and evolution corresponding to Archard model and wear work model are the same basically, but the wear coefficient in Archard model is relatively large, while the results of wear work model are closer to the field measured data, and the calculation efficiency is higher [10]. Therefore, the wear work model is adopted in the calculation of wheel wear in this paper.

The model based on wear work assumes that the wear mass Δm is proportional to the wear energy that is dissipated in wheel track contact due to friction. The basic calculation principle is as follows.

Based on the wear work model, it is assumed that the wear mass of wheel contact spot is proportional to the friction work in the contact spot.

$$\Delta m = K_w \cdot W_w, \tag{1}$$

where Δm and K_w are the wear mass of the wheel and the wear coefficient which is related to the wear energy per unit contact area in the contact spot and W_w is the wear work in the contact spot.

The most realistic simulation of wheel wear is in the 3D and real time, which means that the 3D geometry of the wheel tread should change with each wheel rotation. However, this is either difficult in technology or time-consuming. Moreover, polygonal wear of wheel mainly occurs in the circumferential direction. In order to simplify the simulation, some assumptions are listed as follows:

(1) Assuming that the lateral profile of the wheel is unchanged, only the change of the circumference profile of the wheel is concerned

(2) Assuming that the instantaneous wear of each contact spot on the tread is evenly distributed, calculate the average wear depth

(3) In short-term calculation, the change of wheel and track profile can be ignored

Literature [11] points out that wheelset longitudinal vibration has a significant impact on the profile and wear depth of wheel tread, and the wear is mainly concentrated near the rolling circle. If the radii of the wheel rolling circle θ are $R\ (\theta - 2\pi)$ and $R\ (\theta)$, respectively, the wear depth is $\Delta r = R(\theta - 2\pi) - R(\theta)$. In addition, the ware mass Δm is the product of the wear depth Δr, the wear area A_w, and the material density ρ. The wear work W_w is the product of the longitudinal creep force F_x and the relative sliding distance between wheel and track s_w. Combined with (1), the calculation formula of wear depth Δr can be obtained as

$$\begin{aligned}\Delta r &= R(\theta - 2\pi) - R(\theta) \\ &= \frac{\Delta m}{\rho A_w} \\ &= \frac{K_w . W_w}{\rho \cdot A_w} \\ &= K_w \frac{F_x \cdot s_w}{\rho \cdot b_w \cdot s_w} \\ &= K_w \frac{F_x}{\rho \cdot b_w},\end{aligned} \tag{2}$$

where b_w is the average width of the wear zone.

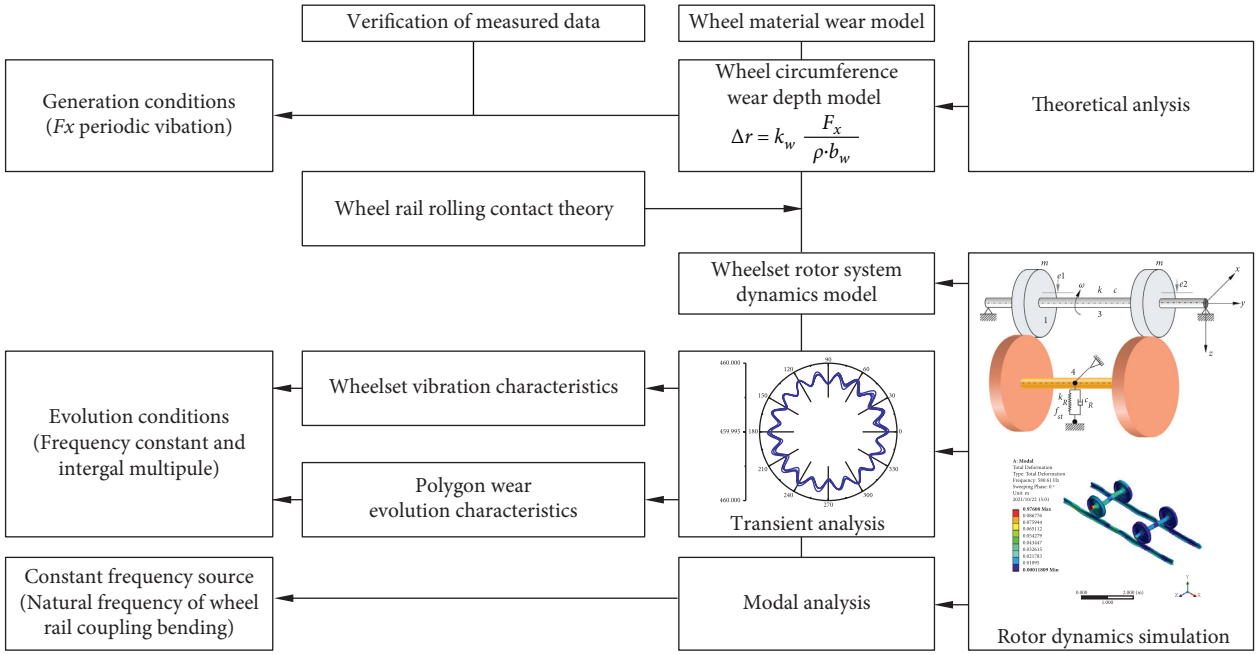

Figure 1: Research process of the generation and evolution conditions of wheel polygonal wear.

2.2. Conditions of Wear. It can be seen from formula (2) that wheel wear is related to longitudinal creep force F_x. When the longitudinal creep force changes periodically according to a certain frequency, it will lead to circumferential non-uniform wear with periodic change of wear depth Δr, resulting in polygon. When the longitudinal creep force is at its maximum, the wear occurs only once in a cycle of longitudinal wheel vibration.

If the longitudinal vibration frequency of the wheel is f_1 and the wheel rotation frequency is f_2, then the time interval between the two adjacent wear peaks is $1/f_1$ and the wheel rotation cycle is $1/f_2$, and the number of wear peaks m within one rotation of the wheel is

$$m = \frac{f_1}{f_2}. \tag{3}$$

The relation between wheel rotation frequency f_2 and train running speed is $f_2 = v/(\pi D)$; then it can be known from equation (3) that the longitudinal wheel vibration frequency f_1 meets

$$f_1 = \frac{mv}{\pi D}, \tag{4}$$

where v is the speed of vehicle and D is the nominal diameter.

2.3. Test Verification. Field measurement of a certain type of EMU wheel shows that when the speed is 300 km/h, there are three high wear periods in the wheel diameter life cycle from 920 mm to 830 mm, corresponding to the wheel diameters of 915 mm, 875 mm, and 830 mm, respectively. In these three wheel diameter stages, the measured wheel polygonal wear order is 20, 19, and 18, respectively [9].

Based on formula (4), wheel angular velocity ω, rotation frequency f_2, and longitudinal vibration frequency f_1 can be calculated from the above data. The result can be seen in Table 1.

It can be seen from Table 1 that the longitudinal vibration frequency corresponding to wheel polygonal wear is around 580 Hz; that is, longitudinal vibration of wheel is the basic condition for generating wheel polygon wear, and its vibration frequency is fixed. This result verifies the research conclusion that wheel polygon wear has "constant frequency" mechanism [11].

3. Polygonal Wear Model of the Wheel

3.1. Wheelset Rotor Dynamics Model. The above analysis and related literature show that the longitudinal creep vibration of wheelset is the main reason for the generation and evolution of polygonal wear of wheel. It is necessary to analyze the state of longitudinal vibration of wheel and determine the range of parameters leading to longitudinal vibration of wheel.

The nonlinear problem of vehicle is very complicated due to its large structure and many degrees of freedom. Modeling is often conducted according to the research needs with specific focus, and the nonfocus items can be appropriately simplified in general. Therefore, wheelset axle box device is selected as the analysis object in this paper, as shown in Figure 2. The dynamics model of wheelset rotor system includes wheel 1, wheel 2, and axle 3, as well as two large diameter axle disks 4 which are used to simulate track.

To analyze the basic characteristics of the rotor, it is assumed that

(1) The wheels are rigid disk

Table 1: Calculation parameters of wheelset rotor system.

Diameter D (mm)	Angular velocity ω (rad.s^{-1})	Rotation frequency f_2 (Hz)	Order (N)	Longitudinal frequency f_1 (Hz)
915	182.1	29.0	20	580.1
875	190.5	30.3	19	576.3
830	200.8	32.0	18	575.6

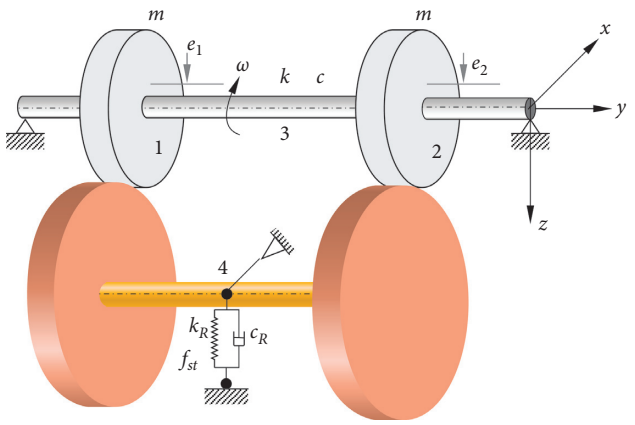

Figure 2: Dynamic model of wheelset rotor system.

(2) The axle is hollow with equal diameter, with a certain bending stiffness and infinite torsional stiffness, and both ends are supported by two identical bearings

(3) The bearing is simplified as hinged, and the mass is not considered

(4) The spring mass is equivalent to the track prepressure

As the left and right wheels are the same, one of them in Figure 2 is selected. $Oxyz$ is taken as the fixed coordinate The intersection O between the plane where the disk is located and the supporting points at both ends of the elastic axis is the origin of the fixed coordinate system, and x axis is along the axis of the rotor, and the plane where the disk is located is the Oxz coordinate reference plane, as shown in Figure 3.

In the figure, O_1 and C are the disk center of shape and mass, and the distance O_1C is the eccentricity e. The mass of the disk is m, and we select x (t) and z (t) as the generalized coordinates of the disk center of shape O_1.

The wheelset use centralized mass element to simulate, and the shaft segment is simulated by Timoshenko beam element, and only two end nodes (A and B) in the beam element are used. Wheel track contact force is used to simulate wheel track contact. Figure 4 is a schematic diagram of Timoshenko beam element.

The nodes A and B in the Timoshenko beam element have 6 degrees of freedom, respectively, which are the displacement and rotation angles of the nodes in the x, y, and z directions. The degree of freedom arrangement of beam elements is $u = [x_A, y_A, z_A, \theta_{xA}, \theta_{yA}, \theta_{zA}, x_B, y_B, z_B\, \theta_{xB}\, \theta_{yB}, \theta_{zB}]^{\mathrm{T}}$. Since the radial deformation of the joints in the model is much larger than its axial deformation, the axial and torsional deformation are ignored, and the degree of freedom of beam elements is simplified as $u = [x_A, z_A, \theta_{xA}, \theta_{zA}, x_B, z_B, \theta_{xB}, \theta_{zB}]^{\mathrm{T}}$. The dynamic equation of the whole rotor system can be expressed as

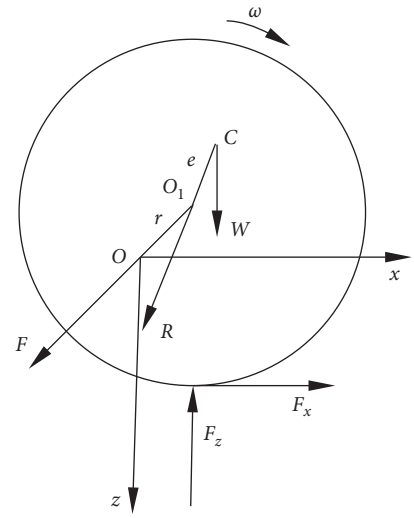

Figure 3: Disk instantaneous position and force.

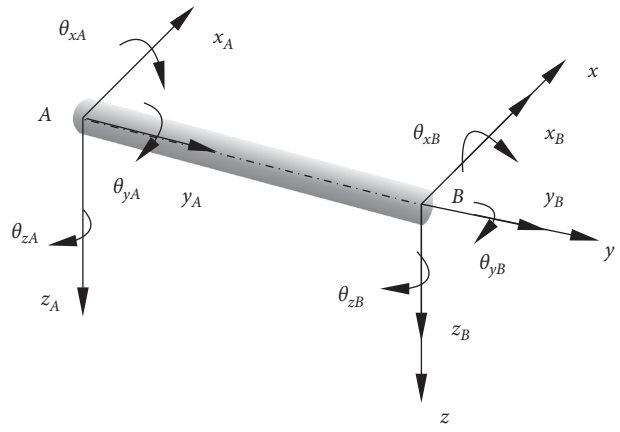

Figure 4: Timoshenko beam element.

$$M\ddot{u} + (C + G)\dot{u} + Ku = F_e + F_r, \tag{5}$$

where M, C, G, K, F_e, and F_r are the mass matrix, damping matrix, gyro matrix, stiffness matrix, unbalanced force vector, and wheel track contact force vector, respectively, and $\ddot{u}, \dot{u}, u$ are acceleration, velocity, and displacement vectors of nodes in the model, respectively.

3.2. Wheel Track Rolling Contact Force. There are many theoretical models that have been studied and developed of wheel track rolling contact, including Kalker linear theory, Kalker simplified theory, Kalker three-dimensional accurate theory, and Shen's theory, among which Kalker's simplified theory is most widely used in railway field. Therefore, this

paper carries out simulation analysis of wheel track rolling contact based on Kalker linear theory. The wheel track rolling contact force F_r can be decomposed into longitudinal creep force F_x and wheel track contact positive pressure F_z, which can be expressed as

$$\begin{cases} F_x = -\mathrm{Gab}C_{11}\xi, \\ F_z = k_R(f_{st} - z), \end{cases} \quad \xi = \frac{v - \omega \cdot R}{v}, \tag{6}$$

where G, a, and b are shear elastic modulus of material, long and short half axes of contact spot, respectively, and C_{11}, ξ, k_R, and f_{st} are Kalker coefficient, longitudinal creep rate, support stiffness, and precompression amount of elastic support, and v, R, and ω are speed of elastic support, radius of disk, and rotational angular velocity of wheelset.

According to the eccentricity of the contact ellipse and the integral of the first and second complete ellipses, the contact spot length and the short semiaxis length can be determined as [12]

$$\begin{cases} a = m_c \left[\dfrac{3\pi(\delta_1 + \delta_2)}{2\beta} F_z\right]^{1/3}, \\ b = n_c \left[\dfrac{3\pi(\delta_1 + \delta_2)}{2\beta} F_z\right]^{1/3}. \end{cases} \tag{7}$$

We have

$$\begin{cases} m_c = \left[\dfrac{2E_p}{\pi(1 - e_c^2)}\right]^{1/3}, \\ n_c = \left[\dfrac{2E_p\sqrt{1 - e_c^2}}{\pi}\right]^{1/3}, \\ \delta_i = \dfrac{1 - \nu^2}{\pi E_i}, \\ \beta = \dfrac{1}{R_{11}} + \dfrac{1}{R_{12}} + \dfrac{1}{R_{21}} + \dfrac{1}{R_{22}}, \end{cases} \tag{8}$$

where E_p is the complete elliptic integral of the second kind; E_c is eccentricity of contact ellipse; ν_i, E_i are Poisson's ratio and elastic modulus of contact i ($i = 1, 2$), respectively. R_{11}, R_{12}, R_{21}, R_{22} are the longitudinal and transverse principal radius of curvature of wheel and track along the contact coordinate system, respectively.

Zhao et al. found that the saturated creep force between wheel and track easily leads to the generation of polygon wear of wheel [13]. Therefore, the creep force saturation state is analyzed in this paper.

4. Simulation of Wheel Polygonal Wear

The shear modulus of wheel $G = 7.9 \times 10^{10}$ Pa, the Kalker coefficient $C_{11} = 5.10$, the longitudinal half-axle length of contact spot $a = 10$ mm, and the lateral half-axle length of contact spot $b = 5$ mm. Main parameters of wheelset rotor system were selected by referring to [14, 15] measured in 1.3, as shown in Table 2.

Table 2: Calculation parameters of wheelset rotor system.

Parameter	Values	Unit
The inner diameter of axle	60	mm
The outer diameter of axle	190	mm
Journal center distance	1956	mm
Rolling circle distance	1493	mm
Track stiffness k_R	20	MN.m^{-1}
Wheel track creep factor μ	0.25	
Material density	7860	kg/m^3
Elastic modulus	2.059×10^{11}	Pa
The wheel radius D	920	mm
Poisson's ratio	0.3	

4.1. Verification of Generation Conditions of Polygonal Wear. In order to verify the conclusion that wheelset longitudinal vibration based on the wear work model found in Section 1 is the basic condition for the generation of polygonal wear of wheels, the wheelset rotor dynamic finite element model in (5) is established. The wheelset rotation system is separated into 13 nodes, which are divided into 12 beam elements and 2 particle elements with 91 degrees of freedom in total. Bearing constraints are applied to nodes 1 and 13 corresponding to the left and right bearings, respectively. We also added the node function load corresponding to formula (6) of wheel track contact force on key points 2 and 4 corresponding to left and right wheels. We set the wheel mass and its eccentricity on key points 2 and 4 corresponding to the left and right wheels and added rotation frequency f_2 on the beam rotor.

In order to observe the influence of rotor speed and eccentricity on the vibration characteristics, transient analysis was conducted when $f_2 = 25.2$~58 Hz and eccentricity $e = 0.01$ mm, 0.10 mm, 0.50 mm, and 1.00 mm. The three-dimensional spectra of the vertical displacement at the left wheel of the wheelset rotor system (Figure 5) and the spectra of the rotation frequency of 30 Hz (equivalent to 300 km/h) were obtained (Figure 6).

Figure 5 shows that wheelset vibration displacement is mainly composed of rotation frequency and high frequency under different eccentricity and rotor speed. With the increase of rotor speed, the degree of dynamic unbalance is aggravated due to the influence of flexibility and eccentricity of wheelsets, so the amplitude of both frequencies increases. The value of rotation frequency increases with the increase of rotor speed and eccentricity, but the high frequency value is always the same (approximately equal to 580 Hz). The results of this study confirm that the "constant frequency" characteristics of polygonal wheel wear found in theoretical analysis and field tests.

When the rotation frequency is 30 Hz, the spectrum of different eccentricity is shown in Figure 6. With the decrease of eccentricity, the amplitude of the rotation frequency gradually decreases until it disappears. The reason is that the degree of wheelset dynamic unbalance is improved. However, the constant frequency is 579.56 Hz, and the corresponding amplitude changes little with the change of eccentricity, indicating that this frequency component is the "constant frequency" mentioned in the previous test and theoretical analysis.

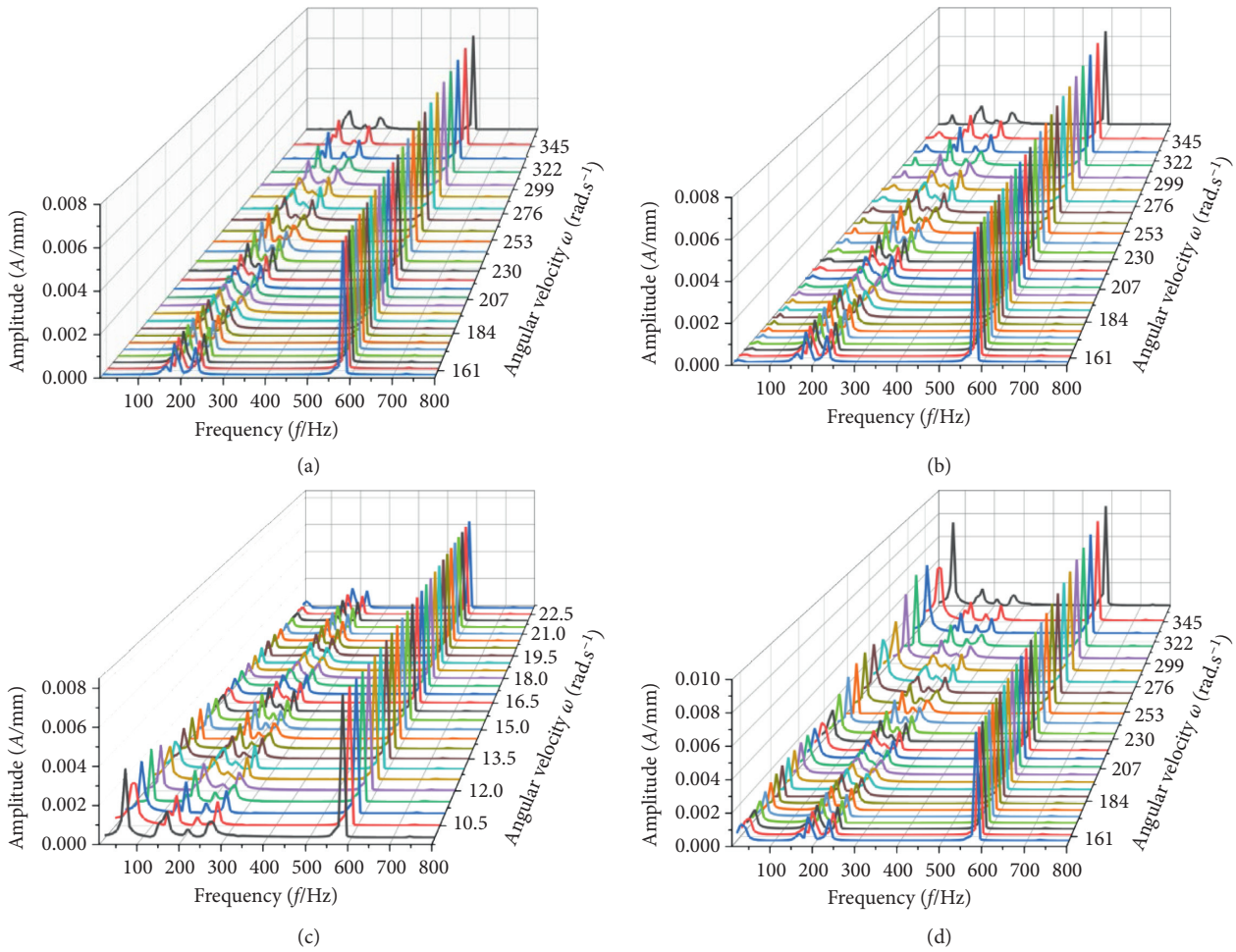

Figure 5: Spectrum diagram under different eccentricity. (a) $e = 0.01$ mm. (b) $e = 0.10$ mm. (c) $e = 0.50$ mm. (d) $e = 1.00$ mm.

The amplitude of both components is increased. The rotation frequency value increases with the increase of rotor speed, while the high frequency value is about 580 Hz, which has nothing to do with rotor speed. The results of this study confirm the "frequency fixed" characteristics of polygonal wear found in theoretical analysis and field tests.

As can be seen from Figure 6, when the rotation frequency is 30 Hz, with the decrease of eccentricity, the amplitude corresponding to the rotation frequency gradually decreases until it disappears. However, the constant frequency is 579.56 Hz, and its amplitude is almost unchanged; that is, the constant frequency has nothing to do with the eccentricity.

4.2. Determination of Evolution Conditions of Polygonal Wear. The above finite element simulation analysis verifies that the longitudinal vibration of wheel is the basic condition for generating polygonal wear of wheel and determines the longitudinal creep force F_x. By substituting it into (2), the characteristics of wheel polygonal wear can be drawn, and then the conditions for the evolution of wheel polygonal wear can be determined.

In order to study the influence of rotor speed on polygonal wear of wheels, transient analysis was carried out at 250 km/h~350 km/h, respectively, and the circumferential wear of wheels was drawn by combining with the formula of wear depth Δr in formula (2). The wear shapes near the order $N = 18$ and 23 are shown in Figure 7.

According to Figure 7, when the speeds are 240 km/h and 260 km/h, the wheel wear will be gradually uniform after a long run. However, when the speed is 262 km/h and 335 km/h, the wheels have obvious polygonal wear of 18th order and 23rd order, respectively. By analyzing the frequencies at different speeds, it is found that polygonal wear occurs when the "constant frequency" 580 Hz is an integer multiple of the rotation frequency, and uniform wear occurs when the wheel is not an integer multiple. It can be seen that when the longitudinal vibration frequency of the wheel is an integer multiple of the wheel rotation frequency, the polygonal wear of the wheel will evolve rapidly. Therefore, if the relationship is destroyed, the generation and development of polygon can be effectively suppressed, and if it can be run at constant speed within the life cycle of wheel diameter, it will be considered as one of the methods.

So far, we have found that the condition for the evolution of polygon wear of wheel is that the longitudinal vibration of

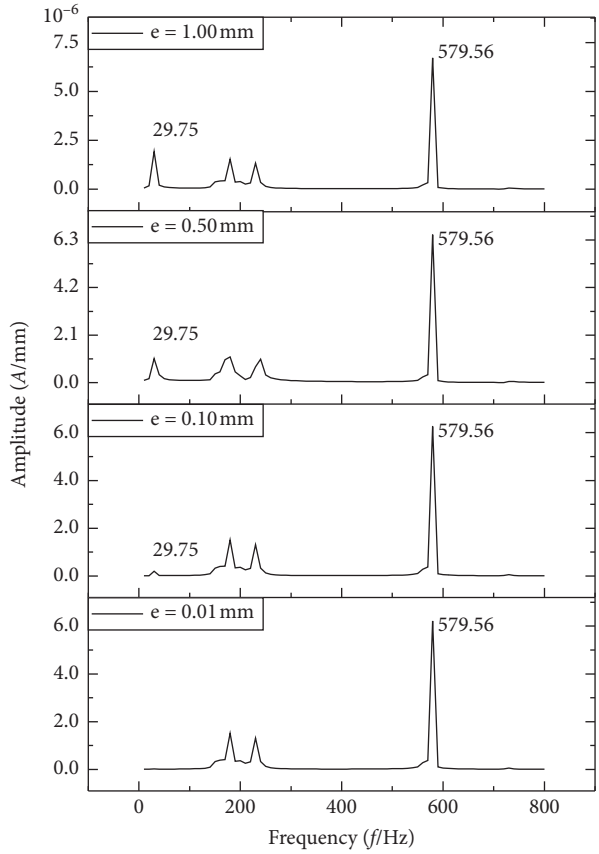

Figure 6: Spectrum diagram under different eccentricity with $f_2 = 30$ Hz.

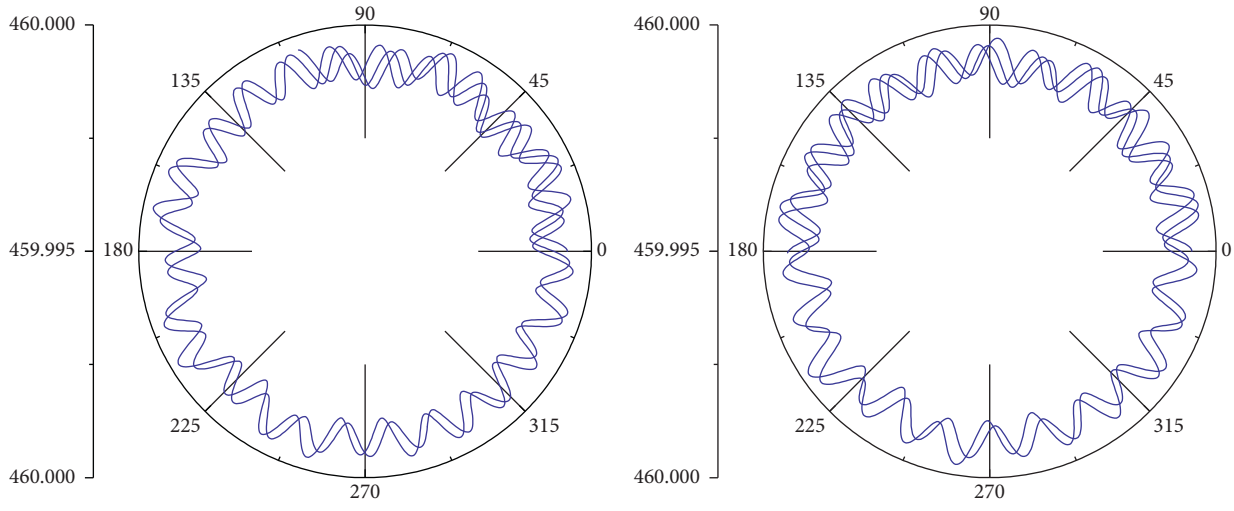

Figure 7: Continued.

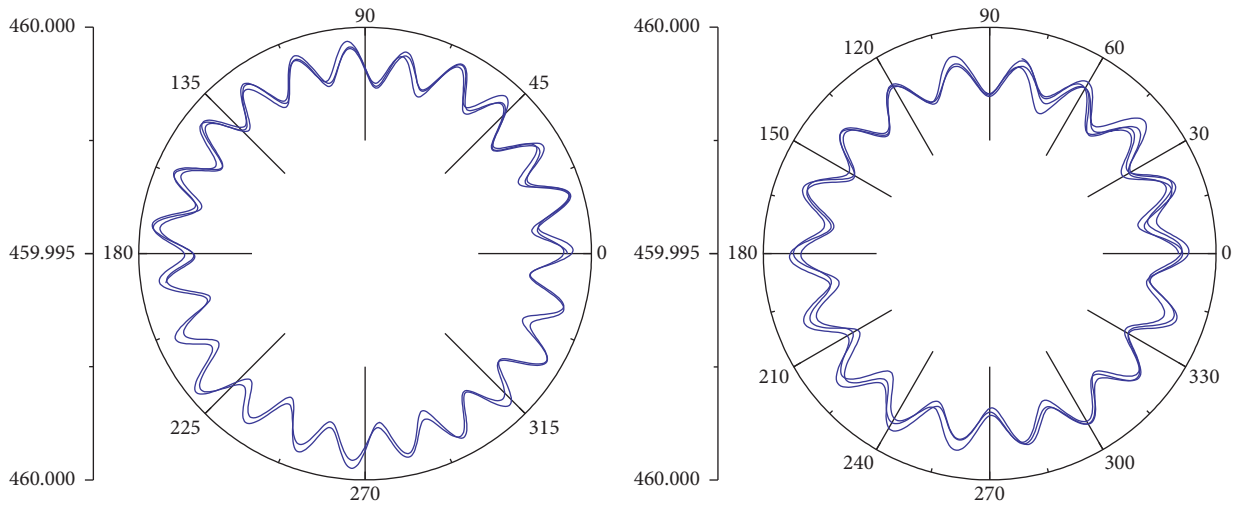

Figure 7: Wheel wear shape at different speeds. (a) $v = 240$ km/h, $N = 25.22$. (b) $v = 260$ km/h, $N = 23.2$. (c) $v = 262$ km/h, $N = 23$. (d) $v = 335$ km/h, $N = 18$.

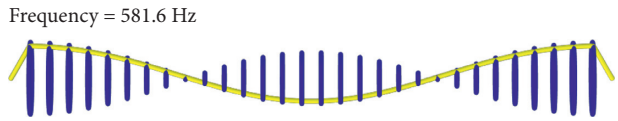

Figure 8: Vibration mode of third-order wheelset bending.

Table 3: Natural frequency of rotor system of wheelset (Hz).

Rotation effect is not considered			Rotation effect is considered
Rigid wheel flexible track	Flexible wheel rigid track	Flexible wheel flexible track	Flexible wheel flexible track
519.4	567.16	565.42	565.42
559.49	567.19	580.73	580.56
574.77	577.74	583.07	582.93
593.11	578.03	584.48	584.33
605.9	585.43	585.47	585.7
608.93	585.45	586.78	587
622.27	748.22	591.33	591.36
648.97	769.92	621.8	621.81

wheelset and the wheel rotation frequency follow the law of "constant frequency and divisible."

5. Determination of Constant Frequency Source

Through the statistical analysis of the measured data and the verification of the theoretical simulation, it is found that the wheel polygonal wear follows the rule of "constant frequency and integer multiple," but the source of this constant frequency remains to be further studied. Therefore, we use beam element and solid element to conduct modal analysis, respectively, and try to find the source of constant frequency around 580 Hz.

The beam element finite element model established in (5) is used for modal analysis, and the first 10 order modal natural frequencies are obtained. The vibration mode of the wheelset system at about 580 Hz is shown in Figure 8 which shows that the natural frequency of this order is 581.6 Hz, and the corresponding vibration mode is third-order wheelset bending.

In order to study the relationship between constant frequency and track, wheelset, and their coupling effect, we take 60 kg track section, the length of 6.0 m, sleeper spacing of 625 mm, fastener width of 170 mm, fastener vertical stiffness of 20 MN/m, bogie fixed wheelbase of 2.5 m, and wheel track wear coefficient $\mu = 0.25$. The solid finite element model of wheel track coupling is established for modal analysis. The influence of rotation effect on the natural frequency of wheel track coupling system is studied under three conditions: flexible wheelset and rigid track, rigid wheelset and flexible track, and flexible wheelset and flexible track. The specific analysis results are shown in Table 3 and Figure 9.

As Table 3 shows, it can be seen from contrasting the natural frequencies of rigid wheelset and flexible track and flexible wheelset and rigid track which do not consider the

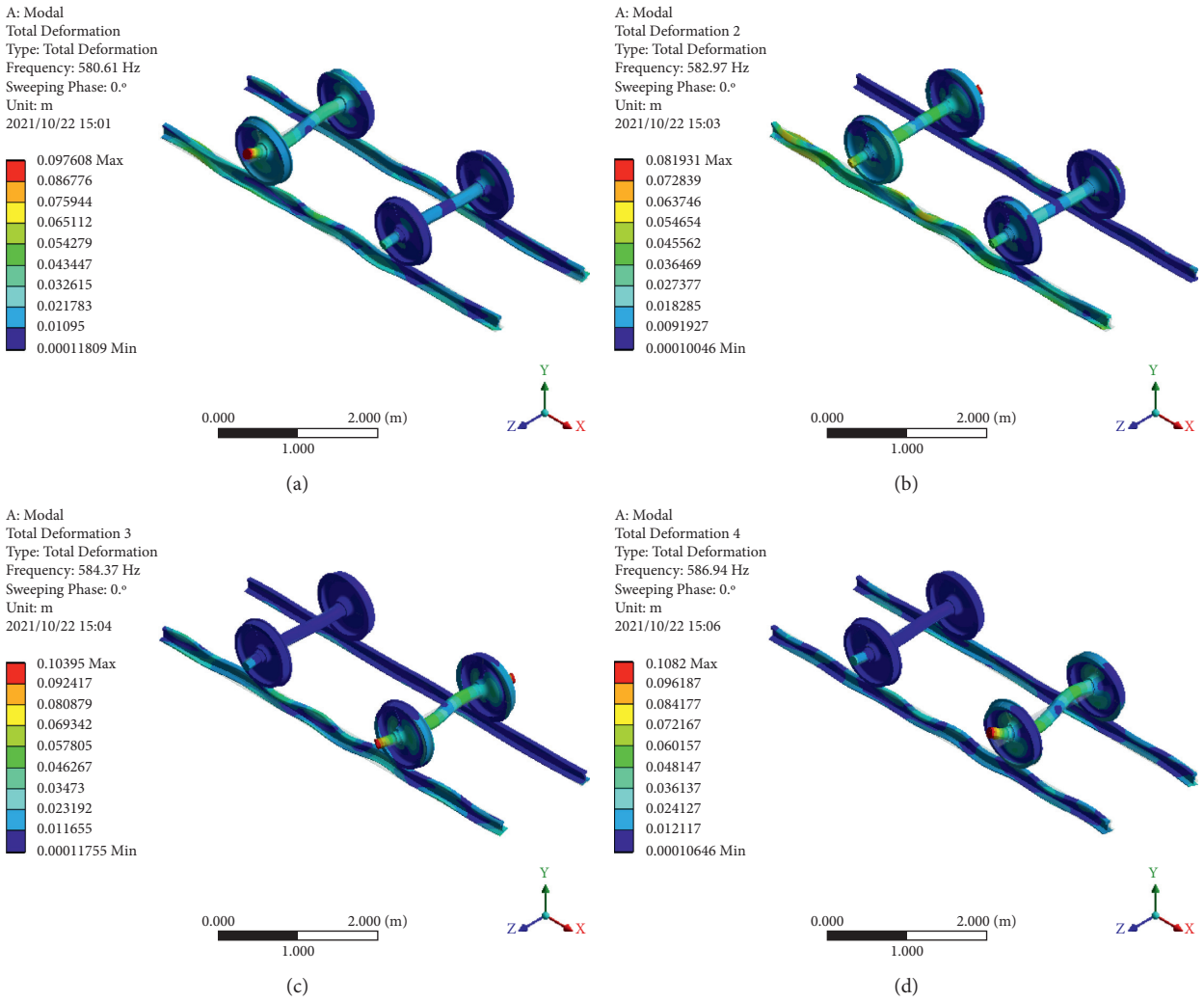

FIGURE 9: Vibration mode of wheel track coupling system with $\omega = 180$ rad/s. (a) Wheelset 3rd vertical bending and track 8th lateral bending. (b) Wheelset 3rd vertical bending and track 8th lateral bending. (c) Wheelset 3rd vertical bending and track 8th lateral bending and vertical bending. (d) Wheelset 3rd vertical bending and track 8th vertical bending.

rotation effect that flexible wheelset and rigid track show more natural frequency close to the constant frequency of 580 Hz. It can be shown that the track flexibility has little effect on the natural frequency near the constant frequency, while the wheelset's contribution to the constant frequency is greater than that of the track. This can also be seen in the analysis of flexible wheelset and flexible track. Although the contribution of track flexibility to "constant frequency" is little, it is more realistic to consider both wheelset and track as flexible. Therefore, when we study the influence of different rotor speeds on the natural frequency of the wheel track coupling system, we consider wheel track as flexible. Considering the rotation effect, the natural frequencies of the wheel track coupling system at different rotor speeds all show five values close to "constant frequency." It shows that the rotor speed has little influence on the natural frequency, which is consistent with the previous simulation analysis.

The vibration modes of flexible wheelset and track at speed of 180 rad/s are shown in Figure 9. The flexible wheel track vibration near the "constant frequency" corresponds to the third-order vertical bending of the wheelset, while the track presents 8th-order lateral bending, 8th-order lateral bending torsion coupling, and 8th-order vertical bending, respectively.

To sum up, the reason for the "constant frequency" phenomenon of about 580 Hz is mainly the third-order vertical bending of wheelset and the 8th-order coupling bending of track. The track flexibility and speed have a little effect on the "constant frequency" of wheel track coupling system.

6. Conclusion

The theoretical analysis and measured verification of the generation and evolution conditions of wheel polygonal wear are carried out based on the wear work model, and the wheelset rotor dynamics model considering wheel eccentricity is established for numerical simulation verification. The following conclusions are obtained:

(1) The generation and evolution of wheel polygon wear present the characteristics of "constant frequency and integer multiple." The longitudinal vibration of wheelset is the basic condition for the generation of wheel polygonal wear, and its vibration frequency is constant. When the frequency is the integral multiple of wheel rotation frequency, the wheel polygonal wear evolves rapidly.

(2) The "constant frequency" of wheel polygonal wear is consistent with the natural frequency of the third-order vertical bending of wheelset excited by wheel rotation and the eighth-order coupled bending vibration of track.

(3) Constant rotor speed operation in the life cycle of wheel diameter can relieve the wheel polygon fault.

Data Availability

The underlying data supporting the results of your study can be found in References.

Conflicts of Interest

The authors declare that they have no conflicts of interest.

Acknowledgments

The authors acknowledge the financial support from the National Natural Science Foundation of China (no. 11872045), Youth Science Foundation of Gansu Province (no. 20JR10RA262), and Tianyou Innovation Team of Lanzhou Jiaotong University (no. TY202006).

References

[1] D. W. Barke and W. K. Chiu, "A review of the effects of out-of-round wheels on track and vehicle components," *Proceedings of the Institution of Mechanical Engineers - Part F: Journal of Rail and Rapid Transit*, vol. 219, no. 3, pp. 151–175, 2005.

[2] M. Meywerk, "Polygonalization of railway wheels," *Archive of Applied Mechanics*, vol. 69, no. 2, pp. 105–120, 1999.

[3] A. Johansson and C. Andersson, "Out-of-round railway wheels-a study of wheel polygonalization through simulation of three-dimensional wheel-rail interaction and wear," *Vehicle System Dynamics*, vol. 43, no. 8, pp. 539–559, 2005.

[4] X. Wu, S. Rakheja, W. Cai, M. Chi, A. K. W. Ahmed, and S. Qu, "A study of formation of high order wheel polygonalization," *Wear*, vol. 424-425, pp. 1–14, 2019.

[5] Y. Ye, D. Shi, P. Krause, Q. Tian, and M. Hecht, "Wheel flat can cause or exacerbate wheel polygonization," *Vehicle System Dynamics*, vol. 58, no. 10, pp. 1575–1604, 2019.

[6] P. T. Torstensson, J. C. O. Nielsen, and L. Baeza, "Dynamic train-track interaction at high vehicle speeds-Modelling of wheelset dynamics and wheel rotation," *Journal of Sound and Vibration*, vol. 330, no. 22, pp. 5309–5321, 2011.

[7] E. Brommundt, "A simple mechanism for the polygonalization of railway wheels by wear," *Mechanics Research Communications*, vol. 24, no. 4, pp. 435–442, 2012.

[8] P. Meinke and S. Meinke, "Polygonalization of wheel treads caused by static and dynamic imbalances," *Journal of Sound and Vibration*, vol. 227, no. 5, pp. 979–986, 1999.

[9] X. S. Jin, Y. Wu, S. L. Liang, Z. F. Wen, X. W. Wu, and P. Wang, "Analysis of polygonal wear, mechanism, influence and countermeasures of high-speed train wheels," *Journal of Mechanical Engineering*, vol. 56, no. 16, pp. 118–136, 2020.

[10] B. Peng, S. Iwnicki, P. Shackleton, and D. Crosbee, "Comparison of wear models for simulation of railway wheel polygonization," *Wear*, vol. 436-437, no. 203010, pp. 1–13, 2019.

[11] W. Liu, W. Ma, S. Luo, and Y. Tian, "The mechanism of wheelset longitudinal vibration and its influence on periodical wheel wear," *Proceedings of the Institution of Mechanical Engineers - Part F: Journal of Rail and Rapid Transit*, vol. 232, no. 2, pp. 396–407, 2018.

[12] Q. H. Guan, X. Zhao, Z. F. Wen, and X. S. Jin, "Calculation method of normal contact stiffness based on Hertz contact theory," *Journal of Southwest Jiaotong University*, vol. 56, no. 4, pp. 883–890, 2021.

[13] X. N. Zhao, G. X. Chen, J. Z. Lv, S. Zhang, B. W. Wu, and Q. Zhu, "Study on the mechanism for the wheel polygonal wear of high-speed trains in terms of the frictional self-excited vibration theory," *Wear*, vol. 426-427, pp. 1820–1827, 2019.

[14] X. N. Zhao, G. X. Chen, Z. Y. Huang, and C. G. Xia, "Study on the different effects of power and trailer wheelsets on wheel polygonal wear," *Shock and Vibration*, vol. 2020, Article ID 2587152, 12 pages, 2020.

[15] W. B. Cai, M. R. Chi, X. W. Wu et al., "Experimental and numerical analysis of the polygonal wear of high-speed trains," *Wear*, vol. 440-441, no. 2203079, pp. 1–12, 2019.